Complementary Computational Chemistry and Surface Science Experiments of Reaction Pathways in Aluminum Chemical Vapor Deposition

by

Brian Gerald Willis

Submitted to the Department of Chemical Engineering
in partial fulfillment of the requirements of the degree of

Doctor of Philosophy

at the

MASSACHUSETTS INSTITUTE OF TECHNOLOGY

February 1999

Author. ....
Department of Chemical Engineering
January 27, 1999

Certified
by.....
Klavs F. Jensen
Lammot Du Pont Professor
Department of Chemical Engineering
Thesis Supervisor

Accepted by.....
Robert E. Cohen
St. Laurent Professor of Chemical Engineering
Chairperson, Committee for Graduate Students

Complementary Computational Chemistry and Surface Science Experiments of Reaction Pathways in Aluminum Chemical Vapor Deposition

Brian G. Willis

Abstract

Continued advances in the semiconductor industry will require the introduction of new materials and processes concurrent with shrinking device dimensions. These simultaneous demands drastically reduce margins for error and necessitate an increasingly quantitative understanding of semiconductor processes. Leaders of the semiconductor industry have recognized these challenges and featured atomistic process modeling as one of the "Difficult Challenges" for designs below 100 nm, predicted beyond the year 2006. Among these tasks, obtaining detailed, quantitative understanding of process chemistry and physics has been identified as on of the biggest hurdles. Another "chief roadblock" is linking atomistic reaction models to reactor scale process simulations. Process modeling includes simulations of reactor transport, thin film growth, morphology, and uniformity, and device feature profile evolution (how well desired features are grown). A key ingredient to processes modeling, whether atomistic or macroscopic, is knowledge of the elementary reaction pathways and chemical intermediates, and reaction thermodynamics and kinetics. Quantum chemistry methods present power tools to investigate these molecular properties for both gas phase and surface reactions. Along with pioneering efforts in applying these tools to semiconductor processes come issues such as understanding accuracy, how to approach a given problem, and defining problems into practical sizes. To this end, a combined experimental/theoretical study of aluminum chemical vapor deposition has been performed. Both conventional *ab initio* and more recent density functional theory methods (DFT) have been investigated and evaluated.

Aluminum chemical vapor deposition (CVD) is a process of interest for semiconductor metalization. Aluminum has been the workhorse metal for interconnect applications since the dawning age of the semiconductor industry. Although aluminum is

traditionally deposited with advanced physical vapor deposition (PVD) techniques, new deposition methods, such as CVD, are required as characteristic feature sizes move into the nanometer range. In the present study, a combined experimental/theoretical approach has been implemented to investigate both vapor phase and surface reaction pathways of the aluminum CVD precursor dimethylaluminum hydride (DMAH). DMAH is arguably the best aluminum CVD precursor available, but it has complications including a puzzling liquid and vapor phase chemistry, and an unknown surface chemistry. Detailed knowledge of the deposition process is necessary to design a robust, high yield aluminum CVD process. In the present studies, experimental observations have been taken from the literature for the vapor phase chemistry, and ultra-high vacuum (UHV) surface science studies have been employed to investigate the surface chemistry. Theoretical studies were performed by combining quantum chemistry calculations with transition state theory (TST) and micro-kinetic style estimation of rate parameters.

Reaction pathways of DMAH vapor phase and surface chemistry have been investigated, quantified, and implemented in simulations of gas phase and surface reactions. Based on a novel chemical mechanism for the liquid and vapor phase chemistry of DMAH, reaction pathways were investigated with quantum chemistry methods to explain an experimentally observed time/processes dependent composition. Simulations of the vapor phase mechanism provide a molecular understanding for a slow approach to equilibrium based on a reaction cycle that includes several polymeric forms of the precursor. The resulting simulations agree nicely with experimental observations, and also suggest new reaction pathways for aluminum organometallic compounds. UHV surface science studies have determined the DMAH growth reaction proceeds via a surface disproportionation mechanism, where trimethylaluminum (another aluminum organometallic compound) is the reaction product. Quantum chemistry investigations with the density functional theory plane-wave pseudo-potential method support the experimentally proposed mechanism as thermodynamically sound. Surface reaction barriers were also investigated, and individual rate constants developed. Simulations of surface reactions (growth) match well with UHV experiments, and provide a physically based, quantified model for understanding DMAH growth chemistry.

Concurrent with the above studies, an evaluation of quantum chemistry methods was performed. Results find that chemically accurate (~ 2 kcal/mol) *ab initio* calculations can be realized for gas phase calculations, but require large CPU investments. For the most part, DFT methods present an alternative approach to *ab initio* calculations, and give reasonable accuracy with better scaling. However, DFT methods have difficulties describing bridge bonding in aluminum compounds, and these difficulties carry over to the determination of rate constants. Results suggest that forward (bimolecular) reactions are adequately described with DFT methods since bridge bonds have not fully formed at the transition state, but reverse reactions (unimolecular) are poorly described. Surface calculations with DFT methods reveal an accuracy ~ 5 kcal/mol, consistent with DFT gas phase calculations. However, results are dependent on the surface representation, and surface chemistry problem sizes are still rather limited. Overall, quantum chemistry methods provide accurate thermodynamic and kinetic parameters for small molecules. And, even in oversized problems, they provide a basis for semi-quantitative understanding, and allow physically based reaction models to be developed. Quantum chemistry methods are powerful tools to link the molecular world to semiconductor processing, and their use can be expected to grow along with advances in computing technologies.

Research Advisor: Professor Klavs F. Jensen
Lammot Du Pont Professor of Chemical Engineering
MIT

Acknowledgments

The combined experimental/theoretical approach of this thesis was made possible by the generosity of several others. I would like to thank Larry Dubois and AT&T Bell Laboratories for donating the Ultra-High Vacuum (UHV) chamber used in these studies. I would also like to thank Dr. Dubois for his careful notation on chamber components and well stocked supply drawers! I thank Ming Xi for travelling with Klavs and I to Bell Laboratories, and helping to get the chamber up and running. On the computational side, I would like to thank Bjørk Hammer, and Jens Nørskov for inviting me to the Danish Technical University and sharing their plane wave code. I would like to thank Lars Hansen for his technical support in implementing and understanding the code.

I would like to thank Matt Healy and Schumacher for donating DMAH and other precursors to the group, and for useful discussion of DMAH's properties. I would like to acknowledge the Semiconductor Research Corporation for financial support.

Special thanks to Professor Jensen for his cherished mentoring throughout my thesis. I thank him not only for his financial support and academic guidance, but also for his confidence and for providing me with abundant freedom and encouragement in my studies. Thanks to his advising, I have had a chance to fulfill my personal academic goals. I would also like to thank the members of my thesis committee: Paul Laibinis, Jack Howard, and Herbert Sawin for their useful comments and guidance.

I would like to thank members of the KFJ group for useful discussions throughout my years at MIT. I especially appreciate the system administrators (Ted, Harsono, Vijay, and Conny) for helping with workstation issues. I would also like to thank Istvan Lengyel

for his vast knowledge of PC's, which I much appreciate. Many thanks go to Joan Chisholm for her help with purchasing questions.

On a personal side, I would like to thank my parents for encouraging me to attend graduate school and taking care of my undergraduate loans while I studied here at MIT (for many years!) I would also like to thank my mother and father in-law Frances and Thomas Buffum Jr. for their hospitality throughout my years in Boston. This includes not only giving us a place to stay for the last several months of my studies, but also for much needed breaks at their summer home in Rhode Island.

Most importantly, I would like to thank my lovely wife, Heather, for her wonderful patience throughout my years at MIT. She has been a constant source of love and understanding.

Table of Contents

List of Tables

Chapter 2

Chapter 3

Chapter 5

Chapter 6

List of Figures

Chapter 1

Chapter 2

Chapter 3

Chapter 4

Chapter 5

Chapter 6

Chapter 1

Introduction: Quantitative Modeling of Semiconductor Processes

1.1 Motivation

Continued advances in the semiconductor industry will require the introduction of new processes and materials concurrent with shrinking device dimensions. These simultaneous demands drastically reduce margins for error and necessitate an increasingly quantitative understanding of semiconductor processes. Leaders of the semiconductor industry have recognized these challenges and featured atomistic process modeling as one of the "Difficult Challenges" for designs below 100 nm, predicted beyond the year 2006. Among these tasks, obtaining detailed understanding of process chemistry and physics has been identified as one of the biggest hurdles. Another "chief roadblock" is the linking of the atomistic reaction models to reactor scale process simulations. Overcoming these challenges is integral to the future success of the semiconductor industry, with far reaching impacts on the global economy.

Detailed chemistry models are by nature unique to each process, and therefore naturally represent an area of difficulty, requiring commensurate effort. Quantum chemistry methods are an emerging area for atomistic-scale research. Although a subject of dedicated academic efforts for many decades, it is fairly recent that quantum chemistry methods have evolved to the point of being useful instruments for developing detailed reaction chemistry models. Spurred by advances in computer algorithms, new techniques, and the growing availability of computer resources, quantum chemistry

methods have increasingly been applied to gas phase, surface, and solid state chemistry problems.[1-5] To date, most applications of these quantum chemistry tools have been limited to rather small systems, with applications in catalysis at the forefront.[6-9] However, computational tools are also being applied to semiconductor subject matter.[4,10-12] Besides generating valuable knowledge in their own right, quantum chemistry methods provide new routes to information useful for developing coarser models such as Kinetic Monte Carlo simulations and Finite Element reactor models.

Development of quantum chemistry tools for semiconductor processes must address several academic concerns before being accepted and incorporated into semiconductor research facilities. The issues include questions of accuracy, selection of the best techniques for a given problem, defining practical problem sizes, and developing a pseudo-methodology for efficiently approaching semiconductor process research. Currently, quantitative modeling of the large organometallic compounds used, for example, in chemical vapor deposition, remains far behind the understanding of small molecules. Regarding the importance of accuracy issues, consider that a 5 kcal/mol error in an activation barrier leads to a two order of magnitude error in a first-order rate constant at a typical process temperatures of 200°C. There is a need to demonstrate to the industry how these methods can be successfully applied before companies will allocate resources to atomistic modeling. Industry leaders need clear answers to what impact these methods can have on applied process research.

Given unlimited computation resources, it would be possible to employ a combinatorial approach to generating reaction mechanisms. The derived reaction mechanisms could then be evaluated based on calculated thermodynamic properties and predicted rate constants. An appropriately sized reaction mechanism could then be trimmed from all possibilities, and desired properties could be calculated with extremely accurate methods. Currently, such a procedure is impractical for all but the simplest of systems, and an alternative approach is required.

One alternative approach is to utilize existing experimental data and information on related chemical systems to propose and evaluate kinetic mechanisms. This kind of paradigm is difficult to apply to surface reactions, however, due to a general lack of

quantitative experimental data. Surface science experiments can often provide qualitative information regarding surface reaction pathways, reaction intermediates, impurity pathways, and growth temperatures. However, it is often difficult to extract quantitative information from surface science experiments, except for simple reaction mechanisms. For example, methods based on thermal desorption experiments can provide information on activation barriers and rate constant pre-exponential factors for simple first- and second-order surface reactions.[13-16] Other thermodynamic aspects can often be inferred and the quantitative data can be implemented in an experimentally derived reaction mechanism. However, for complex mechanisms with several elementary reaction steps, extraction of quantitative data from surface science experiments is difficult. Additionally, even for apparently simple reaction mechanisms, adsorbate-adsorbate interactions can often complicate the interpretation of experimental data. Other surface chemistry aspects such as surface diffusion and adsorbate interactions with defect sites are similarly difficult to interpret experimentally.[17,18] Lastly, the ultra-high vacuum (UHV) environment of surface science experiments can obscure certain reaction pathways that may be operative at higher pressures and with carrier gas interactions (pressure gap[19]). Theoretical quantum chemistry methods can address these shortcomings through the quantification of experimentally observed phenomena, and examination of alternative reaction pathways not observed under UHV conditions.

The present study addresses the above issues through a complementary approach that combines experiment and theory in a practical way. Both gas phase and surface reaction pathways are investigated for aluminum chemical vapor deposition. The present investigations represent only the beginning for this kind of complementary experimental-theoretical approach. Continued investigations along these lines will, hopefully, provide semiconductor research facilities with a new tool, of equal or greater value than other research instruments.

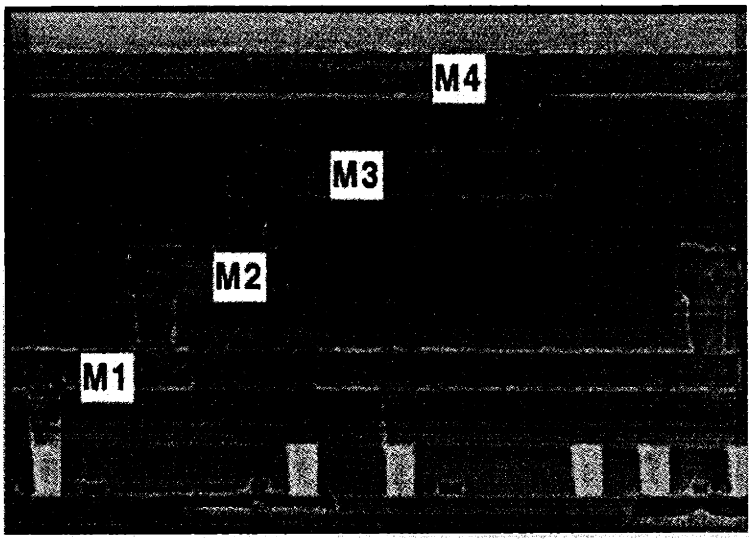

Figure 1.1 Cross section of a 4-layer metalization scheme fabricated with an aluminum CVD process. The lower-level contact metal is Tungsten (lighter shade), while the remaining levels are aluminum. Taken from, Fiordalice, R.W.; Ong , T.; Garcia, S.; Farkas, J.; Fernandes, M.; Freeman, M.; Gall, M.; Jain, A.; Jawarani, D.; Kawasaki, H.; Klein, J.; Roman, B.; Sparks, T.; Venkatraman, R.; Vuong, T.; Weitzman, E.; Pintchovski, F. in *Advanced Metallization and Interconnect Systems for ULSI Applications in 1996*; Havemann, R., Schmitz, J., Komiyama, H., Tsubouchi, K. Eds.; Materials Research Society: Pittsburgh, PA, 1996; p 13.

1.2 Aluminum Chemical Vapor Deposition

As a model system to investigate the applications of quantum chemistry methods in semiconductor processing, aluminum chemical vapor deposition was selected. Aluminum chemical vapor deposition is a technology of interest for interconnect fabrication in semiconductor processing. The shrinking dimensions and simultaneous increase in packing density of integrated circuits has fashioned metalization as a possible limiting aspect of future ULSI (Ultra Large Scale Integration) designs.[20] The gaining complexity of multi-level metalization schemes has brought new challenges to metal deposition processes. The chemical vapor deposition method offers many advantages over traditional deposition methods. One of the most important of these advantages is the ability of CVD methods to deposit conformal films over challenging device geometries. Aluminum chemical vapor deposition has been featured in several recent semiconductor

trade journals.[21,22] Figure 1.1 shows an illustration of a five-layer multi-level metalization scheme using aluminum chemical vapor deposition.

Besides its importance to semiconductor applications, aluminum is a good system for the exploration of quantum chemistry methods. The present study primarily relies on density functional theory based quantum chemistry methods.[8,9,23-33] The computational effort involved with these methods formally scales as N^3, where N is a measure of the system size, such as the number of basis functions or electrons. The "N-cubed" scaling implies a rapidly increasing computational effort as the system/molecules become larger. Being a main group element, aluminum presents a relatively simpler electronic structure problem. Additionally, the aluminum organometallic compounds are primarily composed of aluminum, carbon, and hydrogen, which are relatively simple atoms for gas phase calculations. Aluminum is also a good system for theoretical surface chemistry calculations as it has characteristics of the solid state "nearly free electron metal," and, therefore, is a relatively simple metal to describe with theoretical methods.[34] Investigations of more complicated systems such as the transition metals and metal oxides, nitrides, etc. present challenging systems for future investigations.

Aluminum CVD has been of interest for more than a decade, and many organometallic precursors have been investigated. In addition to semiconductor metalization, aluminum organometallics have applications in aluminum-gallium-arsenide,[35-39] aluminum nitride,[40-43] and aluminum oxide growth.[44-48] Much of the work on aluminum chemical vapor deposition has been summarized in a recent book, *The Chemistry of Metal CVD*.[49] Several other good reviews exist as well.[50-52]

Arguably, the best aluminum CVD precursor currently available is dimethylaluminum hydride, hereafter referred to as DMAH. DMAH is a stable aluminum compound that grows high purity aluminum films. DMAH has a reasonable vapor pressure (~2 Torr and room temperature) and gives acceptable growth rates (10^2-10^3 nm/min).[53-55] Prior to this work, several growth studies of DMAH existed (referenced above), but there was little information about the growth chemistry, especially quantitative understanding. DMAH exhibits a rich chemistry, both in the gas phase and on the aluminum surface. The primary goals of this work are to demonstrate the

complementary experimental-theoretical approach to solving semiconductor process problems, and to develop a quantitative understanding of DMAH growth. A quantitative understanding of the reaction chemistry, both in the gas phase and on the surface, is necessary to build detailed growth models. It is hoped that the detailed gas phase and surface reaction models will be useful for future investigations that link the fundamentals to the reactor scale.

1.3 Summary

Aluminum chemical vapor deposition has been selected as a model system to apply a complementary experimental-theoretical approach for developing detailed reaction chemistry models of semiconductor processes. Aluminum CVD has technological relevance to processes in the semiconductor industry such as integrated circuit manufacturing and III-V compound semiconductor growth. Aluminum presents a somewhat simplified system for the investigation of advanced quantum mechanical reaction engineering tools. The 'model' status of aluminum rests with its relatively simple electronic structure when compared with other relevant materials. Goals of the present research are to twofold: to develop a detailed reaction mechanism for aluminum CVD, and to simultaneously evaluate practical aspects of the application of quantum chemistry methods to semiconductor processes.

1.4 References

(1) Payne, M. C.; Teter, M. P.; Allan, D. C.; Arias, T. A.; Joannopoulos, J. D. *Rev. Mod. Phys.* **1992**, *64*, 1045.

(2) Simons, J. *J. Phys. Chem.* **1991**, *95*, 1017.

(3) Ziegler, T. *Can. J. Chem.* **1994**, *73*, 743.

(4) Ito, T. *J. Appl. Phys.* **1995**, *77*, 4845.

(5) MRS. *Interatomic Potentials for Atomistic Simulations*; Materials Research Society: Pittsburgh, 1996; Vol. 21.

(6) Neurock, M. In *Dynamics of Surfaces and Reaction Kinetics in Heterogeneous Catalysis*; Froment, G. F., Waugh, K. C., Eds.; Elsevier: Belgium, 1997; Vol. 109; pp 3.

(7) van Santen, R. A. *Theoretical Heterogeneous Catalysis*; World Scientific: Singapore, 1991.

(8) *Chemical Applications of Density Functional Theory*; Laird, B. B.; Ross, R. B.; Ziegler, T., Eds.; ACS: Washington, DC, 1996; Vol. 629.

(9) *Density Functional Methods in Chemistry*; Labanowski, J. K.; Andzelm, J. W., Eds.; Springer Verlag: New York, 1991.

(10) Simka, H.; Willis, B. G.; Lengyel, I.; Jensen, K. F. *Prog. Crystal Growth and Charact.* **1998**, *35*, 117.

(11) Simka, H.; Hierlemann, M.; Utz, M.; Jensen, K. F. *J. Electrochem. Soc.* **1996**, *143*, 2646.

(12) Hierlemann, M.; Werner, C.; Spitzer, A. *J. Vac. Sci. Technol. B* **1997**, *15*, 935.

(13) de Jong, A. M. *Surf. Sci.* **1990**, *233*, 355.

(14) Kreuzer, H. J. *Langmuir* **1992**, *8*, 774-781.

(15) King, D. A. *Surf. Sci.* **1975**, *47*, 384.

(16) Redhead, P. A. *Vacuum* **1962**, *12*, 203.

(17) Seebauer, E. G.; Allen, C. E. *Prog. Surf. Sci.* **1995**, *49*, 265.

(18) Gomer, R. *Rep. Prog. Phys.* **1990**, *53*, 917.

(19) Somorjai, G. A. *Introduction to Surface Chemistry and Catalysis*; John Wiley & Sons, Inc.: New York, 1994.

(20) Bohr, M. T. *Int. Electron. Dev. Mtg.* **1995**.

(21) Peters, L. . In *Semiconductor International*, 1998; Vol. 21; pp 83.

(22) Robinson, G. *Electron. Eng. Times* **1996**, 37.

(23) Parr, R. G.; Yang, W. In *Annu. Rev. Phys. Chem.*, 1995; Vol. 46; pp 701.

(24) Weber. . In *Chimia*, 1993; Vol. 47.

(25) Ziegler, T. *Chem. Rev.* **1991**, *91*, 651.

(26) Li, Y. S.; van Daelen, M. A.; Wrinn, M.; King-Smith, D.; Newsam, J. M.; Delley, B.; Wimmer, W.; Klitsner, T.; Sears, M. P.; Carlson, G. A.; Nelson, J. S.; Allan, D. C.; Teter, M. P. *J. Comp. Aid. Mat. Des.* **1993**, *1*, 199-214.

(27) Langreth, D. C. In *Many-Body Phenomena at Surfaces*; Academic Press Inc.:, 1984; pp 51.

(28) Kohn, W.; Becke, A. D.; Parr, R. G. *J. Phys. Chem.* **1996**, *100*, 12974.

(29) Jones, R. O. *Rev. Mod. Phys.* **1989**, *61*, 689.

(30) Lang, N. D. In *Advances in Density Functional Theory*, 1983.

(31) Lang, N. D. *Surf. Sci.* **1994**, *299/300*, 284.

(32) Johnson, B. G.; Gill, P. M. W.; Pople, J. A. *J. Chem. Phys.* **1993**, *98*, 5612.

(33) von Barth, U. In *Many Body Phenomena at Surfaces*; Academic Press, Inc.:, 1984; pp 3.

(34) Ashcroft, N. W.; Mermin, N. D. *Solid State Physics*; Saunders College Publishing: New York, 1976.

(35) Bhat, R.; Koza, M. A.; Chang, C. C.; Schwarz, S. A. *J. Cryst. Growth* **1986**, *77*, 7.

(36) Jones, A. C.; O'Brien, P. *CVD of Compound Semiconductors*; VCH: New York, 1997.

(37) Jones, A. C.; Rushworth, S. A.; Roberts, J. S.; Button, C. C.; David, J. P. R. *Chemtronics* **1989**, *4*, 235.

(38) Zanella, P.; Rossetto, G.; Brianese, N.; Ossola, F.; Prochia, M. *Chem. Mater.* **1991**, *3*, 225.

(39) Hardtdegen, H. *J. Cryst. Growth* **1994**, *145*, 478-484.

(40) Sauls, F. C.; Hurley, W. J. J.; Interrante, L. V.; Marchetti, P. S.; Maciel, G. E. *Chem. Mater.* **1995**, *7*, 1361.

(41) Timoshkin, A. Y.; Bettinger, H. F.; Schaefer, H. F. I. *J. Am. Chem. Soc.* **1997**, *119*, 5668.

(42) Interrante, L. V.; Sigel, G. A.; Garbauskas, M.; Hejna, C.; Slack, G. A. *Inorg. Chem.* **1989**, *28*, 252.

(43) Sauls, F. C.; Interrante, L. V. *Coord. Chem. Rev.* **1993**, *128*, 193.

(44) Moore, J. F.; Strongin, D. R.; Comita, P. B.; Ruckman, M. W.; Strongin, M. *Appl. Phys. Lett.* **1994**, *65*.

(45) Maruyama, T.; Nakai, T. *Appl. Phys. Lett.* **1991**, *58*, 2079.

(46) Kim, J. S.; Marzouk, H. A.; Reucroft, P. J.; Robertson, J. D.; Hamrin, C. E. J. *Appl. Phys. Lett.* **1993**, *62*, 681.

(47) Gustin, K. M.; Gordon, R. G. *J. Electron. Mater.* **1988**, *17*, 509.

(48) Zhao, Y. W.; Suhr, H. *Appl. Phys.* **1992**, *A55*, 176.

(49) Kodas, T.; Hampden-Smith, M. *The Chemistry of Metal CVD*; VCH: New York, 1994.

(50) Gladfelter, W. L. *Chem. Mater.* **1993**, *5*, 1372.

(51) Creighton, J. R. *Crit. Rev. Solid State Mat. Sci.* **1993**, *18*, 175.

(52) Jones, A. C. *J. Cryst. Growth* **1993**, *129*, 728.

(53) Littau, K. A.; Mosely, R.; Zhou, S.; Zhang, H.; Guo, T. *Microelectron. Eng.* **1997**, *33*, 101.

(54) Zhu, N.; Jo, S. D.; Freiler, M. B.; Scarmozzino, R.; R.M. Osgood, J.; Cacouris, T.; Materials Research Society Symposium, 1992.

(55) Kondoh, E.; Ohta, T. *J. Vac. Sci. Technol. A* **1995**, *13*, 2863.

Chapter 2

An Evaluation of Density Functional Theory and ab Initio Predictions for Bridge Bonded Aluminum Compounds

2.1 Introduction

Recent efforts have demonstrated the utility of density functional methods for studying molecular systems.[1] The rapid expansion in the number of papers employing density functional theory can be credited to the inclusion of electron correlation effects within a single configuration representation of the ground state of atoms and molecules. The implementation of electron correlation effects from Density Functional Theory (DFT) methods allows useful thermodynamic data to be calculated for molecules of interest to many applications. Except for the lowest order accounting of electron correlation effects (Møller Plesset perturbation theory on the Hartree-Fock wave function to second order), ab initio methods are typically impractical for routine application as quantum chemistry prediction tools. The trade-off for the advantages offered by density functional theory is the loss of a convergent series for higher order treatments of correlation effects. In addition, there is currently no standard exchange correlation functional as evidenced by the many different implementations in the literature, e.g. SVWN[2,3], BVWN[4,3], SLYP[2,5], BLYP[4,5], BP86[4,6], BPW91[4,7], B3LYP[8], B3PW91.[8]

Common experience has identified the hybrid functionals as the best density functional methods available for molecular calculations.[8,9] These hybrid functionals mix local exchange and correlation functionals with gradient corrections and some component of a Hartree-Fock like exchange calculation. Currently, the most popular methods

(B3LYP, B3P86, and B3PW91, for example[3-8]) have their hybrid expansion parameters based upon a best fit to several properties of a large group of small molecules listed in reference 11. The mixing of DFT functionals with a Hartree-Fock like exchange calculation introduces a semi-empirical component to these functionals. For small molecules, the hybrid functionals have been shown to give good results, comparable to or better than MP2 calculations, and in some cases close to the high level G1 and G2 methods of calculation.[12-14] However, there is still a need to understand their behavior in more diverse molecular compounds. As more systems are encountered, we can expect varying performances for the hybrid methods.

In this chapter, a computational study of "electron deficient" bridging aluminum compounds is reported. These types of molecules have posed a challenge to computational chemistry methods in the past.[15-19] Electron correlation effects were found to be important for obtaining the correct energetics. In general, complex bonding schemes have caused problems for even high level ab initio calculations as demonstrated by the difficulties for G1 and G2 methods with SO_2.[12,13] Results from the present study indicate that *ab initio* methods are capable of describing bridging aluminum compounds. However, contrary to what has generally been observed in the literature for "normal" single-bonded compounds[9], there are large differences between DFT and ab initio calculated energetics. Also in contrast to what has generally been reported, the few experimental results available suggest that for these bridge bonded aluminum compounds MP2 calculations are superior to those from DFT methods. Although further studies are needed to reach any definite conclusions, this study suggests that current DFT methods introduce systematic errors into calculations of bridging aluminum compounds. These findings are unfortunate since the advantages of DFT methods would be particularly useful for studying these types of systems.

The system of study includes the aluminum organometallic compounds dimethylaluminum hydride (DMAH) and trimethylaluminum (TMA). These compounds are useful for the chemical vapor deposition (CVD) of aluminum containing films including applications for semiconductor metalization and compound semiconductor devices.[20,21] DMAH, in particular, has been shown to grow extremely clean aluminum

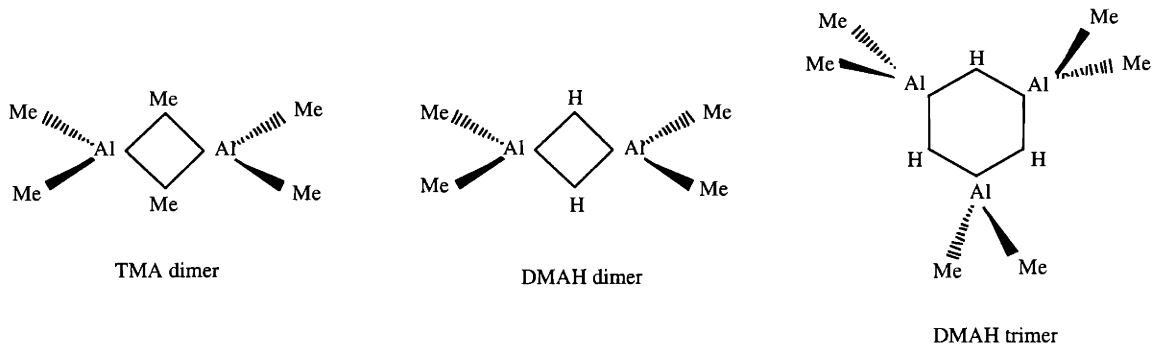

Figure 2.1 Bridge bonded structures of Dimethylaluminum Hydride (DMAH) and Trimethylaluminum (TMA).

films.[22-24] Unlike DMAH, TMA chemical vapor deposition leads to unacceptably high levels of carbon contamination and is not useful for the deposition of high quality aluminum films. However, it has recently been confirmed that TMA is a surface reaction product of the growth reactions of DMAH, and thus its chemistry is important to understanding the growth of aluminum films from DMAH.[25,26] Characterizing the DMAH/TMA gas phase system requires good thermodynamic data. Unfortunately, there are few data available for these chemical compounds, and those which are available are suspect of errors. Therefore, we have pursued a computational chemistry study of this reaction system. Because of the unexpected large errors in energy calculations with DFT methods, several other bridging aluminum compounds were included in the study to broaden the understanding of binding in these types of molecules.

As is common with aluminum compounds, DMAH and TMA form bridging bonds to create associated species (Figure 2.1). For DMAH, monomer units form bridging hydrogen bonds to create dimeric, trimeric, and larger order associated units.[27-29] The monomeric units of TMA form bridging bonds with methyl groups to create dimeric units.[28,30,31] These ring-like structures involve three-centered, two-electron bonds which are termed "electron deficient".[32]

While the author is not aware of any previous density functional theory studies of bridging aluminum compounds, there have been numerous theoretical studies of electron deficient bonding.[15-19] As mentioned above, these early studies discovered the

importance of including electron correlation effects for obtaining accurate energetics. Whereas previously calculated dimerization enthalpies at the self-consistent field (SCF) level have been qualitatively successful for the alane molecule, they are completely wrong for methyl bridges. More recent studies of the dimers of alane, DMAH, and TMA have noted the importance of including polarization functions.[33-35] No geometric or energetic data on the DMAH trimer has been located, either from experiments or previous theoretical studies.

In addition to understanding the energetics of these bridging aluminum compounds, it is of interest to explore the calculated vibrational spectra as a function of method and basis set to better understand the utility of these calculations for bridge bonded aluminum compounds. Recent Hartree-Fock based theoretical studies of the vibrational spectra of DMAH and TMA dimers employed simplified structures with hydrogen atoms replacing terminal CH_3 groups.[36] Comparison with experiment showed these simplified models were helpful for interpreting the experimental vibrational spectra. Here harmonic vibrational frequency calculations are included in the study of geometric structures, association enthalpies, and heats of formation of these complex bridging molecules to better understand the usefulness of density functional methods for predicting vibrational spectra of large molecules.

2.2 Methods of Calculation

Calculations were performed on standard workstations using the Gaussian 94 suite of programs.[10] The Gaussian 94 program was used to obtain minimum energy structures, total energies, harmonic vibrational frequencies, and thermodynamic corrections for temperature effects. Zero point energy corrections to electronic energies were calculated from the harmonic vibrational frequencies and used unscaled. Analytic gradient techniques were used for both optimization and frequency calculations. Several DFT and ab initio methods were employed.

The general strategy was to optimize molecules with the 6-31G(d,p) split-valence basis set, and then expand the basis set for single point energy calculations. Owing to the different computational burdens of DFT versus ab initio methods, larger basis sets could

be used with DFT calculations. The basis sets used for single point energy calculations by DFT and MP2(Full) methods were 6-311++G(2df,pd), and 6-311+G(d,p), respectively. The choice of the 6-311+G(d,p) basis set for MP2 calculations is supported by other successful MP2/6-311+G(d,p) calculations on bridging aluminum compounds.[37]

For geometry optimizations and frequency calculations, the different DFT exchange correlation functionals are expected to perform similarly and the BLYP and B3LYP methods were chosen to represent the pure and hybrid methods. Heats of formation were also computed with the BLYP and B3LYP methods again representing the pure and hybrid DFT methods. For the DMAH and TMA monomers, the resulting heats of formation are compared with those from the more demanding G1 and G2 methods. DFT calculations of heats of reaction were found to be very sensitive to the choice of exchange correlation functional. Therefore, several combinations of exchange and correlation functionals were used to characterize dimerization enthalpies: SVWN, BVWN, SLYP, BLYP, B3LYP, B3P86, and a modified B3PW91.

Harmonic vibrational frequencies were calculated with the BLYP density functional method using the 6-31G(d,p) as well as larger, modified basis sets. The first of the modified basis sets uses a 6-311G(df,pd) basis for the heavy atoms and bridging hydrogen atoms (including hydrogen atoms on bridging methyl groups), and a 6-31G basis for all remaining (non-bridging) hydrogen atoms. The second modified basis set is similar to the first, but adds diffuse s and p functions to the heavy atoms and a diffuse s function on each bridging hydrogen atom (a 6-311++G(df,pd) basis). Again, a 6-31G basis set was used for all non-bridging hydrogen atoms. B3LYP/6-31G(d,p) harmonic frequency calculations were also performed for comparison purposes. For both DFT methods, only the infrared values are reported.

2.3 Results & Discussion

2.3.1 Structure

The general features of the structures considered in this study are shown in Figure 2.1. The compounds of interest are: monomer, dimer, and trimer of DMAH;

Table 2.1 Selected geometric parameters for the Dimethylaluminum Hydride (DMAH) and Trimethylaluminum (TMA) gas phase compounds. Bond lengths are given in Angstroms and bond angles in degrees.

	BLYP/ 6-31G(d,p)	BLYP/ modified†	B3LYP/ 6-31G(d,p)	MP2(Full)/ 6-31G(d,p)	Expt.
$AlH(CH_3)_2$ (DMAH monomer)					
r(Al-H)	1.61	1.60	1.60	1.59	
r(Al-C)	1.98	1.98	1.97	1.96	
a(C-Al-C)	123.7	123.7	123.6	123.4	
$[AlH(CH_3)_2]_2$ (DMAH dimer)					
r(Al-H_b)	1.77	1.76	1.76	1.74	1.676±0.19[a]
r(Al-C)	1.98	1.98	1.97	1.96	1.947±0.003[a]
r(Al-Al)	2.68	2.66	2.65	2.62	2.617±0.006[a]
a(Al-H_b-Al)	98.4	98.2	98.1	97.8	102.6±1.6[a]
a(C_t-Al-C_t)	125.8	126.0	126.1	126.8	118.5±0.9[a]
$[Al(CH_3)_2]_3$ (DMAH trimer)					
r(Al-H_b)	1.72	1.72	1.71	1.69	
r(Al-C)	1.98	1.98	1.97	1.96	
r(Al-Al)	3.27	3.28	3.25	3.20	
a(Al-H_b-Al)	143.5	144.1	143.1	142.2	
a(C-Al-C)	126.4	126.4	126.8	128.2	
$Al(CH_3)_3$ (TMA monomer)					
r(Al-C)	1.99		1.97	1.97	1.957 ± 0.003[b,c]
$[Al(CH_3)_3]_2$ (TMA dimer)					
r(Al-C_b)	2.19	2.18	2.17	2.14	2.140±0.004[b,d*]
r(Al-C_t)	1.98	1.98	1.97	1.96	1.97[d*]
					1.957±0.003[b]
r(Al-Al)	2.65	2.65	2.63	2.60	2.600±0.004[d]
					2.619±0.005[b]

monomer and dimer of TMA; and the DMAH-TMA cross species (pentamethyldialane). Table 2.1 lists the optimized geometrical parameters of these species and includes BLYP, B3LYP, and MP2(Full) optimized structures. Geometry optimizations were performed for each method with a 6-31G(d,p) split valence basis set. This basis set was found to adequately represent the structures and energetics of these compounds. In addition, optimized structures for the BLYP method with a larger, modified basis set are included. As can be seen in the table, the significant increase in basis set size has little effect on the BLYP optimized structures.

Table 2.1 continued.

	BLYP/ 6-31G(d,p)	BLYP/ modified†	B3LYP/ 6-31G(d,p)	MP2(Full)/ 6-31G(d,p)	Expt.
$[Al(CH_3)_3]_2$ (TMA dimer) cont'd					
$a(Al\text{-}C_b\text{-}Al)$	74.8	74.9	74.9	74.7	74.7±0.4[d] 75.5±0.1[b]
$a(C_t\text{-}Al\text{-}C_t)$	122.0	122.4	122.3	123.9	123.1±0.4[d] 117.3±1.5[b]
$[(Al(CH_3)_3)(AlH(CH_3)_2)]$ (pentamethyldialane)					
$r(Al\text{-}C_b)$	2.19		2.17	2.15	
$r(Al\text{-}H_b)$	1.75		1.74	1.73	
$r(Al\text{-}C_t)$	1.98		1.97	1.96	
r(Al-Al)	2.66		2.64	2.61	
$a(C_t\text{-}Al\text{-}C_t)$	124.0		124.3	125.6	
$a(Al\text{-}C_b\text{-}Al)$	74.7		74.8	74.6	
$a(Al\text{-}H_b\text{-}Al)$	98.7		98.5	98.1	

† 6-311G(df,pd) basis set for heavy atoms and bridging hydrogen atoms (including hydrogen atoms on bridging methyl groups), 6-31G basis for all terminal methyl hydrogens. [a]Ref. 27. [b]Ref. 31. *Average of their two values. [c]Compare with a previous study at HF/3-21G* and HF/6-31G*: rAl-C = 1.98,1.98, respectively (Ref. 35). [d]Ref. 41.

For the cases of the DMAH dimer and TMA monomer and dimer where experimental data are available, the hybrid DFT and MP2 geometries agree fairly well with the expected accuracy of approximately 0.01 angstroms for bond lengths and 1.0 degree for bond angles.[38] Exceptions are noted for the DMAH terminal C-Al-C and bridging Al-H-Al bond angles. The seven plus degree difference between the calculated value and experiment for the terminal bond angle is abnormally large and inconsistent with the good agreement among the other geometric parameters. The calculated structural features are consistent with previous theoretical studies of alane where the terminal groups are hydrogen atoms but the optimized geometric parameters of the bridge bonding are similar.[34,39] In the case of alane, the SCF calculated Al-H-Al bridge angle is 97.9° and the H-Al-H terminal bond angle is 127.3°, similar to those calculated for DMAH.

The larger terminal angle of the dimer with bridging hydrogen atoms as opposed to methyl groups can be rationalized by previous arguments founded on the donating

ability of the bridging group.[40] Based on arguments of coupling constants, the previous work qualitatively predicts that the same Me-Al-Me terminal bond should be larger for halogens than OR or NR_2 bridge units. Calculations (not tabulated) agree, with B3LYP/6-31G(d,p) calculations predicting 127.7°, 122.9°, and 121.0° degree angles for bridging Cl, NH_2, and OCH_3 units, respectively. The same logic can explain the large C-Al-C terminal angle in DMAH. These arguments rationalize the differences in calculated terminal C-Al-C bond angles for DMAH and TMA, but do not explain the gas phase electron diffraction results. The error in the bridge angle is similarly difficult to explain. The consistent disagreement for all methods with experiment for these two structural features combined with the good agreement of all methods for the same structural features of TMA suggests the experimental value may need re-evaluation. However, the poor agreement with experiment also leaves open the possibility that higher order corrections are needed to correctly describe the DMAH dimer.

For all methods used, the TMA optimized geometry is consistent with the symmetric bridge bond observed in experimental gas phase electron diffraction studies,[41] rather than the asymmetric structure computed in reference 33. Due to the many CH_3 groups, our optimized TMA structure has C_i symmetry rather than the D_{2h} symmetry of the aluminum carbon skeleton or the C_{2h} symmetry possible with the bridging methyl groups. Long-range H-H interactions aggravate the search for a true minimum (no imaginary frequencies) with the higher symmetries. The H-H interaction problem can be solved by either reducing the basis functions on the H atoms (to reduce the interactions) or increasing the basis functions on the H atoms and allowing them to interact more strongly. The later method was used to rotate the methyl groups into optimized positions at the higher basis set level. Once such a minimum was found, the calculation was repeated at the appropriate basis set level with the new geometry. With this approach it was possible to find minima with no imaginary modes. However, the high symmetry of gas phase molecules with freely rotating methyl groups could not always be maintained. Constraining the molecule to C_{2h} (the highest symmetry possible in a calculation of the TMA dimer) gives an energy that differs from the C_i structure by less than a micro-

Hartree. Geometries are similarly identical except for a 0.1 degree decrease in the terminal C-Al-C bond angle caused by the change in steric interactions.

Experimental gas phase electron diffraction studies of the TMA structure have found D_{2h} symmetry (freely rotating methyl groups) while solid state measurements have indicated an offset/distortion between the two planes of the dimer defined by each Al atom and its two terminal carbon atoms.[31,41] Although the symmetry of the DFT and MP2 optimized structures compare better with the gas phase studies, the bond lengths and angles compare better with the solid state measurements. Therefore, the solid state geometric values for TMA are listed in the table along with the gas phase measurements. Whether the difference between the solid state and gas phase determinations is due to actual physical differences or measurement technique is unclear. Table 2.1 shows that all methods give reasonable dimer structures, the best being the MP2(full) method, and the second best being the hybrid functional.

Unfortunately, there are no experimental results to compare with the DMAH-TMA cross species (pentamethyldialane) data. Compared with the Al-H bridge bond of DMAH, the Al-H bridge bond length in the mixed DMAH-TMA species shows a slight contraction. This structural effect does not appear in the energy calculations (see below). There is also a slight opening of the Al-H_b-Al angle compared with DMAH. The other structural parameters, such as the Al-Al distance, appear to be averages of the parent molecules. The enlargement of the terminal C-Al-C bonds compared with TMA is consistent with either reduced bridge-terminal steric interactions due to the replacement of one bridging methyl group with a hydrogen atom and/or the reduced electron donating ability of the hydride bridge as discussed above.

There are no published structures for the DMAH trimer, but there are some data for related structures such as the AlF_3 tetramer and the $(CH_3)_2AlN(CH_3)_2$ trimer.[42] The DMAH trimer is found to have a six membered ring structure as is consistent with the related compounds, but the planarity of the ring is unique (D_{3h} symmetry). The terminal Al-CH_3 geometric parameters are similar to those of the DMAH dimer but with an even larger terminal C-Al-C angle. The shortening of the aluminum-hydrogen bridge bond is consistent with a more linear bond and the need to decrease the bond length to maintain

overlap.[28] The larger Al-Al lengths would preclude any Al-Al bonding in the trimer, but the heat of association per bridge actually increases.[43]

Comparison of geometric structures between methods shows the same trends that have generally been observed in the literature. BLYP bond lengths are too long, and B3LYP partially corrects this behavior. Increasing the basis set for BLYP calculations has little effect. Comparison with experiment and MP2 results shows that B3LYP bond lengths are still too long. Overall, the MP2 numbers are closest to experiment with the hybrid DFT method second best.

2.3.2 Heats of Association.

Heats of association for the dimeric and trimeric structures of DMAH and TMA are listed in Table 2.2. The important reactions are:

$$(AlH(CH_3)_2)_2 \Leftrightarrow 2\ AlH(CH_3)_2 \quad (1)$$

$$(Al(CH_3)_3)_2 \Leftrightarrow 2\ Al(CH_3)_3 \quad (2)$$

$$2\ (AlH(CH_3)_2)_3 \Leftrightarrow 3\ (AlH(CH_3)_2)_2 \quad (3)$$

$$((AlH(CH_3)_2)(Al(CH_3)_3)) \Leftrightarrow Al(CH_3)_3 + AlH(CH_3)_2 \quad (4)$$

Reactions 1, 2, 3, and 4 correspond to binding of DMAH and TMA dimers, the DMAH trimer, and the DMAH-TMA cross species (pentamethyldialane), respectively. The association enthalpies were calculated with several different computational chemistry methods (Table 2.2). The compounds are discussed in turn below.

Dimethylaluminum Hydride

The calculated association enthalpies of DMAH by all methods that include electron correlation show rough agreement with the experimental estimate of 15-20 kcal/mol per hydrogen bridge.[44] Even the Hartree-Fock value has the correct qualitative (binding) behavior. The hybrid DFT and MP2 methods differ by ~ 5 kcal/mol. The

Table 2.2 Association enthalpies at 298.15K for the Dimethylaluminum Hydride (DMAH) and Trimethylaluminum (TMA) gas phase system. Each method uses its own optimized geometry with a 6-31G(d,p) basis except the MP4 and HF (Hartree-Fock) calculations which use the MP2(Full)/6-31G(d,p) optimized geometry. Zero point energies and thermal energy corrections to 298.15K are based on B3LYP harmonic frequencies for all calculations except G2MP2. All values are given in kcal/mol.

	HF/6-311+G(d,p)	BLYP/ 6-31G(d,p)	B3LYP/ 6-31G(d,p)	MP2(Full)/ 6-31G(d,p)	BLYP/ 6-311++G(2df,pd)
$[AlH(CH_3)_2]_2 \Rightarrow$ 2 $AlH(CH_3)_2$	23.7	26.3	28.0	33.2	25.9
2 $[AlH(CH_3)_2]_3 \Rightarrow$ 3 $[AlH(CH_3)_2]_2$	8.3	12.1	11.9	15.1	9.0
$[Al(CH_3)_3]_2 \Rightarrow$ 2 $Al(CH_3)_3$	0.3	6.5	9.0	19.5	3.5
$[(CH_3)_2AlH(CH_3)Al(CH_3)_2] \Rightarrow AlH(CH_3)_2$ + $Al(CH_3)_3$	12.1	16.4	18.6	26.4	14.8

B3LYP association enthalpy values are ~ 2 kcal/mol more binding than those from the BLYP method.

Compared with the MP2 numbers, the implementation of the MP4 method shows no significant effects of higher order corrections for electron correlation. A G2MP2[13] calculation of the association enthalpy for the DMAH dimer gives the highest value of +34.9 kcal/mol. Overall, the ab initio methods bind the dimer (with respect to two monomers) more than the DFT methods with differences of ~ 5-7 kcal/mol. Comparison with the estimate based on experimental observation favors the ab initio values.

For the association of DMAH to trimer, the discussion parallels that for the dimer. The experimental estimate is very approximate and not useful for extensive discussion. The calculated enthalpy per H bridge is larger for the trimer than the dimer, 19.3 vs. 16.8 kcal/mol at the MP2(Full)/6-311+G(d,p) level. This effect could be due to greater binding of the hydrogen atoms with the shorter bond distance or reduced repulsion between Al atoms.[43]

Table 2.2 continued.

	B3LYP/ 6-311++G(2df,pd)	MP2(Full)/ 6-311+G(d,p)	MP4	G2MP2	Expt.
$[AlH(CH_3)_2]_2 \Rightarrow$ 2 $AlH(CH_3)_2$	28.2	33.6	32.5[†]	34.9	30.0 to 40.0[a]
2 $[AlH(CH_3)_2]_3 \Rightarrow$ 3 $[AlH(CH_3)_2]_2$	9.0	14.7		12.0[*]	15.0 to 20.0 per bridge[a]
$[Al(CH_3)_3]_2 \Rightarrow$ 2 $Al(CH_3)_3$	7.0	18.5	16.6[‡]		20.40 ± 0.34[b] 19.8[c]
$[(CH_3)_2AlH(CH_3)Al(CH_3)_2]$ $\Rightarrow AlH(CH_3)_2 + Al(CH_3)_3$	17.7	26.1			

[a]Ref. 44. [b]Ref. 45. [c]Ref. 32b. [†]MP4(SDQ)/6-311G(d,p). [‡]MP4(SDTQ)/6-31G(d). [*]QCISD step without triples contribution.

Trimethylaluminum

Results for the TMA association reaction reveal even larger differences between DFT and *ab initio* calculations than those for DMAH. Trimethylaluminum is generally accepted to exist in the vapor phase as a dimer with an experimental binding value of 20.4 ± 0.34 kcal/mol.[45] The *ab initio* methods are consistent with the experimental value, but the DFT methods, including the hybrid B3LYP method, show striking disagreement. Errors are within 2 kcal/mol for the ab initio methods, but greater than 10 kcal/mol for the DFT based calculations. In comparisons of B3LYP and MP2 energy calculations for "normal" single-bonded molecules, MP2 numbers are generally inferior.[9] In this case, the experimental value is firm and the conclusion must be that DFT methods are in substantial error. Observation of the large error for the Hartree-Fock dimerization enthalpy gives some indication of the importance of electron correlation for the dimeric structure. The DFT under binding of the TMA dimer complex with respect to monomers is similar in direction to the errors discussed above for DMAH. The under-binding of dimeric units (with respect to monomeric units) is a trend that continues for several other bridging aluminum structures. This observation will be discussed in detail below after results for the cross-species (pentamethyldialane).

Pentamethyldialane

The computed binding enthalpy of the DMAH-TMA cross compound (pentamethyldialane) is intermediate between DMAH and TMA values by all methods. The association strength is nearly the average of the dimerization enthalpies of DMAH and TMA. In contrast to a report that suggested hydrogen bridging in the DMAH-TMA complex is stronger than DMAH hydrogen bridges, these results show no significant strengthening or weakening in the interaction for the two different bridging bonds.[36] Although there are no experimental values to compare, the MP2 calculated energies are suggested to be the best listed here.

Table 2.3 Association enthalpies (298.15K) of several bridging aluminum compounds. All calculations were performed with B3LYP/6-31G(d,p) optimized geometries. Zero point energies and thermal energy corrections were also calculated with B3LYP/6-31G(d,p) harmonic frequencies. All values are given in kcal/mol.

	HF/ 6-31G(d,p)	MP2(Full)/ 6-31G(d,p)	B3LYP/ 6-31G(d,p)	Expt.
$[AlH_3]_2$[a,b] $\Rightarrow$ 2 AlH_3	24.3	32.9	29.8	
$[Al(NH_2)(CH_3)_2]_2 \Rightarrow$ 2 $Al(NH_2)(CH_3)_2$	54.9/ 48.9†	64.7/ 57.8†	53.8/ 46.0‡	
$[AlOH(CH_3)_2]_2 \Rightarrow$ 2 $AlOH(CH_3)_2$	56.6/ 53.2†	63.8/ 57.8†	54.0/ 46.9‡	
$[AlF_3]_2$[c] $\Rightarrow$ 2 AlF_3	57.0/ 48.1†	64.2/ 48.8†	58.7/ 43.9‡	52.2[1], 50.7±4.0[2*]
$[AlCl(CH_3)_2]_2$ $\Rightarrow$ 2 $AlCl(CH_3)_2$	18.6/ 19.1†	29.1/ 32.3†	22.7/ 22.0‡	
$[AlCl_3]_2$[d,e] $\Rightarrow$ 2 $AlCl_3$	17.1/ 18.2†	28.3/ 32.1†	21.9/ 21.6‡	30.3[1], 29.6[4]

† 6-311+G(d,p) basis set for single point energy calculation. ‡ 6-311++G(2df,pd) basis set for single point energy calculation. [1]NBS Technical Note 270-3, Washington D.C., 1968. [2]Porter, R.F.; Zeller, E.E. *J. Chem. Phys.* **1960**, *33*, 858. *Adjusted from 1000K to 298K via calculated differences in thermal energy. [4]Ref. 32. [a]Compare with:(scaled ZPE) 31.5 [MP4/6-31G**], Ref. 34. [b]Compare with:(@ 298K) 27 [HF/3-21G*//HF/3-21G*], 24 [HF/6-31G*//HF/6-31G*], 27 [MP2/6-31G*//HF/6-31G*)]; (with no ZPE or ΔE corrections) 33 [MP2/6-311+G*//HF/6-31G*], Ref 35. [c]Compare with:(ΔH(0K)) 47.6 [MP2/6-311+G(d)//RHF/6-311+G(d)], Ref. 37. [d]Compare with: (no ZPE or ΔE correc.) 25 [HF/3-21G*//HF/3-21G*], 18 [HF/6-31G*//HF/6-31G*], Ref. 37. [e]Compare with:(ΔH(0K)) 31.5 [MP2/6-311+G(d)//RHF/6-311+G(d)], Ref. 37.

Reports of poor performance for the hybrid DFT methods in ground state systems (especially in comparison with MP2 numbers) are uncommon, and the present results (Table 2.2) must be related to this particular system of study. For purposes of discussion, the dimerization enthalpies of several other bridging aluminum compounds are given in Table 2.3. Both "electron deficient" and "normal" 2-center 2-electron bridge bonds are represented. All bridging systems show significant differences between DFT (including the hybrid method) and *ab initio* values for calculated association enthalpies. Although good experimental data are sparse, the available data favor MP2 over DFT numbers. The differences between methods increase as the bridging species changes loosely in the order H, F, Cl, OH, CH_3, and NH_2. The DFT errors are not confined to the electron deficient bonds, but are also exhibited with "normal" bridge bonds. In all cases, the hybrid DFT methods under-bind the dimer with respect to monomers.

Calculations of association enthalpies of bridging structures with different combinations of exchange and correlation functionals (Table 2.4) provide additional insight into DFT results. Table 2.4 shows large (>20 kcal/mol) variations in the association enthalpies calculated by different methods. The values range from over-binding of the dimers (SVWN and SLYP) to strongly under-binding (BVWN). Although each method uses its own converged density, the geometry is the same for all calculations on each bridging compound. These calculations do not rigorously de-couple the electron density and functional evaluations, but they do indicate tendencies of the methods for the same geometric structures. Given that the hybrid method under-binds the dimer (with respect to two monomers) and that all combinations of the Becke exchange functional with a correlation functional under-bind as well, it suggests that the Becke gradient corrected exchange term over-compensates the over-binding of the local exchange term for these systems. The under-binding of dimers by methods that include the Becke gradient corrected exchange term is consistent for all bridging aluminum compounds studied. The relative effects of the several combinations of exchange and correlation functionals appear to be typical.[46]

Table 2.4 Association enthalpies (298.15K) of several bridging aluminum compounds evaluated with various combinations of local and gradient corrected DFT functionals. All energy calculations were performed on B3LYP/6-31G(d,p) optimized geometries. Zero point energies and thermal energy corrections were also calculated with B3LYP/6-31G(d,p) harmonic frequencies. All values are given in kcal/mol. [Note: Some calculations presented here are basis set deficient. However, the binding trends are not expected to be affected by basis set limitations. See Table 3 for larger basis set calculations with the B3LYP method.]

	SVWN/ 6-31G(d,p)	BVWN/ 6-31G(d,p)	SLYP/ 6-31G(d,p)	BLYP/ 6-31G(d,p)	B3LYP/ 6-31G(d,p)
$[AlH_3]_2 \Rightarrow 2\ AlH_3$	43.9	24.7	47.9	28.2	29.8
$[AlH(CH_3)_2]_2 \Rightarrow 2\ AlH(CH_3)_2$	41.6	22.6	45.6	26.3	28.0
$[Al(CH_3)_3]_2 \Rightarrow 2\ Al(CH_3)_3$	30.5	-0.4	38.0	6.5	9.0
$[Al(NH_2)(CH_3)_2]_2 \Rightarrow 2\ Al(NH_2)(CH_3)_2$	68.9	44.4	74.9	49.5	53.8
$[AlOH(CH_3)_2]_2 \Rightarrow 2\ AlOH(CH_3)_2$	67.1	43.6	73.4	49.1	54.0
$[AlF_3]_2 \Rightarrow 2\ AlF_3$	70.2	49.1	77.8	55.9	58.7
$[AlCl(CH_3)_2]_2 \Rightarrow 2\ AlCl(CH_3)_2$	37.6	15.9	43.0	20.6	22.7
$[AlCl_3]_2 \Rightarrow 2\ AlCl_3$	38.3	14.6	44.1	19.7	21.9

The observed disparity between the results of *ab initio* and density functional methods is consistent with a recent study on another "electron deficient" molecule, beryllium borohydride (BeB_2H_8).[47] In that study, the relative stability of two conformers that differed in the number of bridge bonds was compared. Both BLYP and B3LYP calculations favored the conformer with less bridge bonds, whereas both *ab initio* methods and experiment favor the structure with more bridge bonds. These results are consistent with the current observation of under-prediction of dimerization enthalpies for the BLYP and B3LYP methods. In the above paper, the hybrid method with the Perdew 86[6] (P86) correlation functional replacing the Lee-Yang-Parr[5] functional correctly predicted the order of stability. Motivated by these similarities, dimerization enthalpies were re-computed with the B3P86 functional. Table 2.5 tabulates these results.

Table 2.5 Association enthalpies (298.15K) of bridging aluminum compounds for B3P86 and a modified B3PW91 hybrid functional. Table entries are single point energy calculations with B3LYP/6-31G(d,p) optimized geometries. Zero point energies and thermal energy corrections are calculated with B3LYP/6-31G(d,p) harmonic frequencies. All values are given in kcal/mol.

	B3P86/6-31G(d,p)	[a]modified B3PW91/ 6-31G(d,p)
$[AlH_3]_2 \Rightarrow 2\ AlH_3$	33.9	37.0
$[AlH(CH_3)_2]_2 \Rightarrow 2\ AlH(CH_3)_2$	31.9	34.9
$[Al(CH_3)_3]_2 \Rightarrow 2\ Al(CH_3)_3$	14.9	20.1
$2\ [AlH(CH_3)_2]_3 \Rightarrow 3\ [AlH(CH_3)_2]_2$	10.5	9.2
$[(CH_3)_2Al(CH_3)(H)Al(CH_3)_2] \Rightarrow Al(CH_3)_3 + AlH(CH_3)_2$	23.5	27.6
$[Al(NH_2)(CH_3)_2]_2 \Rightarrow 2\ Al(NH_2)(CH_3)_2$	59.2/ 51.9[†]	62.4/ 55.1[†]
$[AlOH(CH_3)_2]_2 \Rightarrow 2\ AlOH(CH_3)_2$	56.9/ 50.5[†]	59.9/ 53.4[†]
$[AlF_3]_2 \Rightarrow 2\ AlF_3$	59.0/ 46.0[†]	61.7/ 48.4[†]
$[AlCl(CH_3)_2]_2 \Rightarrow 2\ AlCl(CH_3)_2$	26.6	29.7
$[AlCl_3]_2 \Rightarrow 2\ AlCl_3$	26.4	29.8

[†] 6-311++G(2df,pd) basis set. [a] See text.

The B3P86 calculations in Table 2.5 represent a sizable improvement over the B3LYP and BLYP methods. The errors are reduced considerably, but the consistent under-prediction of binding energies remains. Greater improvement is obtained by modifying the hybrid expansion to reduce the contribution of the Becke exchange correction. Based on the data in Table 2.4 and the suggested over-compensation of the exchange correction, the modified functional adjusts the expansion recommended in reference 8 by decreasing the contribution of the exchange correction from 0.72 to 0.5.[48]

$$E_{XC}=E_{XC}{}^{LSDA} + a_O(E^{HF}{}_X - E_X{}^{LSDA}) + a_X\Delta E_C{}^{B88} + a_C\Delta E_C{}^{PW91}.$$

The computed dimerization enthalpies for this modified B3PW91 functional are listed in the second column of Table 2.5. All dimerization enthalpies are shifted to more binding values. The dimerization enthalpy for alane is now possibly too strong (a G2 calculation gives a binding energy of +34.5 kcal/mol at 298 K), but values for methyl, chlorine, and fluorine bridges are now in better agreement with experiment. The uniform improvement is somewhat surprising given the fundamental physical differences between

"electron deficient" and "normal" bonds. The observation of improvement for both adjustments in the correlation (B3P86 vs. B3LYP) and exchange functionals (modified hybrid method) illustrates a compensation effect between exchange and correlation for the hybrid methods. The lack of a fixed functional for either exchange or correlation introduces a semi-empirical element to these calculations.

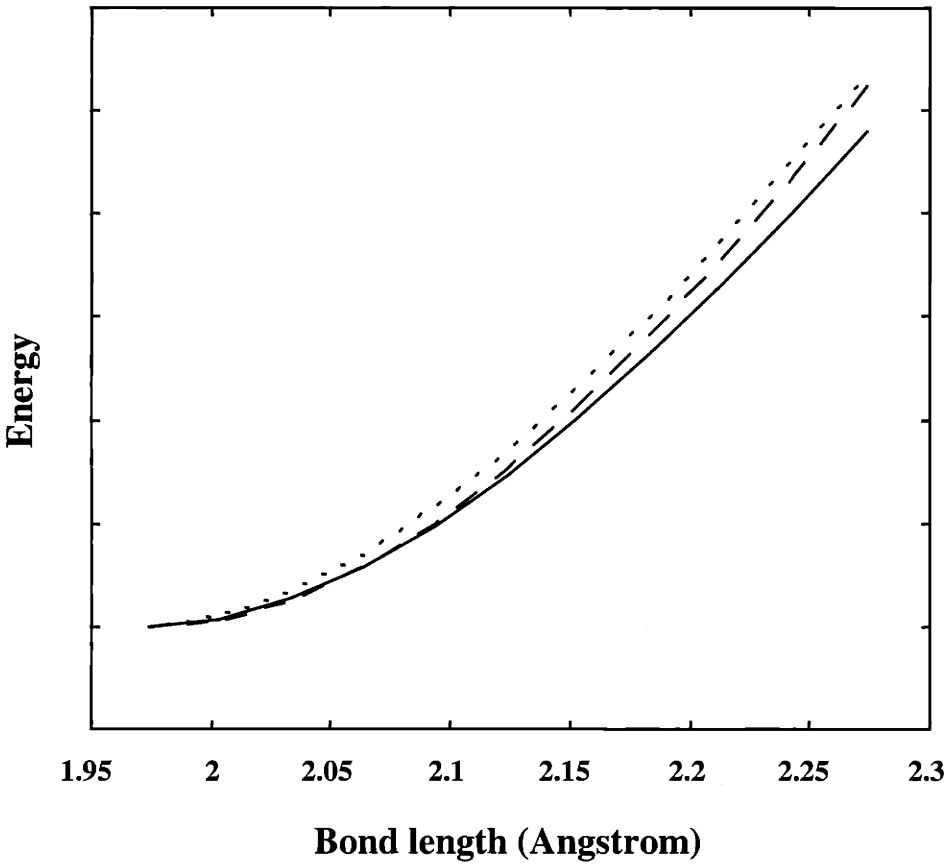

Figure 2.2 B3LYP(—), MP2(Full)(...), and HF(---) energy evaluated with a 6-31G(d,p) basis set as a function of the Al-CH_3 bond length for the TMA monomer. B3LYP has the lowest energy rise in response to the bond extension.

Given that DFT errors for dimerization enthalpies are not restricted to "electron deficient" bonds, it might seem reasonable to associate the error with the long, stretched, and bent bonds of the dimeric units. This analysis is consistent with Wade's partitioning of the dimerization energy into bonding and re-organization terms.[32] Figures 2.2 and 2.3

compare B3LYP, MP2(Full), and Hartree-Fock energy changes accompanying the stretching and bending of a TMA monomer Al-CH_3 bond. The hybrid DFT method shows no abnormal behavior for the extended bonds. Rather, the hybrid DFT method shows a lower energetic cost of bending and stretching the bond than either the Hartree-Fock or MP2 calculations. The errors in dimerization enthalpies can be narrowed to an incomplete treatment of bridge bonding.

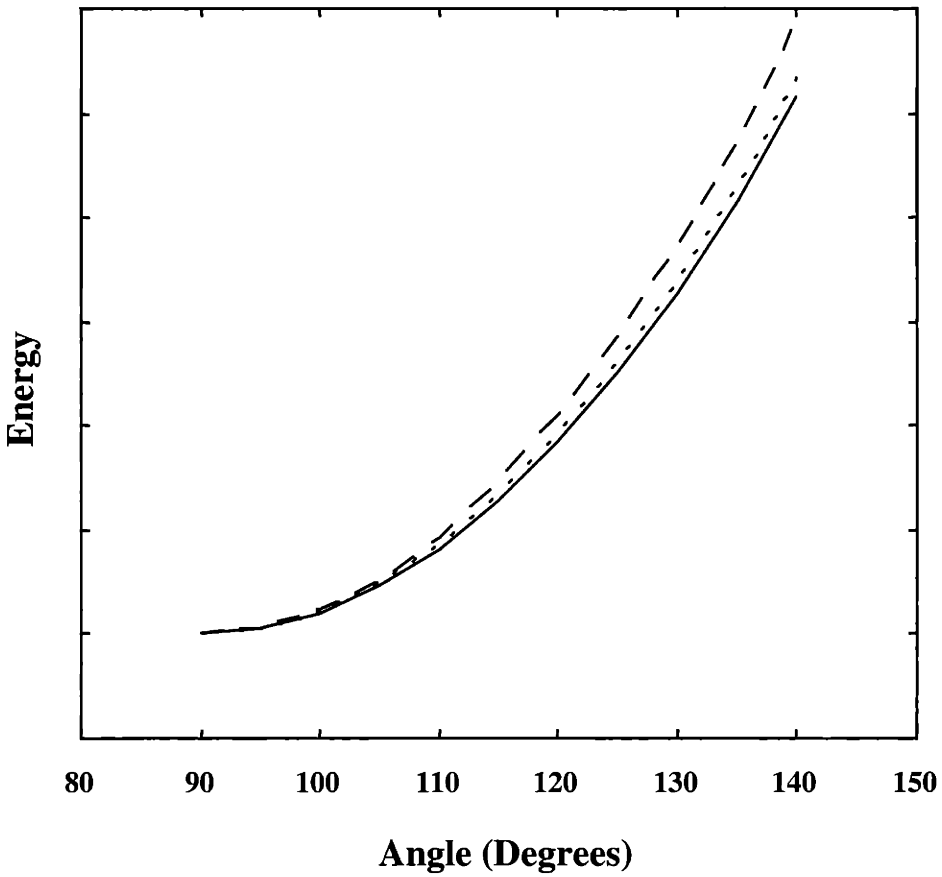

Figure 2.3 B3LYP(—), MP2(Full)(····), and HF(---) energy evaluated with a 6-31G(d,p) basis set as a function of the out of plane angle of a single Al-CH_3 bond in the TMA monomer. B3LYP has the lowest energy rise in response to the angle distortion.

Another aspect of the bridge bonds concerns the parallels of dimerization reactions to transition states (Figure 2.4). The exchange of methyl groups through the dimer may be compared to a transition state. The bond lengths and angles are distorted

and the density is spread over an extended area. From this point of view, it would be interesting to explore the analogy between the under-predicted well depth of these dimers to the reported under-prediction of transition state barriers with DFT methods.[49] Previous studies[50] have identified "exact" exchange as important for obtaining accurate transition state barriers. In these studies of hybrid DFT methods for bridging aluminum compounds, the Hartree-Fock like exchange calculation also has a strong effect on binding enthalpies. Decreasing the ratio of Hartree-Fock to Slater exchange in the hybrid functional gives more binding values for the dimeric structures. Eliminating the HF

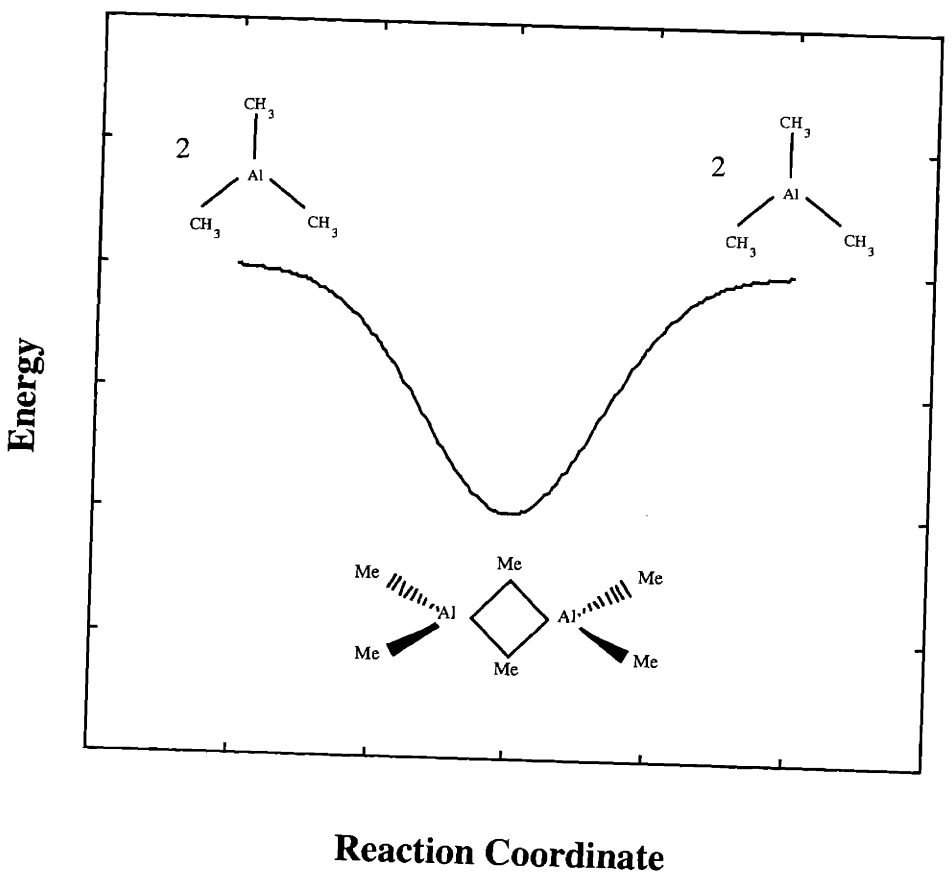

Figure 2.4 Aluminum organometallic dimerization reactions pictured as an "inverse" transition state.

contribution to exchange in the hybrid DFT expansion (a_0=0) gives a TMA dimer binding enthalpy (298.15K) of 18.1 kcal/mol. Increasing the Hartree-Fock component decreases the stability of the "transition state"-like dimer.

To summarize the effects of the components in the hybrid DFT expansion, note that increasing the Hartree-Fock exchange component or the Becke gradient correction causes under-binding for the dimers. Increasing the correlation gradient correction from a_C=0.81 results in stronger binding. In addition, the binding is sensitive to the type of correlation functional.

It is clear from the above results that the improvement in calculated binding enthalpies for bridging compounds from the modified hybrid functional is due to a re-calibration of the hybrid expansion. Although originally intended to be universally applicable, the hybrid functional does not satisfactorily represent bridge bonding. This results is not surprising, perhaps, given that these types of compounds were not included in the original parameterization.[8] As more chemical systems are studied, we can expect more troubled areas for the hybrid methods.[51] Recent studies of high reduced density gradients suggest the exchange term bears the larger portion of the error.[52]

A final note concerns the extension of the above arguments to other types of bridge bonding, where the trimer is an example. Table 2.5 shows that the same corrections that increase the binding of the dimer decrease the relative binding of the trimer. Therefore, the above arguments may not be generally applicable for all bridging aluminum compounds. It may be difficult (if at all possible) to describe all bridging aluminum compounds with a single modification of existing functionals. The current lack of data for the higher order associated units precludes a detailed investigation.

2.3.3 Heats of Formation

Fortunately, systematic errors of DFT methods encountered with heats of association of bridging aluminum compounds should not interfere with the calculation of heats of formation (of monomeric units). The problems experienced with DFT methods for describing enthalpies of association of aluminum compounds are rooted in the bridge

Table 2.6 Heats of formation (298.15K) for the Dimethylaluminum Hydride (DMAH) and Trimethylaluminum (TMA) gas phase system. Each method uses its own harmonic frequencies for calculation of zero point energies and thermal energy corrections. For the BLYP and B3LYP frequency calculations, the 6-31G(d,p) basis was employed. All values are given in kcal/mol.

	BLYP/ 6-31G(d,p)	BLYP/ 6-311++G(2df,pd)	B3LYP/ 6-311++G(2df,pd)	G2MP2	G1	G2*	Expt.
$AlH(CH_3)_2$ (g)	9.3	14.7	6.2	0.9	3.2	-0.4	-6.4[a]
$[AlH(CH_3)_2]_2$ (g)	-7.7	3.5	-15.9	-31.7†	-27.2†	-34.5† (-38.4 to -42.6)	‡
$[AlH(CH_3)_2]_3$ (g)	-17.6	0.7	-28.3	-55.0†	-48.2†	-59.0†(-64.8 to -71.2)	‡
$Al(CH_3)_3$ (g)	-2.6	5.2	-5.6	-13.1	-9.8	-14.8	-17.7[c] to -20.9[b]
$[Al(CH_3)_3]_2$ (g)	-11.7	6.9	-18.2	-44.6†	-38.1†	-48.0†(-51.8 to -56.1)	-55 to -60[d], -55.2[e]
$[(CH_3)_2Al(H)(CH_3)Al(CH_3)_2]$ (g)	-9.7	5.1	-17.1	-38.2†	-32.7†	-41.3†(-45.2 to -49.4)	‡

*Values in parenthesis are corrected for the estimated Al-CH_3 bond error, see text. †Based upon G# values for monomer units and MP2(Full)/6-311+G(d,p) association enthalpies. ‡A best estimate based on calculated and experimental monomer heats of formation and G2MP2 or MP2/6-311+G(d,p) association enthalpies gives -47.7, -77.6, and -53.4 for DMAH dimer and trimer, and DMAH/TMA cross species, respectively. [a] Estimated in Smith, M.B. *J. Organometal. Chem.* **1974,** *76,*171. [b]There is some variability in the literature between -13 and -21 kcal/mol; this number was selected on the advice of the above reference. [c]Wagman, D.D. *J. Phys. Chem. Ref. Data Supplement 2* **1982**. [d]Based upon reported heats of formation of monomer and the experimental enthalpy of association. [e]NBS Technical Note 270-3, Washington D.C., **1968**.

bonds. For calculated properties of the monomers, such as heats of reaction and heats of formation, we might expect good results from DFT calculations.[53]

Table 2.6 summarizes heats of formation for the components of the TMA and DMAH system. Calculations are based on atomization enthalpies and experimental data for heats of formation of H(g), Al(g), and C(g) at 298.15 K. No special procedures such as isogyric or isodesmic reactions were employed. Results show G2 calculations are close to experimental data with errors of ~3-6 kcal/mol. G2MP2 calculations are close to the full G2 results, but G1 calculations have about twice the error (8-11 kcal/mol). DFT calculations have significantly greater errors of ~12-15 kcal/mol for the B3LYP method, and >15 kcal/mol for the BLYP method. The BLYP/6-311++G(2df,pd) heats of formation are inferior to the smaller basis set calculations due to a fortuitous basis set error for the smaller basis set calculations. Further increasing the basis set to 6-311++G(3df,3pd) gives +12.9 and +2.8 kcal/mol for the heats of formation of DMAH and TMA, respectively. At least a portion of the error is due to under-binding of H_2(g) with the large basis set BLYP calculations. In this sense, the G2 values are overrated since their slight over-binding of H_2(g) results in more favorable heats of formation.[54] Both DFT methods yield poor heats of formation, but the hybrid method is a substantial improvement to pure DFT methods (8-10 kcal/mol).

Heats of formation for the dimers and trimer based upon the calculated heats of formation of the monomers and MP2/6-311+G(d,p) dimerization enthalpies are included in Table 2.6. The lack of sufficient experimental data makes these numbers difficult to assess, but the combination of errors from monomer heats of formation and dimerization enthalpies suggest the likelihood of considerable errors. The general behavior of the different methods for these aluminum compounds implies the listed values are lower limits to actual heats of formation.

A crude partitioning of the errors in the heats of formation for DMAH and TMA monomers can be used as a consistency check with the alane compound. Assignment of a G2 Al-CH_3 bond error of -0.97 to -2.03 kcal/mol (per bond) leaves an estimate for the aluminum hydrogen bond error of -1.94 to -4.06 kcal/mol. The combination of these estimates with a G2 heat of formation for alane ($AlH_{3\ (g)}$) of +28.2 kcal/mol (not

tabulated) suggests an improved heat of formation (for alane) of +16.0 to +22.4 kcal/mol. These heats of formation for alane compare well with the +18 kcal/mol estimate from reference 55. Unfortunately, the bond error estimates cannot be used to help localize the dimerization enthalpies since bridge Al-CH_3 and Al-H bonds are completely different from monomer bonds. They can, however, be used to improve heats of formation for the dimers and trimer by at least compensating for the error in the terminal Al-CH_3 bonds. These values are listed in Table 2.6 in parentheses next to the uncorrected values, for the G2 calculations only.

General observations from the heat of formation data suggest that while the pure DFT method has modest errors for geometric optimizations, vibrational frequencies (see below), and general reaction enthalpies, the method has significant errors for the calculation of heats of formation of these aluminum compounds. The hybrid DFT method is an improvement, but still yields poor heats of formation. The observed comparison between G2 calculations and DFT methods is in contrast with a recent study on silicon compounds.[14,54]

2.3.4 IR Vibrational Frequency Calculations.

Infrared spectroscopy is a major tool for experimental studies of aluminum organometallic compounds. Previous *ab initio* IR studies have been performed on model compounds of DMAH and TMA and the cross-bridged species DMAH-TMA (pentamethyldialane).[36,56,57] These complex bridging modes provide a test for the abilities of the various computational chemistry methods to predict harmonic vibrational frequencies. Unfortunately, MP2 vibrational frequency calculations on the herein studied molecules are impractical for workstation calculations. In contrast, DFT methods are currently practical for vibrational frequency calculations on molecules as large as the DMAH trimer. Experimental and DFT calculated values of selected infrared modes are shown in Table 2.7. Given the constraints that the calculations do not account for Fermi resonances or anharmonic affects, the predicted spectra are quite successful in capturing the essence of the experimental spectra, including the complex bridging modes. For

Table 2.7 Selected Infrared harmonic vibrational frequencies for associated aluminum compounds. All values are in wavenumbers (cm^{-1}).

	BLYP/ 6-31G(d,p)	B3LYP/ 6-31G(d,p)	BLYP/ 6-311G(df,pd)†	BLYP/ 6-311++G(df,pd)†	Expt.
DMAH Dimer[1] (D_2h)					
CH_3 ν_{as}	3023-3038	3102-3115	2995-3010	2988-3004	2950-2955
CH_3 ν_s	2957	3031	2941	2936	2902-2905
CH_3 δ_{as}	1437-1446	1473-1480	1433-1442	1428-1437	1444
CH_3 δ_s	1222-1228	1259-1264	1222	1217	1206
CH_3 ρ	732	747	723	721	709
CH_3 ω	714	728	706	703	692
AlH ν_{as}	1388	1442	1401	1399	1368[a]
AlH ν_s	1206	1245	1220	1220	1215
AlC_2 ν_{as}	654	675	658	656	690
AlC_2 ν_s	541	558	543	542	570-571
Me_2Al ρ_S	846	871	850	845	851
DMAH Trimer[1] (D_3h)					
AlH ν_{as}	1828	1899	1827	-	1785-1789
AlH in plane asymmetric motion	867	891	864	-	934-940[b]
AlH out of plane symmetric motion	798	819	796	-	792
TMA Dimer[2]					
CH_3 ν_{as}	3011	3090	2984	2986	2941
CH_3 ν_s	2986,2945	3068,3020	2972,2932	2934,2926	2899,2837
CH_3 δ_{as}	1456	1490	1450	1446	1437
CH_{3t} δ_s	1234	1268	1226	1221	1201
CH_{3b} δ_s	1262	1298	1253	1252	1255
CH_{3t} ρ	725	742	715	715	697
CH_{3b} ρ	778,599	800,618	770,591	768,585	768,608

Table 2.7 continued.

	BLYP/ 6-31G(d,p)	B3LYP/ 6-31G(d,p)	BLYP/ 6-311G(df,pd)†	BLYP/ 6-311++G(df,pd)†	Expt.[1,2,3]
$AlC_t\nu_{as}$	625	645	626	626	
$AlC_t\ \nu_s$	542	559	544	542	564
$AlC_b\ \nu_s$	463	482	461	461	480
$AlC_b\ \nu_{as}$	340	356	342	340	367
ν_{14},ν_{18} [4]	159,155	163,158	162,155	162,156	175
DMAH-TMA Complex[3] (pentamethyldialane)					
$AlH\ \nu_{as}$	1388	1436	-	-	1416
$AlH\ \nu_s$	1342	1382	-	-	1339
$AlC_b\ \nu_{as}$	302	320	-	-	326
$AlC_b\ \nu_s$	444	463	-	-	468
$Me_2Al\ \rho$	810	834	-	-	815

†Modified basis sets. A 6-31G basis set is used for each hydrogen atom in a terminal methyl group. All other atoms have the basis set listed in the table. Experimental assignments: [1]Ref. 56, [2]Ref. 57, [3]Ref. 36. [4]See ref. 59 for mode description. [a]Perturbed by Fermi resonance, estimated. [b]There is some uncertainty to the assignment of this mode. The experimental assignment is to symmetric AlH vibrations of the trimer. The closest calculated mode is a symmetric, in plane motion of the H atoms moving in and out of the ring at ~998 cm^{-1}. However, this mode is of A1' symmetry and not IR active for the D_{3h} point group. There exists a doubly degenerate mode calculated at ~860-870 wavenumbers of the correct symmetry and with significant intensity which is not assigned experimentally. The mode corresponds to in-plane, asymmetric AlH motion. We tentatively assign this calculated mode to the observed mode at 934-940 cm^{-1}. However, it is unlikely that the harmonic mode should appear below the actual vibration. This inconsistency suggests some complications in the experimental spectrum. (Note: the mode was not included in the error analysis).

example, for the largest basis set used, the symmetric Al-H stretch of the DMAH trimer (which has a very broad experimental feature) is predicted within 40 wavenumbers.

A general error analysis was performed using the modes with available experimental data. For both BLYP and B3LYP, there is a general trend (with exceptions) to overestimate modes above approximately 600 wavenumbers and underestimate the lower wavenumber modes. These results are consistent with the general observations in the literature.[58] The average absolute errors for the predicted modes are 29, 53, 25, and 25 wavenumbers for BLYP/6-31G(d,p), B3LYP/6-31G(d,p), BLYP/mod1, and BLYP/mod2, respectively. The larger error of the B3LYP method is due to the greater overestimation of the higher wavenumber modes. Below approximately 600

wavenumbers, the B3LYP method is closer to experiment than all BLYP calculations. The better match with experiment at low wavenumbers for the B3LYP method may give it an advantage with respect to thermal energy corrections. The average absolute percent deviations are 2.9, 3.7, 2.4, and 2.5% for the same ordering as above. Due to over and under prediction, a single linear scaling factor is not helpful for either the BLYP or B3LYP calculated frequencies. Applying both the high and low scale factors recommended in reference 58 with a dividing line of 600 wavenumbers improves the mean absolute errors to 21 and 17 wavenumbers for the BLYP/6-31G(d,p) and B3LYP methods, respectively. After scaling, the errors are distributed with both positive and negative deviations, indicating a limit to the application of linear scaling factors.

The modified basis sets were used to explore the sensitivity of vibrational modes to basis set size. The data show the effect of increasing basis set size to be modest. The average corrections to the BLYP/6-31G(d,p) predicted modes are 9 and 11 wavenumbers for modified basis sets 1 and 2, respectively. When compared with experiments, though, the corrections of the modified basis sets lead to an average improvement of only about 4 wavenumbers. The greatest improvement seems to come from the vibrations at high frequencies that are reduced in magnitude and brought closer to experiment. Since the primary effect of the larger basis sets is to reduce these high wavenumber frequencies, their corrections can largely be captured in scaling factors. It is interesting to note that although the modified basis sets actually reduce the number of basis functions on the hydrogen atoms of the terminal methyl groups, the terminal CH_3 stretching, bending, and rocking modes are better represented than with the 6-31G(d,p) basis set. The overall better match between experiment and theory for BLYP versus B3LYP is probably a favorable consequence of the over prediction of bond lengths by BLYP. Applying the recommended scaling factors appears to reduce the advantage of the BLYP calculated spectra. In addition, even considering the complicated bridging modes it does not seem worthwhile to use oversized basis sets for frequency calculations.

2.4 Conclusions

Consistent with many recently reported computational chemistry studies, results find the Hybrid DFT method (here represented by B3LYP, B3P86, and B3PW91) is the best DFT method available for the examined aluminum compounds and gives good results for geometric optimizations and harmonic vibrational frequency calculations. Heats of formation are significantly in error, but are an improvement to "pure" DFT methods. The "pure" gradient corrected DFT method (BLYP) provides reasonable structures and good vibrational modes, but is not useful for calculating heats of formation of the studied compounds.

Results show that DFT methods under-bind the dimers of bridge bonded aluminum compounds. The under-prediction of binding enthalpies occurs for weak (10 kcal/mol/bridge) to moderate (29 kcal/mol/bridge) bond strengths. For the B3LYP hybrid DFT method, errors range from 5-12 kcal/mol for the various bridging arrangements. A compensation effect between exchange and correlation functionals makes identification of the error difficult. Errors between experiment and theory can be reduced by using a different correlation functional or changing the coefficient for the contribution of the exchange correction in the hybrid functional. The systematic under binding of the aluminum bridge bonded dimers with respect to monomers is not limited to "electron deficient" bonds, but also appears for "normal" 2 center-2 electron bridge bonds. *Ab initio* calculations at the MP2 level are found to provide enthalpies of association close to experimental values, but there are insufficient data for a rigorous measurement of the accuracy. Given the prevalence of bridge bonding in aluminum organometallic chemistry, the poor performance of DFT methods for the compounds studied is unfortunate. Unless the errors can be systematically corrected or new functionals derived, DFT methods may be of limited use for this class of compounds.

Calculation of heats of formation of DMAH and TMA monomers with the G2 method gives errors reasonably close to the proposed target accuracy of 2 kcal/mol.[13] G2MP2 calculations are close to the G2 calculations, but G1 calculations yield errors twice as large. Absolute errors of 0.97-2.03 kcal/mol per Al-CH_3 bond and 1.94-4.06 kcal/mol per Al-H bond are estimated for the G2 calculations.

Infrared frequencies, including the complex bridge modes, are reproduced well by both pure and hybrid DFT methods. The match between experiment and theory is better for the pure BLYP method due to a fortuitous effect of the over-prediction of bond lengths. Both methods tend to over-estimate the vibrational frequencies at high wavenumber, but the error is not consistent throughout the frequency range, and a single linear scale factor is insufficient. Applying recommended scaling factors for both high and low frequencies leads to average absolute errors of less than 20 wavenumbers for the BLYP and B3LYP methods with a 6-31G(d,p) basis set. The scaling factors also appear to offset the advantages of the pure DFT method relative to the hybrid method for vibrational frequency calculations of these compounds.

2.5 References and Notes

1. T. Ziegler, *Chem. Rev.* **1991**, *91*, 651.
2. Slater, J.C. *Quantum Theory of Molecules and Solids, Vol. 4: The Self-Consistent Field for Molecules and Solids*; McGraw-Hill: New York, NY, 1974.
3. Vosko, S.H.; Wilk, L.; Nusair, M. *Can. J. Phys.* **1980**, *58*, 1200.
4. Becke, A.D. *Phys. Rev. A* **1988**, *38*, 3098.
5. Lee, C.; Yang, W.; Parr, R.G. *Phys. Rev. B* **1988**, *37*, 785.
6. Perdew, J.P. *Phys. Rev. B* **1986**, *33*, 4524.
7. Perdew, J.P.; Wang, Y. *Phys. Rev. B* **1992**, *45*, 13244.
8. Becke, A.D. *J. Chem. Phys.* **1993**, *98*, 5648.
9. Baker, J.; Muir, M.; Andzelm, J.; Scheiner, A. in *Chemical Applications of Density Functional Theory*; Laird, B.B., Ross, R.B., Ziegler, T. Eds.; ACS Symposium Series 629: Washington, DC, 1996.
10. Gaussian 94, Revision B.3, Frisch, M.J.; Trucks, G.W.; Schlegel, H.B.; Gill, P.M.W.; Johnson, B.G.; Robb, M.A.; Cheeseman, J.R.; Keith, T.; Petersson, G.A.; Montgomery, J.A.; Raghavachari, K.; Al-Laham, M.A.; Zakrzewski, V.G.; Ortiz, J.V.; Foresman, J.B.; Peng, C.Y.; Ayala, P.Y.; Chen, W.; Wong, M.W.; Andres, J.L.; Replogle, E.S.; Gomperts, R.; Martin, R.L.; Fox, D.J.; Binkley, J.S.;

Defrees, D.J.; Baker, J.; Stewart, J.P.; Head-Gordon, M.; Gonzales, C.; Pople, J.A., Gaussian, Inc., Pittsburgh PA, 1995.

11. Gill, P.M.W.; Johnson, B.G.; Pople, J.A.; Frisch, M.J. in *Int. J. Quantum Chem. Quantum Chem. Symp.*; Löwdin, P-O., Öhrn, N.Y., Sabin, J.R., Zerner, M.C. Eds.; Wiley: New York, NY, *26*, **1992**; p. 319.
12. Curtiss, L.A.; Jones, C.; Trucks, G.W.; Raghavachari, K.; Pople, J.A. *J. Chem. Phys.* **1990**, *93*, 2537.
13. Curtiss, L.A.; Raghavachari, K.; Trucks, G.W.; Pople, J.A. *J. Chem. Phys.* **1991**, *94*, 7221.
14. Hay, J.P. *J. Phys. Chem.* **1996**, *100*, 5.
15. Ahlrics, R. *Theoret. Chim. Acta* **1974**, *35*, 59.
16. Levinson, K.A.; Perkins, P.G. *Theoret. Chim. Acta* **1970**, *17*, 1.
17. Levinson, K.A.; Perkins, P.G. *Theoret. Chim. Acta* **1970**, *17*, 15.
18. Lappert, M.F.; Pedley, J.B.; Sharp, G.J.; Guest, M.F. *J. Chem. Soc., Faraday Trans. II* **1976**, 539.
19. Gropen, O.; Johansen, R. *J. Organometal. Chem.* **1975**, *92*, 147.
20. Bhat, R.; Koza, M.A.; Chang, C.C.; Schwarz, S.A. *J. Cryst. Growth* **1986,** *77*, 7.
21. Biswas, D.R.; Ghosh, C.; Layman, R.L. *J. Electrochem. Soc.* **1983**, *130*, 234.
22. Kondoh, E.; Ohta, T. *J. Vac. Sci. Technol. A* **1995,** *13*, 2863.
23. Zhu, N.; Cacouris, T.; Scarmozzino, R.; Osgood, J., Jr. *J. Vac. Sci. Technol. B* **1992**, *10*, 1167.
24. Fiordalice, R.W.; Ong , T.; Garcia, S.; Farkas, J.; Fernandes, M.; Freeman, M.; Gall, M.; Jain, A.; Jawarani, D.; Kawasaki, H.; Klein, J.; Roman, B.; Sparks, T.; Venkatraman, R.; Vuong, T.; Weitzman, E.; Pintchovski, F. in *Advanced Metallization and Interconnect Systems for ULSI Applications in 1996*; Havemann, R., Schmitz, J., Komiyama, H., Tsubouchi, K. Eds.; Materials Research Society: Pittsburgh, PA, 1996; p 13.
25. Willis, B.G.; Jensen, K.F. in *Advanced Metallization and Interconnect Systems for ULSI Applications in 1996*; Havemann, R., Schmitz, J., Komiyama, H., Tsubouchi, K. Eds.; Materials Research Society: Pittsburgh, PA, 1996; p 29.

26. Strongin, D.R.; Comita, P.B. *J. Phys. Chem.* **1991**, *95*, 1329.

27. Almenningen, A.; Anderson, G.A.; Forgaard, F.R.; Haaland, A., *Acta Chem. Scand.* **1972,** *26,* 2315.

28. Tanaka, J.; Smith, S.R. *Inorg. Chem.* **1969,** *8*, 265.

29. Wartick, T.; Schlesinger, H.I. *J. Am. Chem. Soc.* **1953**, *75*, 835.

30. Lewis, P.H.; Rundle, R.E. *J. Chem. Phys.* **1953,** *21*, 986.

31. Vranka R.G.; Amma, E.L. *J. Am. Chem. Soc.* **1967**, *89*, 3121.

32. Wade, K. *Electron Deficient Compounds*; Nelson: London, 1971; (b) Wade, K., *J. Chem. Education* **1972**, *49*, 502.

33. Hiraoka, Y.S.; Mashita, M. *J. Cryst. Growth* **1994**, *145*, 473.

34. Lammertsma, K.; Leszczynski, J. *J. Phys. Chem.* **1990**, *94*, 2806.

35. Chey, J.; Choe, H.S.; Chook, Y.M.; Jensen, E.; Seida, P.R.; Francl, M.M. *Organometallics* **1990**, *9*, 2430.

36. Russell, D.K.; Claxton, T.A.; Grady, A.S.; Linney, R.E.; Mahmood, Z.; Markwell, R.D. *J. Chem. Soc., Faraday Trans.* **1995**, ***91***, 3015.

37. Williams, S.D.; Harper, W.; Mamantov, G.; Tortorelli, L.J.; Shankle, G. *J. Comp. Chem.* **1996**, *17*, 1696.

38. Hehre, W.J.; Radom, L.; Schleyer, P.v.R.; Pople, J.A. *Ab Initio Molecular Orbital Theory*; John Wiley & Sons: New York, NY, 1986.

39. Liang, C.; Davy, R.D.; Schaefer III, H.F. *Chem. Phys. Lett.* **1989**, *159*, 393.

40. Dewar, M.J.S.; Patterson, D.B.; Simpson, W.I. *J. Chem. Soc., Dalton Trans.* **1973**, 2381.

41. Almenningen, A.; Halvorsen, S.; Haaland, A. *Acta Chem. Scand.* **1971**, *25*, 1937.

42. Oliver, J.P. in *Advances in Organometallic Chemistry*; Academic Press *235*: New York, NY., 1977.

43. Others have noted that the Al-Al distance is close to the sum of the van der Waal radii of the two aluminum atoms and argued that Al-Al bonding is important for stabilizing dimer structures[30,31,34,41,42]. Regarding this idea, it is interesting to note that DMAH and TMA have similar Al-Al distances. Rather than lengthen the Al-Al distance, the bonding in TMA chooses to decrease the Al-C-Al bridging angle.

These geometric features may be linked to the optimal configurations for Al-C bonding and repulsion between Al atoms at small distances rather than to Al-Al bonding.

44. Hoffmann, Von E.G.; Schomburg, G. *Zeitschrift fur Elektrochemie* **1964**, *68*, 1101.

45. Henrickson, C.H.; Eyman, D.P. *Inorg. Chem.* **1967**, *6*, 1461.

46. Mohr, M.; Zipse, H.; Marx, D.; Parrinello, M. *J. Phys. Chem. A.* **1997**, *101*, 8942.

47. Derecskei-Kovacs, A.; Marynick, D.S. *Chem. Phys. Lett.* **1994**, *228*, 252.

48. The modified B3PW91 functional is not suggested as a new functional for any other system. Its purpose is only to demonstrate the compensating effect of the exchange and correlation functionals and the abnormal behavior of the bridging aluminum compounds. Calculations on other systems with this functional would not be expected to give quality results. However, the general approach may have implications for understanding corrections to systematic errors in DFT calculations.

49. Baker, A.S.; Muir, M.; Andzelm, J. *J Chem. Phys.* **1995**, *102*, 2063.

50. Baker, J.; Andzelm, J.; Muir, M.; Taylor, P.R. *Chem. Phys. Lett.* **1995**, *237*, 53.

51. Wesolowski, T.A.; Parisel, O.; Ellinger, Y.; Weber, J. *J. Phys. Chem. A.* **1997**, *101*, 7818.

52. Ruiz, E.; Salahub, D.R.; Vela, A. *J. Am. Chem. Soc.* **1995**, *117*, 1141.

53. Here, heats of reaction is meant to include non-associative reactions. This restriction excludes a large portion of aluminum organometallic chemistry.

54. This statement deserves some comment. The fortuitous effect comes from the difference between the experimental and G2 measurement of the $H_2(g)$ binding enthalpy. The procedure of calculating heats of formation via atomization enthalpies and using the experimental heat of formation for H(g) artificially improves the calculated heats of formation of DMAH and TMA. When using the experimental heat of formation of H(g) , the difference between this number and the G2 value is multiplied by the number of hydrogen atoms in the molecule and added to the calculated heats of formation. In the case of TMA with 9 hydrogen

atoms, the effect is almost 5 kcal/mol. If instead the heats of formation are calculated through a reaction with hydrogen in its standard state (H_2(g)) or, equivalently, using the G2 heat of formation of H(g), the favorable effect is not present and the G2 values are only slightly (~1 kcal/mol) better than the G1 numbers. This effect is not present for the G1 calculations because in the G1 method the higher level correction is specifically designed to make the electronic energy exact for the H atom and hydrogen molecule.[13] The choice of the experimental heat of formation for the H atom to calculate heats of formation has a small favorable effect on B3LYP computed values and an unfavorable effect on BLYP calculations. Note that without this effect, G1 and G2 heats of formation are only ~4 kcal/mol superior to B3LYP calculations.

55. Tirtowidjojo, M.; Pollard, R. *J. Cryst. Growth* **1986**, *77*, 200.

56. Grady, A.S.; Puntambekar, S.G.; Russell,D.K., *Spectrochimica Acta* **1991**, *47A*, 47.

57. Ogawa, T. *Spectrochimica Acta* **1968**, *24A*, 15.

58. Scott, A.P.; Radom, L. *J. Phys. Chem.* **1996**, *100*, 16502.

59. Mole, T.; Jeffery, E.A. Organoaluminum Compounds; Elsevier: New York, NY, 1972,56.

Chapter 3

DMAH Gas Phase Reaction Pathways and Kinetics

3.1 Thermodynamics and Chemical Mechanism

Based on calculations of the previous chapter, a plot of the DMAH monomer-dimer-trimer equilibrium is illustrated in Figure 3.1. The predicted equilibrium is based on chemically accurate[i] calculations and thought to provide an accurate representation of the DMAH equilibrium. The results are consistent with classic experimental data, which indicate a mixture of dimer and trimer in the vapor phase between 83 and 167°C.[1] More recent experiments using infrared studies, however, concluded that DMAH exists predominantly as the dimer at room temperature.[2]

In Chapter 4, experimental surface science experiments determine that DMAH growth proceeds through a surface disproportionation mechanism that produces trimethylaluminum (TMA) as a reaction product. In addition, the studies of Chapter 2 introduced the mixed compound, pentamethyldialane, which forms in DMAH and TMA mixtures. Therefore, it is instructive to also investigate the DMAH-TMA equilibrium. The mixed system equilibrium is shown in Figure 3.2. Quantum chemistry calculations predict that pentamethyldialane is indeed an important component in mixtures of DMAH and TMA. At 60% conversion (3 DMAH(g) $\Rightarrow$ 2 TMA(g) + Al(solid) + 3/2 H_2(g), a DMAH-TMA 50-50 mixture) pentamethyldialane accounts for approximately half the mixture at low temperatures. Experimental data, however, suggest pentamethyldialane

dominates mixtures of TMA and DMAH to a greater extent than the calculations indicate.[3]

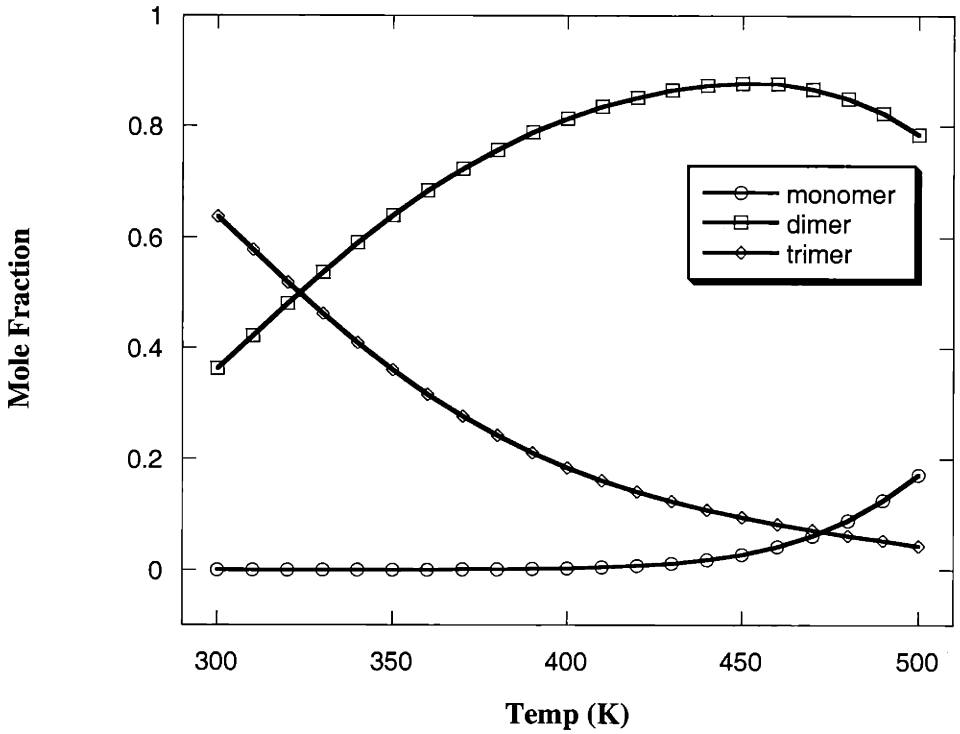

Figure 3.1 Monomer-Dimer-Trimer Equilibrium of DMAH vapor at 2 Torr, predicted from electronic structure calculations.

In addition to the above discrepancies between the (accurate) calculations and experimental observations, others have observed that the liquid properties (primarily viscosity) of DMAH depend strongly on the synthetic route[ii] and processing.[4,5] Considering the accuracy of the electronic structure calculations, these observations taken together indicate that an equilibrium description of the properties of DMAH is not sufficient to determine its composition across various conditions. It is the premise of this chapter that these observations can be explained not by experimental errors, experimental

---

[i]Chemical accuracy is a term introduced here to refer to calculations within a 2 kca/mol error bar which are useful for quantitative predictions in chemistry.

[ii]Private communication with Matt Healy, formerly of Schumacher, Carlsbad, CA.

uncertainties, or chemical contamination, but rather by a kinetic description of the liquid and vapor phase reaction pathways. The present work is restricted to a quantum chemistry study of gas phase reaction pathways. Investigations of the liquid might be expected to give qualitatively similar behavior, but with corrections to account for the liquid environment.

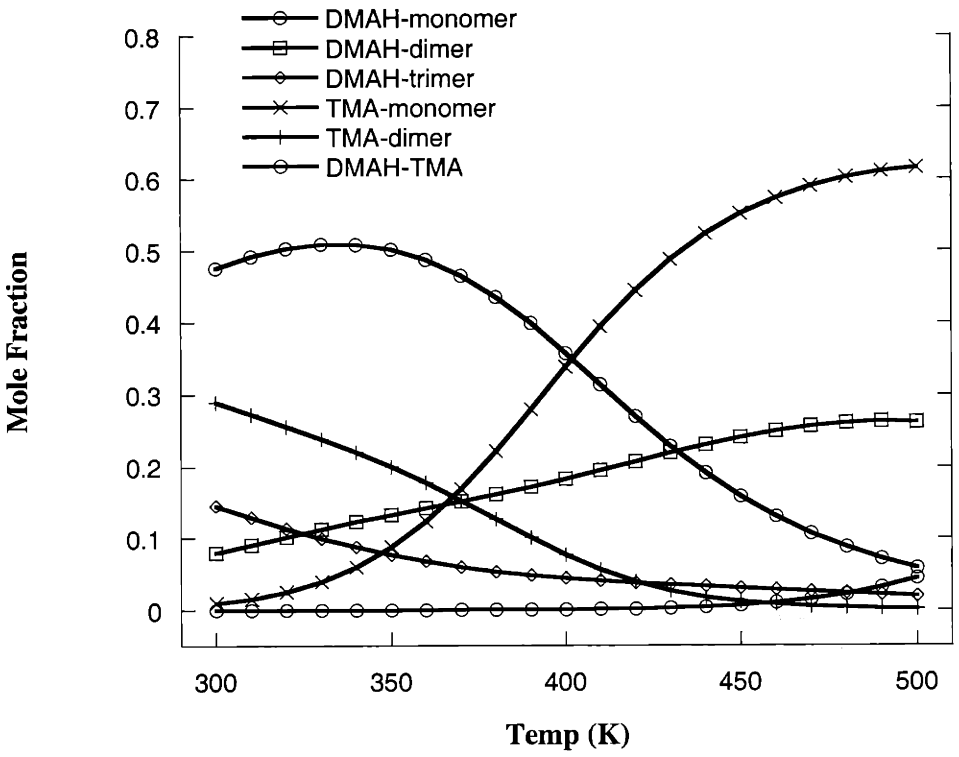

Figure 3.2 Dimethylaluminum hydride – Trimethylaluminum vapor phase Equilibrium at 10 Torr and 60% conversion (DMAH to TMA), predicted from electronic structure calculations.

Interpreting the observed behavior of DMAH in terms of the kinetics of elementary reaction pathways is supported by work on other aluminum organometallic compounds including the alkoxides[6] and amides.[7-9] Experimental studies of these compounds have observed a similar time/process dependent composition with observed half-lives ranging from minutes to weeks or months depending on the compound. Based

on the studies of the above aluminum organometallic compounds, three basic reaction pathways have been proposed for the equilibration of dimers and trimers.

The simplest equilibration mechanism is dissociation of the trimer/dimer into monomers and subsequent recombination of monomers to form dimers or trimers. However, breaking a dimer or trimer into monomers is highly endothermic, +35 and +58.5 kcal/mol for the following reactions, respectively:

$$dimer \Rightarrow 2\ monomers$$

$$trimer \Rightarrow 3\ monomers$$

This mechanism is discounted by all accounts.[6,7,9] A second possible pathway is ring opening of the trimer and self dissociation to form a dimer and monomer. This mechanism is partially supported by cursory evidence of a monomer in experiments with amide compounds.[10] Note that the reverse reaction to form trimers requires the presence of monomers. These monomers must come from the complete dissociation of dimers or, possibly, ring opening of the dimer and attack on another dimer. The latter mechanism - ring opening and attack on another species by either dimer or trimer - comprises the third reaction pathway.

The second mechanism, ring opening and self-dissociation by a trimer, also seems an unlikely pathway. First, the pathway has a significant barrier, since breaking a trimer bridge bond requires almost +20 kcal for DMAH and significantly more for the amide and alkoxide bridges. Additionally, if such a pathway were valid, it would be difficult to explain the widely different rates of equilibrium, since they do not correlate to trimer bridge strengths[iii]. Consistent with the above arguments and experimental observations with amide compounds that larger alkyl groups cause slower equilibration, it was suggested the attack step could be rate limiting. (The larger alkyl groups are expected to

---

[iii] For example, qualitative evidence suggests DMAH has a very slow rate of approach to equilibrium, and there exist alkoxides with significantly faster rates of equilibration. Based on an estimate of the dimer alkoxide bridge strength from the *ab initio* calculations of Chapter 2, and the experimental value of +22.7 kcal/mol for the reaction 2 trimers $\Rightarrow$ 3 dimers for the Me_2AlOPr^n compound, a bridge strength >+30 kcal/bridge for an alkoxide trimer is estimated. Compare this with ~20 kcal/bridge for the DMAH trimer.

have lower trimer bridge strengths.) Formation of an open ring is endothermic by ~20 kcal/mol (for DMAH), but the overall reaction

$$trimer \Rightarrow monomer+dimer$$

is endothermic by only ~24 kcal/mol so that self-attack should occur without a significant barrier. To be rate limiting, the reaction would have to exhibit an anomalous low pre-exponential, which seems unlikely.

The last reaction pathway, ring opening and attack on a neighboring trimer or dimer, seems more consistent with experimental observations, but there are also problems with this mechanism. Ring opening and attack on neighboring molecules would form larger oligomers such as tetramers, pentamers, hexamers, and possibly larger units. Such arguments are consistent with both experimental studies, including mass spectroscopy data[6,11], and the *ab initio* calculations of the present study. Taken literally, a ring opening attack on a neighbor would require a unimolecular ring opening with a high activation barrier (~20 kcal/bridge for DMAH) and again could not explain the trends among the different rates of equilibration for DMAH, amides, and alkoxides. Therefore, in the present study the favored "ring opening and attack on a neighbor" mechanism is modified to consist of a concerted bimolecular reaction rather than a true "ring opening". As shall be demonstrated, such a mechanism is consistent with most experimental observations, and can account for the subtle differences observed with the various types of bridge bonds and terminal ligands.

Before pursuing the development of a kinetic mechanism, it is prudent to emphasize the studies here are primarily motivated by a description of vapor phase reactions or reactions in the neat liquid. The possible experimental observation of monomer in studies of the amide compounds[10], using solvents, suggests solvent effects could be very important. Based on the current studies and chemical intuition, even the trace presence of monomeric species could drastically alter the reaction pathways to equilibrium. Such conclusions are supported by kinetic studies of the pyrolysis of trimethylaluminum-ammonia adduct in the neat liquid that gave significantly different

results from experiments in solution. Although the results were questioned in the report, they could be explained by the absence of the monomer from the neat liquid. Figure 3.1 shows there is virtually no DMAH monomer at low to modest temperatures. Given the additional strength of nitrogen bridge bonds (see Chapter 2), an amide monomer is even less likely (in the neat liquid).

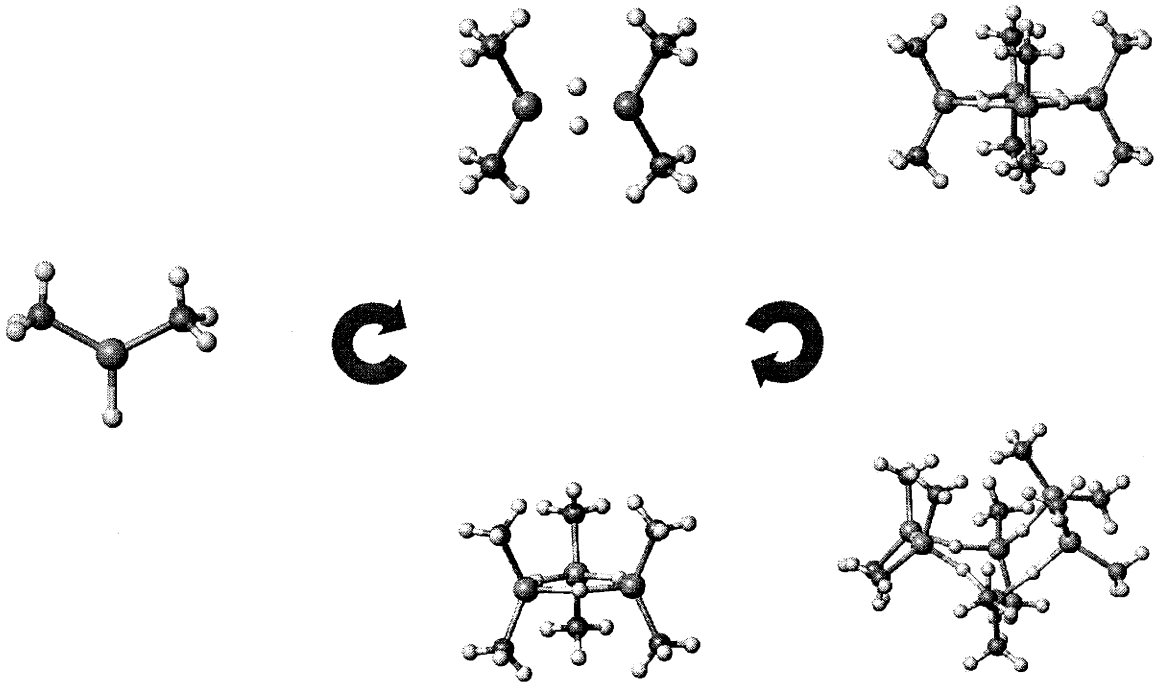

Figure 3.3 Dimethylaluminum hydride proposed reaction pathways. Clockwise, starting from left are: monomer, dimer, tetramer, hexamer, and trimer.

Reaction pathways investigated for DMAH equilibration are shown in Figure 3.3. The pathways involve formation of tetramer and hexamer intermediates. These oligomers allow inter-conversion of dimers and trimers without requiring monomers or other reactive intermediates. As discussed above, monomers are unlikely to be formed at the low temperatures where the equilibrium slowly progresses. Noticeably absent from the mechanism are pentamers. Although it seems reasonable that pentamers should form if hexamers do, pentamers are ignored because they do not lead to a net dimer-trimer inter-conversion, and calculations show that higher oligomers are present only at low

concentrations as reaction intermediates. Therefore, it is reasoned that inclusion of pentamers is not essential to understand the approach to equilibrium. However, studies primarily interested in understanding liquid properties, such as viscosity, may have to consider pentamers. Free energy considerations would most likely favor pentamers over hexamers. Note that fragments assigned to pentamers were observed in previous mass spectroscopy studies of DMAH.[11]

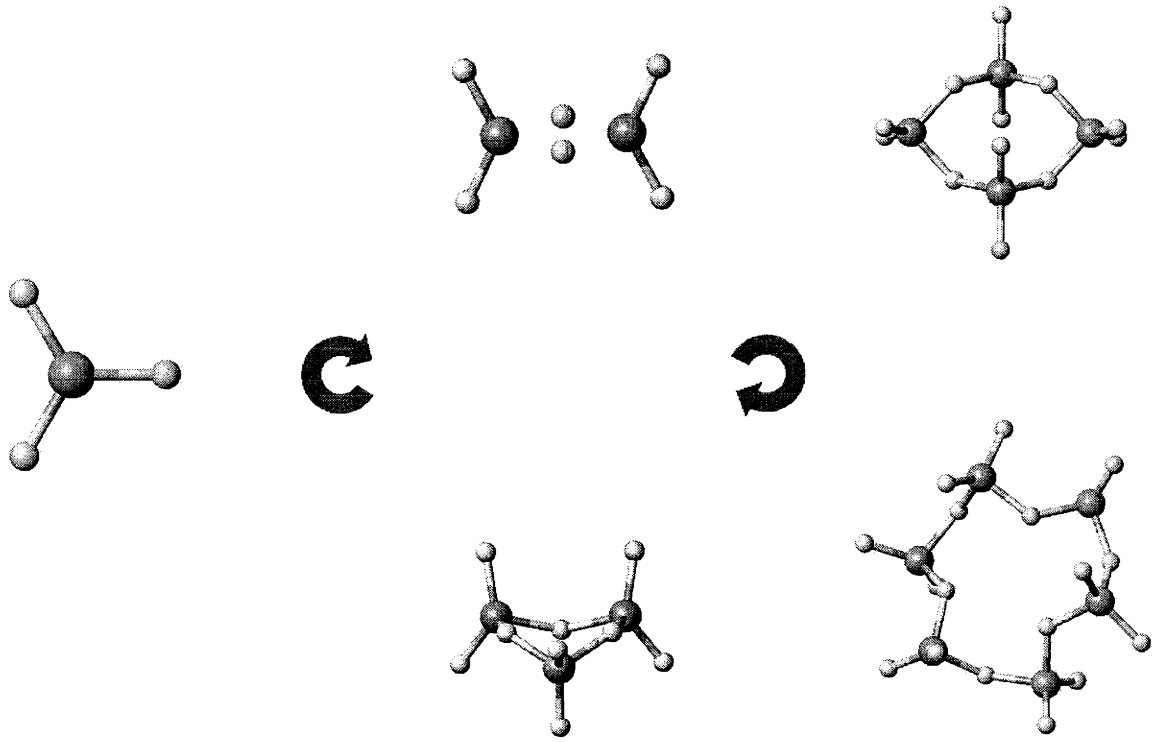

Figure 3.4 Alane reaction pathways, as a model for Dimethylaluminum Hydride (DMAH). Clockwise from left are: monomer, dimer, tetramer, hexamer, and trimer.

For the present *ab initio*/density functional theory (DFT) investigations of the chemical mechanism and kinetics of the DMAH gas phase system, alane (AlH_3) was chosen as a model system. Alane is the simplest analog to aluminum organometallics, and a natural place to begin investigations into the gas phase chemistry of these types of compounds. Alane serves as a model not only for DMAH and TMA systems, but also for other aluminum compounds such as precursors for AlGaAs[12] and AlN deposition.[13-19]

For AlN, these higher order units are suspects for the nucleation of unwanted particles in the gas phase.[15,20] Results reveal that although a strict comparison of alane with DMAH may be inexact, the investigations discover reaction pathways that spawn new ideas about how these compounds interact in the liquid and vapor phase. A precise evaluation of the applicability of the alane system for modeling the chemistry of DMAH and other aluminum organometallic compounds must await further studies on these compounds, themselves, but in the meantime the alane model provides useful insight.

Table 3.1 Heats of reaction ($\Delta H^{298.15}$) of DMAH and alane gas phase association reactions (values in kcal/mol). Differences between DMAH and alane heats of reaction are shown in the last column. For calculations not involving the hexamer, differences are taken between MP2 calculations. For calculations involving the hexamer, DFT differences are given. (The B3PW91/6-31G(d,p) method was used for alane in that case.) Note the under-binding of DFT methods when compared to the MP2(Full) calculations.

	DMAH		Alane	Δ
	MP2/ 6-31G(d,p)	B3LYP/ 6-31G(d,p)		
dimer ⇔ 2 monomer	33.2	28.0	33.0	0.2
trimer ⇔ monomer + dimer	23.6	19.4	20.9	2.7
tetramer ⇔ 2 dimer	9.2	7.6	7.7	1.5
hexamer ⇔ dimer + tetramer	10.8	2.7	2.8	0.1
hexamer ⇔ 2 trimer	5.0	-1.6	-0.1	-1.5

The replacement of two methyl groups on DMAH with hydrogens to form alane presents a considerable simplification for the electronic structure calculations and makes quantum chemistry calculations practical for studying the gas phase system. Besides the efficiency considerations of this substitution, there is support for the substitution based on comparisons of thermodynamic calculations on the two systems, DMAH and alane. Figure 3.4 shows an alane chemical mechanism consisting of monomers, dimers, trimers, tetramers, and hexamers, analogous to that of DMAH. Table 3.1 lists *ab initio* and DFT calculated heats of reaction for DMAH and alane reaction pathways. Comparisons between the two systems reveal similar heats of reaction for the corresponding reaction steps. The largest difference of ~2.7 kcal for the *trimer* ⇒ *monomer* + *dimer* reaction is relatively small compared with the overall thermodynamics. These similarities in

computed thermodynamics for the reaction cycle provide support for using alane as model system. It is an assumption of the present investigations to expect that the same similarities would exist for calculations of activation energies and corresponding reaction rate constants, at least semi-quantitatively. Results will show, however, that although DMAH and alane share many similarities, there are differences that could be important.

3.2 Theoretical Methods

Optimized minimum structures and transition state geometries were computed using the Gaussian 94 suite of programs.[21] Frequency calculations were performed with analytic gradient techniques to provide zero point energies and thermal energy corrections. Statistical mechanical relations were used to compute entropies and Gibbs free energies for the calculation of equilibrium constants. Equilibrium predictions were accomplished using temperature dependent equilibrium constants and the ideal gas approximation. Rate constants were computed using transition state theory.

Transition states were optimized using the Synchronous Transit-Guided Quasi-Newton QST methods[22,23] to attain approximate transition state structures. Analytic force constants were calculated for the QST structures, and the Berny saddle point algorithm was used to subsequently optimize the structures.[24,25] For reactions involving the hexamer, considerable difficulty was encountered in both minimum and transition state optimizations. The apparently flat potential energy surface required numerous iterations, because while forces remained small, large displacements continued. Optimizations were considered complete when the forces became vanishingly small.

Calculations were performed using primarily density functional methods with some additions of MP2(full) single point energy calculations. Transition state calculations involving the large hexamer-like structures employed a 3-21G* basis set. The 3-21G* and 3-21G** basis sets were previously found to provide reasonable accuracy for these types of aluminum organometallic systems.[26] The small 3-21G* basis set was used for efficiency because of the need to calculate force constants analytically. Unfortunately, the difficult nature of the potential energy surface made it unrealistic to simply re-optimize transition state structures at higher basis set levels. As an example, a

simple re-optimization of the hexamer at 3-21G** using the 3-21G* converged structure as an initial guess required > 100 iterations with the Berny optimization scheme. For saddle point optimizations involving dimeric and tetrameric structures and for all minimum optimizations, a larger 6-31G(d,p) basis set was used.

Chapter 2 showed that DFT methods may not properly represent the thermodynamics of bridge-bonded structures such as these aluminum organometallics. Whether the problems with calculating heats of reaction will extend to calculating activation energies is yet unknown. However, given the errors in heats of reaction, at least one of either the forward or reverse activation barriers may be in error. MP2(full)/6-31G(d,p) calculations are included to briefly explore this issue, but the size of the molecules prohibits extensive investigation of differences between *ab initio* and DFT predictions. Instead, DFT methods are relied upon to produce at least a semi-quantitative account of the chemical mechanisms. A rigorous comparison between *ab initio* and DFT predictions of activation barriers for reactions of bridge bonded compounds remains a fruitful area for future investigation.

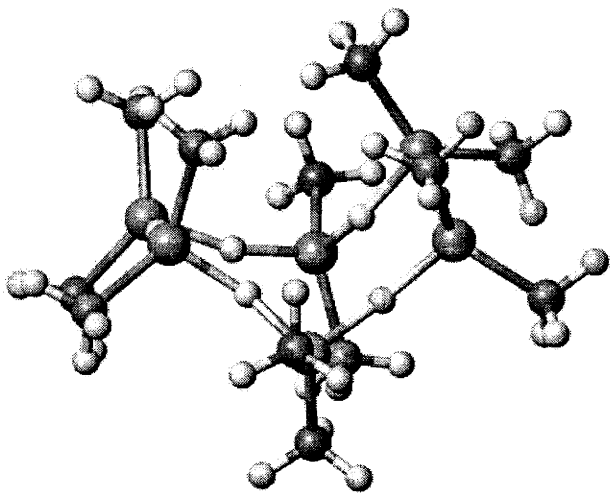

Figure 3.5 DMAH hexamer optimized with the B3LYP/3-21G** method.

3.2 DMAH and Alane Structures

Chapter 2 showed that density functional theory methods are reliable for predicting geometric structures of bridge bonded aluminum compounds. Therefore, only a brief account of the alane and DMAH structures is given here, to aid in visualization of the reactions. Figures 3.3 and 3.4 illustrate the optimized structures for the monomer, dimer, trimer, tetramer, and hexamer of DMAH and alane, respectively. Monomeric and dimeric structures of DMAH and alane are similar, but have D_{3h} symmetry for the alane monomer and C_{2h} symmetry for the DMAH monomer. Both alane and DMAH dimers have D_{2h} symmetry. Calculations show that while the DMAH trimer and tetramer prefer a planar arrangement with high symmetry (D_{3h} and D_{4h}), alane adopts pseudo-tetrahedral Al-H bonds and a lower overall symmetry. The planarity of DMAH rings is somewhat of a irregularity among these types of aluminum organometallics. For other planar trimers, such as the t-butyl amide trimer, steric arguments have been employed to explain the anomaly. The observation that DMAH trimers and tetramers are planar suggests electronic effects may also be important. (Terminal methyl ligands would not appear to be sterically demanding, unless the ring is abnormally small compared to other trimers.) The alane trimer adopts a boat configuration with C_s symmetry, and the tetramer takes a C_{2h} structure. The C_{2h} tetramer is significantly different from a previously reported structure with C_{2v} symmetry.[27] In the previous work, an energy difference of ~1 kcal/mol was noted between the more stable C_{2v} structure and the planar D_{4h} structure of the alane tetramer. For the present C_{2h} structure, the energy difference is closer to 3 kcal/mol, indicating the C_{2h} isomer may be more stable than the C_{2v} form. Al-H-Al bond angles of the C_{2v} structure from the above reference are reported near linear, whereas the present C_{2h} structure gives angles close to 130°. These rather large differences may be due to the use of the SCF (Hartree-Fock) optimization in the previous work, versus the present studies, which include electron correlation effects in geometry optimizations (DFT methods). For calculation of the reaction energy of *tetramer* $\Rightarrow$ *2dimers*, where electron correlation was included in the previous work, their value of +8.0 agrees fairly well with the present results (Table 3.1).

Hexamers of both alane and DMAH have complex, distorted ring structures. The DMAH hexamer arranges itself into a non-planar contorted ring with terminal methyl groups projecting out of the ring, and pseudo-tetrahedral environments of bridging hydrogen atoms around each aluminum atom (Figure 3.5). Although not constrained by symmetry in the optimization, the minimized structure appears to have at least a C_2 symmetry axis. Apparently, the angle strain of a planar D_{6h} structure becomes prohibitive for DMAH in the hexamer. The difference in energy between the D_{6h} and C_2 structure is small, however, approximately 1.5 kcal/mol calculated with the B3LYP/6-31G(d,p) method[iv]. Due to the absence of imposed symmetry in the calculation, the DMAH hexamer bond angles vary around the ring with values of ~93° for H-Al-H, two each of 159°, 146°, and 177° for Al-H-Al bond angles, and ~126-127° for terminal C-Al-C angles. Bond lengths are approximately 1.69-1.70 Å for Al-H_{bridge} bonds, and ~1.97 Å for Al-$C_{terminal}$ bonds. Al-Al distances vary around the ring with two each of 3.33, 3.25, and 3.37 Å. The double degeneracy of the Al-H-Al angles and Al-Al distances reflect the implied C_2 axis of the hexamer. A higher molecular symmetry could be obtained by imposing symmetry on the Al-H-Al angles and Al-Al distances, but unfortunately, verifying that a higher symmetry structure was indeed a true minimum (via a frequency calculation) is not currently practical.

The optimized alane hexamer in the present study has no apparent symmetry (C_1). However, calculations indicate the hexamer traverses a rather flat PES, so that many conformations may be nearly equivalent. One way to visualize the alane hexamer is to consider six AlH_2 groups, arranged in a ring with bridging hydrogen atoms and pseudo-tetrahedral environments. Another approach is to imagine a ring formed from three dimers, each with one terminal-hydrogen acting as a bridge to another dimer on one side of the dimer, and accepting a terminal-hydrogen bridge from another dimer on the other side. The first approach provides a closer parallel to the DMAH hexamer, but the second

[iv] For the C_2 DMAH hexamer, the B3LYP/6-31G(d,p) calculation is a single point energy calculation on the B3LYP/3-21G** optimized geometry. The D_{6h} structure was minimized at the B3LYP/6-31G(d,p) level, so the actual difference (within the DFT approximation) may be slightly larger.

underscores an ambiguity as to the labeling of terminal and bridging hydrogen atoms in the alane hexamer.

3.3 Results - Alane Kinetics

Investigations of reaction pathways and kinetics for simulations of the inter-conversion of dimers and trimers have been quantified through calculations using a combination of transition state theory and collision theory to obtain rate constants. For each elementary reaction, reverse rate constants are derived using relation (1) between the equilibrium constant K_c and the forward and reverse rate constants.

$$K_c = k_f / k_r \qquad (1)$$

Units of moles, liters, and seconds are used throughout. Following presentation of the details of the individual elementary reactions, a simulation is included to model the *trimer* $\Leftrightarrow$ *dimer* approach to equilibrium. Simulations are accomplished by integrating the kinetic rate equations using the LSODE integrator package.[28]

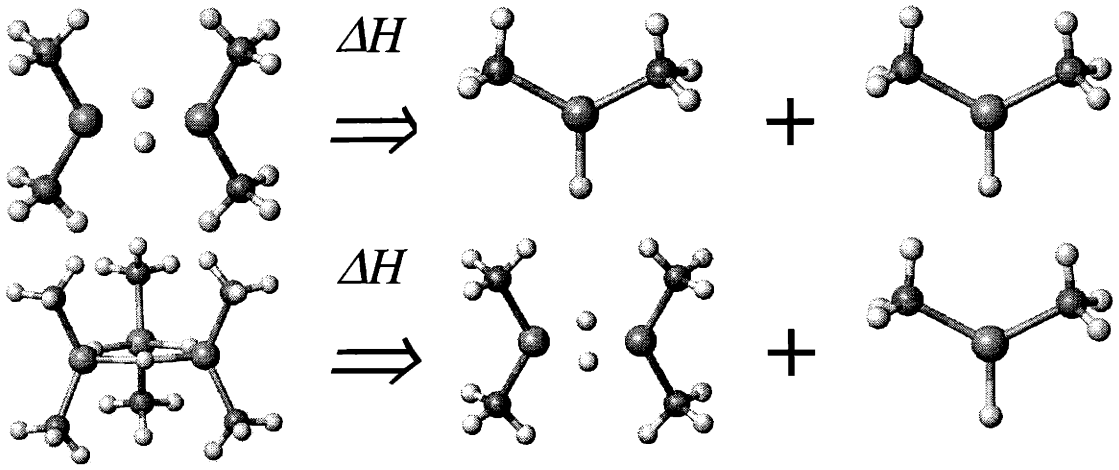

Figure 3.6 Unimolecular decomposition reactions of DMAH dimer and trimer. The reactions are found to have no reverse activation barrier. The forward activation barrier is the heat of reaction, ΔH.

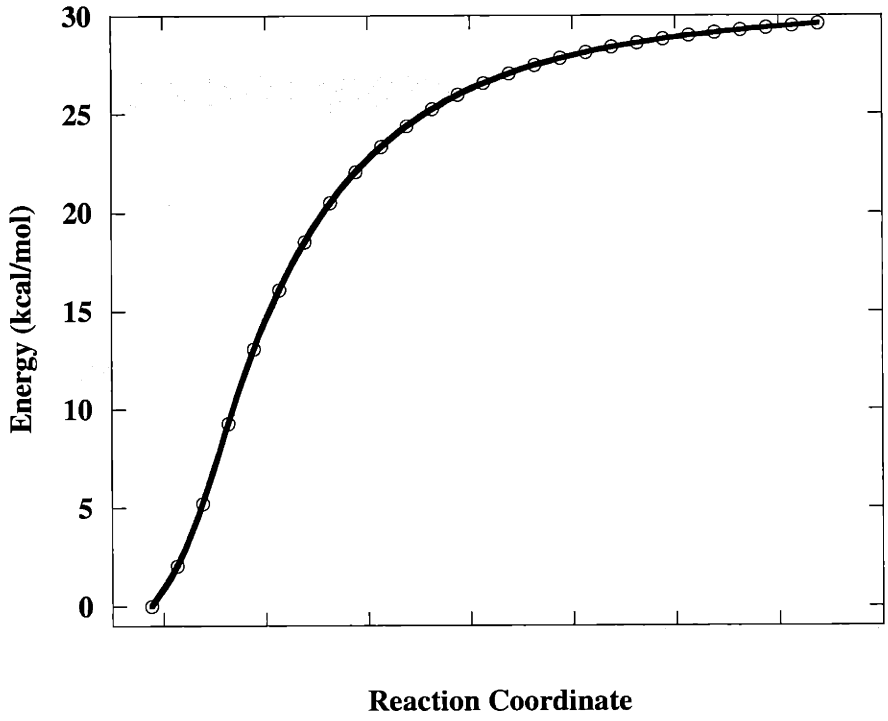

Figure 3.7 Potential energy vs. reaction coordinate for the reaction (DMAH) dimer ⇔ 2monomer, from density functional theory calculations. There is no apparent activation energy for the reverse, recombination reaction. The reaction coordinate is defined here as the aluminum-aluminum distance as the dimer is stretched into 2 monomers.

3.3.1 Collision Theory Description of Monomer Reactions

It is clear from equilibrium calculations (Figure 3.1), that monomers are essentially non-existent at low to moderate temperatures, because DMAH is bound as higher units such as dimers and trimers. However, for completeness, we include two reactions involving monomers in the gas phase model. As discussed in the introduction, monomer reactions are not expected to be important for the DMAH system. However, these reactions could have importance to other systems where monomers are initially bound as adducts and subsequently react to form dimers, trimers, etc. The reactions considered are (Figure 3.6):

$$dimer \Leftrightarrow monomer + monomer \qquad (2)$$

trimer ⇔ *monomer* + *dimer* (3)

Other reactions such as *monomer* + *trimer* ⇔ *tetramer*, *monomer* + *tetramer* ⇔ *pentamer,* and *monomer* + *pentamer* ⇔ *hexamer* are also conceivable, but are not considered operative due to the absence of monomers at low temperatures. The primary reason for including reactions (2) & (3) is to ascertain whether these reactions are involved in the *dimer* ⇔ *trimer* inter-conversion. In the above reaction scheme, dimers and trimers decompose via unimolecular reactions and free monomers then attack other molecules to form dimers, trimers and possibly higher order units. In this way, a contribution to the *dimer* ⇔ *trimer* inter-conversion could occur.

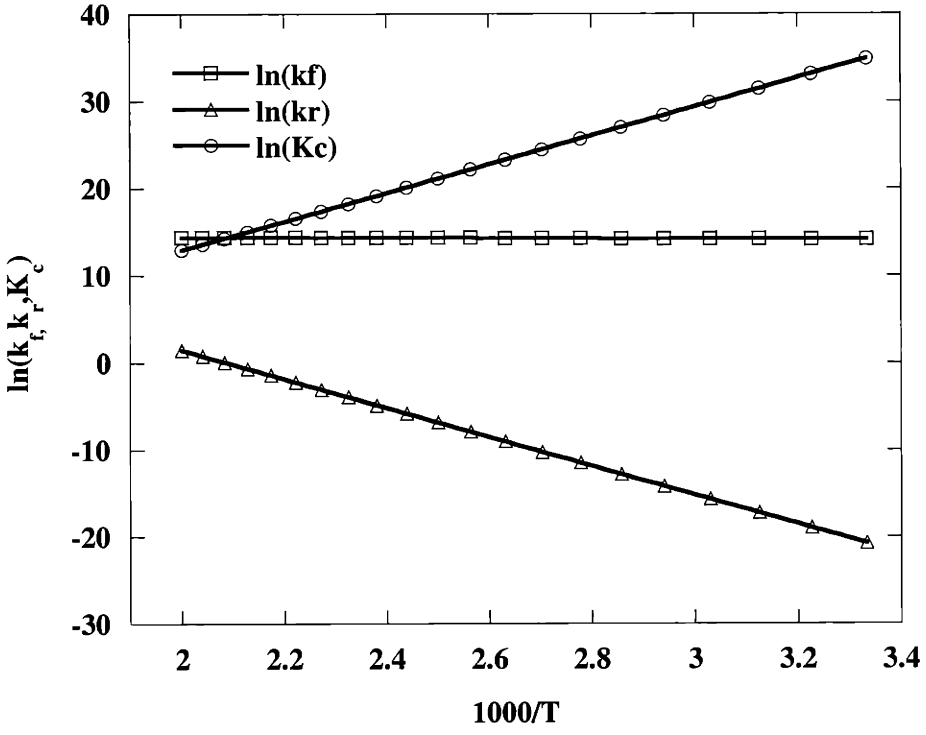

Figure 3.8 Arrhenius plot of the forward and reverse rate constants for the reaction *2monomer* ⇔ *dimer*, computed via collision theory. The equilibrium constant, K_c, is also plotted.

DFT calculations find that neither of these reactions has a classical transition state. Figure 3.7 plots the potential energy as a DMAH dimer is stretched to form two monomers. The reaction path is purely endothermic with a large barrier, corresponding to the heat of dissociation. Note the plot was generated with DFT methods that under-predict binding strengths of bridge-bonded compounds (Chapter 2). The actual barrier for dissociating the DMAH dimer is near +35 kcal/mol. Investigations determined that dissociation of trimer into monomer and dimer also shows no classical transition state, and the heat of reaction "barrier" is close to +24 kcal/mol. Since neither of these reactions has a classical transition state, rate constants were derived applying collision theory and a "steric" factor of 10^{-5} as recommended by Moore and Pearson.[29] Arrhenius Plots of forward and reverse rate constants for both reactions are shown in Figures 3.8 and 3.9 over the temperature range of interest (300-500 K). In the collision theory treatment, forward reactions are bimolecular reactions of monomers and dimers, and reverse reactions are unimolecular decompositions of dimers and trimers (the reverse of equations (2) and (3) above). Mass and atomic size parameters used in the collision theory treatment are based on the DMAH compounds rather than the model compound alane. The figures also show plots of the equilibrium constants (K_c) for these reactions. In Arrhenius form, the derived rate constants for the reverse (unimolecular) reactions are:

$$k_f = 1.38 \times 10^{15} \exp(\frac{-33{,}100}{RT})$$

$$k_f = 4.17 \times 10^{12} \exp(\frac{-22{,}000}{RT})$$

for *dimer* $\Leftrightarrow$ *2 monomers* and *trimer* $\Leftrightarrow$ *monomer + dimer* reactions, respectively. The large pre-exponential for the dimer dissociation reaction is consistent with these types of reactions.[30]

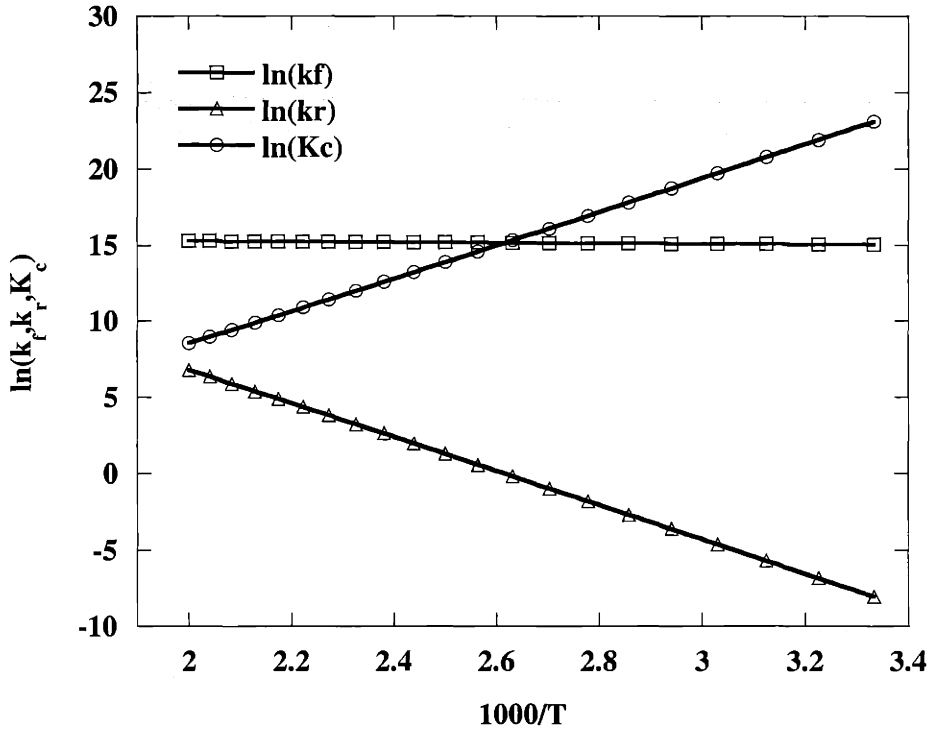

Figure 3.9 Arrhenius plot of the forward and reverse rate constants for the reaction *monomer + dimer* ⇔ *trimer*, computed via collision theory. The equilibrium constant, K_c, is also plotted.

3.3.2 Dimer, Trimer, Tetramer, and Hexamer Reactions

Reactions among dimers, trimers, tetramers, and hexamers were explored employing alane as a model system. The reactions of interest are:

$$dimer + dimer \Leftrightarrow tetramer \quad (4)$$

$$dimer + tetramer \Leftrightarrow hexamer \quad (5)$$

$$trimer + trimer \Leftrightarrow hexamer \quad (6)$$

These reactions provide pathways between dimers and trimers that involve only stable intermediates rather than the reactive and virtually non-existent monomer. In this scheme (Figures 3.4), dimers react via an exothermic reaction (see Table 3.1) to form energetically stable tetramers. Tetramers further react with dimers in another exothermic

Table 3.2 DMAH binding energies (298.15K) per bridge for each oligomer (values in kcal/mol). A 6-31G(d,p) basis set was used for both DFT and *ab initio* calculations.

	B3LYP	MP2
monomer	0.0	0.0
dimer	13.4	16.0
trimer	15.2	18.3
tetramer	15.0	18.0
hexamer	14.7	18.9

reaction to form hexamers. Hexamers subsequently decompose into either 2 trimers or back to dimers and tetramers. In the opposite direction, two trimers combine in a mildly exothermic reaction (MP2 values) to form hexamers that then may decompose to dimers and tetramers. Tetramers further decompose to dimers. Ultimately, this reaction pathway results in equilibrium between dimers and trimers. From the reaction pathway, entropic considerations favor dimers, while enthalpies of reaction favor the higher order units. Table 3.2 lists binding strengths of each species (per bridge). Calculations indicate the hexamer has the strongest bridge bonds. Equilibrium calculations (Figure 3.1) demonstrate that in the vapor at modest temperatures, trimers are apparently the best compromise, with the lowest free energy. Higher temperatures shift the balance in favor of dimers. A condensed phase could favor the larger oligomers: tetramers, pentamers, and hexamers.

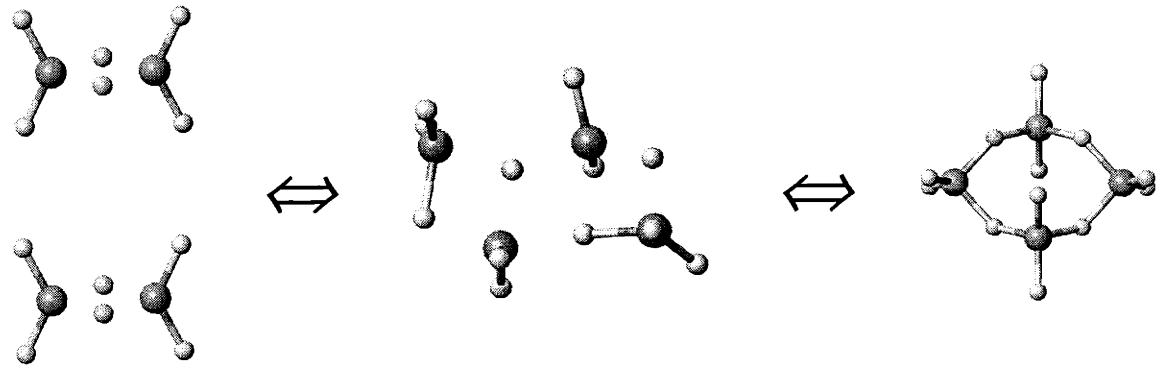

Figure 3.10 Reactants, Transition State, and Product for alane reaction: 2 dimer ⇔ tetramer.

3.3.2.1 Dimer Association to Form Tetramer

For the concerted reaction between two dimers to form a tetramer (equation (4)), a transition state was located. The reaction occurs via a "side-on" collision of two dimers, in which bridging hydrogen atoms are conserved (see later discussion) (Figure 3.10). The transition-state is skewed away from planar, and involves two five-coordinate-like aluminum atoms (Figure 3.11). Given the relatively small size of the molecules in this reaction (16 atoms), a comparison between *ab initio* (MP2) and DFT predicted activation barriers was performed, at a reasonable basis set level. A schematic of the potential energy versus reaction coordinate is shown in Figure 3.12. As expected, the reverse reaction barriers are significantly different (> 3 kcal/mol) for *ab initio* and DFT

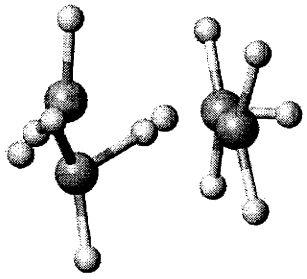

(a)

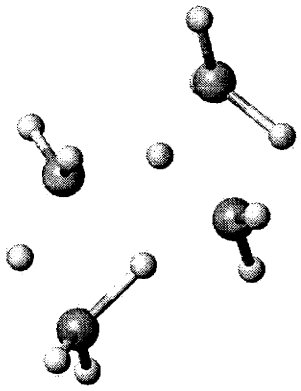

(b)

Figure 3.11 Transition state for alane reaction *2 dimer ⇔ tetramer*. (a) side view. (b) top view.

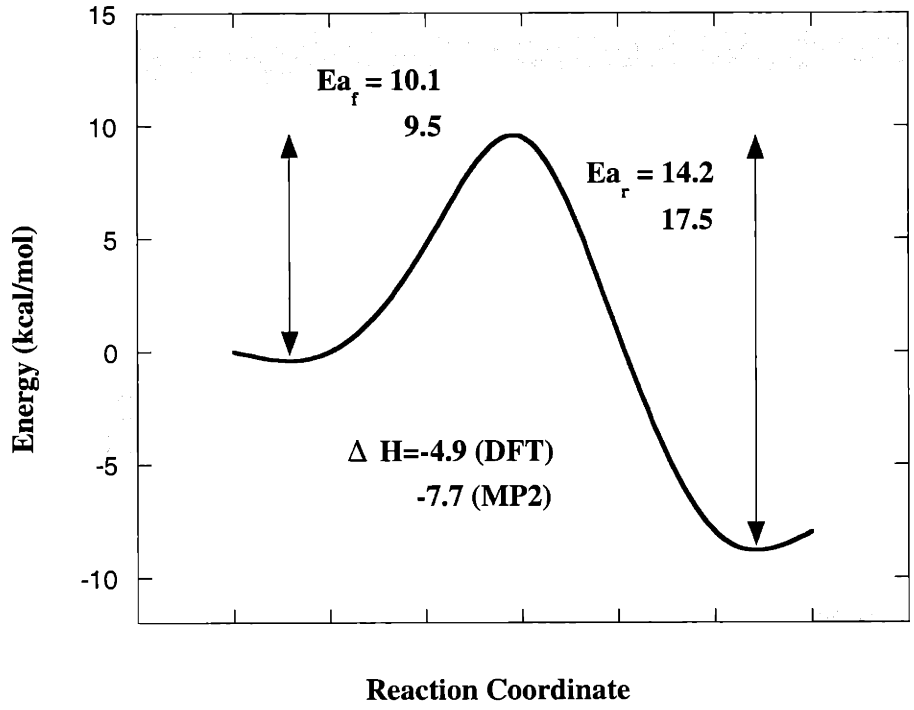

Figure 3.12 Potential Energy Surface along the reaction coordinate for the alane reaction *2 dimer ⇔ tetramer*. Both DFT and MP2 calculations are presented.

predictions. Fortunately, forward activation barriers are in good agreement at 10.1 and 9.5 kcal/mol for the DFT and MP2 methods, respectively. The poor agreement for the reverse reaction barrier is consistent with DFT errors in calculations of heats of reaction (Chapter 2). It is apparent that a description of bridge bonding is more crucial for the reverse reaction. The results suggest the transition-state is not too different from normal bonding arrangements so that DFT methods are successful at predicting the forward barrier. Forward and reverse reaction rate constants calculated with transition state theory are plotted in Figure 3.13. A plot of the equilibrium constants K_c for the reaction is included in the figure. MP2 calculated rate constants, in Arrhenius form, are:

$$k_f = 5.69 \times 10^8 \exp\left(\frac{-10{,}500}{RT}\right)$$

$$k_r = 6.2\times10^{12}\exp\left(\frac{-19{,}100}{RT}\right)$$

for forward and reverse reactions, respectively.

3.3.2.2 Reaction Pathways of the Hexamer

Reactions involving formation of the alane hexamer are found to exhibit an associative complex between the reactants (*dimer + tetramer,* and *trimer + trimer*). Transition states for the reactions occur between the associated complexes and the product, hexamer. For the *dimer + tetramer* reaction, the associated complex is -1 to -2 kcal/mol more stable than the separated reactants, by DFT methods (Figure 3.14). Interestingly, MP2 calculations predict no associated complex. Figure 3.15 illustrates the associated complex formed from dimer and tetramer. From the reactant complex, the molecules surmount a ~ 7-8 kcal barrier to form hexamer.

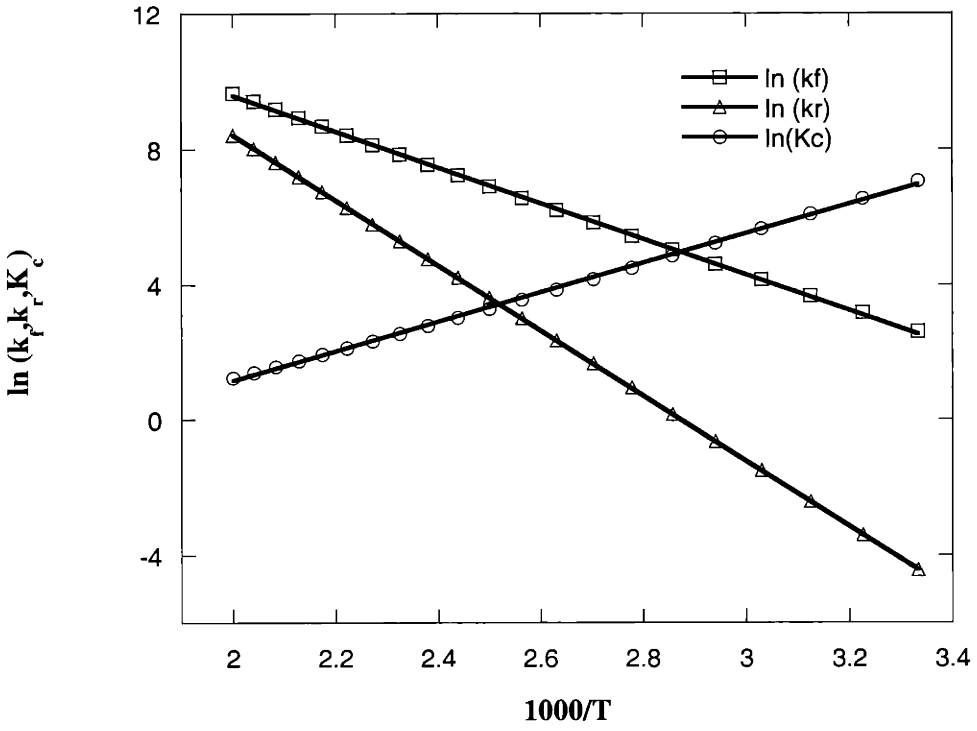

Figure 3.13 Arrhenius plot of the forward and reverse rate constants for the reaction *2dimer* ⇔ *tetramer*. The equilibrium constant, K_c, is also plotted.

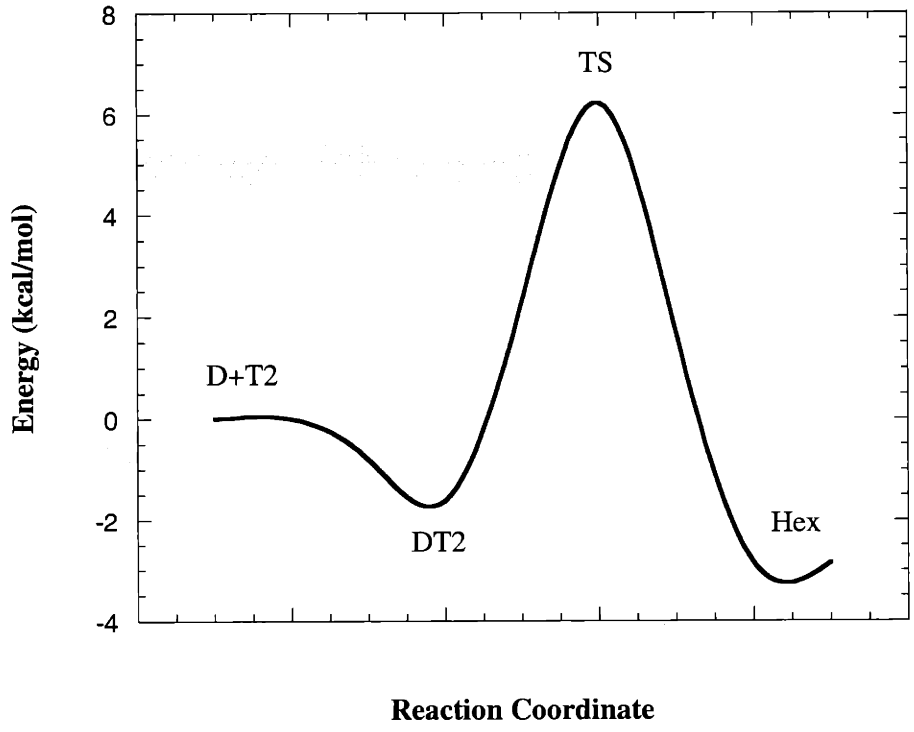

Figure 3.14 Potential energy surface of *dimer + tetramer* ⇔ *hexamer* with DFT methods. In the figure, D = dimer, T2 = tetramer, DT2 = dimer + tetramer complex, TS = Transition State, and Hex = hexamer.

The transition-state for the pathway between the associated dimer-tetramer complex and the hexamer is illustrated in Figure 3.16. In the associated complex, terminal hydrogen atoms of the dimer are attracted to aluminum atoms in the tetramer, forming a five-coordinate-like structure. Terminal hydrogen atoms of the tetramer are likewise attracted to the aluminum atoms of the dimer. The reaction proceeds through a partial interchange of bridge and terminal hydrogen atoms. Due to the complex nature of the bonding in the alane hexamer, it is not convenient to strictly label bridge and terminal bonds, but in the transition state it is clear that bridge and terminal characteristics are interchanged. Forward and reverse reaction rate constants calculated with transition state theory (based on MP2 single point energy calculations) are plotted in Figure 3.17. A plot of the equilibrium constants K_c for the reaction is included in the figure.

Verification that the transition-state corresponds to the reaction of interest was accomplished by displacing the complex on either side of the barrier and allowing the

structure to minimize. Displacing the transition state towards the reactant (associated dimer and tetramer) clearly converged to the associated complex. Following the other side of the transition state downhill towards products realized a linear form of the alane hexamer (Figure 3.18). The linear isomer is more stable than the cyclic form by ~2.9 kcal/mol. To test whether results are an artefact of the small basis set (3-21G*) used in the minimization, the B3PW91/3-21G* optimized linear and cyclic forms were compared to a single B3PW91/6-31G(d,p) calculation. The larger basis set did not change the order of stability. The transition state is identified with the *dimer + tetramer* ⇔ *hexamer* reaction; however, the product side of the transition state exhibits a flat PES where both

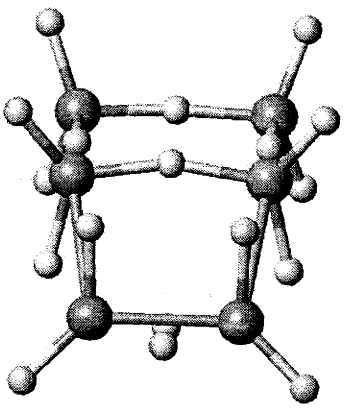

(a)

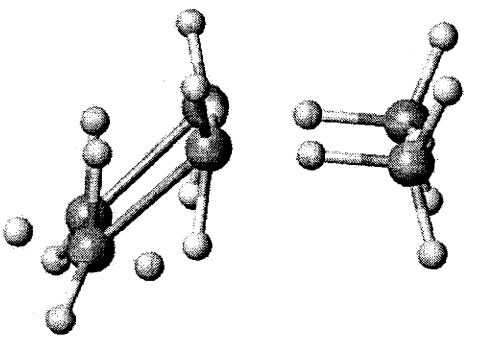

(b)

Figure 3.15 Alane dimer-tetramer associated complex. (a) top view (b) side view.

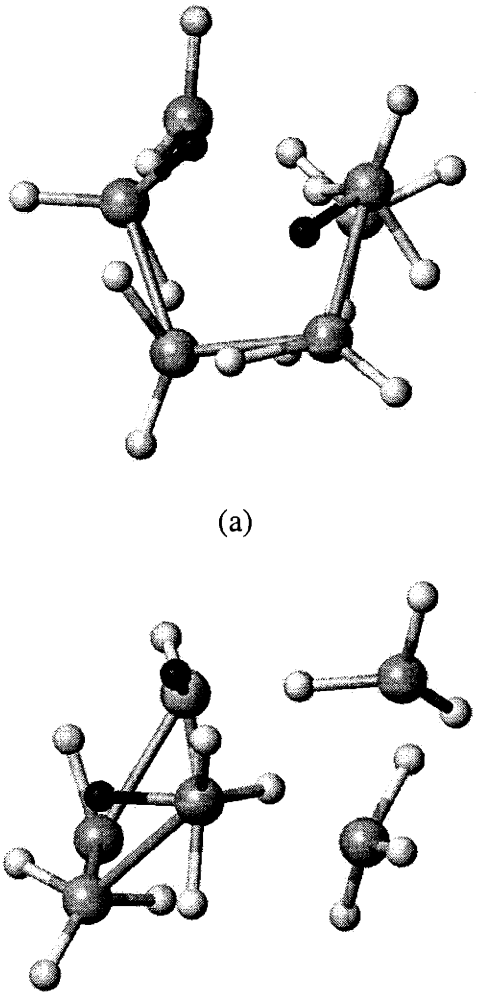

Figure 3.16 Transition state structure for the alane reaction *dimer* + *tetramer* ⇔ *hexamer*. Two representative hydrogen atoms that interchange bridge-terminal roles are highlighted.

linear and cyclic isomers are possible products. Simply following the transition state downhill via an optimization results in the lowest energy conformer, the linear hexamer. The unbound state of the cyclic hexamer with respect to the linear form is apparently an indication that the choice of alane as a model for DMAH breaks down. The equivalence of terminal and bridge bonds in the alane structure allows it to form chains and retain most of the stability of the hydrogen bridges while relieving ring strain. DMAH, on the other hand, is expected to prefer the cyclic structure, as this arrangement maximizes the number of hydrogen bridge bonds. Substituting hydrogen bridge bonds with methyl

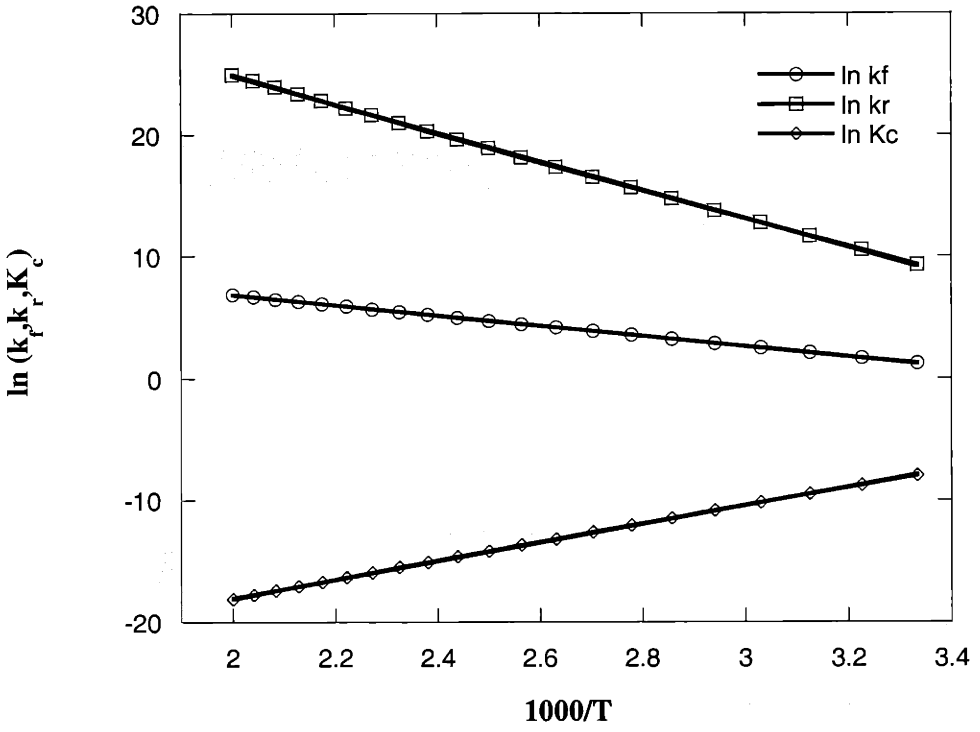

Figure 3.17 Arrhenius plot of the forward and reverse rate constants for the reaction *dimer + tetramer* ⇔ *hexamer*. The equilibrium constant, K_c, is also plotted.

bridges to form a DMAH linear hexamer is expected to be less favorable. Note, there must be at least a small barrier to dissociation of the cyclic alane hexamer into the linear isomer, since geometric optimizations of the hexamer were successful. Unfortunately, searches along the intrinsic reaction coordinate, to locate the reaction product more exactly, are not currently practical.

The *2 trimers* ⇔ *hexamer* reaction is similar to the above *dimer + tetramer* reaction. In the case of trimers, the associated complex is 5.7 kcal (ΔE^{0K}) below the reactants, and the forward barrier to hexamer from the complex is +8.4 kcal (ΔE^{0K}) (Figure 3.19). A drawing of the associated complex is shown in Figure 3.20. Hexamer formation from the trimer complex again involves bridge-terminal exchange. A single transition state between the associated trimer complex and the hexamer was not located. The endothermic nature of the reaction, with DFT methods, suggests the transition-state may lie near the hexamer. Due to the many ring modes of the contorted alane hexamer, it

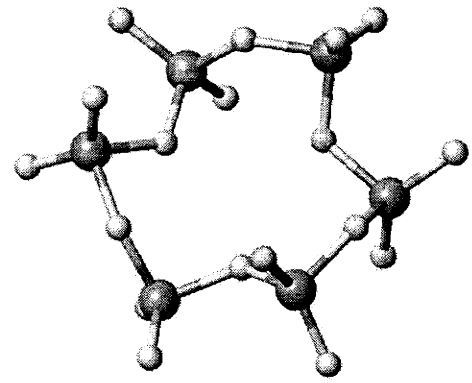

(a)

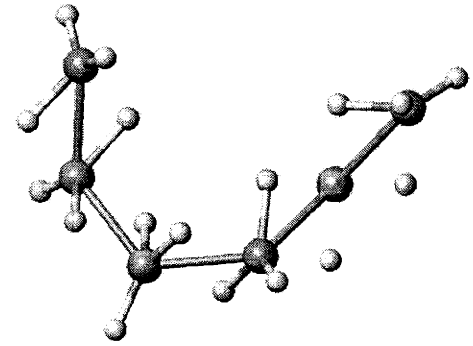

(b)

Figure 3.18 a) Cyclic alane hexamer structure. b) Linear alane hexamer structure.

is difficult to characterize that portion of the PES. Alternatively, there may not be a single transition state that separates the reactants and products. Transition state searches found two similar configurations involving the opening of each trimer ring. These observations indicate the reaction could occur through sequential opening of trimer rings. The ring openings occur through a bridge-terminal exchange similar to the *dimer* + *tetramer* reaction. In any case, these reactions appear characteristic of a *trimer-complex* $\Leftrightarrow$ *hexamer* reaction path, and were used to derive an estimate for TST rate constants.

The presence of the "2 trimer" associated complex, even for MP2 calculations, requires some assumption about the effective barrier to reaction, since the energy of the

associated complex is below the separated reactants (2 trimers). One way to approach this problem would be to separate the problem into two reactions: formation of the associated complex, and further reaction to form hexamer. Collision theory could then be used to estimate a rate of formation for the complex. A simpler approach, and that used here, is to adjust the potential energy surface so that reactants are shifted down to the level of the associated complex. The resulting rate expressions appear consistent with the other reactions studied above. Forward and reverse rate constants (based on MP2 single point energy calculations) are plotted in Figure 3.21.

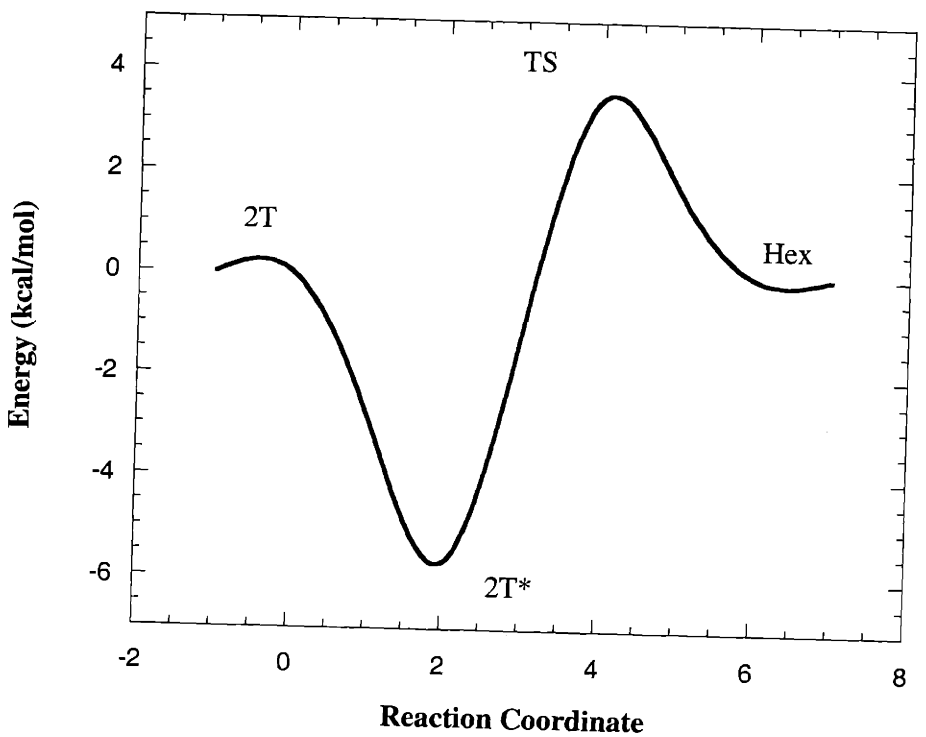

Figure 3.19 Potential energy surface for *2 trimer ⇔ hexamer* with DFT methods. In the figure, 2T = 2 trimers, 2T* = 2 trimer complex, TS = transition state, Hex = hexamer.

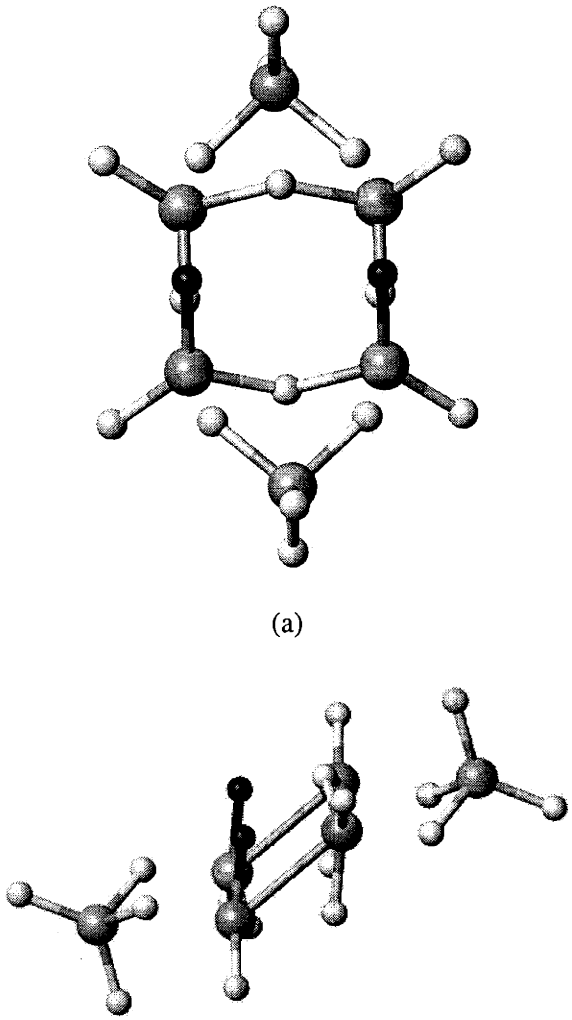

Figure 3.20 Alane trimer-trimer associated complex. (a) top view. (b) side view. Two representative hydrogen atoms that interchange bridge-terminal roles are highlighted.

3.3.3 Kinetic Simulations

Employing a combination of the accurate thermodynamic data used to construct Figure 3.1 and the rate constants derived above, gas phase simulations of the approach to equilibrium were performed. Rate constants used for the simulations were derived as follows. A combination of accurate DMAH equilibrium constants and collision theory was used to derive rate expressions for reactions (1) & (2), involving the monomer. The accurate equilibrium constants ensure the simulations approach the correct equilibrium (at

Table 3.3 Rate expressions used for DMAH kinetic simulations (units are moles, liters, and seconds).

2 monomer ⇔ dimer	$k_f = 2.7x10^6 * \exp\left(\frac{-383}{RT}\right)$
	$k_r = 1.38x10^{15} * \exp\left(\frac{-33{,}100}{RT}\right)$
monomer + dimer ⇔ trimer	$k_f = 6.45x10^6 * \exp\left(\frac{-383}{RT}\right)$
	$k_r = 4.17x10^{12} * \exp\left(\frac{-22{,}000}{RT}\right)$
2 dimer ⇔ tetramer	$k_f = 5.7x10^8 * \exp\left(\frac{-10{,}500}{RT}\right)$
	$k_r = 1.07x10^{12} * \exp\left(\frac{-19{,}100}{RT}\right)$
dimer + tetramer ⇔ hexamer	$k_f = 4.2x10^6 * \exp\left(\frac{-8{,}350}{RT}\right)$
	$k_r = 1.1x10^{21} * \exp\left(\frac{-23{,}500}{RT}\right)$
2 trimer ⇔ hexamer	$k_f = 5.2x10^5 * \exp\left(\frac{-8{,}150}{RT}\right)$
	$k_r = 3.2x10^{20} * \exp\left(\frac{-16{,}900}{RT}\right)$

long times). For reactions involving dimers, trimers, tetramers, and hexamers, forward rate constants were derived from DFT optimized transition states on the alane system detailed above, with MP2(Full)/6-31G(d,p) single point energy calculations. Equilibrium constants were derived from *ab initio* MP2(Full)/6-31G(d,p) calculations on DMAH structures using B3LYP calculated vibrational frequencies (for zero point energies and thermal corrections). A 6-31G(d,p) basis set was used for the dimer, trimer, and tetramer frequency calculations, while a 3-21G** basis was used for the hexamer. Additionally, the hexamer frequency data was obtained from the D_{6h} structure, which has 7 imaginary modes. Differences in vibrational modes (between the C_2 and D_{6h} structures) and the absence of some modes (imaginary frequencies) introduce a relatively small error (see Appendix).

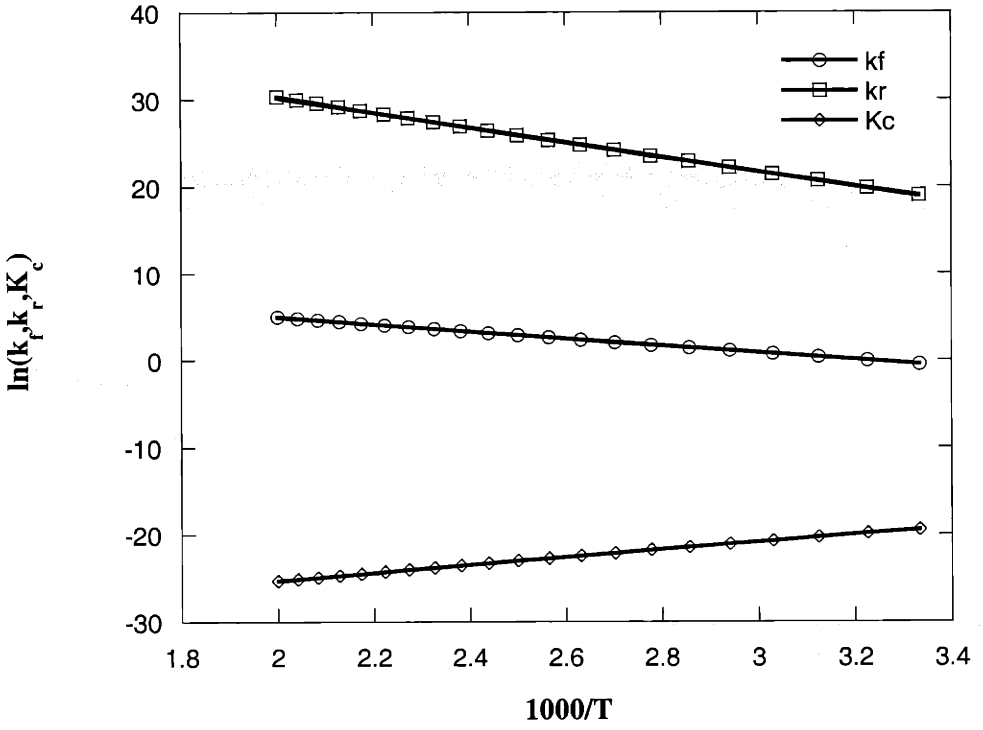

Figure 3.21 Arrhenius plot of forward and reverse rate constants for the reaction *2 trimers* $\Leftrightarrow$ *hexamer*. The equilibrium constant, K_c, is also plotted in the figure.

Table 3.3 summarizes the rate constants employed in the simulations. Note the unusually high pre-exponential factors for the hexamer decomposition reactions. These high pre-factors are caused by opposing entropy and enthalpy considerations. The enthalpy of reaction favors the hexamer, and requires a high barrier to the unimolecular decomposition reaction. Entropy, meanwhile, favors the dimers, trimers, and tetramers, and requires a fast reverse rate constant. High pre-factors are needed to simultaneously give a fast reverse (dissociation) rate constant and a large reverse activation barrier. These unphysical pre-factors suggest classical transition state theory may not be adequate for these large molecules, and energy partitioning methods may be preferred.[31] However, these awkward rate expressions are accepted here, for semi-quantitative understanding.

Figures 3.22 & 3.23 show simulation results for the monomer pathways involving reactions (2) & (3) only. The two figures illustrate the approach to equilibrium for two

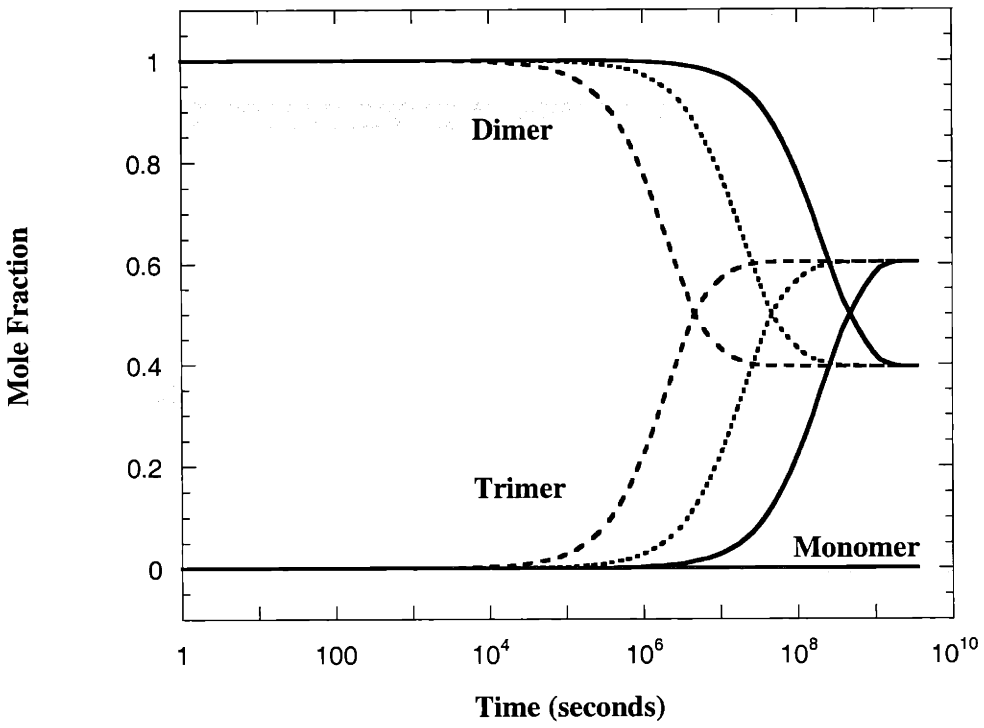

Figure 3.22 DMAH kinetic simulations of the monomer pathway. Only reactions (2) & (3) are included (see text). Initial conditions are 100% dimer.

initial conditions, 100% dimer and 100% trimer. In accordance with the use of the accurate thermodynamic data (equilibrium constants), the simulations produce the correct long time composition. Note, however, the final states are slightly different in the figures since the simulations were performed at constant volume. In the figures, results for three different choices of steric factor are illustrated. Using the 10^{-5} steric factor as recommended gives a very slow approach to equilibrium, requiring ~ 10^9 seconds for completion. Recall from the introduction that experimental observations include half lives on the order of weeks to months or longer. The time scale is changed to ~10^7 sec if the steric factor is increased to 10^{-3}, and the reaction is half-completed on the order of 10^6 seconds (~10 days). Unfortunately, not enough is known about the kinetics of these types of systems, and further refinement of the collision theory rate constants may require dynamic simulations. The Lewis acid nature of aluminum organometallic monomers may

give rise to relatively long-range forces that contribute to the collision rate ("steering") and justify larger steric factors.

Simulations without the monomer pathway are shown in Figures 3.24 & 3.25. Because of the lack of high quality thermodynamic data for the DMAH tetramer and hexamer, these simulations do not approach the same equilibrium in Figure 3.1. Further understanding of the DMAH system would benefit from accurate (G2) equilibrium calculations on the large tetramer and hexamer. Based on experimental observations, it is expected that good equilibrium constants for the tetramer and hexamer reactions should produce an equilibrium composition closer to that of Figure 3.1. Unfortunately, high quality calculations on these DMAH oligomers are currently beyond workstation capabilities. Therefore, MP2 calculations were employed. Due to bridge bonding

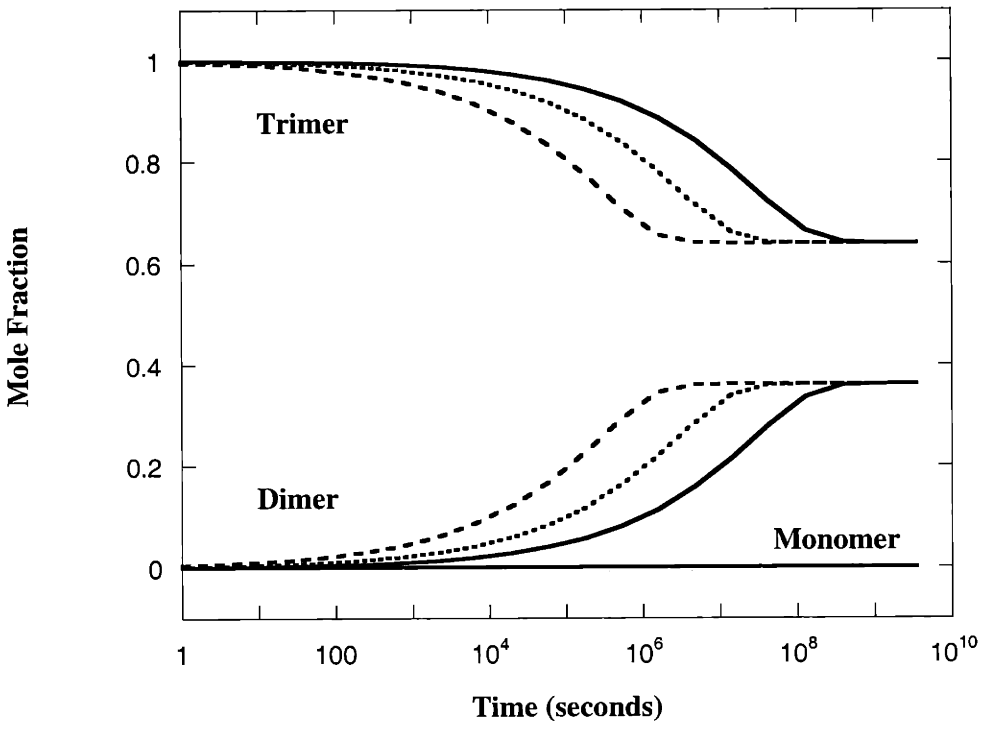

Figure 3.23 DMAH kinetic simulations of the monomer pathway. Only reactions (2) & (3) are included (see text). Initial conditions are 100% trimer.

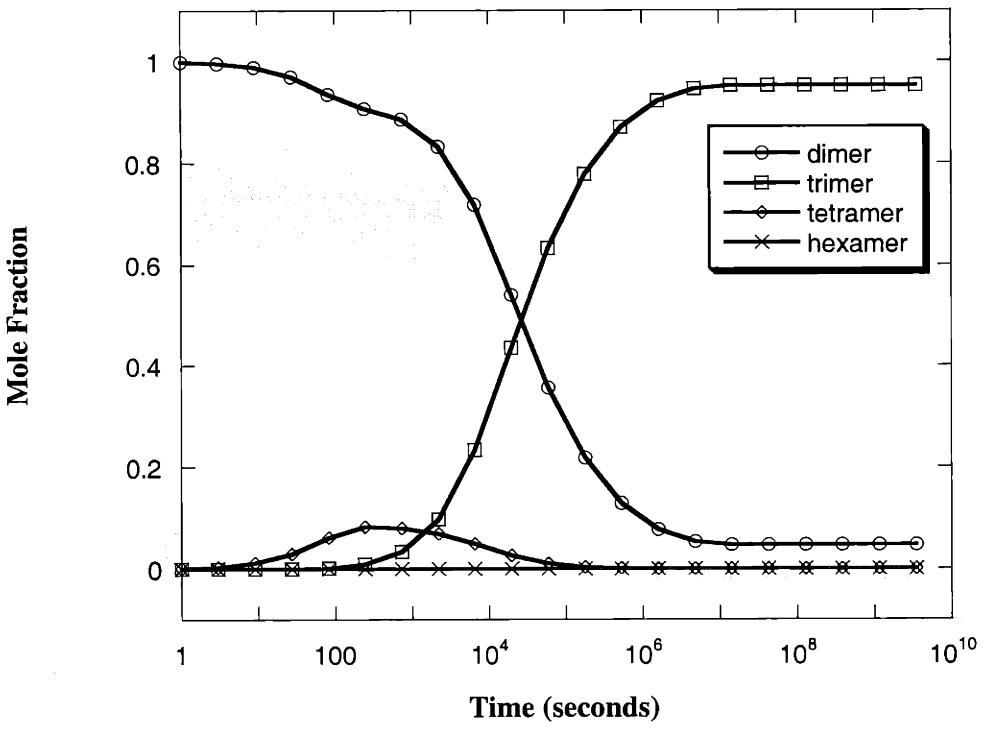

Figure 3.24 DMAH kinetic simulations without monomer pathway. Reactions (4), (5), & (6) are included. Initial conditions are 100% dimer.

considerations, the MP2(Full)/6-31G(d,p) derived equilibrium constants are thought to be superior to the DFT values, but even a small error has a profound impact on the equilibrium: for example, a 5 kcal/mol error in ΔG at 300 K gives a ~$4x10^3$ error in the equilibrium constant. The simulated equilibrium now favors trimers to a greater extent. The preference for trimers can be understood dynamically by considering that dimers are consumed in reactions to form tetramers and hexamers, while hexamers prefer to decompose to trimers. Shifting the trimer-hexamer equilibrium slightly towards hexamer by decreasing the decomposition rate (raising the reverse barrier) results in more dimer. Nonetheless, the approach to equilibrium is at least as fast as that for the monomer pathway. Full equilibrium is obtained on the order of 10^6-10^7 seconds, which is close to the results for the monomer pathway with the smaller, most favorable (10^{-3}) steric factor.

Simulations of the full equilibrium mechanism (with a 10^{-5} steric factor) are shown in Figures 3.26 & 3.27. As is evident in Figure 3.28, the full mechanism is faster than either partial equilibrium, and both pathways appear to contribute towards the rate.

Note, the inclusion of the monomer pathway has also modified the equilibrium (long time behavior) to increase the dimer fraction. The full mechanism reaches equilibrium on the order of 10^6 seconds, which is compatible with experimental observations of these types of compounds. The concentration of monomers and hexamers is predicted to be quite low, but these species act as important intermediates in the reaction mechanism. As shown in Figure 3.26, for initial conditions of 100% dimer, tetramers have a significant concentration during the approach to equilibrium.

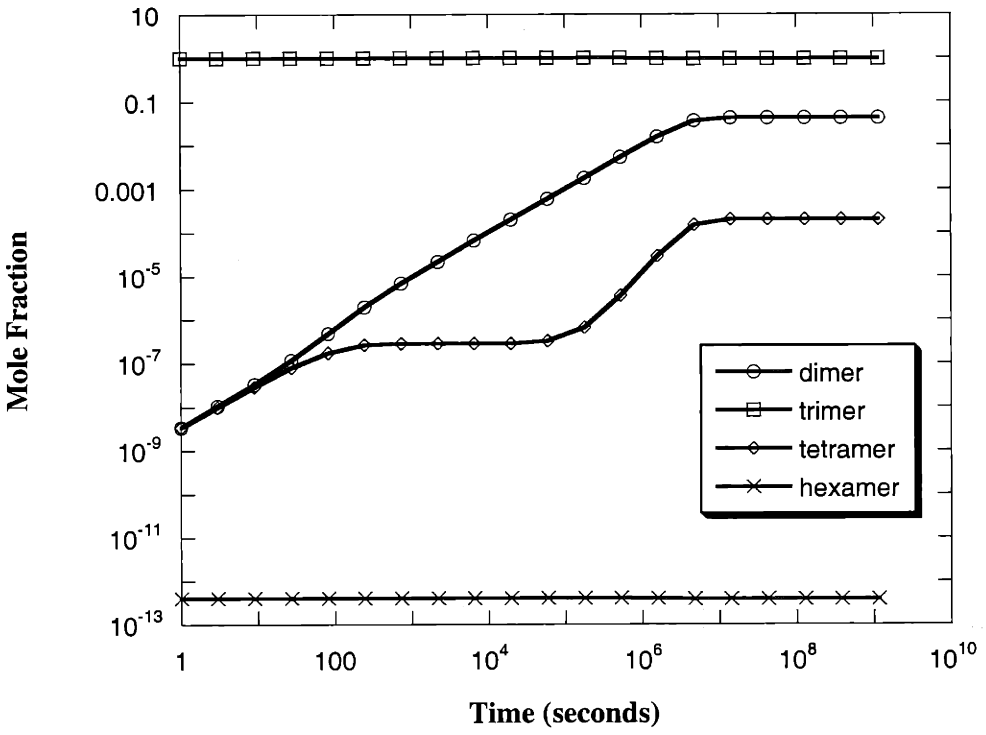

Figure 3.25 DMAH kinetic simulations without monomer pathway. Only reactions (4), (5), & (6) are included (see text). Initial conditions are 100% trimer.

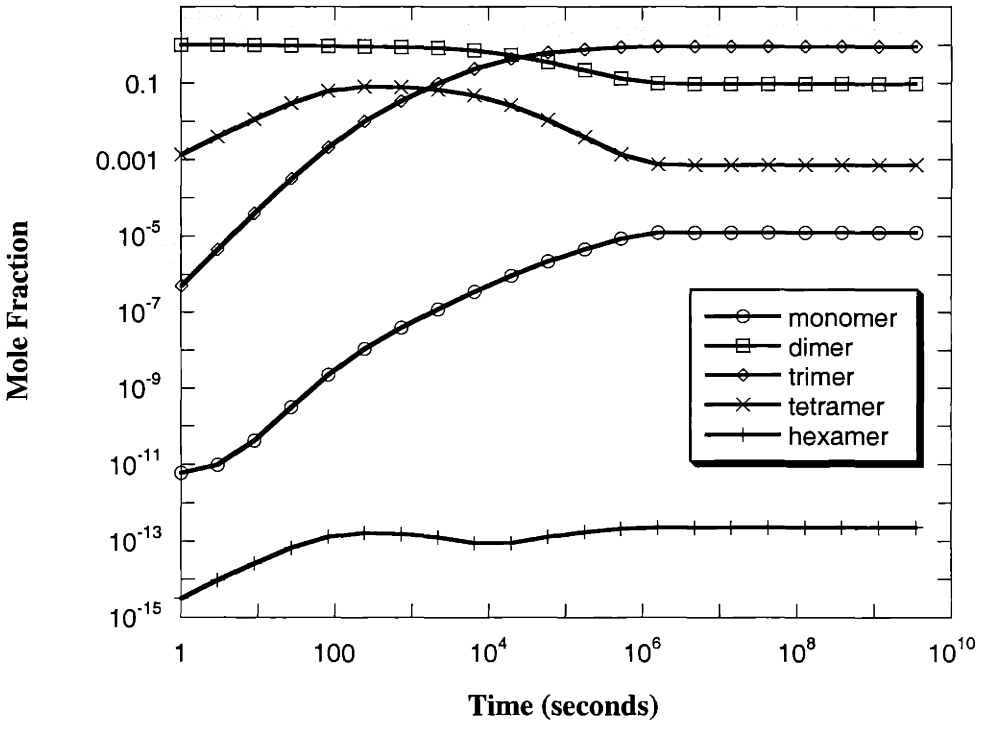

Figure 3.26 Kinetic simulations of the full DMAH gas phase reaction mechanism. Reactions (2), (3), (4), (5), & (6) are included (see text). Initial conditions are 100% dimer.

3.4 Discussion

3.4.1 Reaction Mechanism & Kinetics

The concerted reaction pathways presented in the previous sections present plausible alternatives to reaction mechanisms requiring ring opening and bridge bond breaking. Bimolecular reaction barriers are substantially less than bond dissociation energies, and barriers for the unimolecular reactions are also less than ring opening reactions. The reactions are discussed in turn below.

2 dimer ⇔ tetramer

In the reaction of two dimers to form a tetramer, the +10 kcal/mol barrier is nearly half the cost of breaking open a 17.5 kcal/mol dimer bridge bond. Therefore, "side-on" attack is a probable reaction pathway for formation of tetramers, and the alane model for

the reaction seems reasonable. In the reaction between dimers to form tetramers, "side-on" collision retains the identity of the bridge bonds, and terminal groups are relatively inert to the reaction. In this case, the analogy with DMAH is relatively straightforward, and both the mechanism and activation barrier may be well described with the alane model. If it is assumed the transition state is electron deficient, the reduced electron withdrawing character of terminal methyl groups may lower the activation barrier for DMAH. However, steric interactions of the larger terminal groups may act in the opposite direction.

The reverse, unimolecular, reaction has a barrier near 17.5 kcal/mol (MP2 value) which is comparable to a ring opening step. Depending on the details of the self-attack reaction pathway, a ring opening mechanism and re-closing to form trimer or dimer could compete with the concerted reaction. However, unlike the concerted reaction, ring-opening reactions would be expected to have an extremely fast reverse reaction as well, since the equilibrium would favor the ring structure. Of course, further investigations of the accuracy of the MP2 calculated unimolecular barrier would be in order before pursuing a ring opening mechanism. If methyl ligands lower the forward barrier as suggested above, the barrier of the reverse reaction may also be lowered. Consider, however, the overall heat of reaction for unimolecular dissociation is more endothermic for DMAH than alane. This difference would partially offset effects from any lowering of the forward barrier. In addition, steric interactions could also play a role in raising reaction barriers for DMAH.

Calculating half-lives of both the forward and backward reactions for *2 dimers* $\Leftrightarrow$ *tetramer* sheds some light on the experimentally observed behavior of DMAH. Using standard formulas for first and second order reactions (equations (7) & (8) below, respectively), and a concentration of 1.076×10^{-4} moles/liter (~2 Torr, the vapor pressure of DMAH) gives values of $t_{1/2} \approx$ 2.5 minutes, and 0.8 seconds for the forward and backward reactions, respectively, at 298 K. These calculations are only semi-quantitative and represent only a portion of the equilibrium pathway, but they suggest the vapor phase equilibrium proceeds through a series of slow bimolecular reactions and relatively faster unimolecular reactions.

$$t_{1/2} = \frac{\ln 2}{k} \tag{7}$$

$$t_{1/2} = \frac{1}{k[A_o]} \tag{8}$$

Reactions Involving Hexamer

The choice of alane as a model system for DMAH appears appropriate for the formation of tetramer, but for reactions involving hexamer, the analogy is less clear. Reactions involving hexamer are more complicated since they introduce an associated complex, a mixed terminal-bridge bonding arrangement of the alane hexamer, and a linear hexamer. Efforts were made to uncover a side-on collision for formation of hexamer that proceeded through dimer insertion into a tetramer, or trimer insertion into

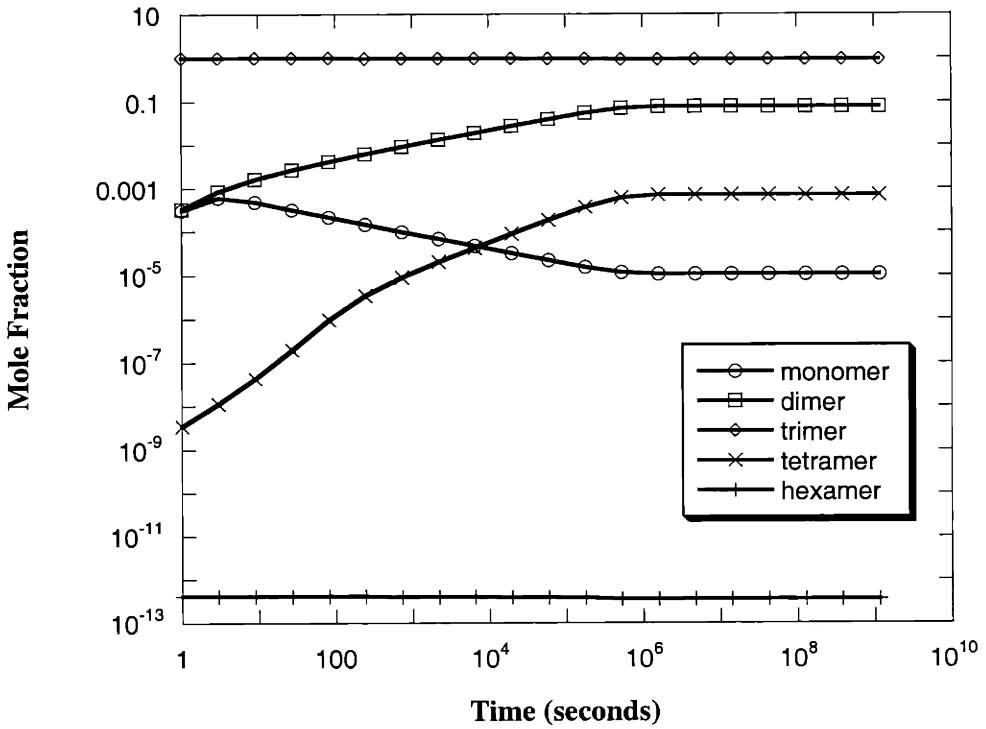

Figure 3.27 Kinetic simulations of the full DMAH gas phase reaction mechanism. Reactions (2), (3), (4), (5), & (6) are included. Initial conditions are 100% trimer.

another trimer. These pathways are analogous to reaction (4) where dimers insert into one another, conserving the labeling of bridge atoms. Transition state searches for such configurations resulted in numerous imaginary modes, which upon relaxation drastically changed the look of the transition-state, and the presumed reaction coordinates developed into hexamer ring vibrations. The cause for these distortions is evident in the appearance of the complex shape of the alane hexamer (Figure 3.4). The simple D_{2h} and C_{2h} structures of the dimer and tetramer, respectively, require significant distortion to form the contorted hexamer. While the transitions state searches could not cover every possibility, it may be there is no single saddle-point that separates the reactants and products in a fashion that occurs through a "side-on" collision of alane dimer and tetramer. Given the DMAH hexamer is similarly contorted, while the dimer, trimer, and tetramer reactants are of high symmetry (D_{2h}, D_{3h}, D_{4h}), it seems likely transition state

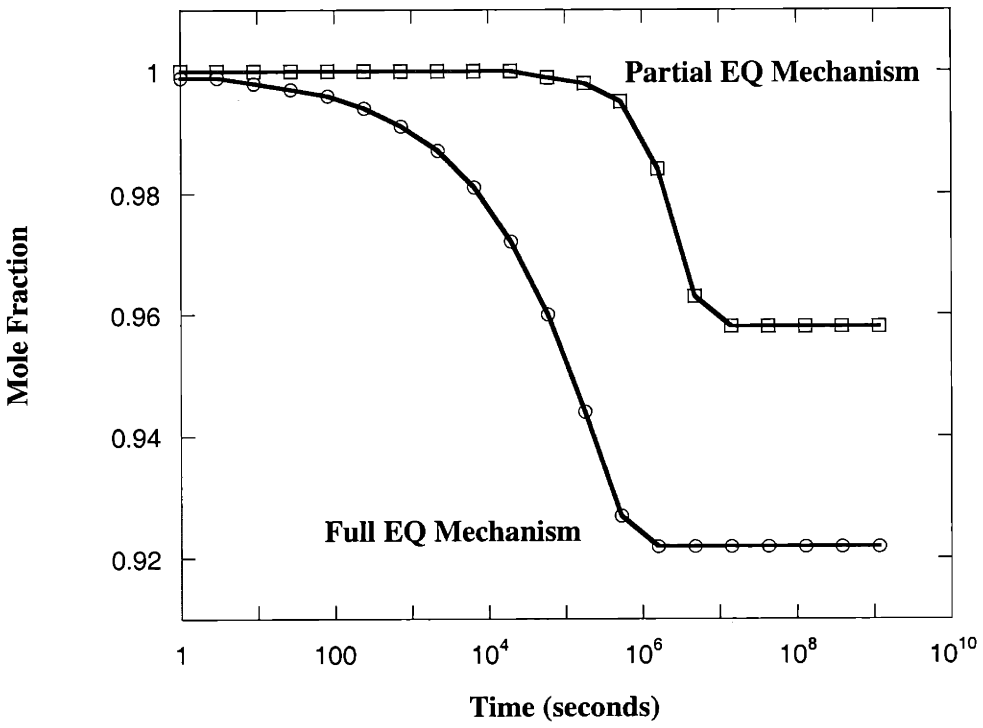

Figure 3.28 DMAH kinetic simulations comparing trimer concentrations in the full and partial (without monomer) mechanisms. Reactions (4), (5), & (6) are included (see text). Initial conditions are 100% trimer.

optimizations involving DMAH hexamers may encounter similar difficulties. It is simple enough to imagine an insertion of dimer into tetramer, but considering the lower symmetry structure of the final product it is a challenge to find a single saddle point separating reactants and product. It may also be that DFT methods are not particularly suited for searches on the PES of these bridge-bonded compounds.

The formation of an associated complex between dimers and tetramers or two trimers provides the necessary precursor to the formation of hexamers. Bridge-terminal exchange of hydrogen atoms allows a concerted reaction between the relatively symmetric D_{2h}, C_s, and C_{2h} structures of the dimer, trimer, and tetramer, respectively, and the distorted zig-zag form of the hexamer. From the reverse reaction point of view, forming a dimer or trimer from the hexamer can also proceed through a concerted reaction step where the ring narrows, terminal bonds fold into bridge bonds, and vice versa. These reverse reactions occur with low barriers due to the relatively flat PES of the hexamer, and the downhill formation of the associated complex.

Peculiarities of the alane reaction pathways impose some uncertainty as to the applicability of alane as a model system for DMAH, but also suggest unconventional reaction pathways for these types of compounds. DMAH most likely also forms associated complexes between dimers, trimers, tetramers, and hexamers, but with much weaker forces. Such associated complexes may then go through similar concerted reaction steps in which terminal methyl groups exchange with bridging hydrogen atoms, temporarily. Methyl bridges are significantly weaker than hydrogen bridges (~10 and ~17 kcal/bridge for TMA and DMAH dimers, respectively), but once hexamer is formed, a rapid intra-molecular bridge-terminal exchange produces the thermodynamically more stable hydrogen-bridged structure. Bridge-terminal exchange reactions are known to occur rapidly in these types of compounds.[11] For TMA, it is necessary to go to low temperatures (-75 °C) to resolve bridge and terminal signals in NMR experiments. The methyl-bridge mediated kinetic pathway may be an alternative pathway to an insertion or ring opening mechanism. The concerted mechanism could also operate for other *dimer* $\Leftrightarrow$ *trimer* systems such as the aluminum nitride compounds. In this case, the stronger

bridge bonds of the nitride compounds make it even more likely a concerted mechanism is operative.

The preference of alane for the linear hexamer represents a failure of alane as a model for DMAH, but is not expected to invalidate the semi-quantitative picture formed from the alane system. Starting from the associated reactant complex, the forward activation barrier should not be affected by the presence of the linear hexamer on the other side of the barrier. The alane linear hexamer credits its stability to the equivalence of terminal and bridge hydrogen atoms. DMAH would not be expected to exhibit a linear hexamer due to the energetic inequivalence of hydrogen and methyl bridges. A downhill search from a DMAH transition state to the product would be expected to arrive at the optimized cyclic hexamer. The formation of the associated reactant complexes presents more of an issue for using alane as a model system than the presence of a linear hexamer.

3.4.2 Kinetic Simulations

Although the above discussion raises some caution to using alane as a model system, kinetic simulations provide a first order model to understanding the behavior of these types of aluminum organometallic compounds. The simulations clearly illustrate the importance of a kinetic description of DMAH gas phase chemistry. The results are also consistent with experimental observations on oxygen bridged compounds where reactions were observed to be excruciatingly slow. The results provide a basis for an explanation of the complex behavior of DMAH. Different synthesis routes of DMAH or processing the liquid (heating, for example) shift the composition away from equilibrium towards dimers or trimers, and response of the system is slow. The slow response leads to a time dependent composition, and no doubt varying liquid properties. The time dependence of the composition provides one possible explanation for the conflicting experimental results mentioned in the introduction. Heating DMAH may be expected to shift the equilibrium towards dimers. While the elevated temperatures may speed the kinetics to form dimers on a reasonable time scale, the return of the system to equilibrium at room temperature may be very slow.[2] Subsequent experiments may then observed elevated amounts of dimer at room temperature. A similar explanation can be applied to

the qualitative differences between experiments and theory for the mixed system, DMAH-TMA. While experiments observe the mixed compound dominating the mixture, calculations predict closer to 50% pentamethydialane.[32] Theoretical studies of the equilibrium (Figure 3.2) predict the balance is made up of DMAH trimers and TMA dimers. Processing the mixture so that DMAH trimers are shifted to dimers would then shift the equilibrium towards the mixed compound (pentamethyldialane) and result in a composition consistent with experiments.

In the introduction, it was hypothesized that monomer pathways are unimportant to the equilibrium mechanism. Results of the simulations, however, indicate this may not be true. Simulations of the "all monomer" pathway indicate the rate is dependent on the choice of steric factor. Using a 10^{-5} factor, as recommended for non-linear molecules, imparts a very slow rate, apparently disproportionate to experimental observations. A complete monomer pathway would require a small steric factor $< 10^{-3}$ in the collision theory treatment, and it is not known whether such values are feasible. However, the monomer pathway is not necessary since the time dependence of the hexamer pathway is consistent with experimental observations. The hexamer pathway allows *dimer* $\Leftrightarrow$ *trimer* equilibration even in systems with very strongly bound dimers and trimers, where the monomer pathway would be even slower than for DMAH. However, the observation that full equilibrium simulations result in a faster equilibrium than the hexamer pathway alone suggests the monomer pathway does actually make a contribution. Therefore, it seems likely that in the range of aluminum organometallic compounds, both monomer and hexamer pathways are active, with the relative proportion depending on the strengths of the bridge bonds and, perhaps, steric considerations. External factors such as solvents may shift the balance in one or the other direction, and give qualitatively different behavior.

Determining which reaction pathways dominate the approach to equilibrium is an experimental challenge. Because of the low concentrations of the monomer and hexamer, it is not expected these compounds can be directly observed. Simulations suggest, however, that tetramer concentrations may be measurable, at least with initial conditions of mostly dimer. Following dimer, trimer, and tetramer concentrations and mapping them

onto the above simulations may elucidate the reaction pathways transpired in actual experiments. Perhaps IR or NMR spectroscopy could be used to quantify concentrations and monitor the reaction progress.

3.5 Summary

A gas phase mechanism has been investigated for *dimer* ⇔ *trimer* inter-conversion to explain the complicated time/process dependent composition of DMAH. A reaction pathway involving units from monomer up to hexamer is considered. As a practical model for electronic structure calculations, alane is implemented to develop kinetic parameters for the reaction pathways. A reaction mechanism that relies only on concerted reaction steps is explored. Transition states are located for *2 dimers* ⇔ *tetramer, dimer + tetramer* ⇔ *hexamer*, and *2 trimers* ⇔ *hexamer* reactions. Transition state theory and collision theory were applied to derive rate constants.

Results with the alane system find the formation of tetramers from dimers proceeds through a "side on" collision with conservation of bridging H atoms. (A bridge atom on the dimer becomes a bridge atom on the tetramer). Reactions involving the tetramer, however, proceed through a bridge-terminal exchange reaction that does not conserve the labeling of bridge and terminal bonds. Formation of hexamers from dimers, trimers, and tetramers proceeds through the initial formation of an associated reactant complex. The reactant complex then progresses through a classical transition state to the hexamer product. The concerted reaction occurs through a bridge-terminal exchange mechanism. The formation of the associated reactant complex raises some caution with regards to the use of alane as a model system for DMAH, but also suggests an alternative pathway for DMAH and other bridging aluminum compounds.

Based upon derived rate constants, time dependent simulations of the approach to equilibrium are performed. Kinetic simulations of the reaction mechanism qualitatively agree with experimental observations of a slow time response of the DMAH system. The simulations show a slow approach to equilibrium from initial conditions of either dimer or trimer with a characteristic time scale of 10^6 seconds (~ weeks). The simulations suggest perturbation from equilibrium via processing or synthesis procedures results in a

slow return to equilibrium and time dependent properties of the material. The process dependence of the composition of DMAH offers an explanation for discrepancies between different experiments, and between experiments and theory.

Due to uncertainties of the applicability of alane as a model system, limited basis sets, and the use of primarily DFT methods, the results represent only a first-order model. However, the simulations do capture qualitative features of the behavior of these types of systems. Linking these results to a viscosity model could provide further information for a processing/performance relationship. Additionally, the gas phase reactions may be used in CVD models of growth from DMAH and likened compounds.

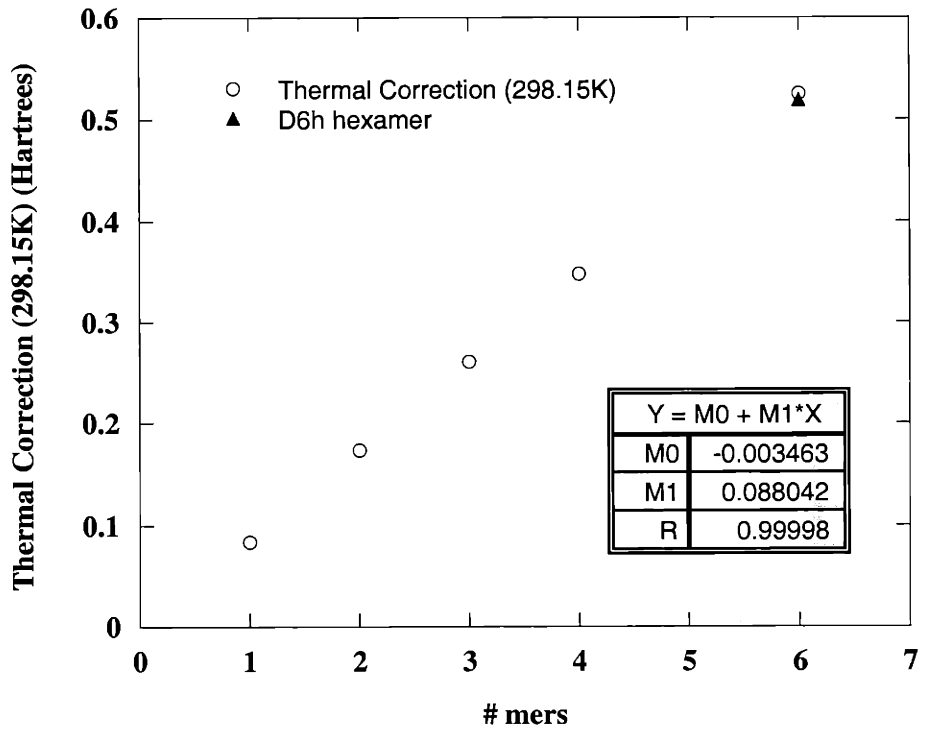

Figure 3.29 Estimation of DMAH hexamer thermal energy at 298.15 (includes zero point energy). Thermal energy is estimated through an extrapolation of data for monomer, dimer, trimer, and tetramer. Also shown is a single point for the calculated thermal energy of the hexamer with D_{6h} symmetry. The D_{6h} symmetry structure is not a minimum, but the calculation provides an estimate of the hexamer thermal energy. Note that a similar procedure for the alane hexamer (where hexamer data is available) slightly overestimates the thermal energy and leads to a 0.77 kcal/mol error.

3.6 Appendix

Due to the size of the DMAH hexamer (60 atoms), a frequency calculation at the minimum structure was not performed. Confidence that the given structure is truly a minimum is based on the likeness of the DMAH hexamer to that of alane, and also a complete optimization without symmetry constraints. Motivated by the planar structures of the trimer and tetramer, a D_{6h} hexamer was initially investigated. However, this structure had several imaginary frequencies associated with symmetry breaking motions. Employing the calculated force constants for further optimization with no symmetry produced the structure shown in Figure 3.5, which was used throughout the calculations. The thermal energy required for calculations of $\Delta H^{298.15K}$ in Table 3.1 was estimated by extrapolating the thermal energy per oligomer from monomer, dimer, trimer, and tetramer calculations (Figure 3.29). The error from this procedure is estimated to be less than 1 kcal/mol by analogy to the alane system where the thermal energy was available from frequency calculations. Rate constant determinations require calculation of equilibrium constants over the temperature range of interest. Equilibrium constants were calculated based on vibrational frequency data obtained from a B3LYP/3-21G** calculation of the D_{6h} hexamer. As shown in Figure 3.29, the error from this assumption is expected to be on the order of 1 kcal/mol.

3.7 References

(1) Wartick, T.; Schlesinger, H. I. *J. Am. Chem. Soc.* **1953**, *75*, 835.

(2) Grady, A. S. *Spectrochim. Acta* **1991**, *47A*, 47-56.

(3) Russell, D. K. a. G., A.S. *J. Chem. Soc. Faraday Trans.* **1995**, *91*, 3015-3020.

(4) Kondoh, E.; Ohta, T. *J. Vac. Sci. Technol. A* **1995**, *13*, 2863.

(5) Yun, J. H.; Lee, J. H.; Park, J. W.; Rhee, S. W. *J. Electrochem. Soc.* **1998**, *145*, L23.

(6) Rogers, J. H.; Apblett, A. W.; Cleaver, W. M.; Tyler, A. N.; Barron, A. R. *J. Chem. Soc. Dalton Trans.* **1992**, 3179.

(7) Sauls, F. C.; Czekaj, C. L.; Interrante, L. V. *Inorg. Chem.* **1990**, *29*, 4688.

(8) Schauer, S. J.; Robinson, G. H. *J. Coord. Chem.* **1993**, *30*, 197.

(9) Storr, A.; Thomas, B. S. *J. Chem. Soc. A* **1971**, 3850.

(10) Sauls, F. C.; Interrante, L. V.; Jiang, Z. *Inorg. Chem.* **1990**, *29*, 2989.

(11) Tanaka, J.; Smith, S. R. *Inorg. Chem.* **1969**, *8*, 265.

(12) Jones, A. C.; O'Brien, P. *CVD of Compound Semiconductors*; VCH: New York, 1997.

(13) Amato, C. C.; Hudson, J. B.; Interrante, L. V. *Appl. Surf. Sci.* **1992**, *54*, 18.

(14) Sauls, F. C.; Hurley, W. J. J.; Interrante, L. V.; Marchetti, P. S.; Maciel, G. E. *Chem. Mater.* **1995**, *7*, 1361.

(15) Timoshkin, A. Y.; Bettinger, H. F.; Schaefer, H. F. I. *J. Am. Chem. Soc.* **1997**, *119*, 5668.

(16) Okamoto, Y. *J. Cryst. Growth* **1998**, *191*, 405.

(17) Interrante, L. V.; Sigel, G. A.; Garbauskas, M.; Hejna, C.; Slack, G. A. *Inorg. Chem.* **1989**, *28*, 252.

(18) Zhiping, J.; Interrante, L. V.; Kwon, D.; Tham, F. S.; Kullnig, R. *Inorg. Chem.* **1992**, *31*, 4815.

(19) Sauls, F. C.; Interrante, L. V. *Coord. Chem. Rev.* **1993**, *128*, 193.

(20) Chen, C. H.; Liu, H.; Steigerwald, D.; Imler, W.; Kuo, C. P.; Craford, M. G.; Ludowise, M.; Lester, S.; Amano, J. *J. Electron. Mater.* **1996**, *25*, 1004.

(21) Frisch, M. J.; Trucks, G. W.; Schlegel, H. B.; Gill, P. M. W.; Johnson, B. G.; Robb, M. A.; Cheeseman, J. R.; Keith, T. A.; Petersson, G. A.; Montgomery, J. A.; Raghavachari, K.; Al-Laham, M. A.; Zakrewski, V. G.; Ortiz, J. V.; Foresman, J. B.; Cioslowski, J.; Stefanov, B. B.; Nanayakkara, A.; Challachombe, M.; Peng, C. Y.; Ayala, P. Y.; Chen, W.; Wong, M. W.; Andres, J. L.; Replogle, E. S.; Gomperts, R.; Martin, R. L.; Fox, D. J.; Binkley, J. S.; Defrees, D. J.; Baker, J.; Stewart, J. P.; Head-Gordaon, M.; Gonzalez, C.; Pople, J. A. ; Gaussian, Inc.: Pittsburgh, 1995.

(22) Peng, C.; Ayala, P. Y.; Schlegel, H. B.; Frisch, M. J. *J. Comp. Chem.* **1995**.

(23) Peng, C.; Schlegel, H. B. *Israel J. Chem.* **1993**, *33*, 449.

(24) Schlegel, H. B. *J. Comp. Chem.* **1982**, *3*, 214.

(25) Frisch, M. J.; Frisch, A.; Foresman, J. B. *Gaussian 94 User's Reference*; Gaussian, Inc.: Pittsburgh, 1996.

(26) Barron, A. R.; Dobbs, K. D.; Francl, M. M. *J. Am. Chem. Soc.* **1991**, *113*, 39.

(27) Shen, M.; Liang, C.; Schaefer, H. F. I. *Chem. Phys.* **1993**, *171*, 325.

(28) Hindmarsh, A. *ACM-SIGNUM Newsletter* **1980**, *15*, 11.

(29) Moore, J. W.; Pearson, R. G. *Kinetics and Mechanism*; John Wiley & Sons: New York, 1981.

(30) Benson, S. W. *Thermochemical Kinetics*, 2nd ed.; John Wiley & Sons: New York, 1976.

(31) Truhlar, D. G.; Garrett, B. C.; Klippenstein, S. J. *J. Phys. Chem.* **1996**, *100*, 12771.

(32) Russel, D. K.; Claxton, T. A.; Grady, A. S.; Linney, R. E.; Mahmood, Z.; Markwell, R. D. *J. Chem. Soc. Faraday Trans.* **1995**, *91*, 3015.

Chapter 4

Experimental Studies of DMAH Growth Chemistry

4.1 Introduction

Dimethylaluminum Hydride (DMAH) is an aluminum organometallic chemical vapor deposition (OMCVD) precursor that has received much attention for its potential application in semiconductor metalization. DMAH is a stable aluminum organometallic compound that has been shown to grow very pure (C and O below AES detection) aluminum films.[1,2] Trimethylaluminum (TMA) is another aluminum OMCVD precursor used for the growth of aluminum containing films. TMA has been used extensively for the growth of compound semiconductors[3] and AlN[4-7] films. TMA is not suitable for deposition of pure aluminum, however, because of its propensity to deposit carbon-contaminated aluminum films. Similarities in structure between DMAH and TMA make it natural to study both together, and as shall be demonstrated, their chemistries are intimately related.

Previous growth studies of DMAH have included investigations of thermal growth,[2,8,9] photo-induced growth,[10-24] and selective growth.[25-31] These previous investigations include (industrially motivated) process development research for the semiconductor industry.[9] These studies have indicated that DMAH is useful for growing very pure aluminum films, and may also be of interest for selective growth. Despite the previous investigations, however, little is known about the detailed growth chemistry of DMAH. In contrast to the consensus that very clean films are obtained from growth experiments, previous investigations of the surface chemistry of DMAH indicated large

amounts of carbon deposited on the aluminum surface after experiments.[32,33] The apparent conflict between UHV surface science and actual growth experiments is addressed in the present paper and it is show that the observed growth behavior correlates nicely with surface chemistry investigations.

Previous discussions of the mechanism of DMAH growth have suggested DMAH eliminates methane as a reaction product.[8,19,28,30] However, in light of what is known about hydrogen's reluctant chemisorption on aluminum surfaces, such a mechanism does not seem likely on aluminum.[34] More recent studies have noted the likelihood that TMA is a reaction product from DMAH growth.[9,35] One possible route to such an observation is the gas phase disproportionation of DMAH:

$$3\ AlH(CH_3)_2(g) \Leftrightarrow AlH_3(g) + 2\ Al(CH_3)_3(g)$$

A gas phase disproportionation mechanism would involve a scrambling of bridge and terminal bonds through the formation of dimers and possibly higher oligomers to produce alane and TMA. Clean aluminum film deposition could then occur from the alane compound. As written, the above chemical equation has a heat of reaction less than 0.1 kcal/mol DMAH, according to accurate quantum chemistry calculations[v]. However, considering the formation of dimers of both DMAH and alane, the heat of reaction is expected to be close to +12 kcal/mol per DMAH[vi].

In the present study, it is found that gas phase disproportionation to alane is not necessary for clean aluminum growth. Surface science experiments reveal that DMAH grows on aluminum surfaces via a *surface* disproportionation mechanism, illustrated in Figure 4.1. The reaction products are molecular hydrogen and trimethylaluminum (TMA), itself an aluminum organometallic compound. A full understanding of the relative importance of a gas phase and surface disproportionation mechanism would require a full scale reactor simulation, coupling fluid dynamics, heat transfer, and gas

---

[v] G2 calculations.[36] Note the reaction of concern is an isodesmic reaction, i.e. the number of different types of bonds is conserved. These types of reaction should be predicted very accurately by quantum chemistry methods.

[vi] The TMA dimer is ignored, since it would not be expected to form in the hot region near the surface.

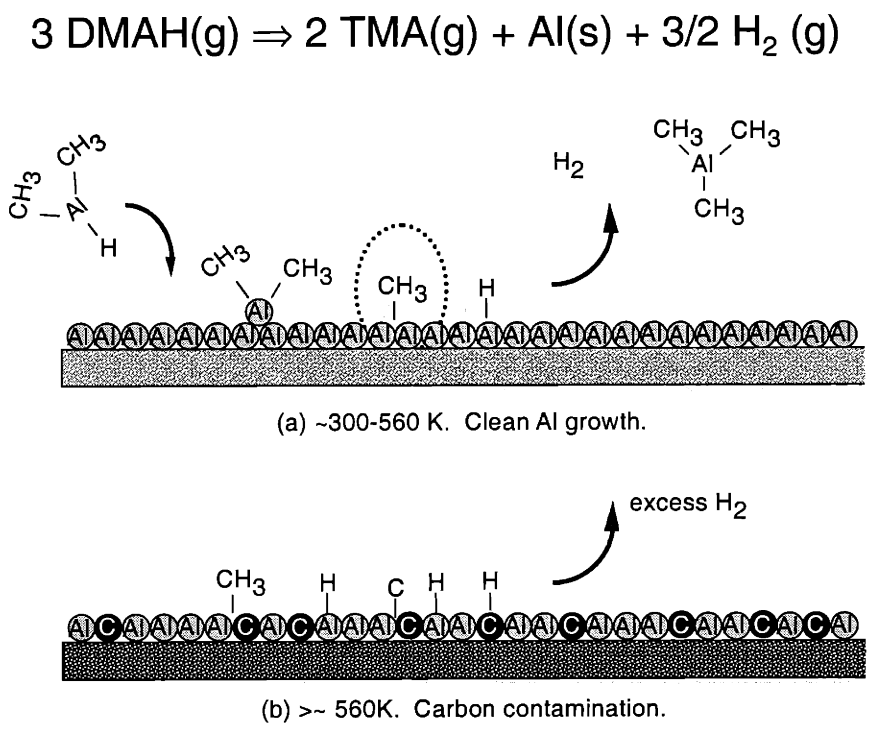

Figure 4.1 Illustration of the low temperature disproportionation mechanism and the high-temperature carbon incorporation pathways of DMAH.

phase and surface chemistry. The present paper is concerned with the surface chemistry only.

The stoichiometry of the presently observed growth reaction:

$$3\ \mathrm{DMAH(g)} \Rightarrow 1\ \mathrm{Al(bulk)} + 2\ \mathrm{TMA(g)} + 3/2\ \mathrm{H_2(g)}$$

suggests the precursor efficiency of DMAH has a upper limit of 1/3. The stoichiometry also explains why DMAH leads to clean aluminum growth while TMA does not. Results show that DMAH has a carbon impurity-free growth mechanism for temperatures up to 560-600 K (290-325°C). Beyond these temperatures, a competing carbon incorporation pathway dominates and leads to carbon contaminated films. It is found that this second, carbon contaminated reaction regime, is the only growth pathway available to TMA, thus

explaining the high temperatures necessary for growth and the resulting contaminated films.

A further matter with DMAH and TMA growth behavior is the complex gas phase chemistry of these compounds. DMAH and TMA are known to exist as associated complexes in the liquid and gas phase. In the case of DMAH, the equilibrium involves dimers, trimers, and higher order associated units.[37-39] TMA, on the other hand, manifests a monomer-dimer equilibrium.[39-41] Although the gas phase chemistry of these complexes is fairly well understood, very little is known about its influence on the surface chemistry and hence growth manners. In the present study, it is found that DMAH displays a complex sticking behavior that is most likely related to its molecular structure in the gas phase. The adsorption step is an important aspect of chemical vapor deposition (CVD) with these kinds of compounds, and it is low sticking coefficients that give CVD its advantages in terms of conformal thin films. While some observations are presented here, the general knowledge of adsorption chemistry for these types of compounds is relatively unexplored, and remains an area for further investigations.

4.2 Experiment

Experiments were performed in a stainless-steel UHV chamber equipped with a Auger electron spectrometer (AES), quadrupole mass spectrometer (QMS), sputter gun, high resolution electron energy loss spectrometer (HREELS), and low energy electron diffraction analyzer (LEED) (Figure 4.2). The main chamber is pumped with a diffusion pump, which is equipped with a liquid nitrogen trap. The mass spectrometer is differentially pumped with a 250 liter/sec turbomolecular pump. A titanium sublimation pump is used to help speed pump-down during experiments. The main chamber had a base pressure of 5.0×10^{-10} Torr.

DMAH was obtained as a gift from the Schumacher chemical company[vii], and TMA was obtained from Morton International[viii]. Several issues were encountered regarding precursor handling. As is well known, aluminum alkyls are extremely sensitive

[vii] Carlsbad, CA.
[viii] Danvers, MA.

to trace levels of water and oxygen. Products from reactions with these residual gases may be volatile alkoxides that can easily contribute to carbon and oxygen impurities.

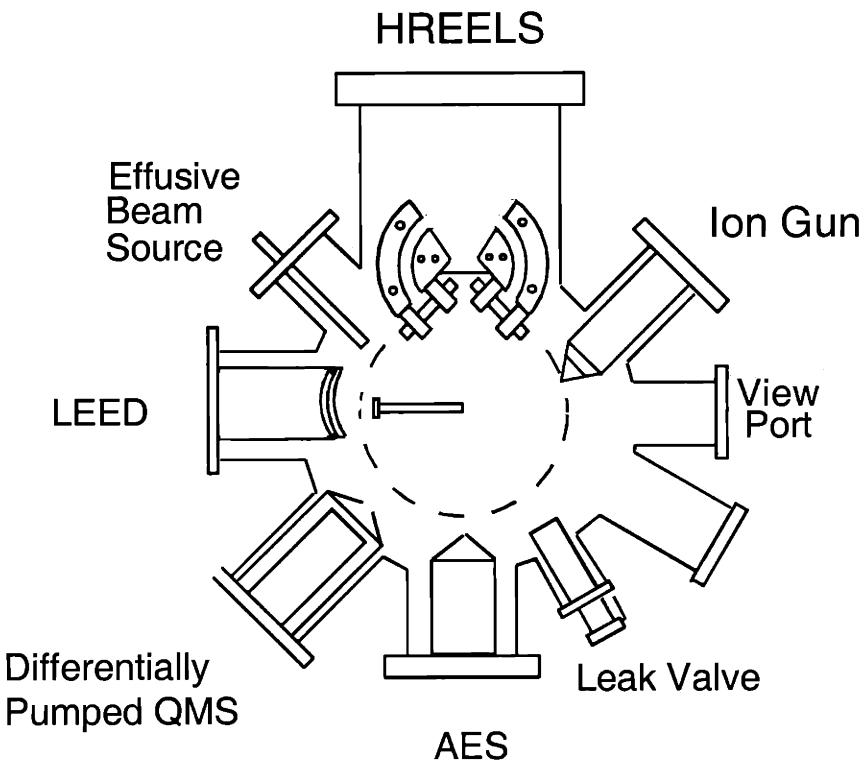

Figure 4.2 Schematic of the Ultra-High Vacuum chamber used for surface science investigations. (Not to scale).

High temperature bakeouts (~300°C) with a turbomolecular pump and gas line pressures ~ 1.0 x10^{-8} was insufficient to rid the gas lines of trace contaminates. Flowing precursor through gas lines to passivate the stainless steel tubing walls was one way of handling the problem. A more efficient method (providing there are no leaks!) involved flowing liquid nitrogen boil-off through the gas lines while torching the lines till red-hot. This procedure was preferred, and repeated each time gas lines were opened to atmosphere. The same procedure was followed whenever new compounds were opened to the gas lines. With this procedure no detectable oxygen contamination was observed.

Another, related issue, concerns organic solvents used in synthesis of DMAH. Residual solvents were detected continually, until the bubbler was empty. These solvents were undesirable due to their ability to cause carbon contamination on the crystals. The higher vapor pressure of the solvents compared to DMAH caused an accumulation of the organic compounds in the bubbler. These contaminants could be reduced below detection by opening the bubbler and pumping on the contents for several minutes.

Despite the cleanliness of the gas lines, side reactions were apparently still a problem in the main chamber. Even with base pressures below 5.0×10^{-10} Torr, large amounts of methane persisted in the UHV chamber from decomposition of the precursor on chamber walls. However, the presence of methane did not seem to affect the surface chemistry studies. In one sense, the decomposition reactions were actually advantageous since they gave a virtually infinite pumping speed for the higher mass fragments of DMAH and TMA. After several months in vacuum, and with the gradual passivation of the chamber, pumping speeds for the large mass signals decreased noticeably. On the down side, due to the low pumping speeds for methane and the high apparent partial pressures, it was not possible to satisfactorily eliminate the possibility of methane formation from surface reactions. The evidence does, however, suggest that such a pathways is negligible, if not absent.

Surface science experiments were performed on Al(100) and Al(111) crystals obtained from Monocrystals[ix]. Two crystal sizes of ½" x 2 mm and 10 x 2 mm were used in the studies. Crystals were mounted onto button heaters with Tantalum tabs. 0.5 x 0.5 mm thermocouple holes were drilled into the sides of the crystal for temperature measurements. Measuring temperatures with a TC wire spot-welded to a holding mount is not recommended since temperature gradients between the heater and the front of the crystal can be large, and it is relatively easy to inadvertently melt an aluminum crystal. The crystal could be cooled to ~ 120-130 K through contact of the button heater with a liquid nitrogen reservoir. Crystals were cleaned through alternating cycles of sputtering with Argon ions and annealing at 725-750 K. With careful sputtering and high

---

[ix] Monocrystals Company, 24400 Highland Rd. Richmond Heights, OH 44143

temperature anneals (750+ K), crystals could be maintained with reasonable mirror finishes, rather than the hazy appearance noted earlier.[42] Both types of crystal conditions were used, and no differences in results could be discerned.

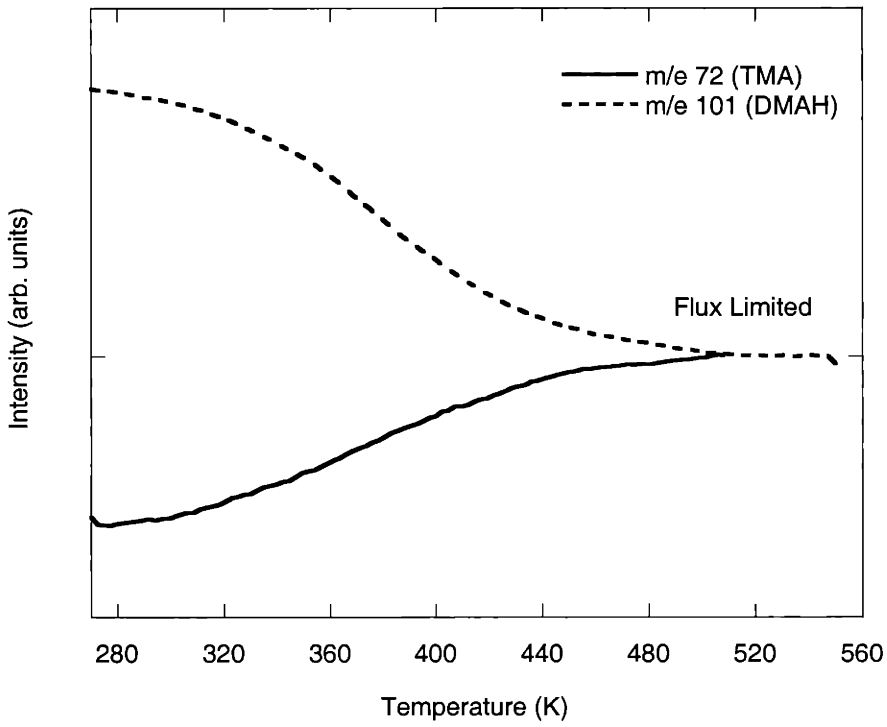

Figure 4.3 Scattering experiments show evidence of TMA as a surface reaction product. The m/e 101 (DMAH) signal decreases due to reaction, while the signal for m/e 72 (TMA) increases. At high temperatures, the reaction becomes flux-limited.

Due to the relatively low surface coverages and precursor fluxes involved, Temperature Programmed Desorption (TPD) and scattering experiments were performed without scanning the mass spectrometer. Scattering experiments were performed with an effusive beam generated by a small orifice at the end of a 1/8" stainless steel pipe. Fluxes were quantified using a 2.4×10^{-11} mole/sec methane calibrated leak obtained from

Vacuum Technology Inc[x]. TPD experiments were performed using a 6" long, 1/8" diameter stainless steel tube as a doser, which could be heated to 300°C.

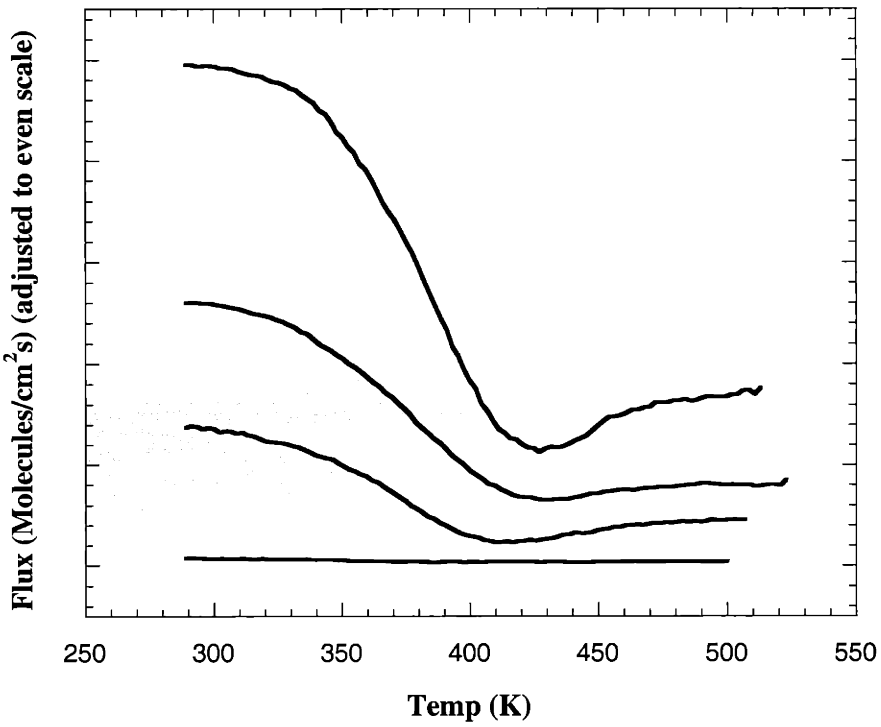

Figure 4.4 Scattering data on Al(111) shows the reactant signal, DMAH (m/e 101), for several fluxes.

4.3 Results

4.3.1 Scattering Experiments

Effusive beam scattering studies were used to identify reaction regimes and possible surface reaction products. Figure 4.3 Illustrates the growth reaction of DMAH on Al(100). The m/e 101 signal of DMAH, corresponding to the dimer, decreases as the temperature is ramped due to the growth reaction. Two different reaction regimes are apparent from the scattering data. A low temperature, kinetic regime exists for temperatures ~300-500 K, beyond which the reaction is flux-limited. Figure 4.4 and 4.5

[x] Oak Ridge, TN.

show equivalent data for the Al(111) surface. The overlap of the ramp and cool curves in Figure 4.5 indicates the surface has remained unchanged throughout the reaction. For experiments on Al(111), there is an experimental artefact where the signal drifts upwards in the flux limited regime. This signal drift is because of desorption from the crystal support. The effect is more noticeable for the Al(111) experiments because of smaller fluxes and a smaller crystal. The crystal support has a better line of sight to the mass spectrometer for the smaller crystals. Also shown in Figure 4.3 is signal m/e 72, which increases with temperature. This signal is assigned as a reaction product. Similar data for the Al(111) surface is plotted in Figure 4.6. As shown in Figure 4.7, m/e 72 is not a significant cracking fragment of DMAH.[39] On the other hand, m/e 72 is the parent ion of the TMA monomer (72 amu). On the basis of these results and others below, the product signal is assigned to TMA. The reproducibility of the results and the care in precursor handling assures the signal is not due to drift or TMA contamination in gas lines. Also,

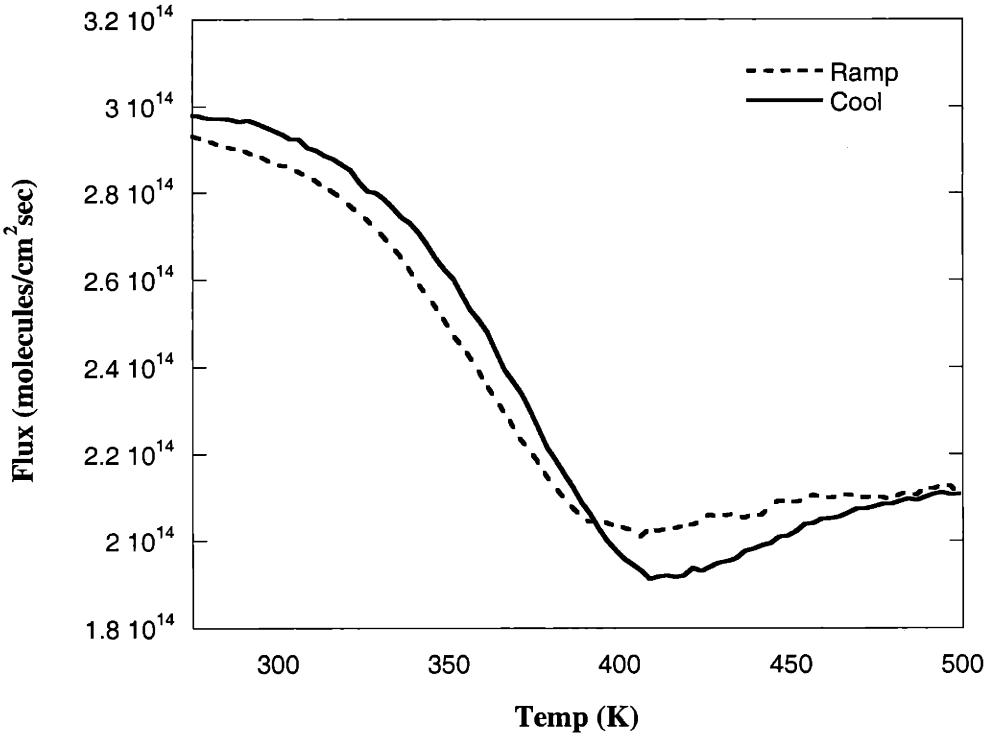

Figure 4.5 DMAH (m/e 101) scattering data on the Al(111) surface. Overlap of ramp-up and cool-down experiments indicates the surface has not changed.

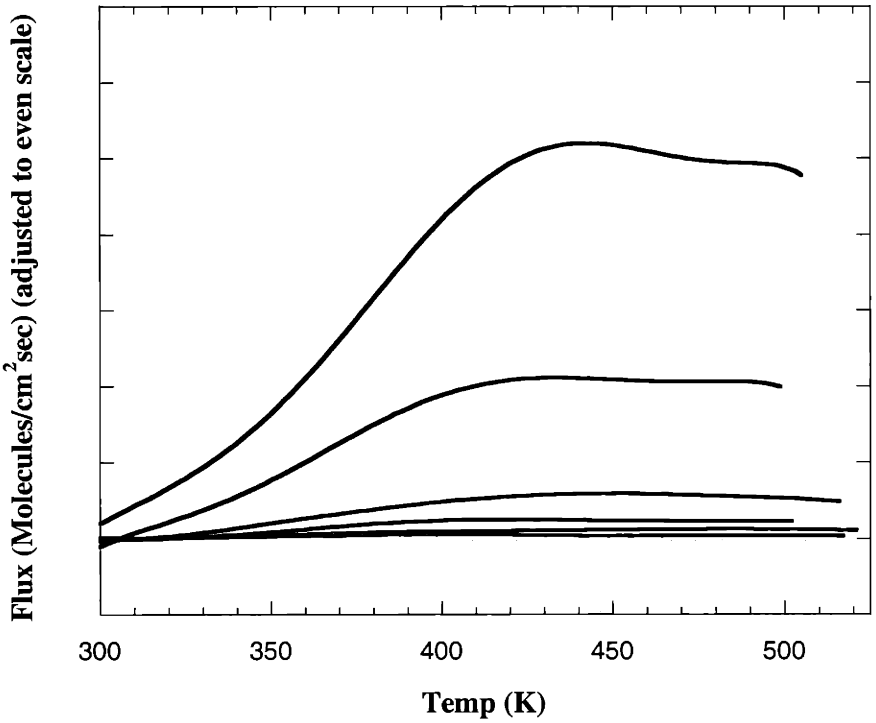

Figure 4.6 Scattering data on Al(111) show the product signal, TMA (m/e 72), for several fluxes.

the mass to charge ratio of 72 eliminates the possibility the product is DMAH monomer from a dimer "cracking" reaction, or a radical fragment formed from the monomer. Note that interpretation of other mass signals is complicated by overlap from both DMAH and TMA contributions.

At high temperatures, DMAH exhibits a second *kinetic* regime, similar to TMA (Figure 4.8). Beyond the flux-limited region of pure aluminum growth, clean growth of DMAH competes with a carbon incorporation pathway. As shown in Figure 4.8, the low temperature reaction (ramp) is similar to the scattering experiments in Figure's 4.3–4.5. As mentioned above, the increasing signal in the flux-limited region is drift due to desorption from the crystal support. At high temperatures (> 600 K) a new AlC_x surface nucleates, and once nucleated, the flux decreases again due to reaction on the new surface. The scattering experiments indicate the reaction on the AlC_x surface is not yet

flux limited even at 800 K. Upon cooling the crystal, reaction characteristics have changed due to the new surface composition. As shown in Figure 4.8, the signal obtained while cooling the crystal is then reproducible in further scattering experiments which ramp the temperature. The shape of the scattering curves for the AlC_x surface shows two different slopes, indicating two kinetic regimes. AES spectra taken before and after the reaction are shown in Figures 4.9 and 4.10. The AES spectra indicate large amounts of carbon being incorporated into the growing film. In fact, at ~650 K, the surface is nearly stoichiometric Al_4C_3. At higher temperatures, greater purity aluminum films are obtained with Al/C ratios near 2-3. Precise AES measurements at these temperatures are difficult, however, since carbon rapidly diffuses into the bulk, and the films show a time dependent AES. The observation of two reaction regimes, clean aluminum growth, and carbon incorporation, are consistent with other experiments using weight-gain measurements, where two different growth rate regimes were observed.[43] The characteristic two kinetic regimes are observed on both Al(100) and Al(111) crystals.

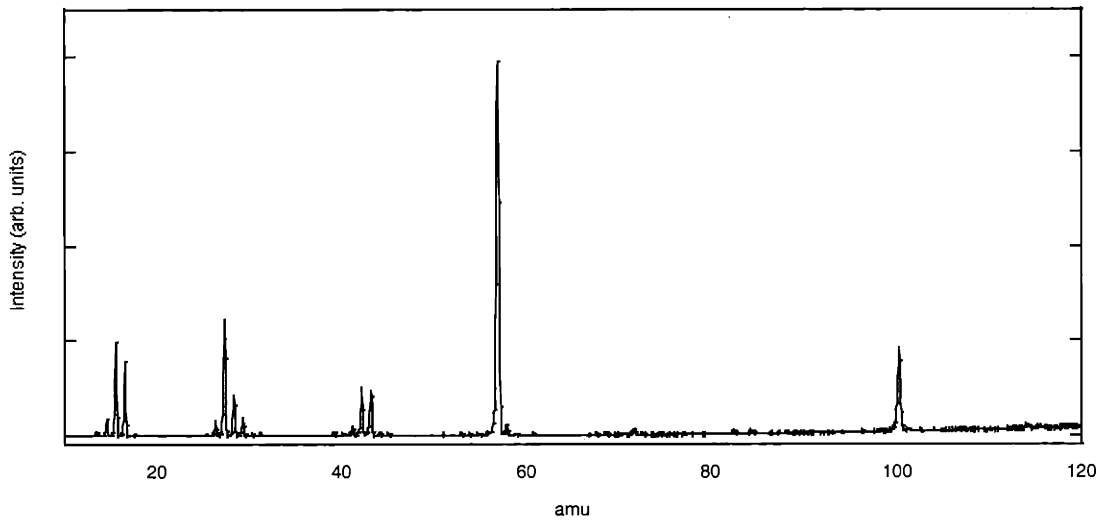

Figure 4.7 Mass spectrum of DMAH.

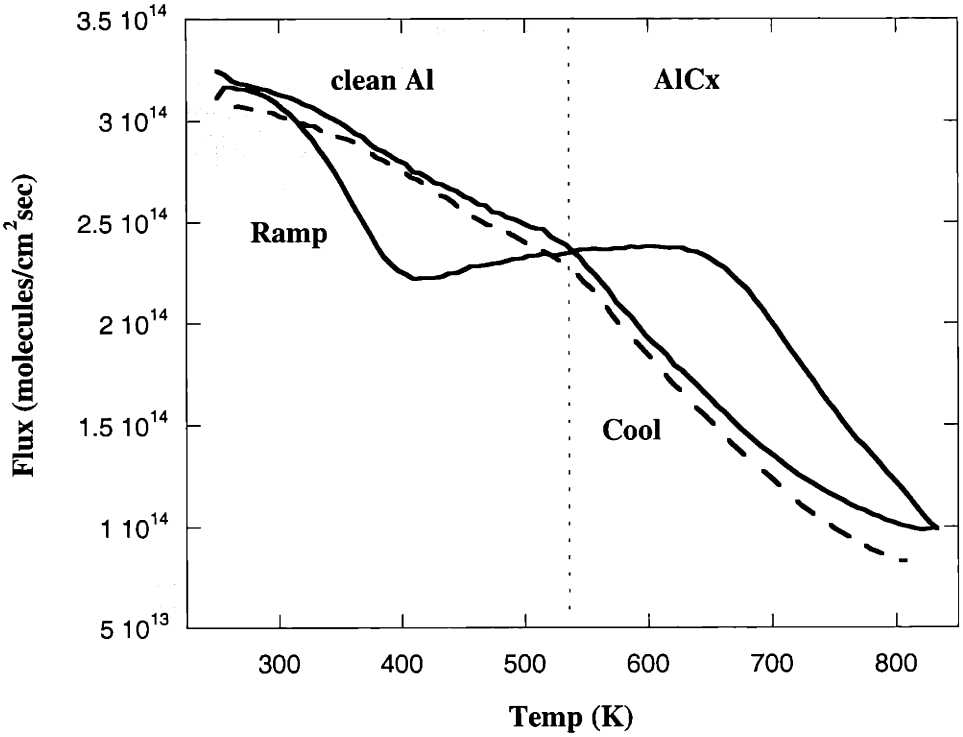

Figure 4.8 High temperature scattering experiments with DMAH. Figure shows the low temperature disproportionation regime followed by a second kinetic regime. The ramp-down cooling curve shows the surface has changed after the high temperature excursion.

In contrast with DMAH, TMA shows no low temperature growth reaction. As shown in Figure 4.11, TMA does not begin to grow until high temperatures, associated with AlC_x growth from DMAH, are reached. Only the high temperature region of the TMA signal (m/e 72) is shown because while there is no net growth regime analogous to DMAH, there is a desorption feature (discussed below). At high temperatures, both DMAH and TMA show the same reaction behavior, and both precursors grow carbon-contaminated films. The signal for DMAH (m/e 57) shows a greater temperature dependence as compared to TMA. The difference is probably due to a superposition of the simultaneous consumption of DMAH, and an end/reduction of the TMA production channel (which contributes to the signal). As shown for TMA in Figure 4.12, the high temperature/carbon incorporating growth regime is accompanied by the evolution of hydrogen. Similar results are obtained for DMAH. DMAH might be expected to give

slightly lower concentrations of carbon due to its stoichiometry and the additional disproportionation channel for growth, but this was not verified.

4.3.2 Temperature Programmed Desorption Experiments

Temperature programmed desorption studies reflect the complicated nature of DMAH even in molecular desorption experiments. There is a noticeable enhancement of mass signals associated with trimers upon desorption. This observation is consistent with a mixture of dimers and trimers incident on the surface and re-arrangement to form the thermodynamically favored trimer in the condensed multi-layer phase. This effect has been seen previously in low temperature IR studies.[44,45] Molecular desorption plots show zero order desorption behavior for both DMAH and TMA. Figure 4.13 illustrates molecular desorption features for TMA. The zero-order desorption behavior can be understood in terms of associative interactions in the condensed multi-layer. Unlike "normal" TPD molecular desorption features, which exhibit a monolayer peak which saturates and then develops into multilayer peaks, for DMAH there appears to be

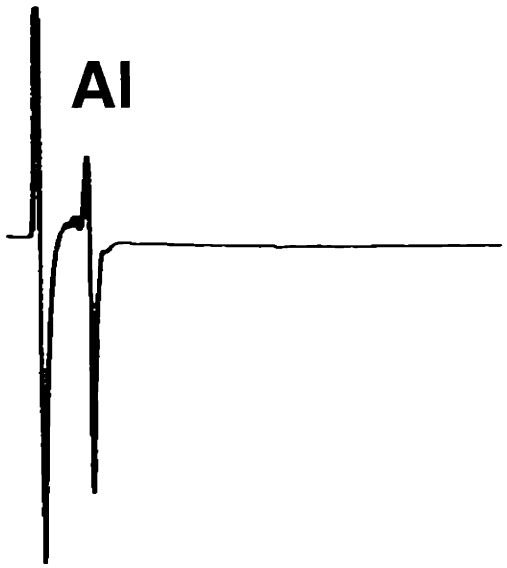

Figure 4.9 Auger electron spectra of the aluminum surface after reaction/growth with DMAH.

simultaneous monolayer and multilayer desorption due to self-association, and directional effects of the doser. Unfortunately, background dosing (i.e. counting Langmuirs) is not reliable since the precursor obviously decomposes on chamber walls. These molecular desorption observations appear consistent with earlier UHV studies of DMAH and TMA.[32]

Investigations of DMAH surface reaction pathways via TPD experiments were performed on Al(100) crystals. DMAH was dosed on the surface at temperatures > 240 K to avoid the dominant molecular desorption feature. Plots of the reaction-desorption features are shown in Figure 4.14. Thermal desorption measurements observe a broad feature extending from 300 K to beyond 500 K. The desorption signal, m/e 57, shifts to lower temperatures with increased coverage, but reaches a fixed low temperature maximum at approximately 335 K. The desorption signal is assigned to the surface reaction product, TMA. The assignment is based on several observations. One argument

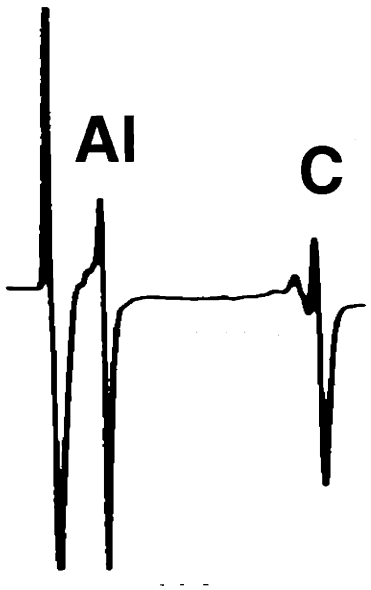

Figure 4.10 Auger electron spectra of the aluminum surface after high temperature reaction/growth with DMAH.

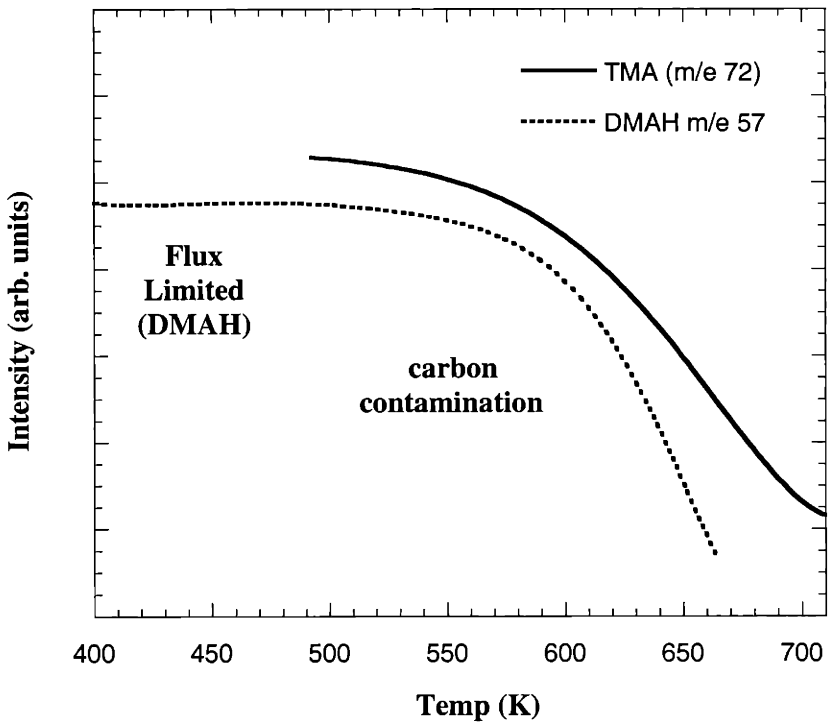

Figure 4.11 Comparison between DMAH and TMA shows that at high temperatures both precursors have a kinetic region where carbon incorporation occurs.

is that TMA desorption is consistent with the scattering experiments from the previous section. Additionally, the m/e 57 signal in the figure is a fragment from an identical desorption feature for m/e 72 (not shown), and this observation excludes the possibility the signal is DMAH monomer desorption. The low-temperature molecular desorption features argue the signal is not from a higher oligomer of DMAH, as does the relatively high temperature range of the desorption signal (300-500 K). Also, TPD experiments measuring m/e 101 (DMAH dimer) show no high-temperature desorption features. Further evidence for TMA as the reaction product is provided below. Note, the long tails of the desorption features of Figure 4.14 are not due to pumping speed effects. For the higher mass signals, decomposition of the precursors on chamber walls gives a very high effective pumping speed. Experiments were also performed on Al(111) crystals, but insufficient surface coverages were obtained, and no desorption features were observed.

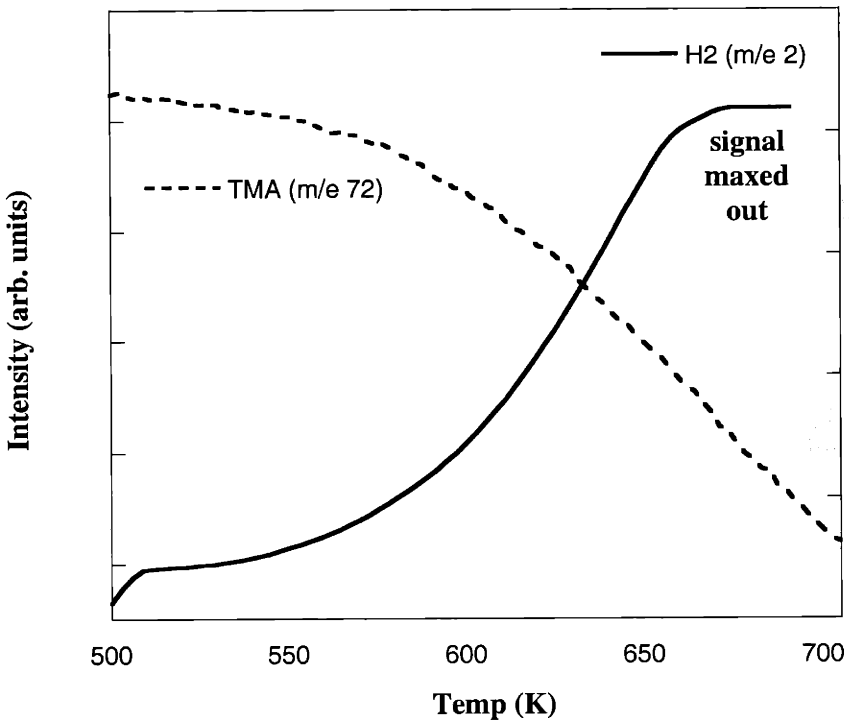

Figure 4.12 Scattering experiments with TMA (m/e 72) show the evolution of hydrogen (m/e 2) from the high temperature, carbon incorporation regime of TMA growth. Similar behavior is observed for DMAH, but unlike DMAH, TMA does not grow at low temperatures.

Perhaps the most convincing evidence for TMA being the DMAH growth product are TPD experiments of TMA itself. TMA chemisorbs on the aluminum surface and desorbs with the same feature observed in the DMAH experiments (Figure 4.15). The desorption features are nearly identical, with differences attributed to higher coverages obtained in TMA experiments. The similarities of the features along with other arguments introduced both above and below suggest both features correspond to the same surface chemistry, desorption of TMA. Interestingly, the experiments suggest TMA, the reaction product, may adsorb onto the growing aluminum surface and block surface sites from DMAH (competitive adsorption).

Several additional experiments were performed to test the developing mechanism. As stated above in the experiment section, a characteristic of the surface science experiments was a relatively large background pressure of methane. The possible

evolution of methane from the growth reaction was studied via TPD experiments and Figure 4.16 is illustrative of the results. TPD spectra of m/e 15&16 show a similar desorption feature to the TMA desorption trace, which suggests the m/e 15&16 signals are cracking fragments of TMA. Note in the plot that m/e 16 > m/e 15 and the signals do not return to the baseline after desorption. These observations are attributed to the formation of methane from decomposition reactions of the precursor in the mass spectrometer housing. Due to the relatively low pumping speeds of methane, it is not possible to quantify the features as cracking fragments of TMA, but the overall shape of the features would be consistent with such an assignment.

Figure 4.17 shows results from TPD experiments where DMAH is dosed at increasing surface temperatures. These experiments show a desorption feature that shifts to higher temperatures as the dosing temperature is increased. Contrary to a simple

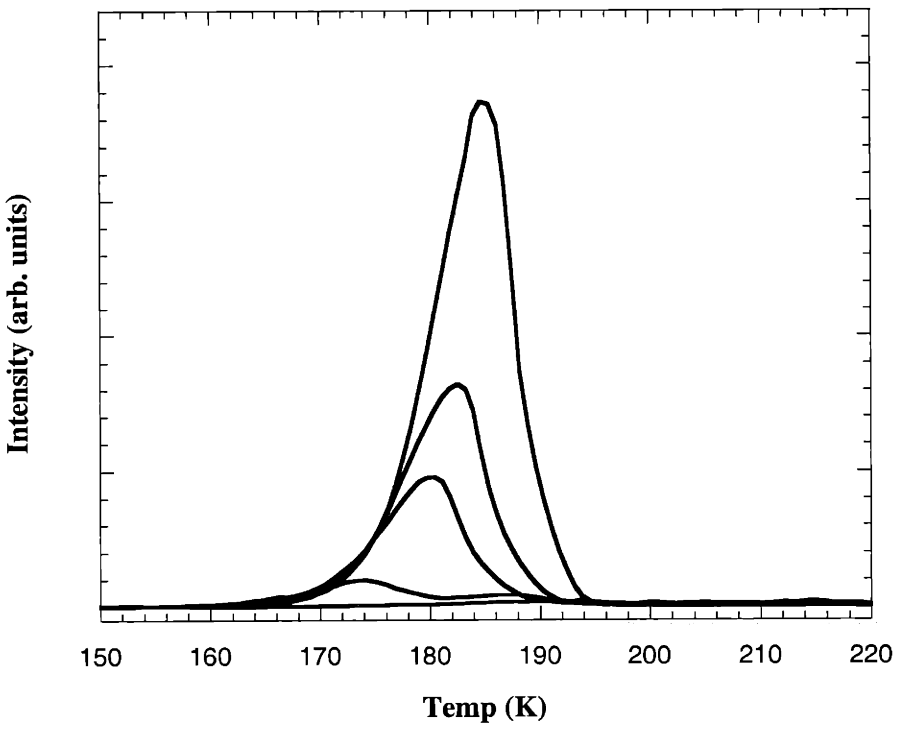

Figure 4.13 Temperature programmed desorption plots show molecular desorption of TMA (m/e 72) off Al(111).

second order desorption feature, the curves maintain a relatively constant peak area over a 100 K dosing range. The low temperature sides of the desorption features shift continuously to higher temperatures, while the high temperature side remains fairly constant. If the reaction were a simple first or second order desorption, increasing the dosing temperature beyond the peak (~330 K) might be expected to greatly reduce the feature area. In later sections (discussion), it will be argued the desorption feature is the result of a multi-step reaction sequence. Similar behavior is observed from TMA experiments.

The last TPD experiments to be presented involve the use of a model compound, methyl iodide. Methyl iodide is used to unambiguously prepare methyl groups on the surface. Iodine is also present on the surface, but previous studies along these lines have suggested the halogen is fairly neutral at low coverages.[46] Experiments find that TMA can be produced in a etching reaction where it is believed the methyl groups etch an aluminum atom to form TMA, which then desorbs from the surface. Results of TPD

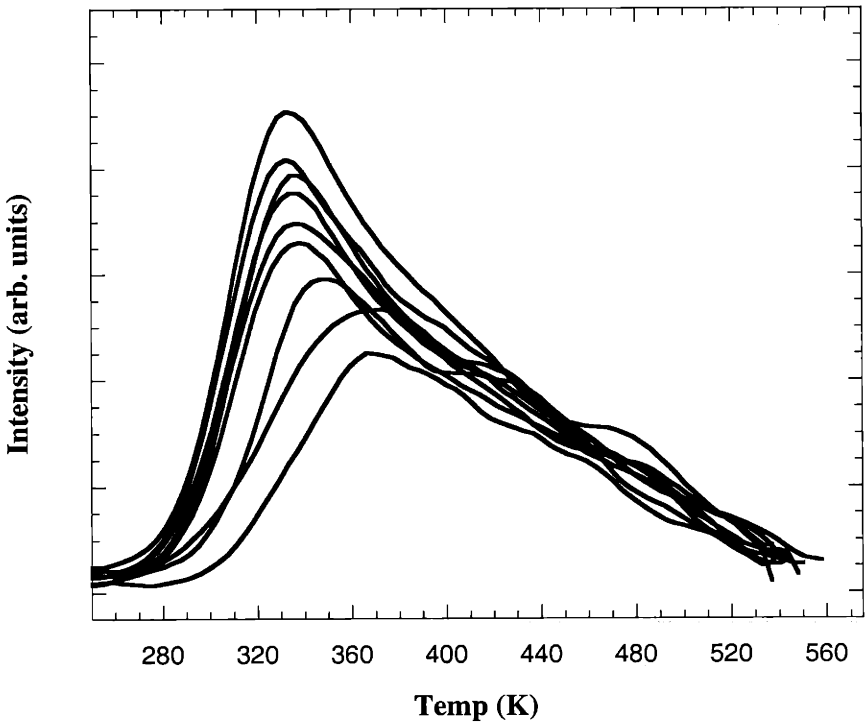

Figure 4.14 Temperature programmed desorption plots for DMAH (m/e 57) off Al(100).

experiments are shown in Figure 4.18. Also shown in the figure are desorption features from TMA and DMAH dosed onto the surface at elevated temperatures (>400 K). Based on the reaction mechanism proposed below, a surface populated by TMA or DMAH at raised surface temperatures should approach the same feature as that for MeI. The figure shows these desorption curves approaching the MeI signal. The remaining offset is ascribed to incomplete decomposition of TMA and DMAH fragments.

Methyl iodide was also used to explore DMAH and TMA carbon incorporation pathways. In the clean aluminum growth mechanism introduced below, surface methyl groups are primary intermediates of the growth reaction. Evidence suggests dehydrogenation of these methyl groups is the rate-limiting step to forming carbon on the surface (Figure 4.19). A methyl dehydrogenation reaction was explored through TPD experiments on Al(100) with the model compound, MeI. Figure 4.20 shows the hydrogen (m/e 2) signal from TPD experiments. Experiments find a hydrogen desorption feature

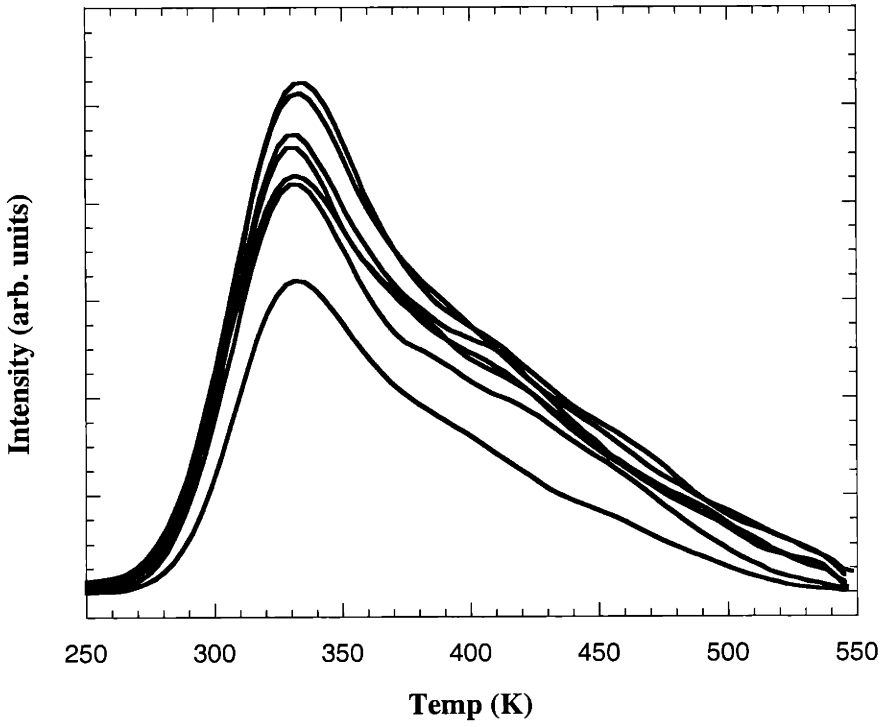

Figure 4.15 Temperature programmed desorption plots for TMA (m/e 57) off Al(100).

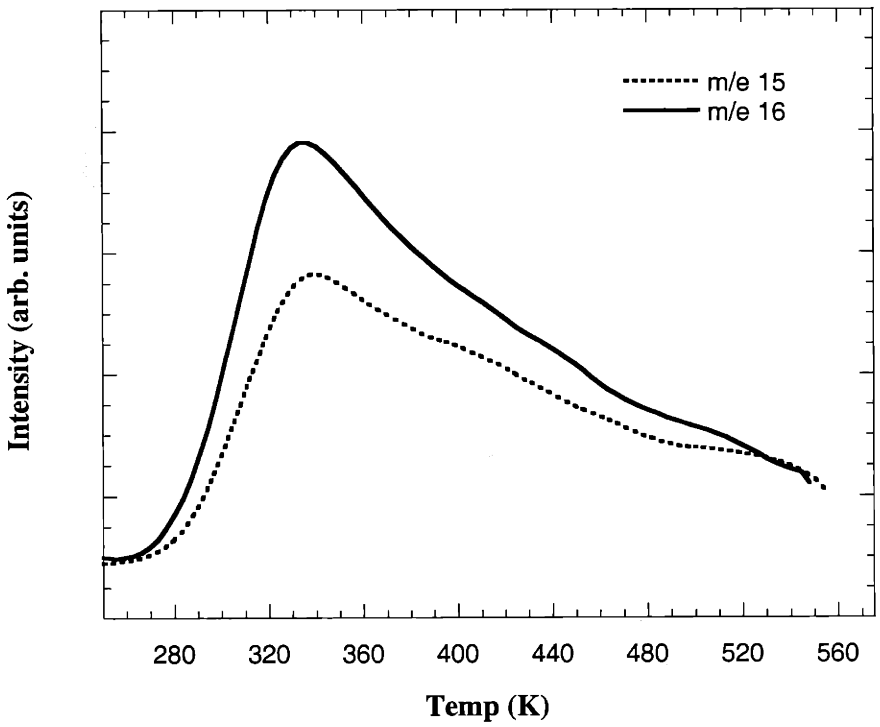

Figure 4.16 Temperature programmed desorption plots of DMAH, m/e 15 & 16. These signals overlap the TMA desorption signal. Note the low pumping speed for methane, at 550K, the signal has not returned to the base line.

for MeI with a maximum at ~660 K. Hydrogen, by itself, desorbs from aluminum surfaces at much lower temperatures,[34] and the signal is assigned to a unimolecular decomposition of surface methyl groups. Consistent with a methyl dehydrogenation reaction, AES spectra indicate the presence of carbon after these experiments. A simple Redhead type of analysis with an assumed pre-exponential of $1x10^{13}$ gives an activation energy of ~ 40 kcal/mol for this unimolecular reaction. It is assumed, without proof, that loss of the first hydrogen is rate limiting. Given the rapid evolution of hydrogen at these temperatures, and the observed carbon, the reaction is not expected to be reversible.

Al_4C_3 and higher Al/C ratios observed from DMAH and TMA high temperature growth indicate methyl dehydrogenation is not the only high temperature reaction pathway. If it were, TMA would give films with Al/C ratios of 1/3. Prompted by the *ab initio* calculations of Chapter 5, methyl radical ejection was investigated with TPD experiments. Results from these experiments, with DMAH, are displayed in Figure 4.21.

The plot shows two desorption features: one (m/e 57) low-temperature feature assigned to TMA recombination and desorption from AlC_x, and a second, high temperature, m/e 16/15 peak assigned to methyl radicals. The peak of the radical desorption feature is approximately 610-620 K, which implies an activation energy near 41 kcal/mol ($1x10^{14}$ pre-exponential assumed). It is not generally possible to distinguish methyl and methane signals in a mass spectrometer, however, the first order character of the plot and the apparent activation energy are consistent with methyl ejection from the surface. From a general understanding of DMAH and TMA surface chemistry, it is clear that formation of surface methyl groups is not a rate-limiting step. Therefore, the first order nature of the desorption peak is representative of the radical ejection. The clear separation of the methyl ejection signal from the TMA recombination-desorption feature confirms the high temperature peak is not a cracking fragment of TMA.

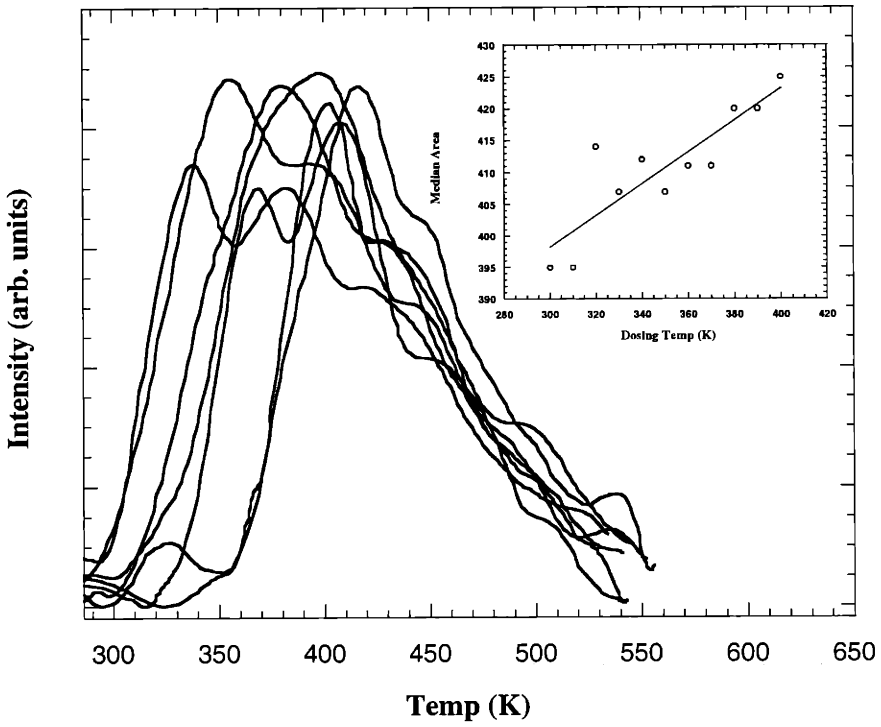

Figure 4.17 Temperature programmed desorption experiments from DMAH dosed at increasing surface temperatures on Al(100). The inset plot shows the correlation between surface temperature (x-axis) and the center of mass of the desorption feature (y-axis).

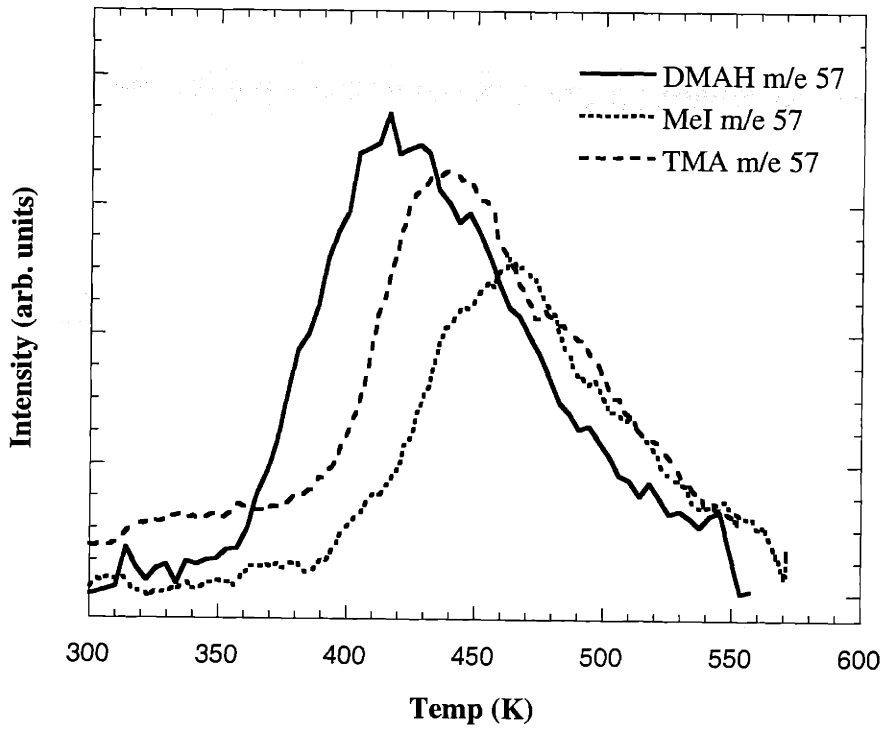

Figure 4.18 Temperature Programmed Desorption experiments illustrate how Methyl Iodide dosed onto the surface etches Trimethylaluminum (m/e 57). Also shown in the plot are two curves from high (surface) temperature dosed TMA & DMAH TPD experiments. The DMAH and TMA desorption features approach the MeI curve because the initial surface populations become similar.

4.4 Discussion

4.4.1 Clean Aluminum Growth

Considering the above experiments, the following ligand rearrangement on the aluminum surface is proposed.

$$[HAl(CH_3)_2]_2(g) \Rightarrow 2\ Al(CH_3)_2{}^* + 2\ H^*$$

$$2\ H^* \Rightarrow H_2(g)$$

$$Al(CH_3)_2{}^* \Leftrightarrow Al(CH_3)^* + CH_3{}^*$$

$$Al(CH_3)^* \Leftrightarrow Al^* + CH_3{}^*$$

$$Al^* \Leftrightarrow Al(crystal)$$

$$Al(CH_3)_2^* + CH_3^* \Leftrightarrow Al(CH_3)_3(g)$$

The chemical equations are understood as follows: DMAH dimers (or trimers) adsorb onto the surface, breaking into $Al(CH_3)_2^*$ fragments. Hydrogen diffuses rapidly on aluminum and recombines to evolve $H_2(g)$. $Al(CH_3)_2^*$ fragments gain and loose ligands to form Al*, $Al(CH_3)^*$, and $Al(CH_3)_3(g)$. The net result is a ligand re-distribution which produces TMA via desorption of $Al(CH_3)_3(g)$. It is assumed that at CVD reactor conditions growth coverages are generally low, so that TMA dimers do not form on the surface. The above disproportionation reaction results in a stoichiometric re-arrangement where three DMAH monomer units are converted to two TMA units and an aluminum adatom. The aluminum adatom diffuses on the surface until it finds a place in the bulk structure. This impurity-free growth pathway is operative for temperatures below approximately 560-600 K. The assumption that chemisorption occurs via breaking a bridging hydrogen bond rather than a terminal methyl group is based on the known greater reactivity of Al-H bonds,[47] and ab initio calculations (Chapter 5).

Interestingly, the above chemistry is essentially the same for TMA. In the case of TMA, however, the disproportionation mechanism is not available, and there is no net low-temperature growth reaction. TPD experiments and comparison with DMAH indicate that TMA participates in a dynamic equilibrium where adsorption and desorption occur readily at growth temperatures. The presence of TMA at high conversions may inhibit growth rates due to competitive adsorption. Note this effect would also occur even if a gas phase disproportionation mechanism were dominant. The observation of no net growth with TMA at temperatures where DMAH grows is consistent with previous TMA growth studies, which indicate TMA growth requires temperatures in excess of 350°C.[48]

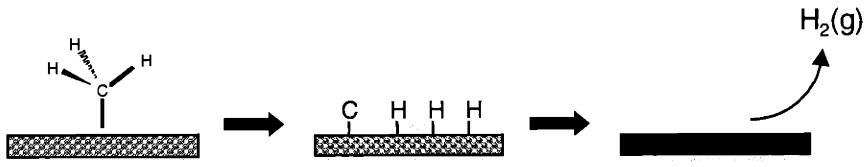

Figure 4.19 Illustration of methyl dehydrogenation reaction on Al.

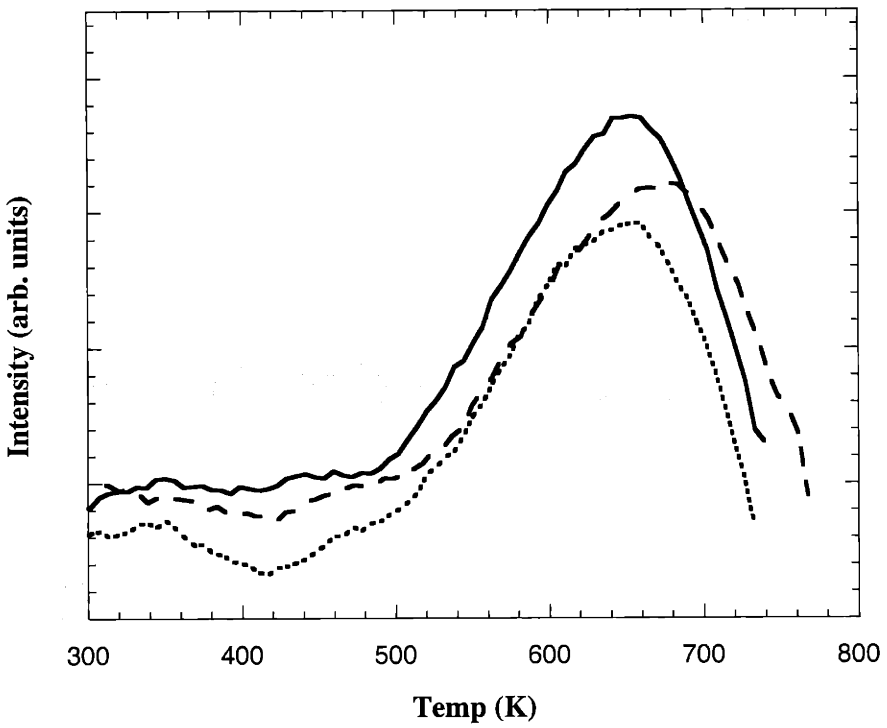

Figure 4.20 Temperature programmed desorption experiments showing hydrogen desorption (m/e 2) from the decomposition of methyl iodide and DMAH on Al(100). The solid curve is the DMAH feature.

The above reaction mechanism is consistent with all the available experimental data. Both scattering and TPD experiments support the assignment of TMA as a reaction product. The equivalence of DMAH and TMA desorption features indicates that a recombination of $*Al(CH_3)_2$ and methyl ($*CH_3$) groups is operative. The existence of free surface methyl groups, which participate in the recombination-desorption step, requires breaking dimethylaluminum (DMAl) fragments into monomethylaluminum (MMAl). According to the proposed mechanism, growth with DMAH requires further splitting of MMAl fragments into aluminum ad-atoms and free methyl groups ($*CH_3$). Reversible formation of MMAl and DMAl surface species is supported by MeI experiments, where etching is the reverse of the growth reaction. In addition to its compatibility with the experimental data, the proposed reaction sequence has been

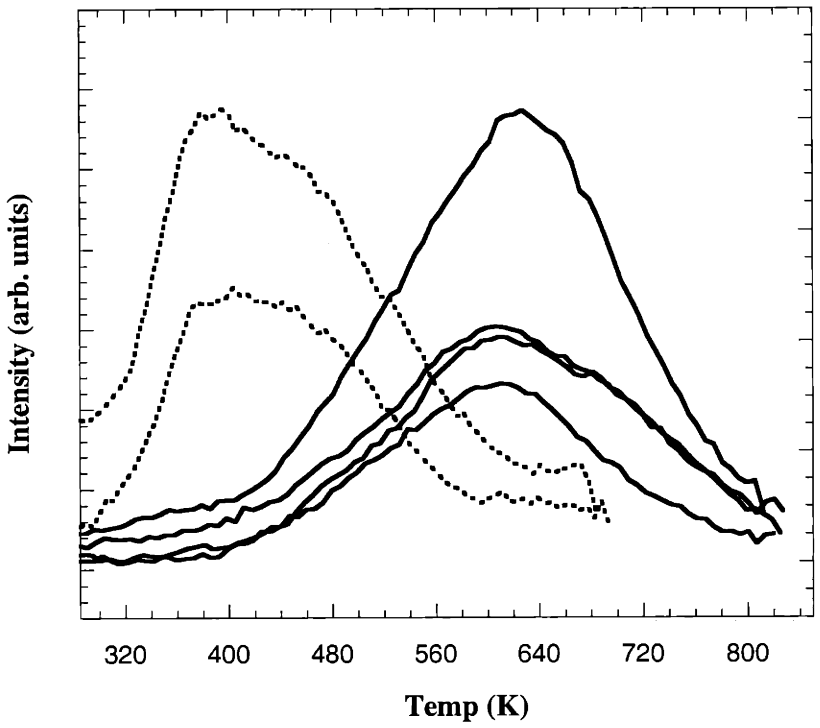

Figure 4.21 Temperature programmed desorption experiments of DMAH off the AlC_x surface. The low and high temperature peaks are assigned to TMA (m/e 57) and methyl radicals (m/e 15), respectively.

explored with computational chemistry methods (Chapter 5) and has been found to be thermodynamically reasonable.

The TMA desorption feature, both from DMAH and TMA adsorption, is interpreted as follows. The low temperature peak corresponds to the recombination of dimethylaluminum fragments with surface methyl groups. The recombination-desorption reaction necessitates fairly low barriers for 1) breaking a dimethylaluminum fragment into MMAl and free methyl groups, 2) diffusion of free methyl groups, and 3) recombination of methyl groups with dimethylaluminum species. The middle region of the desorption features is assigned to a more strongly activated decomposition of MMAl adsorbates. Peak shifts from dosing at increasing temperatures (Figure 4.17) is attributed to a changing population of surface adsorbates, with higher surface temperatures giving rise to more MMAl and surface methyl groups. In the limit of total precursor decomposition, the desorption curve should approach that for methyl Iodide etching (Figure 4.18).

Previous investigations of TPD simulations have revealed that complex desorption features like those of Figures 4.14 and 4.15 can also be explained in terms of neighbor interactions.[49] In the present case, the low surface coverages and the overall compatibility of the experimental results with a multi-step surface mechanism argue against interpretation of desorption features in terms of adsorbate-adsorbate interactions.

The matter of hydrogen on aluminum is more complicated than indicated in the above mechanism. From the experiments, there is no discernable effect from the presence of hydrogen on the surface. Hydrogen is known to desorb from aluminum surfaces near 300-350 K, and here it is assumed hydrogen recombination and desorption is fast compared to the growth reaction.[34,50,51] Hydrogen is necessary to provide the stoichiometry for the disproportionation mechanism, but otherwise hydrogen does not interfere with the progress of the reaction. However, several previous investigations have found that hydrogen may etch alane (AlH_3) from aluminum surfaces.[52] Such an etching reaction would most likely parallel the mechanism for methyl groups, and the observation of AlH_3 from surface H provides additional support for the presently proposed mechanism.

Hydrogen desorption from aluminum surfaces has been found to exhibit zero order desorption behavior rather than a bimolecular recombination implied above.[50,52] In contrast to the low hydrogen surface coverges expected in DMAH growth, the previous investigations have been performed at high surface coverages prepared using atomic hydrogen dissociated with a hot tungsten filament. It is likely that high surface coverages induce the formation of alane-like island structures, stabilized with bridging hydrogen bonds. However, at low coverages it is reasonable to expect that surface hydrogen rapidly couple to from gas phase molecular hydrogen, with alane formation being a minor pathway. This expectation is implicitly supported by growth data, since DMAH and alane adduct compounds would not grow aluminum films if alane etching were dominant. However, because of its ability to etch aluminum, alane formation (as well as methyl etching) could be important for understanding growth morphologies. Simultaneous deposition and etching of alane could explain the low apparent sticking/reaction probability observed in studies of dimethylethylamine alane.[53]

The overall reaction:

$$3\ DMAH\ (g) \Rightarrow 1\ Al\ (bulk) + 2\ TMA\ (g) + 3/2\ H_2\ (g)$$

is consistent with several previous observations. Recent studies comparing growth rates of a dimethylethylamine adduct of DMAH and that of alane measured approximately 1/3 the growth rate for the DMAH adduct as compared to the alane adduct.[54] These observations are consistent with a disproportionation mechanism for DMAH. Other recent growth studies that investigated the effects of adding TMA to the reaction system also support the surface science experiments.[9] Consistent with the disproportionation growth mechanism, TMA was found to inhibit growth of DMAH. Recent infrared studies, under actual CVD conditions, also indicate TMA is the only reaction product, and observe no methane.[35] Keep in mind, however, the above observations could also be explained in terms of a gas phase disproportionation mechanism.

The proposed reaction sequence is also consistent with older synthesis routes. One example involves forming TMA from aluminum turnings and methyl iodide.[55] Exposed aluminum defects may form sites for methyl binding and recombination to form TMA. Although less intuitive, it may also be possible for methyl groups to pull aluminum out of the surface and form a MMAl and vacancy pair. The DMAH growth reaction is, theoretically, reversible, and the hydrogenolysis of trialkylaluminum compounds to dialkylaluminum hydrides under hydrogen pressures of 300 atm and temperatures of ~120°C is known, and has also been used as a synthesis route.[47]

$$2\ R_3Al(g) + Al(g) + 3/2\ H_2(g) \Leftrightarrow 3\ R_2AlH(g)$$

Given the low sticking coefficient of hydrogen on aluminum surfaces, however, for practical purposes, the reaction is expected to be irreversible under CVD conditions. Lastly, the surface disproportionation mechanism is also consistent with studies of carrier gas effects, where hydrogen is not necessary for clean aluminum growth.

A curious feature of the growth studies is a low apparent activation energy. Apparent activation energies for DMAH growth have been measured at 12.0 and 10.8 kcal/mol,[8] 12.0 kcal/mol,[56] 9.2 kcal/mol,[57] 13.1 kcal/mol,[9] 6.9 kcal/mol,[12,13] 6.5 kcal/mol,[35] and 9.7 kcal/mol[xi]. In the scattering studies of the present article, apparent activation energies were measured in a range of 6.9-11.5 kcal/mol for the Al(111) surface (Figure 4.3-4.6). Considering the lowest barrier for a gas phase decomposition reaction of DMAH is > 40 kcal/mol ($Al(CH_3)_2(g) \Rightarrow Al(CH_3) + CH_3(g)$), the apparent activation energies are quite low. Growth simulations of Chapter 6 demonstrate how the above reaction mechanism can contain activation barriers on the order of 20 kcal/mol while still giving a low apparent activation energy.

4.4.2 Methane Elimination

Although thermodynamically favored, experimental observations suggest the absence of a methane elimination pathway. Based on available heats of formation (Chapter 2), the following heats of reaction are calculated (per DMAH monomer):

$$3\ DMAH\ (g) \Rightarrow 2\ TMA\ (g) + Al(bulk) + 3/2\ H_2\ (g) \qquad \Delta H_{rxn} = -5.4\ kcal/mol$$

$$DMAH\ (g) + 1/2H_2\ (g) \Rightarrow Al(bulk) + 2CH_4\ (g) \qquad \Delta H_{rxn} = -29.4\ kcal/mol$$

Thermodynamics favors the formation of methane by 24 kcal/mol per DMAH monomer. A methane formation mechanism as given above is not likely on aluminum surfaces primarily because molecular hydrogen does not appreciably chemisorb on aluminum surfaces. Reports of studies with different carrier gases have verified that hydrogen does not influence the DMAH growth reaction, aside from transport effects.[9] On the other hand, in view of the large thermodynamic driving force, hydrogen from DMAH itself could contribute to a partial methane elimination pathway. If methyl groups could eliminate from the surface as methane, the theoretical maximum efficiency of DMAH could be greater than 1/3. Such a pathway would compete with rapid hydrogen

---

[xi] Presentation given by researchers from Motorola, T.P. Ong, et al.

desorption at growth temperatures. The chemistry of methyl and hydrogen recombination to methane on aluminum is, as far as the authors are aware, unknown. Previous investigations of the thermal decomposition of TMA found that only CH_3 radicals were produced, with no CH_4 or C_2H_6.[58] Quality quantum chemistry investigations indicate formation of methane from aluminum is near thermo-neutral (Chapter 5), and the reaction may have a large activation barrier. A large activation barrier for methane formation would be consistent with practical experience where the presence of methane in the UHV chamber does not appear to cause carbon contamination on hot aluminum surfaces. A high barrier for methane chemisorption and (the reverse) hydrogen + methyl recombination would be consistent with the known low reactivity of aluminum surfaces.[59] The absence of a methane elimination pathway is further supported by growth experiments where addition of methane to the reactor did not impede the growth reaction.[9] Additionally, experiments on trimethylgallium decomposition, which exhibits a methyl radical ejection pathway, find no evidence for surface methane formation.[60] Other reaction pathways, such as methyl coupling, are not considered here.

4.4.3 Impurity Pathways

Surface methyl groups are key intermediates in the disproportionation growth mechanism. Methyl groups must diffuse freely on the surface and undergo reactive collisions to form $*Al(CH_3)$, $*Al(CH_3)_2$, and $Al(CH_3)_3(g)$. At high temperatures methyl dehydrogenation competes with the clean growth mechanism, and carbon becomes irreversibly incorporated into the surface. The onset of carbon incorporation at temperatures 560-600 K proceeds by the following proposed reaction sequence.

$$CH_3* \Rightarrow CH_2* + H*$$

$$CH_2* \Rightarrow CH* + H*$$

$$CH* \Rightarrow C* + H*$$

$$C* \Rightarrow C(bulk)$$

$$H* + H* \Rightarrow H_2(g)$$

These reactions are assumed irreversible; there is a large thermodynamic driving force for the forward reaction[61] ($\Delta H_f^{298}(Al_4C_3)$=-39.9 kcal/mol[62]). The evolution of hydrogen is apparent in the scattering data shown in Figure 4.12. Based on the TPD experiments with MeI and DMAH, an activation energy of ~40 kcal/mol is obtained ($\nu=1x10^{13}$). It is assumed that loss of the first hydrogen ligand is rate limiting. Dehydrogenation of other alkyl groups such as iso-butyl ligands may also be the mechanism for carbon incorporation from other precursors, since the present studies indicate a simple beta elimination of methyl groups would not necessarily result in surface carbon. The above mechanism is consistent with the current studies, but somewhat at odds with previous high-resolution electron energy loss spectroscopy (HREELS) studies.[63] In the former studies, a CH* adsorbate was observed, and carbon incorporation occurred at temperatures as low as 450 K. However, the low temperature carbon observation is inconsistent with growth experiments where clean growth is obtained at these temperatures.

The above mechanism for carbon incorporation and the onset of growth with TMA cannot be the entire high-temperature growth mechanism. Methyl dehydrogenation alone would impart AlC_3 surface stoichiometry to the growing surface, using TMA. Actual growth, however, gives a stoichiometry near Al_4C_3 at 650 K, and less carbon at higher temperatures. Methyl ejection from the surface is a likely candidate for the accompanying reaction. From the desorption feature in Figure 4.21, an activation barrier near 41 kcal/mol is expected. To manifest a Al_4C_3 stoichiometry at 650 K, the methyl ejection rate must be approximately 3.0x the rate of dehydrogenation. Given the closeness of the experimental activation barriers and an expectation for a slightly larger pre-exponential for the radical ejection reaction, the 3.0x ratio is reasonable. The observation of methyl radicals is consistent with previous studies of the decomposition of TMA.[58] In fact, the previously measured activation energy value for the decomposition of TMA, 11 kcal/mol, is consistent with the gradual slopes for the high temperature scattering experiments in Figures 4.8 and 4.11. At higher temperatures, quantum chemistry calculations suggest other radical ejection reactions ($Al(CH_3)_2(g)$, for example) may commence. Also, at higher temperatures carbon diffuses into the bulk and the

apparent surface Al/C ratio increases. These suggestions are consistent with the chemistry of trimethylgallium where a methyl ejection pathway has been proposed, and $Ga(CH_3)_x$ desorption is suspected at higher temperatures.[60]

The commencement of the impurity incorporation mechanism may, at least partially, explain the loss of selectivity observed in selective growth experiments. While the disproportionation mechanism relies on facile diffusion of surface methyl groups and recombination reactions, the impurity mechanism is more local. Methyl dehydrogenation and radical ejection reactions may occur with similar, or even lower barriers on other surfaces. Once an AlC_x layer is formed, clean aluminum growth may be sustained. (See below).

4.4.4 Sticking Behavior

A complex sticking behavior for DMAH is apparent from both scattering and TPD experiments. In the scattering experiments, the DMAH growth reaction initially becomes flux limited, but is then followed by a second kinetic regime once AlC_x is nucleated. In TPD experiments, initial uptake of the precursor is reasonably fast, but the surface appears to saturate at a low coverage. It is clear from the scattering data that either of the sticking probability or the number of adsorption (chemisorption) active sites has increased on going from the Al surface to the AlC_x surface. Although TPD surface coverages are not reported due to the difficulty of establishing one monolayer with these precursors, it is known from comparison with molecular desorption curves that surface coverages saturate at a low value. Three possible adsorption-limiting effects, not necessarily independent, are considered below with the aid of the following form for the rate of adsorption:

$$R_{ads} = s(\Theta) * \Phi_{flux/site} * N_{sites/area}$$

In the flux-limited reaction regime, the rate of consumption of precursor is equal to the rate of adsorption. The terms refer to (from left to right) a coverage dependent sticking

coefficient, flux of molecules per adsorption site, and number of adsorption sites per unit area.

One factor that could contribute to the observed adsorption behavior is a sticking coefficient that is small and strongly coverage dependent. The greater rates of adsorption on the AlC_x surface could then be explained as $S_{AlCx} >> S_{Al}$. Given the negligible desorption features for the Al(111) surface, it could also be reasoned $S_{Al(100)} >> S_{Al(111)}$. In the flux-limited regime, however, normally $\Theta \rightarrow 0.0$, so that coverage dependence should be less important. But, it could be that $S_{Al(100)}$ is very small and limits the adsorption rate at the given flux. In addition to a very small sticking probability, a strong coverage dependence could explain the small TPD features.

A second possible factor contributing to the apparent sticking behavior is defect-mediated adsorption. A "defect"-catalyzed chemisorption could explain the apparent saturation at low coverages and the premature flux limited growth. The need for specific "defect" sites to aid adsorption is reasonable considering the strong binding of DMAH dimers and trimers. The enthalpy of dissociation of the dimer in the gas is approximately +35 kcal/mol.

$$[HAl(CH_3)_2]_2(g) \Leftrightarrow 2\ HAl(CH_3)_2(g) \qquad \Delta H_{rxn}=+35\ \text{kcal/mol}$$

Dissociation of trimers into monomers is even more endothermic. In support of these arguments, quantum chemistry calculations estimate that chemisorption of the DMAH dimer is activated by at least +15 kcal/mol (the heat of chemisorption).

Experiments with a heated doser were performed to investigate the possibility that at higher temperatures a more reactive monomer could be observed. Comparison of the uptake behavior for both room temperature and 193°C doser experiments is shown in Figure 4.22. Results show no apparent enhancement of the chemisorption (as measured by the TPD peak area). However, considering the equilibrium calculations of Chapter 3 as a guide, even at 190°C (460 K) there may not be appreciable monomer. Higher temperatures were not explored, since at higher temperatures, pyrolysis may occur, and

invalidate the experiment. In contrast to DMAH, TMA monomers should be observable at high temperatures, due to the weaker bridge binding via methyl groups.

$$[Al(CH_3)_3]_2 \Leftrightarrow 2\ Al(CH_3)_3 \qquad \Delta H_{rxn}=+20\ kcal/mol$$

Therefore, TMA was chosen as a model to test for enhanced reactivity of monomers. Note that according to quantum chemistry calculations, TMA dimer chemisorption is also activated (~20 kcal/mol), but for monomers the reaction could have a much lower barrier. The heat of chemisorption of TMA monomer is approximately thermoneutral. Unfortunately, these experiments were ill defined due to an effect that becomes a third factor possibly influencing the observed DMAH sticking manner. (See below).

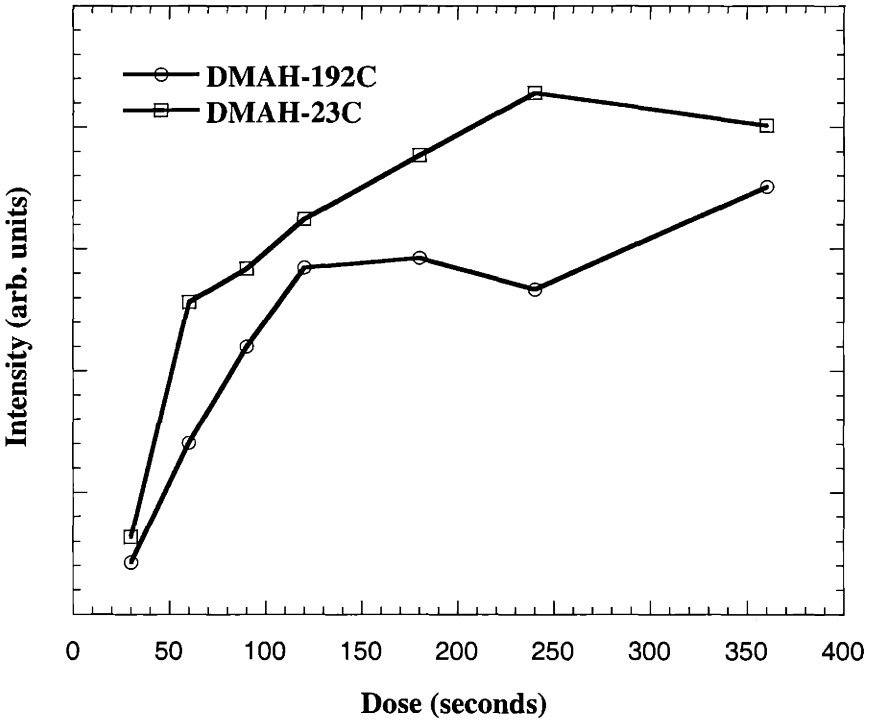

Figure 4.22 Temperature programmed desorption peak area vs. dosage for a hot (192°C) and cool (23°C) doser.

A third factor that may contribute to the observed sticking character of DMAH is a non-negligible surface coverage, even in the flux-limited growth regime. A consequence of the recombination reactions in the growth mechanism is that some methyl groups remain on the surface after TPD experiments. The remaining methyl groups account for carbon incorporation during TPD experiments with excursions to high temperatures. This effect is thought to have led to unexpected carbon contamination in the previously reported surface science studies.[32] The number of such methyl groups can be appreciated from AES plots after high temperature TPD experiments, which give Al/C ratios close to 1.0. Results from the present studies are similar. Even though the observed TMA desorption features are small, the relatively large amounts of carbon remaining on the surface after high temperature ramps indicate a significant presence of surface methyl groups, which undergo dehydrogenation. The methyl groups are left adsorbed on the surface (after TPD experiments) because of a lack of sufficient $Al(CH_3)_x$ groups, and the recombinative nature of the disproportionation mechanism. At growth temperatures, these freely diffusing surface methyl groups could block the chemisorption of further DMAH, even in the flux-limited regime. As discussed above, during AlC_x growth, methyl groups may be ejected into the gas phase, thus leading to a lower surface coverage and a greater adsorption rate. One problem with this interpretation is that the Al(111) surface does not seem to have any adsorption, based on the lack of a desorption feature. Note that for the previously discussed heated doser experiments, residual methyl groups invalidated attempts to correlate gas temperatures with measured desorption peak areas.

4.4.5 Nucleation & Comments on Alternative Precursors

Alternate Precursor Chemistry

It is an interesting feature of DMAH growth chemistry that the clean growth mechanism has more to do with the precursor stoichiometry than an inherently clean reaction mechanism. Precursors such as tri-isobutylaluminum and most likely tri-ethylaluminum attribute their clean growth mechanism to a β-hydride elimination step.

Alane adducts avoid strong aluminum carbon bonds to achieve high purity aluminum films. For DMAH, the actual surface chemistry is rather passive, and not very different from TMA. A hypothetical dimethyl-isobutylaluminum precursor should give the same high purity films as DMAH with a similar efficiency, while a hypothetical H_2AlCH_3 precursor would provide high purity films with a greater maximum precursor efficiency of 2/3. Unfortunately, in the case of the former compound, the ligands may disproportionate to give TMA and TIBA, whereas the latter may be impractical due to the extra hydrogen ligand, which may cause a polymerization in the liquid/solid. Precursors such as diethylaluminum hydride and diisobutylaluminum hydride would be expected to give similar purity as DMAH, with possibly faster growth rates and greater precursor efficiency. Hydrogen bridging would contribute to stability in the liquid, whilst the β-hydride elimination step of the isobutyl and ethyl ligands would sidestep the disproportionation mechanism and allow clean films with higher growth rates. Again, however, such precursors may suffer from impractical handling issues (low vapor pressures and disproportionation instability, for example).

One common feature of all aluminum CVD precursors that have been studied is the essential involvement of hydrogen on the surface, either as a ligand (alane, DMAH) or from a reaction step (β-hydride elimination). Considering the ability of hydrogen to etch aluminum surfaces, it is possible hydrogen contributes to surface roughness and less desirable film characteristics compared to the physical vapor deposition (PVD) processes. As a product of the disproportionation reaction, DMAH has a relatively lower concentration of surface hydrogen than many of the other precursors such as the alane adducts and precursors which undergo a β-hydride elimination step. It would be an interesting study to compare surface morphologies for these different types of precursors and correlate the surface properties with the alane etching kinetics. Additionally, alternate precursors, which avoid introducing hydrogen onto the surface, may be worth investigation. Depending on the relative rates of β-hydride elimination and radical ejection, perhaps tritertiarybutylaluminum would be a candidate.[64]

Nucleation

It is evident from the DMAH growth mechanism that any surface with the following features should be a good nucleation layer: a reasonable sticking probability for DMAH, low barriers for dissociating DMAl and MMAl surface fragments, low diffusion barriers for hydrogen and methyl groups, rapid hydrogen desorption rates, and high barriers for methyl decomposition. It is expected that metallic surfaces will meet most of these requirements and act as good nucleation layers. Support for these ideas come from previous growth studies that report metallic surfaces such as titanium provide the best nucleation characteristics for DMAH.[13] Surfaces that inhibit these processes may require higher temperatures to nucleate aluminum, and the high temperatures may result in carbon contamination at the interfaces. The low temperature scattering regime shown in Figure 4.8 for the AlC_x surface (ramp & cool) corresponds to the nucleation/growth of aluminum on the AlC_x surface. (Note the inflection point ~ 550 K) The disproportionation reaction proceeds at a somewhat slower rate on the AlC_x surface. However, the clean growth mechanism is active on the AlC_x surface, and AES measurements show that clean aluminum is eventually formed. Thereafter, the reaction behavior returns to that characteristic of the clean aluminum surface. As mentioned earlier above, a surface that does not support a disproportionation mechanism may nucleate and loose selective growth behavior when unimolecular reactions such as methyl dehydrogenation and methyl radical ejection initiate.

4.5 Conclusions

A surface disproportionation mechanism has been proposed for dimethylaluminum hydride (DMAH) growth on aluminum surfaces. The mechanism is supported by several observations, including experiments of the present paper, and previously published reports. Trimethylaluminum (TMA) is found to have a surface chemistry similar to DMAH, but lacks the disproportionation growth mechanism due to stoichiometry. TMA can be expected, however, to react with aluminum surfaces and impede DMAH growth. At high temperatures, both DMAH and TMA exhibit a kinetic regime whereupon carbon is incorporated via a methyl dehydrogenation reaction. Based

on the observed film stoichiometry (with AES), a methyl radical ejection reaction is thought to accompany the dehydrogenation reaction. An additional feature of DMAH growth is a complex sticking process. The sticking behavior is most likely related to the stability of dimers and trimers of DMAH in the gas phase, but further studies are needed to elucidate the adsorption step. Finally, based on features of the proposed surface reaction mechanism, it is expected that metallic-like surfaces will provide the best nucleation layers for DMAH growth.

4.6 References

(1) Cacouris, T.; Scelsi, G.; Shaw, P.; Scarmozzino, R.; Osgood Jr., R. M.; Krchnavek, R. R. *Appl. Phys. Lett.* **1988**, *52*, 1856.

(2) Zhu, N.; Cacouris, T.; Scarmozzino, R.; Osgood, J., R.M. *J. Vac. Sci. Technol.* **1992**, *10*, 1167.

(3) Jones, A. C.; O'Brien, P. *CVD of Compound Semiconductors*; VCH: New York, 1997.

(4) Sauls, F. C.; Hurley, W. J. J.; Interrante, L. V.; Marchetti, P. S.; Maciel, G. E. *Chem. Mater.* **1995**, *7*, 1361.

(5) Timoshkin, A. Y.; Bettinger, H. F.; Schaefer, H. F. I. *J. Am. Chem. Soc.* **1997**, *119*, 5668.

(6) Interrante, L. V.; Sigel, G. A.; Garbauskas, M.; Hejna, C.; Slack, G. A. *Inorg. Chem.* **1989**, *28*, 252.

(7) Sauls, F. C.; Interrante, L. V. *Coord. Chem. Rev.* **1993**, *128*, 193.

(8) Kondoh, E.; Ohta, T. *J. Vac. Sci. Technol. A* **1995**, *13*, 2863.

(9) Littau, K. A.; Mosely, R.; Zhou, S.; Zhang, H.; Guo, T. *Microelectron. Eng.* **1997**, *33*, 101.

(10) Hanabusa, M.; Hayakawa, K.; Oikawa, A.; Maeda, K. *Jpn. J. Appl. Phys.* **1988**, *27*, L1392.

(11) Hanabusa, M.; Oikawa, A.; Cai, P. Y. *J. Appl. Phys.* **1989**, *66*, 3268.

(12) Hanabusa, M.; Nitta, T. *Appl. Surf. Sci.* **1996**, *106*, 22.

(13) Nitta, T.; Nishitani, K.; Hanabusa, M. *Jpn. J. Appl. Phys.* **1995**, *34*, L1500-L1502.

(14) Nitta, T.; Hanabusa, M. *Appl. Phys. Lett.* **1996**, *69*, 340.

(15) Uesugi, F.; Nishiyama, I. *Appl. Surf. Sci.* **1992**, *62*, 151-156.

(16) Uesugi, F.; Nishiyama, I. *Appl. Surf. Sci.* **1992**, *54*, 284-290.

(17) Uesugi, F.; Nishiyama, I. *Appl. Surf. Sci.* **1992**, *60/61*, 587-591.

(18) Okawa, M.; Tsuruta, H.; Hanabusa, M. *Appl. Surf. Sci.* **1994**, *79/80*, 444.

(19) Masu, K.; Yokoyama, M.; Matsuhashi, H.; Tsubouchi, K. *Appl. Surf. Sci.* **1994**, *79/80*, 237.

(20) Kawai, T.; Hanabusa, M. *Jpn. J. Appl. Phys.* **1993**, *32*, 4690-4693.

(21) Kawai, T.; Okawa, M.; Komatsu, A.; Shimada, T.; Hanabusa, M. *Appl. Surf. Sci.* **1994**, *79/80*, 385-388.

(22) Ouchi, H.; Ishida, K.; Hanabusa, M.; Shogen, S.; Kawasaki, M. *Jpn. J. Appl. Phys.* **1992**, *31*, 1979.

(23) Sahara, K.; Ouchi, H.; Hanabusa, M. *Jpn. J. Appl. Phys.* **1991**, *30*, 1545.

(24) Ohashi, M.; Shogen, S.; Kawasaki, M.; Hanabusa, M. *J. Appl. Phys.* **1993**, *73*, 3549.

(25) Zhu, N.; Jo, S. D.; Freiler, M. B.; Scarmozzino, R.; R.M. Osgood, J.; Cacouris, T.; Materials Research Society Symposium, 1992.

(26) Matsumiya, Y.; Kitahara, K.; Ohtsuka, N.; Nakajima, K. *Jpn. J. Appl. Phys.* **1995**, *34*, L17-L19.

(27) Tsubouchi, K.; Masu, K.; Shigeeda, N.; Matano, T.; Hiura, Y.; Mikoshiba, N. *Appl. Phys. Lett.* **1990**, *57*, 1221.

(28) Tsubouchi, K.; Masu, K. *J. Vac. Sci. Technol. A* **1992**, *10*, 856.

(29) Takeyasu, N.; Kawano, Y.; Kondoh, E.; Katagiri, T.; Yamamoto, H.; Shinriki, H.; Ohta, T. *Jpn. J. Appl. Phys.* **1994**, *33*, 424.

(30) Tsubouchi, K.; Masu, K.; Sasaki, K. *Jpn. J. Appl. Phys.* **1993**, *32*, 278.

(31) Sakaue, H.; Katsuda, Y.; Konagata, S.; Shingubara, S.; Takahagi, T. *Jpn. J. Appl. Phys.* **1996**, *35*, 1010.

(32) Strongin. *J. Phys. Chem.* **1990**, *95*, 1329-1333.

(33) Strongin, D. R.; Comita, P. B.; Mater. Res. Soc. Symp., 1990.

(34) Paul, J. *Phys. Rev. B* **1988**, *37*.

(35) Sugiyama, M.; Shimogaki, Y.; Egashira, Y.; Yoshimi, T.; Itoh, H.; Aoyama, J.; Komiyama, H.; 194th Meeting of the Electrochemical Society, Inc., 1998, Boston, MA.

(36) Curtiss, L. A., Krishnan Ragavachari, Gary W. Trucks, and John Pople. *J. Chem. Phys.* **1991**, *94*, 7221.

(37) Wartick, T.; Schlesinger, H. I. *J. Am. Chem. Soc.* **1953**, *75*, 835.

(38) Almenningen, A.; Anderson, G. A.; Forgaard, F. R.; Haaland, A. *Acta Chemi. Scand.* **1972**, *26*, 2315.

(39) Tanaka, J.; Smith, S. R. *Inorg. Chem.* **1969**, *8*, 265.

(40) Lewis, P. H.; Rundle, R. E. *J. Chem. Phys.* **1953**, *21*, 986.

(41) Vranka, R. G. a. A., E.L. *J. Am. Chem. Soc.* **1967**, *89*, 3121.

(42) Bent, B. E.; Nuzzo, R. G.; Dubois, L. H. *J. Am. Chem. Soc.* **1989**, *111*, 1634-1644.

(43) Matsumiya, Y.; Nakajima, K. *J. Cryst. Growth* **1997**, *181*, 437.

(44) Imaizumi, Y.; Zhang, Y.; Tsusaka, Y.; Urisu, T.; Sato, S. *J. Mol. Struct.* **1995**, *352/353*, 447.

(45) Imaizumi, Y.; Tsusaka, Y.; Urisu, T. *J. Electron. Spect. Rel. Phenom.* **1996**, *80*, 93.

(46) Bent, B. E. *Chem. Rev.* **1996**, *96*, 1361.

(47) Mole, T. *Aust. J. Chem.* **1964**, *17*, 1050.

(48) Biswas, D. R.; Ghosh, C.; Layman, R. L. *J. Electrochem. Soc.* **1983**, *130*, 234.

(49) Meng, B.; Weinberg, W. H. *J. Chem. Phys.* **1994**, *100*, 5280.

(50) Winkler, A.; Pozgainer, G.; Rendulic, K. D. *Surf. Sci.* **1991**, *251/252*, 886.

(51) Berger, H. F.; Rendulic, K. D. *Surf. Sci.* **1991**, *253*, 325.

(52) Hara, M.; Domen, K.; Onishi, T.; Nozoye, H.; Nishihara, C.; Kaise, Y.; Shindo, H. *Surf. Sci.* **1991**, *242*, 459.

(53) Karpov, I.; Gladfelter, W.; Franciosi, A. *Appl. Phys. Lett.* **1996**, *69*, 4191.

(54) Taylor, C. J.; Roberts, J. T.; Gladfelter, W.; Franciosi, A.; Advanced Metalization and Interconnect Systems for ULSI Applications in 1996, 1996, Boston, MA.

(55) Pitzer, K. S.; Gutowsky, H. S. *J. Am. Chem. Soc.* **1946**, *68*, 2204.

(56) Tsubouchi, K.; Masu, K.; Shigeeda, N.; Hiura, Y.; Mikoshiba, N.; Matsumoto, S.; Asaba, T.; Murai, T.; Kajikawa, T.; Proc. Symp. IEEE VLSI Technol., 1990, New York.

(57) Sugai, K.; VLSI Multilevel Interconnects Conference, 1993, San Jose, CA.

(58) Squire, D. W.; Dulcey, C. S.; Lin, M. C. *Chem. Phys. Lett.* **1985**, *116*, 525.

(59) Masel, R. I. *Principles of Adsorption and reaction on Solid Surfaces*; John Wiley & Sons, Inc.: New York, 1996.

(60) Francis, J. T.; Benson, S. W.; Tsotsis, T. T. *J. Phys. Chem.* **1991**, 4583.

(61) Carlsson, J. O.; Gorbatkin, S.; Lubben, D.; Greene, J. E. *J. Vac. Sci. Technol. B* **1991**, *9*, 2759.

(62) Wicks, C. E.; Block, F. E. Bureau of Mines, Washington DC,1963.

(63) Chen, J. G. *J. Am. Chem. Soc.* **1987**, *109*, 1726-1729.

(64) Jones, A. C.; Auld, J.; Rushworth, S. A.; Critchlow, G. W. *J. Cryst. Growth* **1994**, *135*, 285-289.

Chapter 5

Theoretical Studies of DMAH Growth Chemistry

5.1 Introduction

Rapid advances in the power and availability of computing resources have had a dramatic effect on theoretical condensed matter physics, and it is now possible to calculate many material properties from first principles.[1] In the area of theoretical surface science, investigations have focused on areas such as surface re-constructions,[2-5] chemisorption,[6-8] surface electronic structure and reactivity,[9-12] prediction of vibrational spectra,[13,14] and surface reaction pathways[15-17] for both semiconductor materials and metals. These investigations are often compared with experiment to simultaneously evaluate the theoretical tools and contribute to an understanding, but the methods also have potential for discovering new materials with unique properties.[18,19] One major advantage of these methods over experiments is the ability to specify atomic arrangements, thus breaking the problem into more manageable sizes. For example, decoding the reactivity of surface defects such as steps and vacancies may be more amenable to theoretical investigation than experiment. In addition, theoretical tools can provide quantitative estimates for surface related phenomena that are difficult to measure experimentally.

In the area of surface chemistry on metals, most work has focused on the catalytic properties of transition metals. Theoretical methods have been used to investigate chemisorption, surface reaction pathways, and reaction energetics on single crystal surfaces. Hydrogen chemisorption has been a favorite subject among investigators,

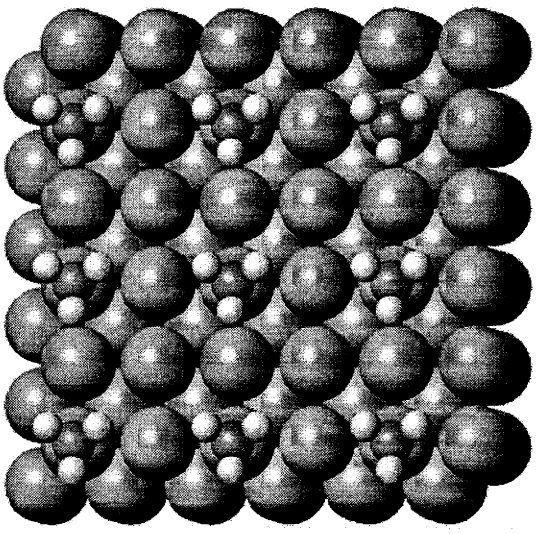

(a)

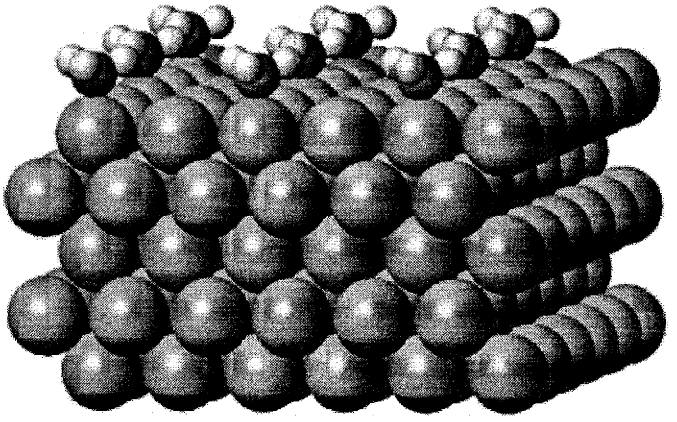

(b)

Figure 5.1 (a) Top-down view of a periodic slab with a 2x2 Al(100) cell and methyl adsorbed into "on-top" sites. (b) side view.

and studies include hydrogen chemisorption on Au,[20] Cu(100) and Cu(111),[21,22] Ru(0001),[23-25] Ni(111) and Ni(100).[26] Another system that has received much attention is carbon monoxide. Surfaces investigated include Rh and Pd,[27] Ni(111), Ni(110), and Ni(100),[28] Cu(100) and Cu(111),[29] and FeO(100).[30] More recently, investigations have

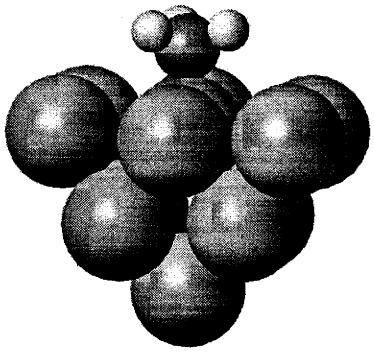

Figure 5.2 Illustration of a methyl group adsorbed in an on-top site on a 12 atom aluminum cluster.

explored larger adsorbates such as ethylene, acrolein, and acetate on Pd(111),[31] and methane chemisorption on Ni(111).[32]

Due to its relatively simple electronic structure and relevance to semiconductor manufacturing, aluminum has also been a system of interest for theoretical studies. Previous investigations have explored issues such as: surface electronic structure,[33] self-diffusion on Al(111) and Al(100),[34,35] vacancy formation energies,[36,37] adsorption near a step,[38] hydrogen dissociation on Al(110),[39,40] hydrogen induced faceting,[41] surface carbon on Al(111),[42] and oxygen covered Al(111).[43] Compared to the transition metals, however, there have been relatively few theoretical studies of reaction mechanisms on aluminum.

Central to the field of *ab initio* theoretical surface science is choosing a representation of a surface, which contains infinitely many atoms when viewed from the atomic scale. Although several methods have been devised, the two most popular among problem-oriented theoretical surface science groups are the cluster method and the slab method [cluster[15,31,44-47]; slab[20,22,32,39,40]]. Slab and cluster models are illustrated in Figures 5.1 a&b and Figure 5.2, respectively, for the calculation of CH_3 adsorbed in an on-top site of Al(100). The cluster method consists of a finite number or atoms (usually 10-50) which are arranged to represent a surface face where surface-adsorbate interactions can be studied. Slab calculations are similar to cluster calculations in that only a finite number of atoms are a central part of the calculation, however, in slab

calculations the finite cluster is repeated periodically (via boundary conditions/ Bloch's Theorem) in all directions to make an effectively infinite 2-D surface. Slab calculations create surfaces by including a vacuum region between slabs made of several metal layers. Therefore, the atomic periodicity is interrupted in the z direction, and a finite number of metal layers represents the surface. Only one slab is pictured in Figure 5.1, imagine an infinite number of layers above and below.

Each method, cluster or slab, has its advantages and disadvantages, and the choice between surface models may depend on factors such as the desired properties, level of accuracy, available computational resources, and the material being investigated.[46] The major advantages of the cluster method are attributed to its similarity to a molecular wave function problem. A cluster-adsorbate problem can be treated as a large or "super" molecule and studied using the same quantum chemistry techniques that are used in atomic and molecular problems. This is a significant advantage since molecular quantum chemistry software packages are efficient, robust, and commercially available. Molecular quantum chemistry software packages support high-level quantum chemistry methods (beyond density functional theory), and given sufficient computer resources, these advanced quantum chemistry methods can be used to calculate systematic improvements in accuracy. Even for density functional theory (DFT) calculations, cluster/molecular quantum chemistry codes offer advantages through efficient minimization techniques and transition-state searching algorithms.[48] Finally, cluster methods offer vibrational frequency calculations and thus extend calculations to include zero point energies and thermal energy corrections.

There are, however, several problems with cluster calculations, and these have mainly to due with the suitability of representing an infinite surface with a finite cluster of atoms.[46] Since the cluster wave function is constrained to occupy the space of the cluster and decay to zero outside, cluster calculations produce discrete energy levels rather than band structures, characteristic of real metals. The interaction of the discrete energy levels with adsorbates may not accurately describe actual surface-adsorbate interactions, and values of binding energies from cluster calculations have often been found to vary (sometimes dramatically) as the cluster size is varied.[49,50] As the cluster size is

increased, energy levels become narrower, and in the limit of an infinite cluster, bands form. Therefore, larger clusters may stabilize the energies at the cost of increased computation resources. Reports do seem to indicate that, at least for some systems, convergence with cluster size is reasonable.[31,49] Lastly, the advantages ascribed to higher level quantum chemistry methods and frequency calculations are currently limited to rather small clusters, so those benefits are somewhat eroded.

Cluster calculations have been used extensively to model reactions among the transition metals, where the narrow d-bands and local adsorbate-d band interactions may be well described by cluster methods. As with aluminum, however, transition metals have a energetically broad s-p band and these features are not captured with cluster methods. Ultimately, the success of cluster methods may depend on the relative strengths of the local and extended bonding interactions.

Slab calculations capture more physics of surfaces and bulk materials, and can reproduce the band structures of bulk metals or surfaces. Slab calculations do not suffer from the cluster size effects except that convergence may depend on the number of layers of metal chosen to represent the surface (slab thickness). Slab (or periodic density functional plane wave pseudopotential (PWPP)) calculations treat the core electrons as chemically inert, and replace the nuclei and core electrons with a pseudopotential.[51] Pseudopotentials allow valence wave functions to be expanded in plane waves, which are the natural choice (and computationally convenient) for a nearly free electron (NFE) metal such as aluminum. Depending on the strength of the pseudopotential and the solids departure from a NFE metal, more or less plane waves are needed for convergence of the valence wave functions. Localized states such as the narrow d-bands in transition metals can require large numbers of plane waves and deduct from the advantages of PWPP methods. However, the development of increasingly efficient pseudopotentials and advancements in computer hardware has begun to offset this disadvantage.[52-55]

PWPP calculations model a finite coverage on the surface via the periodic boundary conditions, which may be an advantage or disadvantage depending on the desired calculations. Large periodic cells may be necessary to avoid adsorbate-adsorbate interactions and slab-slab interactions (in the z-direction). Again, these come at a large

cost in computational efficiency. Slab calculations may be more appropriate than clusters for representing certain types of defects on a surface, such as steps and kinks. The last major issue with PWPP calculations is they are not currently as efficient or user-friendly as commercial molecular quantum chemistry software. Important additional features such as higher level calculations (beyond DFT), minimization or transition state searching algorithms, and vibrational frequency calculations are not yet available. Future investments in these codes will help bridge the gap between features and ease of use of PWPP methods compared to cluster calculations. (The origin of the differences between slab and cluster methods may be traced to the differences between the academic groups which developed the software: solid-state physicists rooted in DFT methods with investigations of extended structures, and quantum chemists concentrated on *ab initio* methods and molecular properties.)

The choice of slab vs. cluster method for the present investigations of aluminum surface chemistry was weighted by the free-electron nature of aluminum and an expectation that cluster calculations on reasonably sized clusters may be unreliable. In addition, although binding energies may be extracted from calculations on small clusters (with enough atoms to generate surface and sub-surface sites for the adsorption site of interest), reactions involving bond breaking of surface molecules would require prohibitively large clusters due to edge effects, which can be very strong. Slab methods have the advantage that there are no edge effects and molecules may be manipulated on a surface just large enough to avoid strong adsorbate-adsorbate interactions.

Although PWPP and cluster surface chemistry tools are powerful and applicable to a wide range of problems, the level of calculation involved is currently too large to develop reaction mechanisms from scratch. Therefore, for the present investigations of aluminum surface chemistry, the calculations have been employed to investigate the experimentally proposed surface reaction mechanism discussed in Chapter 4. Based on the theoretical calculations, a thermodynamic map of the DMAH growth reaction is constructed. The quantitative nature of the calculations provides detailed information about reaction energetics and allows inspection of the experimentally proposed reaction mechanism. In general, calculations can be used to refine a reaction mechanism by

eliminating reactions with large barriers, which fall outside the experimentally suggested window. The thermodynamic map is also useful for identifying rate limiting reaction steps. In addition, quantum chemistry calculations provide information about reaction energy barriers and aid estimation of rate constants for simulations of growth. Based on the experimental data and a quantitative understanding of elementary reaction steps, the theoretical calculations also provide clues to alternative reaction pathways. This feedback can be useful for further experimental investigations.

5.2 Theoretical Methods

A plane wave pseudopotential (PWPP) density functional theory code has been employed to investigate surface reactions in the chemical vapor deposition of aluminum with DMAH.[1,36,56-61] Calculations were used to locate preferred adsorbate surface sites, optimize adsorbate structures, and calculate binding energies, heats of reaction, activation energies, and surface diffusion barriers. Norm conserving[62] Bachlet-Hamman-Schlüter [63] and Troullier-Martins[52] type pseudopotentials were used for aluminum and carbon, respectively. Hydrogen was treated as a bare coulomb potential (no pseudopotential). The pseudopotentials were derived from all electron calculations using the local density approximation (LDA) as the exchange correlation functional.[64] The pseudopotentials are implemented in the Kleinman & Bylander separable form.[65] The Perdew-Wang Generalized Gradient Approximation (GGA) for exchange and correlation was applied self-consistently in the density functional theory calculations.[66-72] Optimized structures were minimized to less than 0.05 eV/Angstrom (usually 0.02 eV/A) using a molecular dynamics minimization algorithm.

The Schrödinger equation was solved using iterative methods to diagonalize the hamiltonian matrix.[1] Iterative methods are used since only a small number of eigenvalues and eigenvectors (occupied states) are important while the matrix is of order 10^6-10^8. A robust conjugate gradient algorithm[73] was adopted to initially converge the wave function, whereupon a damped density/residual minimization algorithm was utilized to further converge the wave function after each optimization step.[74] The PWPP code makes frequent use of Fast Fourier Transforms (FFT) to shuttle the charge density

between real and reciprocal space, and results can be dependent on the FFT grid used for the transform. Due to memory limitations and CPU efficiency issues, FFT grids were chosen to be the next available transform length allowed by the FFT algorithm. Larger grids were not investigated for their possible effects on the calculations. Charge density mixing was accomplished using the Pulay mixing algorithm.[60,75] A Monkhorst-Pack grid was used for k-space sampling with an NxNx1 mesh in the surface Brillouin zone.[76,77] Grids with up to 64 **k** points in the zone were used for CH_3 binding on Al(100), but the majority of the calculations used 16 and 4 **k** points in the 2-D Brillouin zone. The number of actual points in the irreducible zone was usually 3 or 4 with symmetry or 8 when no symmetry (except time-inversion symmetry) was present.

With an adsorbate on only one side of the slab, an electric field may develop due to differences in work functions between the two sides of the slab. The strength of the interaction depends on the proximity of the two surfaces which is determined by the size of the super-cell and the number of layers of vacuum between slabs. To offset this effect, a dipole is positioned between the slabs and allowed to self-consistently adjust to offset the electric field.[78]

Lastly, because of the continuous nature of the band structures of metals across the Fermi surface, difficulties are encountered locating the Fermi level of a metal (unlike semiconductors where there is a band gap, and it is clear which bands are occupied and unoccupied). A small change in the energy level of a band can abruptly change the band from occupied to unoccupied, and this causes convergence problems unless a very large number of **k** points are used. To avoid the need for large sets of **k** points, an electronic temperature (Fermi-Dirac distribution) is used to allow for partially filled electronic states. In this case it is a generalized free energy functional that is minimized, and the energy is obtained by extrapolation to 0 K.[79,80] Electronic temperatures of 0.05 to 0.1 eV were used.

Several different periodic cells were used for the calculations, including 3x2 and 2x2 Al(100) cells with three layers of metal and five layers of vacuum, and a 2x2 Al(100) cell with five layers of metal and five layers of vacuum. The larger 3x2 cell was used for large adsorbates [DMAH, TMA, $Al(CH_3)_2$,$AlH(CH_3)$], and the 2x2 cells were used for

the remaining calculations. For all calculations, the aluminum lattice constant was fixed at 3.96 Å, the local density functional theory approximation (LDA) minimum value.[81] According to the work of García et al, optimization of the lattice parameter within a GGA treatment of the valence electrons does not change the lattice parameter significantly.[82] For binding energy calculations, a 40 Rydberg plane wave cutoff was used. Some investigations of reaction barriers employed a lower cutoff of 30 Ry for an affordable estimate of reaction barriers, see figures for details in individual cases. Most calculations were concerned with the Al(100) surface since this surface was most thoroughly investigated experimentally. To allow some comparison, an investigation of CH_3 on Al(111) was included in the study. For convenience, the Al(111) cell was chosen to be rectangular of dimensions $\sqrt{2}\mathbf{a}$ x $\sqrt{(3/2)}\mathbf{a}$ rather than a hexagonal cell commensurate with the surface unit cell. Two different slabs of three and five layers each with five layers of vacuum were investigated.

As a reference for heats of reaction calculations (surface reactions), gas phase calculations were performed using the Gaussian 94 package of programs.[83] Calculations were done using the BPW91/6-31G(d,p) and G2 methods.[68,84,85] The BPW91 method was chosen because it is the closest available DFT functional to the GGA used in the PWPP calculations. The 6-31G(d,p) is a modest basis set which is sufficient for the aluminum compounds of interest. The G2 method is very different from both the GGA and BPW91 methods, and serves as a reference for the calculations. The G2 method is representative of the most accurate quantum chemistry methods available and is estimated to be accurate to ~ 2 kcal/mol.[85]

Transition state theory characterizes transition-states as optimized configurations with a single imaginary frequency (negative force constant) along the reaction coordinate separating reactants and products. In molecular calculations the existence of a transition state can be confirmed by calculating a vibrational spectra for the molecule. A transition state will have one imaginary frequency associated with motion along the reaction coordinate. In the present studies, transition states were identified as the point along the reaction coordinate where the forces vanish and a steepest descent on either side of the

Table 5.1 Selected geometrical parameters of gas phase aluminum molecules and molecule fragments computed with both the plane wave pseudopotential code and the Gaussian G94 package. Values are given in Angstroms and degrees. Plane wave calculations were performed with a cutoff energy of 40 Ry. G94 calculations use the BPW91 exchange correlation functional with a 6-31G(d,p) basis set.

	3 layer/ 4 kpts.	3 layer/ 16 kpts.	5 layer/ 4 kpts.	5 layer/ 16 kpts.	BPW91/ 6-31G(d,p)
$AlH(CH_3)_2$					
r (H-Al)		1.58			1.61
r (C-Al)		1.93			1.98
a (C-Al-C)		119.0			123.7
a (H-C-Al)		110.8 (4)			111.2 (4)
		114.4 (2)			113.8 (2)
$Al(CH_3)_3$					
r (C-Al)		1.93			1.98
a (H-C-Al)		110.8 to 113.7			111.1 (6)
					113.7 (3)
$Al(CH_3)_2$					
r (C-Al)	1.94				2.00
a (C-Al-C)	118.9				118.6
a (H-C-Al)	109.8 (4)				110.1 (4)
	114.2 (2)				113.5 (2)
$AlH(CH_3)$					
r (H-Al)	1.60				1.63
r (C-Al)	1.93				1.99
a (H-Al-C)	118.2				117.5
a (H-C-Al)	109.7 (2)				109.6 (2)
	114.5 (1)				114.0 (1)
AlH_2					
r (H-Al)				1.59	1.62
r (H-Al-H)				118.3	117.5
$Al(CH_3)$					
r (C-Al)	1.96	1.96	1.96	1.96	2.01
a (H-C-Al)	111.9	112.0	111.9	112.0	112.2
AlH					
r (H-Al)				1.65	1.69

[1]The BPW91 exchange-correlation functional is closely related to the GGA used in the plane wave code.

transition-state leads to the reactant or product. Although this approach may encounter difficulties for large, complex molecules, it is though to be reliable for small systems with few degrees of freedom, such as the current systems of interest.

5.3 Evaluation of Theoretical Methods

Before pursuing a quantum chemistry study of the surface reactions involved in DMAH growth, it is instructive to make some measure of the accuracy of the PWPP method for these types of calculations[xii]. The most obvious way to do this would be to compare quantum chemistry calculations with experimentally determined values, and this shall be done where possible in later sections. However, before moving to surface reactions a general comparison is made between the PWPP method and the more familiar Gaussian software package (G94), for gas phase reactions. Optimized structures of gas phase molecular fragments relevant to surface reactions are compared between the PWPP method and G94 calculations in Table 5.1. The table shows PWPP optimized structures for super-cells of 5.6x5.6x15.84 and 5.6x5.6x19.8 Å, with 4 and 16 **k** point sampling in the calculation. G94 optimizations were performed using the BPW91/6-31G(d,p) method.[68,84] As mentioned above, the BPW91 exchange-correlation functional is the closest available to the PW GGA used in the PWPP calculations, and the two functionals should give similar results. A 6-31G(d,p) basis set was used as it is a reasonable basis set size and gives good results for aluminum organometallic compounds. (See Chapter 2).

Because of the fair separation of molecules, (the closest approach is 3.3 Å for hydrogen atoms in TMA), there should not be a substantial effect of **k** point sampling in the gas phase calculations, and only one **k** point should suffice. This expectation can be evaluated from Table 5.1 for the fragment $AlCH_3$. As expected, there is essentially no difference for 4 or 16 **k** point sampling in the 2-D BZ. There is also no effect of **k** point sampling in the 3rd dimension, z direction (not shown). The $AlCH_3$ calculations also show the size of the cell in the z-direction has no significant influence on the optimized structures.

Compared with the G94 BPW91/6-31G(d,p) calculations, the PWPP structures have significantly shorter Al-C bond lengths. For DMAH and TMA, Al-C bond lengths

---

[xii] A general note to the reader unfamiliar with PWPP calculations: the NFE nature of Al makes a PWPP calculation natural for this metal, and convergence with plane wave cutoff is fast. Examples of plane wave cutoffs used for aluminum by others include 24 Ry.[82] However, due to the absence of carbon p core electrons, the carbon 2p electrons feel a strong pseudopotential (the 2s electrons are shielded by the 1s core). Hydrogen has no PP, and it also has a strong potential. Therefore, the main concerns with PWPP calculations on the DMAH system stem from carbon and hydrogen bonding arrangements.

are 1.93 and 1.98 Å for the PWPP and G94 methods, respectively. The differences are significant since quantum chemistry methods are generally accurate to 0.01 Å.[86] From previous studies and experiments (Chapter 2) it is clear that G94 values are reliable and the PWPP calculations must be in error. The Al-C bond length discrepancy is consistent for all Al-C bonds considered (DMAH, TMA, $Al(CH_3)_2$, and $AlH(CH_3)$. Given that BPW91 and PW GGA are similar it is reasonable to expect them to give similar results[xiii]. Errors could be related to molecule-molecule interactions between cells, perhaps compressing the bonds. However, the Al-C bond length appears insensitive to the super-cell size, (15.84 Å vs. 19.8 Å, with the C_2 axis of DMAH parallel to the z-axis), and the results do not support an inter-cell interaction. Insensitivity of the Al-C bond lengths for three different orientations in the cell (symmetry axis parallel to x, y, and z axes) also argues against molecule-molecule induced distortions. The plane wave cutoff could be responsible for the errors, but the general results of the studies detailed below suggest a 40 Ry cutoff is sufficient. Therefore, the Al-C bond error is ascribed to the particular choice of pseudopotential in this work. The pseudopotentials used for both aluminum and carbon were derived from all electron calculations using the LDA approximation for exchange-correlation, and this may be the origin of the errors. Further studies testing newer PP's derived with GGA core calculations may yield improved results.[54,82] PWPP values for the Al-H bond lengths are also short compared to G94 results and the results parallel those above for Al-C bonds. Since in this case hydrogen has no pseudopotential, the observed errors may be related to the Bachlet-Hamman-Schlüter[63] pseudopotential for aluminum.

Another difference noted in the table, the C-Al-C bond angle in DMAH, is also worth mention. Although there are no experimental results available for the DMAH monomer, the studies of Chapter 2 suggest the G94 predicted angle of 123.7° is large, and the PWPP results of 119.0° could be closer to the true value. The otherwise good

---

[xiii] In his paper Dr. Perdew refers to the BPW91 functional as slightly superior to the PW GGA, and recommends its use. Replacing the semi-local exchange component of the BPW91 functional with a local exchange functional (SPW91) results in shorter Al-C bonds (~1.94Å). But, given that the PW GGA does contain a gradient corrected exchange functional it still seems reasonable to expect similar optimized

agreement for C-Al-C and H-Al-C bond angles in $Al(CH_3)_2$, $AlH(CH_3)$, and AlH_2 supports the PWPP method for predicting bond angles.

Structural parameters for C-H bonding are well described by the PWPP method. Carbon-hydrogen bond angles and bond lengths (not shown) are in good agreement with G94 calculations. The good agreement for the C-H parameters further supports the argument against the plane wave cutoff being responsible for the short Al-C bonds. Additionally, the good results for CH geometries suggest the Troullier-Martins[52] type pseudopotentials may not be responsible for the short Al-C bond lengths.

Table 5.2 Gas phase reaction energies as a function of plane wave cutoff energy (no zero point energy or thermal corrections added). Calculations were performed in a rectangular 5.6 x 5.6 x 11.9 (Angstrom) cell at the **k**=0 point. Also shown are BPW91[1] and G2 reaction energies computed using the Gaussian G94 package. (Values in kcal/mol).

	40 Ry	50 Ry	60 Ry	BPW91/ 6-31G(d,p)	G2
$AlCH_3(g) \Rightarrow Al(g) + CH_3(g)$	70.7	70.7	70.7	68.4	73.7
$CH_3(g) \Rightarrow CH_2(g) + H(g)$	111.8	112.2	112.6	115.2	117.5

[1]The BPW91 exchange correlation functional is closely related to the GGA used in the PWPP calculations.

Additional evaluation of the PWPP method is accomplished by examining the gas phase reactions:

$$AlCH_3(g) \Rightarrow Al(g) + CH_3(g)$$

$$^2CH_3(g) \Rightarrow {}^3CH_2(g) + H(g)$$

These are representative of the bond dissociation reactions of interest in DMAH surface chemistry. Bond dissociation energies (uncorrected for zero point energies) are displayed in Table 5.2 for several plane wave cutoff values. The PWPP calculations are compared to G94 calculations with BPW91/6-31G(d,p) and G2 methods. Results for the $AlCH_3$ bond compare well with both G94 DFT and G2 methods, and the values appear to be

structures to BPW91. Unfortunately this hypothesis could not be confirmed due to the absence of the PW GGA functional from the G94 package.

converged at 40 Ry. Calculations of the C-H bond strength are in fair agreement with G94 BPW91/6-31G(d,p) calculations (~3-4 kcal) but the convergence is seen to be slow with increasing plane wave cutoff energy. The results suggest an accuracy of ~2-3 kcal for Al-CH_3 bonds and ~ 3-5 kcal for C-H bonds. These error bars should be kept in mind when considering calculations presented in the following sections.

5.4 Theoretical Studies of DMAH Surface Chemistry

5.4.1 Adsorbate Structures on Aluminum Surfaces

Adsorbates geometrical structures were studied on aluminum surfaces using both three and five layer slabs to represent the surface. Table 5.3 contains structural parameters for adsorbates on Al(100). The smaller adsorbates: AlH_2, $AlCH_3$, AlH, Al, CH_3, CH_2, and H were studied using a 2x2 cell with three and five layer metal slabs, and five layers of vacuum. The larger adsorbates: DMAH, TMA, $Al(CH_3)_2$, and $AlH(CH_3)$ were investigated in a 3x2 cell with three layers of metal and five layers of vacuum. The larger 3x2 cell was utilized to alleviate adsorbate-adsorbate interactions.

The results presented in Table 5.3 allow investigation of the influence of the number of metal layers and **k** point sampling on adsorbate geometries. Comparison of structures for $AlCH_3$ and CH_3 on three and five layer slabs suggest only minor differences for the two surface representations. The $AlCH_3$ surface bond is identical for the three and five layer slabs at 4 **k** points, but shows a small ~0.03Å difference for the 16 **k** point calculation. CH_3 bonding to the surface also shows only minor differences in bond distances, and angles differ by ~0.7° or less. The results suggest a three-layer slab is sufficient to determine adsorbate structures for these aluminum-carbon compounds on aluminum surfaces. Investigation of the effect of **k** point sampling seem to indicates that for these sized cells 4 **k** points is sufficient for geometry optimizations. The largest difference observed is a 0.06 bond difference for the $AlCH_3$-surface bond length and 1.4° for a surface-C-H bond angle.

Table 5.3 Selected values of surface adsorbate structural parameters (values in Angstroms). The number of layers of metal and the number of **k** points in the 2-D surface Brillouin zone are indicated in each column. A plane wave cutoff of 40 Ry was used in each calculation. A 2x2 Al(100) surface unit cell was used for all calculations except those involving $AlH(CH_3)_2$, $Al(CH_3)_3$, $Al(CH_3)_2$, and $AlH(CH_3)$ where a 3x2 Al(100) unit cell was used.

	3 layer/ 4 kpts.	3 layer/ 16 kpts.	5 layer/ 4 kpts.	5 layer/ 16 kpts.
$AlH(CH_3)_2$ (4 fold)				
r (Al-surface)	2.29			
r (H-Al)	1.74			
r (C-Al)	1.95			
a (C-Al-surface)	125.1			
	118.7			
a (H-Al-surface)	71.1			
a (C-Al-C)	114.0			
a (H-Al-C)	106.7			
	107.6			
$Al(CH_3)_3$ (4 fold)				
r (Al-surface)	3.22			
r (C-Al)	1.92			
a (C-Al-surface)	100.8			
a (C-Al-C)	111.3			
	112.9			
	131.5			
$Al(CH_3)_2$ (4 fold)				
r (Al-surface plane)	2.14	2.14		
r (C-Al)	1.95	1.95		
a (C-Al-C)	109.6	109.6		
a (H-C-Al)	116.8 (2)	116.7 (2)		
	108.1 (4)	108.1 (4)		
$AlH(CH_3)$ (4 fold)				
r (Al-surface plane)	2.08*	2.08		
r (H-Al)	1.59*	1.60		
r (C-Al)	1.93*	1.95		
a (H-Al-surface)	107.1*	114.9		
a (C-Al-surface)	137.4*	131.4		
a (H-Al-C)	115.5*	113.7		
a (H-C-Al)	113.0 (1)*	114.3 (1)		
	109.7 (2)*	109.0 (2)		
AlH_2 (4 fold)				
r (Al-surface plane)				1.99
r (H-Al)				1.59
r (H-Al-H)				116.6
r (H-Al-surface)				121.7
$Al(CH_3)$ (4 fold)				
r (Al-surface plane)	1.70	1.76	1.70	1.73
r (C-Al)	1.93	1.93	1.94	1.94

a (H-C-Al)	110.9	110.9	110.8	110.8
AlH (4 fold)				
r (Al-surface plane)				1.71
r (H-Al)				1.57
Al adatom (4 fold)				1.81
r (Al adatom-surface)				
CH_3				
top				
r (C-surface plane)		1.99	1.99	1.99
a (H-C-surface plane)		110.1 (2)	110.8 (2)	1.09.9 (2)
		111.4 (1)	111.3 (1)	110.7 (1)
bridge				
r (C-surface plane)		1.74	1.74	1.74
a (H-C-surface plane)		112.9	112.5 (2)	112.9 (2)
			114.3 (1)	112.8 (1)
4 fold				
r (C-surface plane)		2.04		2.03
a (H-C-surface plane)		110.7 (2)		110.1 – 110.7
		110.3 (1)		
CH_2 (bridge)[1]				
r (C-surface plane)				1.40
r (H-C)				1.10
a (H-C-surface)				125.1
H				
bridge				
r (H-surface plane)				1.06
top				
r (H-surface plane)				1.59
4 fold				
r (H-surface plane)				.74

*For this calculation, the Al atom was allowed to minimize in the x-y plane, and moved ~0.3 A away from the four-fold hollow towards the CH_3 ligand.
[1]Hydrogen atoms are in the plane perpendicular to the plane defined by the carbon atom and the two aluminum atoms that comprise the bridge site.

The calculations in Table 5.3 employ a rigid aluminum surface frozen to its bulk structure. Freezing the surface neglects surface relaxation of the clean slab, and adsorbate-induced surface reconstructions. On real surfaces these interactions may be important and could have significant effects on adsorbate geometries. Studies of surface relaxations and adsorbate-induced surface reconstructions would most likely require large slabs to correctly model a true surface. Such calculations are most likely not practical

except for those with large computing budgets and a special interest in adsorbate-induced surface reconstructions.

In the present studies, calculations involving molecular adsorbates containing aluminum atoms (DMAH, TMA, $Al(CH_3)_x$, and $AlH(CH_3)$) fix the aluminum atom in a four-fold site where it is allowed to vary in the z-direction only. Fixing the aluminum atom in a four fold site is reasonable for symmetric adsorbates, but the relaxation of the $AlH(CH_3)$ adsorbate (Table 5.3) shows that significant changes can occur for non-symmetric adsorbates, if they are unconstrained.

Compared to gas phase structures, adsorbed structures show a mix of some small and some significant changes. Aluminum-carbon and aluminum-hydrogen bond lengths are similar to gas phase values for TMA and the di-bonded structures $Al(CH_3)_2$, $AlH(CH_3)$, and AlH_2. The mono-substituted ligand structures, $AlCH_3$ and AlH, show a significant shortening of the Al-C and Al-H bonds, however. For example, the AlH bond goes from 1.65 Å in the gas phase to 1.57 Å when adsorbed. Bond angles also appear to be significantly changed upon adsorption. The C-Al-C angle in the $Al(CH_3)_2$ changes from near 120° in the gas phase to ~110° on the surface. Similar, though smaller, changes take place for H-Al-C and H-Al-H angles in $AlH(CH_3)$ and AlH_2. The adsorbate aluminum-surface bonds follow the expected trend from bond order arguments with values of 2.14, 2.08, 1.99, 1.73, 1.71 for the series $Al(CH_3)_2$, $AlH(CH_3)$, AlH_2, $AlCH_3$, and AlH, with hydrogen apparently more electronegative than methyl groups.[8,50]

CH_3 groups bind to an on-top site with a bond length similar to gas phase Al-C bonds (~1.98 Å). The bond length is increased to ~2.04 Å in the 4-fold site and the CH_3-bridge bond is considerable shorter at 1.74 Å. For CH_3 groups, bonding was also explored on the close packed Al(111) surface (Table 5.4). On Al(111) the results are again relatively insensitive to the number of metal layers, with bond differences ~ 0.01 Å and < 1.0° between three and five layer slabs. CH_3 bond lengths on Al(111) follow a different trend than on Al(100) with values of 2.03, 1.90, and 1.84 for top, bridge, and 3fold sites, respectively. The results reflect differences in the electronic structures of Al(100) and Al(111).[33]

Table 5.4 CH_3 adsorbate geometry on the Al(111) surface (values in Angstroms and degrees). Calculations were performed in rectangular $\sqrt{2}$**a** x $\sqrt{3/2}$**a** x 4**a** and $\sqrt{2}$**a** x $\sqrt{3/2}$**a** x 5**a** periodic cells with a plane wave cutoff of 40Ry and 16 **k** points in the surface Brillouin zone.

	3 layer	5 layer
CH_3		
top		
r (C-Al surface)	2.04	2.03
a (H-C-surface)	110.9 (2)	111.0 (2)
	111.6 (1)	111.2 (1)
bridge		
r (C-Al surface)	1.92	1.90
a (H-C-surface)	109.6 (2)	110.2 (2)
	116.7 (1)	116.1 (1)
3 fold		
r (C-Al surface)	1.84	1.84
a (H-C-surface)	111.9 (2)	112.5 (2)
	114.9 (1)	114.0 (1)

Adsorbed structures for the stable molecules TMA and DMAH were investigated in a 3x2 cell, but results suggest the cell is too small for accurate structural determinations. As can be seen in Table 5.3, TMA has only a weak interaction with the surface, and the TMA-surface bond is near 3.2 Å. The D_3 symmetry of the gas phase TMA is disrupted on the surface due to adsorbate-adsorbate interactions, and the C-Al-C angles are distorted to ~112.0° (2), and 132.0°. The super-cell gives only a ~ 2.0 Å minimum separation between TMA molecules, which is insufficient. Whereas TMA lies in a planar configuration with the D_3 axis perpendicular to the surface, DMAH adopts a different kind of adsorbate structure with a hydrogen bridge type bond. (Note, other possible TMA-surface adsorption configurations, such as bonding through the methyl groups, were not investigated.) The DMAH monomer pivots around the adsorbate aluminum atom in a four-fold site so that the hydrogen ligand forms a bridge-like bond to a surface atom (not to be confused with hydrogen bridge bonds in gas phase molecules). The remaining two methyl ligands rotate away from the surface into an adsorbed $*Al(CH_3)_2$ like structure. The overall picture of the adsorbed DMAH monomer can be likewise described as a distorted $Al(CH_3)_2$ adsorbate with a hydrogen bridge to the

surface at the base of the adsorbate. These changes are reflected in the shorter (DMAH) Al-surface bond which is near 2.3 Å, approaching the $Al(CH_3)_2$-surface bond (2.14 Å).

Despite problems with the super-cell calculations, several observations regarding DMAH and TMA molecule-surface interactions can be inferred. It is evident the distortions of the adsorbed DMAH monomer may give a stronger interaction with the surface than for TMA, even in the absence of adsorbate-adsorbate repulsion. Stronger binding of DMAH monomers is confirmed by binding energy calculations presented below. In addition, the ~101.0° TMA C-Al-surface bond indicates there is steric repulsion of methyl groups away from the surface. The methyl-surface repulsion may give rise to the large TMA-surface bond of ~3.2 Å. DMAH, on the other hand, relieves the methyl repulsion through distortions, which form the DMAH monomer hydrogen-surface bridge. Therefore, even considering adsorbate-adsorbate interactions, the calculations suggest DMAH monomers have a stronger interaction with the surface than TMA. Based on the above, it may be reasonable to expect the DMAH dimer to also have a stronger interaction with the aluminum surface. However, the strong binding of DMAH dimers and trimers in the gas phase (+35 kcal/mol) may still result in lower sticking probabilities for DMAH (dimers & trimers) compared to TMA.

5.4.2 Adsorbate Binding Energies on Aluminum Surfaces

PWPP calculations were used to calculate binding energies of adsorbates (Tables 5.5 and 5.6). As above, an Al(100) 2x2 super-cell was used for the mono-substituted fragments and AlH_2, and a larger Al(100) 3x2 super-cell was used for the remaining di-substituted fragments, DMAH, and TMA (monomers). Overlap between calculations on three and five layer slabs, and variations in **k** point sampling allow further understanding of these parameters. Unlike the case of adsorbate geometry optimization, bonding energetics show significant variations (> 5 kcal/mol) with both slab thickness and **k** point sampling. For $AlCH_3$ binding, the five layer slab leads to ~6-7 kcal stronger bonding than the three layer slab. Brillouin zone (BZ) sampling also seems to be important for $AlCH_3$-surface bonding. Both three and five layer slabs show differences > 10 kcal for the binding energies calculated with 4 and 16 **k** points. Results for CH_3 binding on

Al(100) also show a strong **k** point dependence, but a smaller dependence on the slab thickness, at least for the 16 **k** point calculation. There is less than 1 kcal difference between the three and five layer slab calculations at 16 **k**-points. A binding energy calculation of CH_3 with 64 **k** points suggests the values are sufficiently converged at 16 **k** points. In contrast to calculations on Al(100), CH_3 binding on Al(111) does show a notable effect of slab thickness (~4 kcal). Calculations of di-substituted fragments in the larger 3x2 cells show less of a **k** point dependence (~2 kcal) as would be expected. (Due to computing resource limitations, a 3x2 cell with 5 layers of metal could not be evaluated.)

Table 5.5 Surface Binding Energies (values in kcal/mol).

	3 layer/ 40Ry		5 layer/ 40Ry		
	4 kpts.	16 kpts.	4 kpts.	16 kpts.	64 kpts.
1. $AlH(CH_3)_2$	6.5	9.8			
2. $Al(CH_3)_3$	-4.6*, 1-2#				
3. $Al(CH_3)_2$	41.7	43.7			
4. $AlH(CH_3)$	45.2	47.0			
5. $Al(CH_3)$	50.2	60.4	56.2	67.4	
6. AlH_2				53.2	
7. AlH				71.5	
8. CH_3	34.1	39.3	45.1	38.9	39.4
9. CH_2				91.8	
10. Al				68.9	
11. H				53.2	

*Unbound. #A bound value is obtained when super-cell interactions are included in the gas phase calculation.

Unfortunately, there is a lack of experimental data to compare, but binding energies are consistent with other theoretical studies and the experiments of Chapter 4. A previous study of hydrogen on Al(100) predicted the bridge site as the minimum, and a bond distance of 1.06 Å[87], in good agreement with the results obtained here (1.06 Å). The previously reported binding energy of 53.0 kcal is also in good agreement with the present results (53.2 kcal). Note, the value given for the binding energy of Al in Table 5.5 refers to the binding of an aluminum adatom on a Al(100) terrace. The binding energy is ~ 10 kcal less than the heat of sublimation of aluminum (78kcal). Most of the

difference can be attributed to the isolation of the adatom since GGA PWPP calculations with an LDA core give values for the cohesive energy near ΔH_{sub} at 75.9 kcal/mol.[82]

Table 5.6 CH_3 binding energies on the Al(111) surface (values in kcal/mol). Calculations were performed in $\sqrt{2}$**a** x $\sqrt{3}/2$**a** x 4**a** and $\sqrt{2}$**a** x $\sqrt{3}/2$**a** x 5**a** periodic cells for the 3 and 5 layer slabs, respectively, with a plane wave cutoff of 40Ry, and 16 **k** points in the surface Brillouin zone.

	3 layer	5 layer
CH_3 (on top)	31.7	35.4

Binding energies for monomers of DMAH and TMA are also included in Table 5.5. DMAH is predicted to be bound by ~10 kcal/mol via the 16 **k** point (single point) calculation. In this case the **k** point dependence is larger than expected; there is a ~3.5 kcal/mol difference between the 4 and 16 **k** point calculations. Due to strong adsorbate interactions, TMA is predicted to be unbound with respect to the gas phase molecule. If the gas phase molecule is oriented with the C_3 symmetry axis parallel to the z axis, as on the surface (to induce the super-cell interactions), the adsorbate is bound by ~ 1-2 kcal/mol. Calculations were also performed for TMA adsorbed in a larger 3x3 Al(100) cell, but with a lower 30 Ry plane wave cutoff. The large 3x3 cell alleviates adsorbate-adsorbate interactions and the C-Al-C angles are close to 120°, with variance attributed to the surface rather than other adsorbates. These calculations predict a binding energy of ~ 1.1 kcal/mol. It is expected that identical calculations with a larger cutoff would give a slightly larger binding energy. Even considering a large periodic cell and adequate basis set, there are some questions regarding the accuracy of DFT methods for weakly bound complexes.[88] Incidentally, if the DMAH gas phase monomer is constrained to a planar adsorbed structure similar to TMA, the binding energy is reduced to ~1-2 kcal/mol. The binding energies confirm that DMAH interacts more strongly with the surface than TMA, but they also suggest the stronger interaction originates from the formation of the hydrogen bridge like structure, rather than from an electronic affinity for the DMAH monomer. This conclusion follows since the results suggest there would be only a small

difference in binding energies, given the same (constrained) planar geometry and no adsorbate-adsorbate repulsion. Because of the adsorbate interactions, it is not justified to compare the calculations with experiments. All molecules have some binding interaction with surfaces, but the magnitudes of the binding energies are unknown for DMAH and TMA monomers. Results of Chapter 4 are indicative of the DMAH and TMA dimers, and little can be inferred about monomer binding energies. It may, however, be expected that the lower molecular weight of the TMA monomer and its corresponding higher vapor pressure may result in a weak interaction with the surface, on the order of ~5 kcal/mol.

Table 5.7 Gas Phase Reference Data at 298.15K, 1 atm. (values in kcal/mol).

		ΔH (298.15K)	Method
1.	$AlH(CH_3)_2(g) \Rightarrow (CH_3)AlH(g) + CH_3(g)$	84.0	G2[1]
2.	$AlH(CH_3)_2(g) \Rightarrow Al(CH_3)_2(g) + H(g)$	86.8	"
3.	$Al(CH_3)_3(g) \Rightarrow Al(CH_3)_2(g) + CH_3(g)$	84.2	"
4.	$AlH(CH_3)(g) \Rightarrow AlH(g) + CH_3(g)$	43.7	"
5.	$AlH(CH_3)(g) \Rightarrow AlCH_3(g) + H(g)$	44.7	"
6.	$Al(CH_3)_2(g) \Rightarrow Al(CH_3)(g) + CH_3(g)$	41.8	"
7.	$AlH_2(g) \Rightarrow AlH(g) + H(g)$	46.8	"
8.	$Al(CH_3)(g) \Rightarrow Al(g) + CH_3(g)$	72.3	"
9.	$AlH(g) \Rightarrow Al(g) + H(g)$	73.2	"
10.	$2\ Al(CH_3)(g) \Rightarrow Al(CH_3)_2(g) + Al(g)$	30.5	"
11.	$Al(CH_3)_2(g) + AlCH_3(g) \Rightarrow Al(CH_3)_3(g) + Al(g)$	-11.9	"
12.	$2\ AlH(g) \Rightarrow AlH_2(g) + Al(g)$	26.4	"
13.	$AlH_2(g) + AlH(g) \Rightarrow AlH_3(g) + Al(g)$	-12.9	"
14.	$AlH_2(g) + H(g) \Rightarrow AlH_3(g)$	-86.1	"
15.	$CH_3(g) \Rightarrow CH_2(g) + H(g)$	109.6	Atkins[2]
16.	$CH_3(g) + H \Rightarrow CH_4(g)$	-104.8	"
17.	$2\ CH_3(g) \Rightarrow C_2H_6(g)$	-89.9	"
18.	$2\ H(g) \Rightarrow H_2(g)$	-104.2	"

[1]G2 method.
[2]Atkins, P.W. *Physical Chemistry*, 4th Ed., W.H. Freeman and Co., NY, 1990.

5.4.3 Reaction Energetics on Aluminum Surfaces

Based on the binding energies calculated with the PWPP method (Table 5.5) and high quality gas phase thermodynamic data (Table 5.7) a thermodynamic cycle was employed to calculate heats of reaction (Figure 5.3). The reaction energetics are

Table 5.8 Surface Reaction Thermodynamics (values in kcal/mol).

	ΔE (no ZPE)
Chemisorption	
$AlH(CH_3)_2(g) + * \Leftrightarrow Al(CH_3)_2* + H*$	-10.1
$AlH(CH_3)_2(g) + * \Leftrightarrow AlH(CH_3)* + CH_3*$	-2.5
$Al(CH_3)_3(g) + * \Leftrightarrow Al(CH_3)_2* + CH_3*$	1.1
Unimolecular Surface Reaction	
$AlH(CH_3)_2* + * \Leftrightarrow Al(CH_3)_2* + H*$	4.9[a]
$AlH(CH_3)_2* + * \Leftrightarrow AlH(CH_3)* + CH_3*$	12.5[a]
$Al(CH_3)_3* + * \Leftrightarrow Al(CH_3)_2* + CH_3*$	11.1[a]
$AlH_3* + * \Leftrightarrow AlH_2* + H*$	-
$AlH(CH_3)* + * \Leftrightarrow Al(CH_3)* + H*$	-28.9
$AlH(CH_3)* + * \Leftrightarrow AlH* + CH_3*$	-20.1
$Al(CH_3)_2* + * \Leftrightarrow Al(CH_3)* + CH_3*$	-21.3
$AlH_2* + * \Leftrightarrow AlH* + H*$	-24.7
$Al(CH_3)* + * \Leftrightarrow Al* + CH_3*$	31.4[b]
$AlH* + * \Leftrightarrow Al* + H*$	22.6[b]
Bimolecular Surface Reaction	
$Al(CH_3)_2* + Al(CH_3)* \Leftrightarrow Al(CH_3)_3(g) + Al*$	30.3
$AlH_2* + AlH* \Leftrightarrow AlH_3(g) + Al*$	42.8
$2\ Al(CH_3)* \Leftrightarrow Al(CH_3)_2* + Al*$	52.7
$2\ AlH* \Leftrightarrow AlH_2* + Al*$	47.3
Recombinative Desorption	
$AlH(CH_3)* + H* \Leftrightarrow AlH_2CH_3(g) + *$	-
$AlH_2* + CH_3* \Leftrightarrow AlH_2CH_3(g) + *$	-
$AlH_2* + H* \Leftrightarrow AlH_3(g)$	20.2
$2\ H* \Rightarrow H_2(g) + 2*$	2.1
$CH_3* + H* \Leftrightarrow CH_4(g) + 2*$	-12.2
$2\ CH_3* \Rightarrow C_2H_6(g) + 2*$	-11.0
Radical Ejection	
$Al(CH_3)_2* \Leftrightarrow Al(CH_3)_2(g) + *$	43.7
$AlH(CH_3)* \Leftrightarrow AlH(CH_3)(g) + *$	47.0
$AlH_2* \Leftrightarrow AlH_2(g) + *$	53.2
$Al(CH_3)* \Leftrightarrow Al(CH_3)(g) + *$	67.4
$AlH* \Leftrightarrow AlH(g) + *$	71.5
$CH_3* \Leftrightarrow CH_3(g) + *$	39.4
Impurity Mechanism	
$CH_3* + * \Rightarrow CH_2* + H*$	4.1
$CH_2* + * \Rightarrow CH* + H*$	-
$CH* + * \Rightarrow C* + H*$	-

[a]Estimated from binding energies of 10 and 15 kcal/mol for TMA and DMAH, respectively.

[b]These calculations assume the aluminum adatom is left standing in a terrace. Assuming Al*(bulk) and using the heat of sublimation (78kcal) would give approximately 10 kcal less endothermic values.

displayed in Table 5.8. In principal one could calculate reaction energetics directly with a large periodic cell rather than through a thermodynamic cycle. The super-cell would have to be large enough to separate products sufficiently, for negligible adsorbate-adsorbate interactions. However, using large cells would require a tradeoff in the number of plane waves, number of metal layers, and **k** point sampling, and may give inferior results. The binding energy calculations used in the thermodynamic cycle approach also correspond to a finite coverage (1/4 monolayer for the 2x2 cell and 1/6 monolayer for the 3x2 cell), but the coverage is low enough for reasonable separation of adsorbates.

Discussion of reaction energetics is facilitated by reference to the potential energy plot shown in Figure 5.4. Chemisorption of DMAH monomer to form dimethylaluminum and hydrogen surface fragments is exothermic by approximately 10 kcal/mol, whereas breaking the methyl bond to form *$AlH(CH_3)$ and a surface bound methyl group is less favorable by about 7.5 kcal/mol. Although the Al-H bond is stronger than the Al-C bond, adsorption of DMAH through the hydrogen bond is consistent with the known reactivity of dialkylaluminum compounds.[89] Considering that DMAH is bound by +17-20 kcal/mol per monomer in the gas phase as dimers and trimers, chemisorption is activated by at least +15 kcal/mol per dimer (the heat of reaction). The large chemisorption barrier may partially explain the complex sticking behavior of DMAH, and reinforces the argument for "special" or "defect" sites which "catalyze" dissociative adsorption. (See Chapter 4).

Decomposition of dimethylaluminum (DMAl) groups to monomethylaluminum (MMAl) and a surface methyl group is exothermic (ΔH~ -20 kcal/mol) due to the stability of surface MMAl groups. Breaking down $AlHCH_3$ into AlH and surface methyl groups or $AlCH_3$ and surface hydrogen are also exothermic. MMAl and monohydridealuminum (MHAl) fragments are strongly bound to the surface and further reactions to remove methyl or hydrogen groups are significantly endothermic. The stability of these surface adsorbates parallels gas phase chemistry where removal of the last CH_3 or H group from MMAl is significantly more endothermic than removing the previous ligand from DMAl.

Removing the last methyl group from MMAl is uphill by 20-30 kcal depending on the resting place of the resulting aluminum adatom. Calculating the heat of reaction by

applying the heat of sublimation for binding of the aluminum adatom gives a lower value near +20 kcal, whereas using the GGA value for Al adatom binding on an open Al(100) terrace (1/4 monolayer coverage) results in a higher value of near +30 kcal/mol. On an actual growing surface, MMAl groups may diffuse to step sites or vacancies where the heat of reaction is lowered due to the stronger binding of the aluminum adatom. Step sites and other defects could also influence the decomposition of MMAl groups by lowering activation barriers. The heat of reaction for transferring the hydrogen atom in MHAl to a surface bridge site is lower than the corresponding reaction for MMAl by close to 10 kcal due to stronger binding of H on Al(100).

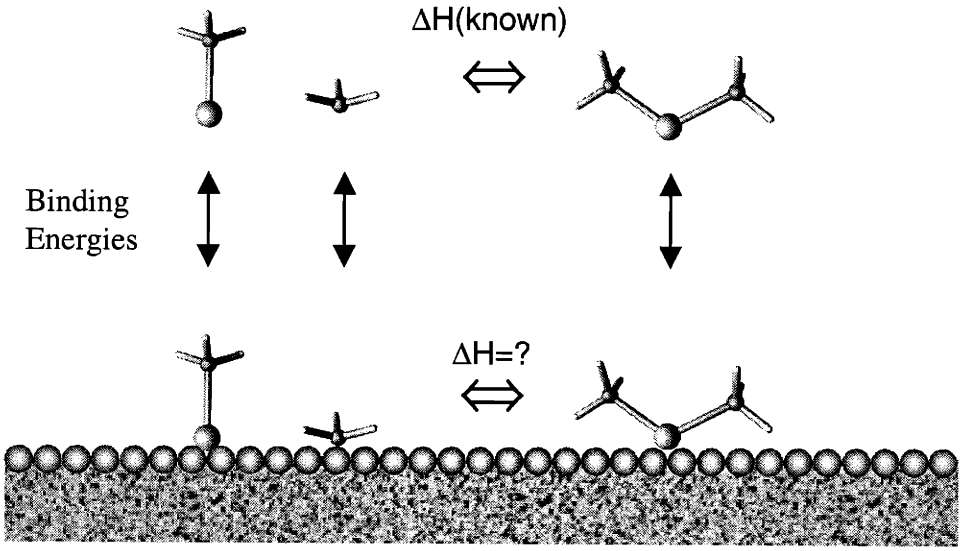

Figure 5.3 Thermodynamic cycle illustrates how binding energies and gas phase data can be used to calculate heats of reaction on surfaces.

Recombination reactions lead to the eventual desorption of the surface reaction products hydrogen and trimethylaluminum (TMA). Desorption of hydrogen is roughly thermoneutral at +2 kcal/mol and the same is true for TMA at ~ -1.1 kcal/mol. Hydrogen desorption is expected, however, to have a fairly large activation barrier, approximately +17.4 kcal on the Al(100) surface.[90] The near thermo-neutral heat of reaction and large desorption barrier for hydrogen are consistent with activated hydrogen adsorption on

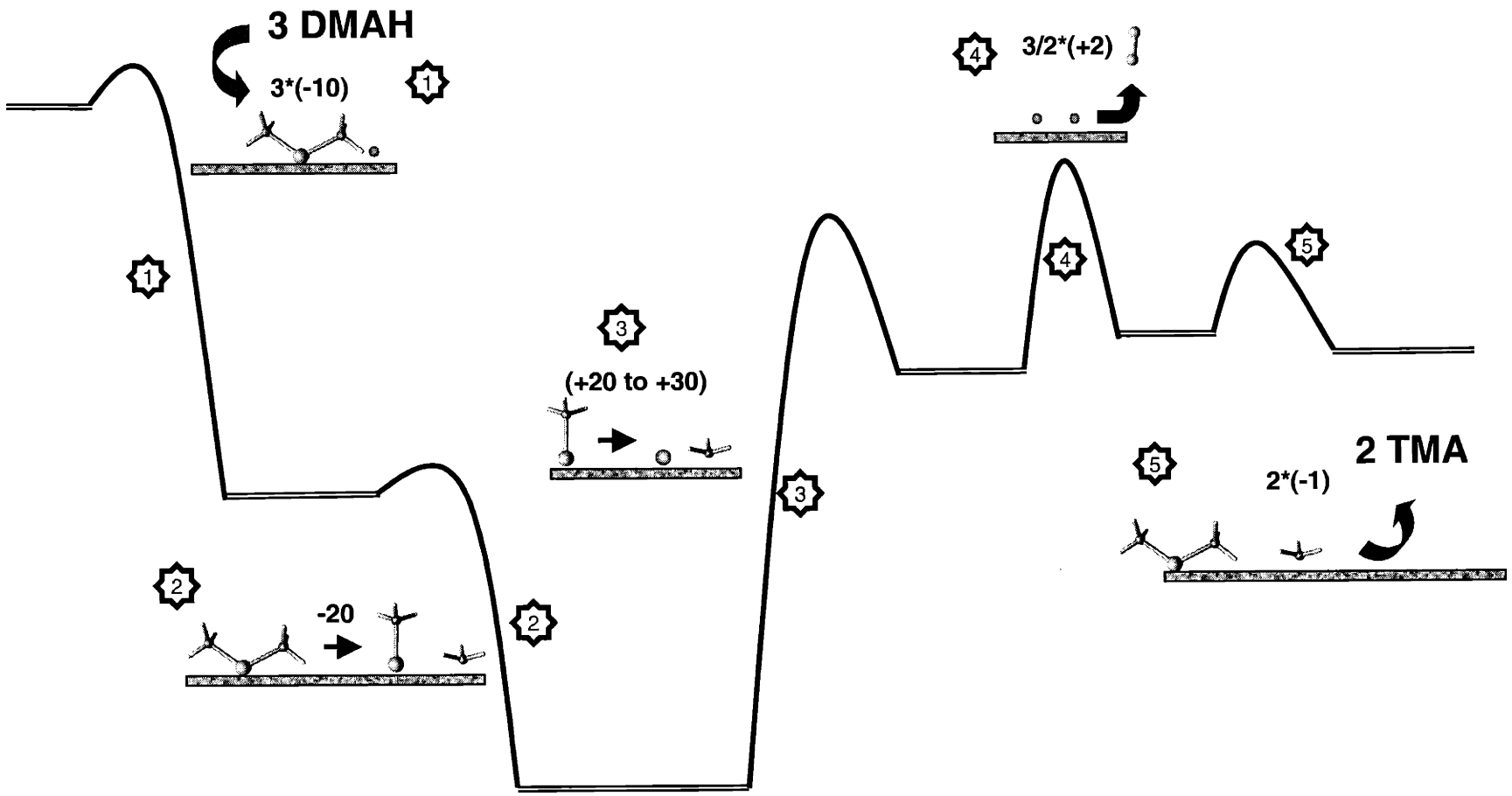

Figure 5.4 Thermodynamic map of the DMAH disproportionation mechanism: 3 DMAH (g) ⇒ 2 TMA(g) + Al(Bulk) + 3/2 H_2(g). Values are given in kcal/mol. Activation barriers in the potential energy plot are for illustration purposes only.

aluminum surfaces.[40,91] Given the near thermo-neutral recombination of DMAl and methyl groups to form TMA, it may be reasoned that if TMA monomer reaches the surface, there is at least a small adsorption barrier. The activation barrier follows since experimentally TMA chemisorption shows a complex (activated) behavior, and the heat of adsorption is near thermoneutral. An adsorption barrier implies a comparable recombination-desorption barrier.

Chemisorption of TMA dimer is expected to be activated by at least 10 kcal/mol per monomer, and that could explain the complex sticking behavior without requiring an activation barrier for surface TMA recombination (or adsorption). However, uncertainty as to the exact proportion of TMA dimers reaching the aluminum surface in UHV experiments complicates the matter (see Chapter 7, Recommendations for Future Studies). At high surface coverage, there is the possibility of forming TMA dimers on the surface, however, this seems unlikely given the low surface coverages encountered in DMAH growth. At high surface coverages, AlH_x bridging structures could also form and complicate matters further.[92]

In addition to the above chemistry, several other possible reaction steps were evaluated including: alternative bimolecular surface reactions, radical ejection reactions, and reactions parallel to those of DMAH, but involving alane. As can be seen in Table 5.8, bimolecular reactions involving DMAl and MMAl or two MMAl are unfavorable because of the strong binding of MMAl groups. The same is true for the parallel reactions of alane. Heats of reaction would be reduced if stronger binding of the aluminum ad-atom were used, however; so steps, vacancies, and other defects could alter the energetics to make these reactions more favorable. Radical ejection reactions are likewise not favorable at normal DMAH growth temperatures, but could become important for understanding high temperature/carbon contaminated growth. (See Chapter 4).

Alane reactions included in Table 5.8 parallel those of DMAH and TMA, but also compete with hydrogen desorption. While it is known that hydrogen has a complex chemistry on aluminum surfaces, and alane formation is possible, previous studies of hydrogen have involved atomic adsorption with hot filaments, which produce artificially

high coverages. Hot filaments are used since hydrogen does not adsorb molecularly on aluminum surfaces.[90,92,93] At low hydrogen surface coverage, molecular hydrogen desorption must dominate alane etching reactions. The relative unimportance of alane etching reactions at growth conditions is implied by the observation that alane adducts such as trimethylamine alane do, in fact, lead to growth (as does DMAH). However, for a detailed understanding of growth morphology, the hydrogen interactions could be very important since hydrogen has the ability to re-construct aluminum surfaces.[41]

Concurrent to the surface reactions discussed above, the aluminum surface is growing and evolving. Reactions listed in Table 5.8 are only a starting point for understanding DMAH growth and applying theoretical surface chemistry methods. On a true growing surface, reactions occur at a myriad of different sites and configurations, and a full treatment of the surface chemistry requires a better understanding of the growing surface. A simplified simulation of DMAH growth is explored in the next chapter (Chapter 6, Simulations of DMAH Growth).

Table 5.9 $AlCH_3$ surface diffusion barriers (values in kcal/mol). Barriers are given with respect to the lowest energy site.

	3 layer Al(100) 30 Ry/ 16 kpts.
$AlCH_3$	
4 fold	0.0
bridge	16.7
top	31.6

5.4.4 Surface Diffusion

One important aspect of surface reactions is the mobility of adsorbed ligands. The mobility of adsorbates may be important for understanding reaction rates and where reactions occur on the surface. As discussed above for heats of reaction calculations, the surface structure around the reacting adsorbate can influence the thermodynamics and kinetics of a reaction. A full surface reaction model therefore requires information about

diffusion rates of adsorbates in order to follow the configuration dependence of the surface chemistry.

Diffusion barriers for MMAl, CH_3, CH_2, and hydrogen are shown in Tables 5.9-5.13, respectively. Diffusion of hydrogen is facile on aluminum surfaces as would be expected, but the mobility of the molecular fragments MMAl, DMAl, CH_2, and others, is less intuitive. As discussed earlier, reactions involving the decomposition of MMAl and MHAl could occur preferentially at surface defect sites, and therefore, their mobility is important. The results shown in Table 5.9 suggest that MMAl adsorbates (and likely DMAl as well) have diffusion barriers on the order of 15-20 kcal. These parameters would be of value for surface growth simulations employing techniques such as kinetic Monte Carlo methods.

Table 5.10 Surface Diffusion Barriers of CH_3 on Al(100) (values in kcal/mol). Barriers are given with respect to the lowest energy site.

	3 layer Al(100)/ 40 Ry		5 layer Al(100)			
	4 kpts.	16 kpts.	40 Ry/ 4 kpts.	40 Ry/ 16 kpts.	40 Ry/ 64 kpts.	50 Ry/ 4 kpts.
CH_3						
top	0.0	0.0	0.0	0.0	0.0	0.0
bridge	7.8	8.7	10.0	8.3	8.8	8.4
4fold	-	31.9	-	31.0	-	-

The most important surface mobility is the diffusion of methyl groups because rapid methyl diffusion is crucial to the proposed disproportionation growth mechanism for DMAH. Calculations show that methyl diffusion occurs on the Al(100) surface through motion along rows of atoms with a barrier near +9-10 kcal/mol. As show in Table 5.10, the calculations appear well converged for both **k** point sampling (up to 64 **k** points) and plane wave energy cutoff (up to 50 Ry). Diffusion across 4-fold sites is much less favorable with a barrier > +30 kcal. Diffusion barriers are low enough that methyl diffusion should indeed be rapid at growth temperatures.

Table 5.11 Hydrogen surface diffusion barriers on Al(100) (values in kcal/mol). Barriers are given with respect to the lowest energy site.

	3 layer Al(100)/ 40 Ry/ 16 kpts.	5 layer Al(100)/ 40 Ry 16 kpts.
Hydrogen		
bridge	0.0	0.0
top	6.2	7.1
4 fold	12.9	9.2

Table 5.12 CH_2 surface diffusion barriers on Al(100) (values in kcal/mol). Barriers are given with respect to the lowest energy site.

	3 layer Al(100)/ 30 Ry/ 4 kpts.
CH_2	
bridge	0.0
4 fold	22.3
top	28.6

Methyl diffusion on Al(111) (Table 5.10) shows a somewhat different behavior than Al(100), with larger barriers but a flatter PES. On Al(111) methyl groups diffuse from favored on-top sites across bridge and 3-fold sites with approximately equal barriers around +14 kcal, approximately +5 kcal larger than on Al(100). While the barriers are still low enough for facile methyl diffusion at growth temperatures, the calculations suggest growth may have a different temperature dependence for different crystal planes, and this may be important for surface morphology simulations. Unfortunately, the experiments of Chapter 4 were unable to observe such a shift in the kinetics due to experimental difficulties in obtaining sufficient surface coverages on Al(111). (See Chapter 4).

Table 5.13 CH_3 Diffusion Barriers on Al(111) (values in kcal/mol). Calculations were performed in $\sqrt{2}$**a** x $\sqrt{3}/2$**a** x 4**a** and $\sqrt{2}$**a** x $\sqrt{3}/2$**a** x 5**a** periodic cells for three and five layer slabs, respectively, with a plane wave cutoff of 40Ry and 16 **k** points in the surface Brillouin zone. Barriers are given with respect to the lowest energy site.

	3 layer	5 layer
CH_3		
top	0.0	0.0
bridge	14.6	13.7
3 fold	13.8	14.3

5.5 Surface Reaction Kinetics

Thermodynamic calculations are invaluable for understanding which reactions are most likely and judging the merit of a proposed reaction mechanism. Heats of reaction may eliminate pathways with prohibitively high barriers and identify possible rate limiting steps.[94] In addition, thermodynamic calculations allow a quantitative basis for predictions of equilibrium constants, and thus establish a link between forward and reverse rate constants. To obtain estimates for rate constants, however, it is necessary to have some information about activation barriers. Including information about the entropy of activation along with the activation barriers allows transition state theory to be applied

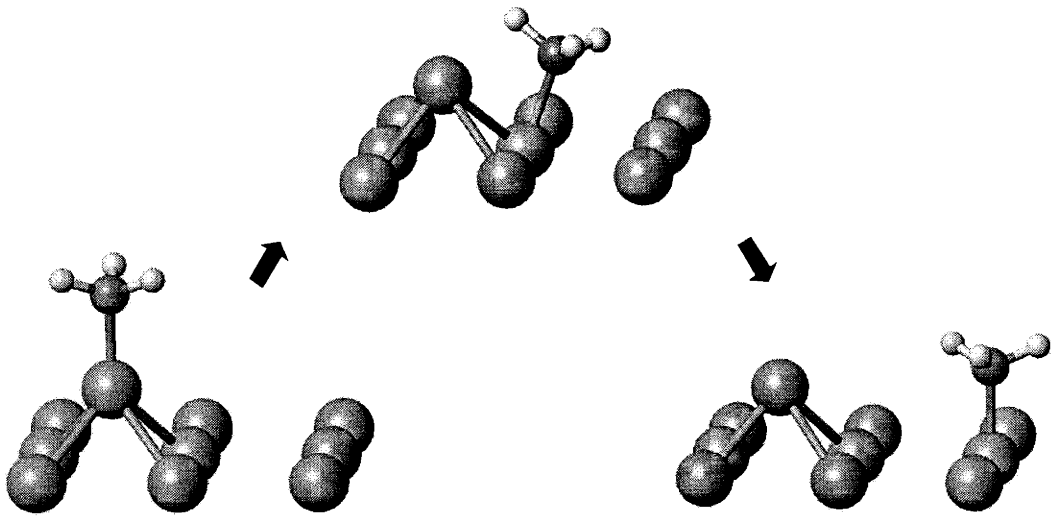

Figure 5.5 Illustration of surface reaction path for $*AlCH_3 \Rightarrow *Al + *CH_3$.

to estimate rate constants. In the near future, calculation of partition functions for surface reactants, products, and transition states will become routine, thus allowing TST to be fully utilized and even improved upon with variational TST and other variants.[95,96] At this time, however, such calculations are not practical for slab calculations, and efforts have been focussed on locating transition states and obtaining estimates for activation barriers. Pre-exponential factors can be estimated from micro-kinetic theory and group contribution methods.[97,98] Pre-exponential factors could also be estimated from experimental data for similar reaction mechanisms on different surfaces.

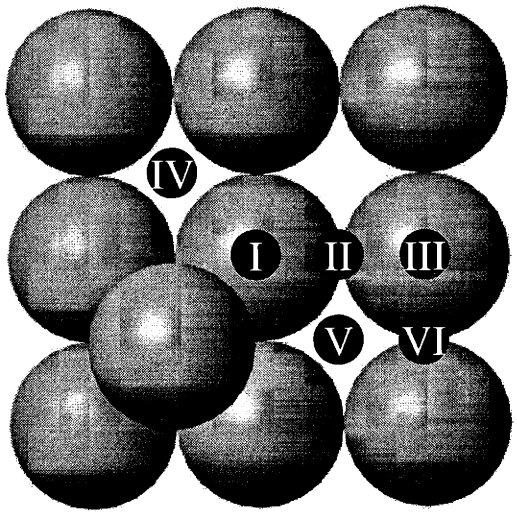

Figure 5.6 Site labels for reaction pathways on Al(100).

Based on calculations listed in Table 5.8, the decomposition of MMAl and MHAl groups would appear to be rate limiting in the growth mechanism (kinetic regime). Therefore, it is worthwhile to explore the kinetics of these processes. Binding energy calculations reveal that MMAl and MHAl groups are bound in 4-fold symmetry sites while the products CH_3 or H are bound on-top and bridge sites, respectively. The product aluminum ad-atom remains bound in the 4-fold site. The reaction path considered for both MMAl and MHAl is illustrated in Figure 5.5, for the case of methyl transfer. The reaction is assumed to occur by transfer of a CH_3 or H ligand off the aluminum adatom

along the top of a surface atom and then along a surface bridge site into a neighboring on-top site for CH_3, or stopping at the bridge site in the case of hydrogen. From Table 5.8, heats of reaction for these steps are +31.4 and +22.6 kcal/mol for MMAl and MHAl, respectively. Given the strong aversion of methyl groups from 4-fold sites (see Table 5.10), transfer along the top of a surface atom is most likely the favored reaction path ("on-top"-I-II-III in Figure 5.6). In the case of hydrogen, the three layer slab calculations (Table 5.11) also suggest transfer across the top of a surface atom is preferred over a path through 4-fold sites. However, the five layer slab calculations indicate a smaller difference between binding energies of hydrogen in on-top and 4-fold sites. Transition state searches were performed on the three-layer slab, however, so for this surface model a path across a surface atom would most likely be preferred. Both reaction pathways may be available to MHAl.

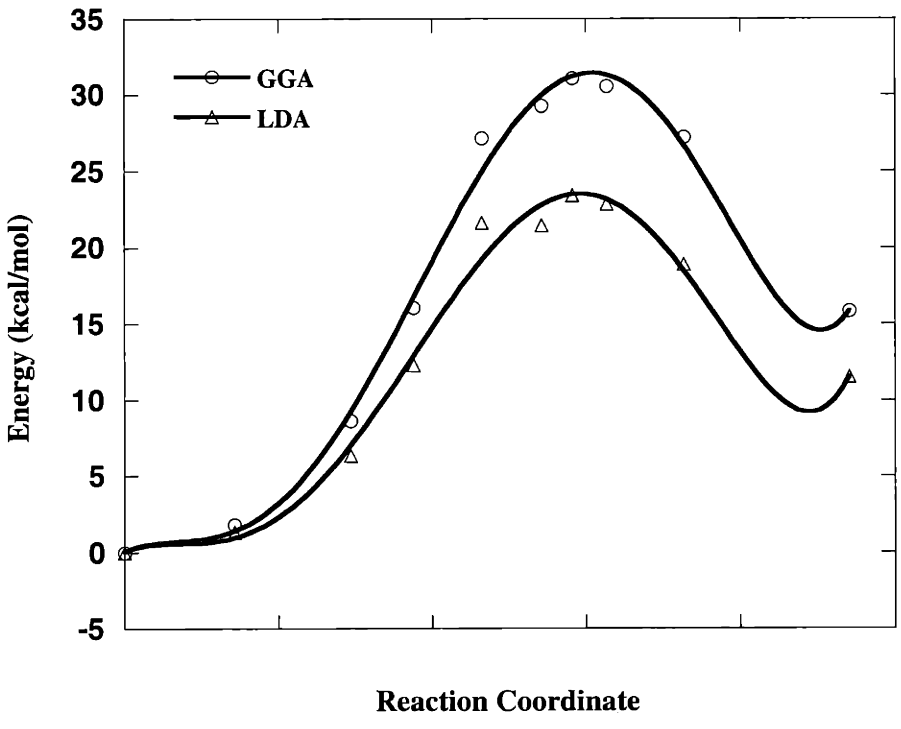

Figure 5.7 Potential Energy vs. Reaction Coordinate for the surface reaction $*AlCH_3 \Rightarrow *Al + *CH_3$. The reaction path is illustrated in Figure 5.5.

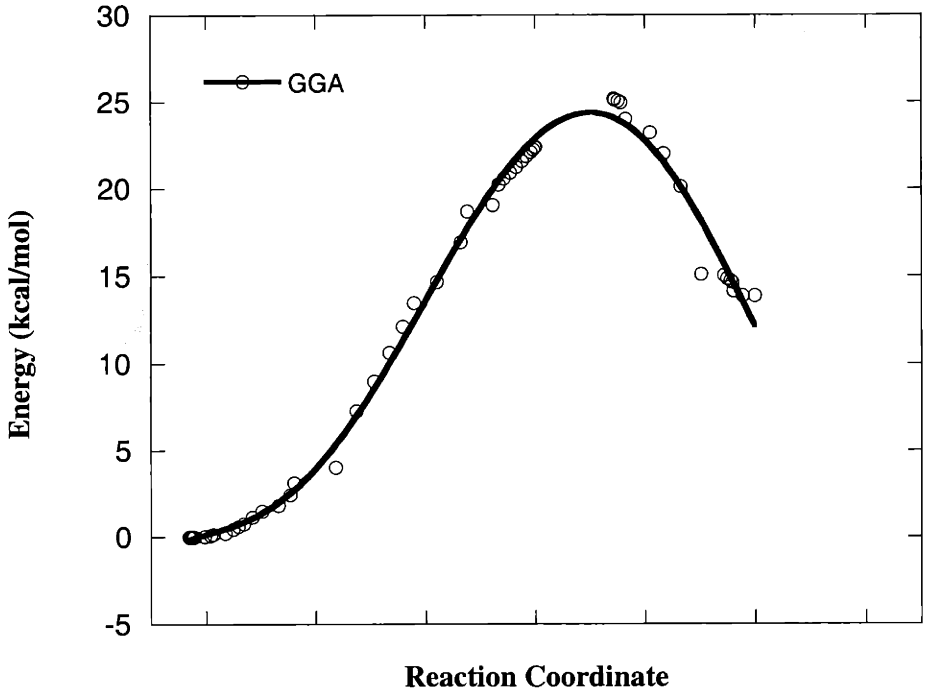

Figure 5.8 Potential Energy vs. Reaction Coordinate for the surface reaction *AlH ⇒ *Al + *H. The reaction path is similar to that of $AlCH_3$ indicated in Figure 5.5.

Plots of the potential energy surface (PES) along the reaction coordinate for MMAl and MHAl transfer reactions are shown in Figure 5.7 and 5.8, respectively. Note that heats of reaction from the PES plot are different from those listed in Table 5.8. The differences arise from several factors including a different super-cell, lower plane wave cutoff, less **k** points, and, most importantly, adsorbate-adsorbate interactions. Potential energies for the forward part of the reaction are expected to be more reliable than heats of reaction, since the forward interaction is predominantly Al-CH_3 bond breaking and more localized than the adsorbate-substrate interaction of the products, CH_3 and aluminum adatom. In addition, the adsorbate-adsorbate interactions should be less important for the transition-state since these configurations are fairly well separated from other super-cells. The activation barriers are calculated to be approximately +25 and > +30 kcal for the MHAl and MMAl reactions, respectively. The barriers occur late in the reaction path where the transferring ligand is atop a surface atom neighboring the aluminum adatom.

The late barrier is consistent with the reactions being endothermic. The activation barriers should be considered upper bounds within the surface model, since in the calculations the aluminum adatom was permitted to optimize its position in the z-direction, but frozen in the x-y directions. In a true transition state the aluminum adatom would participate to a greater extent in the reaction. Additionally, a dynamic surface would be expected to adjust locally to lower the barrier. Lastly, steps, kinks, vacancies, and other surface defects could also lower activation barriers. This is especially true if MMAl and MHAl groups diffuse freely to these defects. Given that MMAl and MHAl groups are strongly bound surface intermediates, these encounters seem likely.

The other principal reactions involved in the disproportionation mechanism are decomposition and recombination reactions involving DMAl and the parallel reactions of dihydridealuminum (DHAl), for the alane system. Accurate studies of the recombination of DMAl and methyl groups to form the product TMA would require a prohibitively large unit cell, but unimolecular decomposition reactions of DMAl and DHAl were investigated. The $Al(CH_3)_2$ and AlH_2 groups are assumed to bind in 4-fold sites, and the expected reaction path transfers a methyl or hydrogen ligand into a neighboring on-top or bridge site, for methyl and hydrogen, respectively. The reaction path is assumed to steer over the top of a surface atom, analogous to the mechanism for the mono-substituted ligands (I-II-III, Figure 5.6). Methyl transfer along the proposed reaction pathway is again reasonable due to the large aversion of methyl groups for the 4-fold site. In the case of the dihydride (and also most likely for the $AlH(CH_3)$ moiety) pathways along the top of a surface atom and through a 4-fold site may coexist.

Figure 5.9 shows a potential energy plot along the reaction coordinate for the surface reaction $*AlH_2 \Rightarrow *AlH + *H$. Calculations predict this reaction to be exothermic with a heat of reaction near -25 kcal/mol (Table 5.8). The reaction proceeds without significant barrier, and the reaction product is an *AlH group with a hydrogen atom at the base of the monohydride-aluminum adsorbate (product). Although not clear from the figure, there must be at least a small barrier to reaction, since the reactant ($*AlH_2$) was optimized to a minimum. Diffusion away from the base of the *AlH encounters a barrier for travel over adjacent surface atoms. The barrier is expected to be

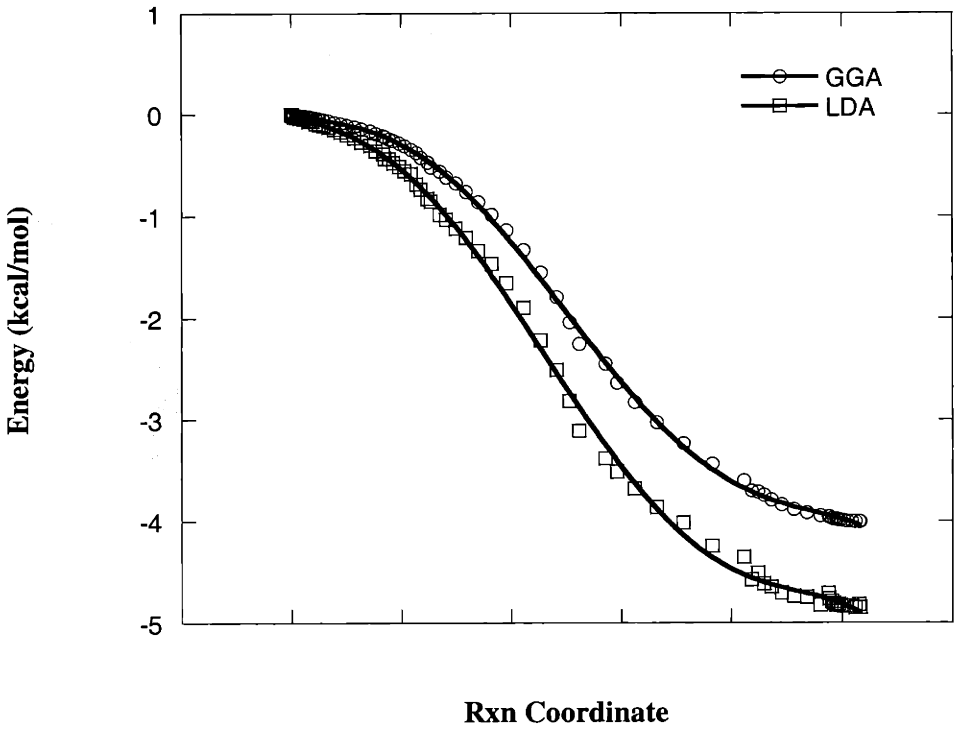

Figure 5.9 Potential Energy vs. Reaction Coordinate for the surface reaction $*AlH_2 \Rightarrow *AlH + *H$. The reaction coordinate is defined as $\sum_{hydrogens}\sqrt{\left(\Delta X^2 + \Delta Y^2\right)}$. Calculations were carried out with a 40 Ry plane wave cut-off, and 4 **k** points in the surface Brillouin zone.

similar to surface diffusion barriers (Table 5.11). For the detached product (hydrogen) in surface sites II and VI (Figure 5.6) heats of reaction are –6.4 and –9.0 kcal/mol, respectively. The discrepancies between these values and the heat of reaction (-25) are due to differences in the surface model and calculation parameters.

A caveat to the above calculations is that results were found to be dependent on properties of the surface model. Calculations restricted to only one **k** point in the BZ (**k**=0), gave qualitatively different results, which could be misinterpreted. With only the **k**=0 point, the reactant (AlH_2) was found to be unstable with hydrogen atoms aligned along the diagonal of the Al(100) surface lattice, and the reactant spontaneously minimized to a four fold site (IV,V). In fact, calculations found there was no barrier to hydrogen transfer when the path navigated around the base of the *AlH adsorbate, into a

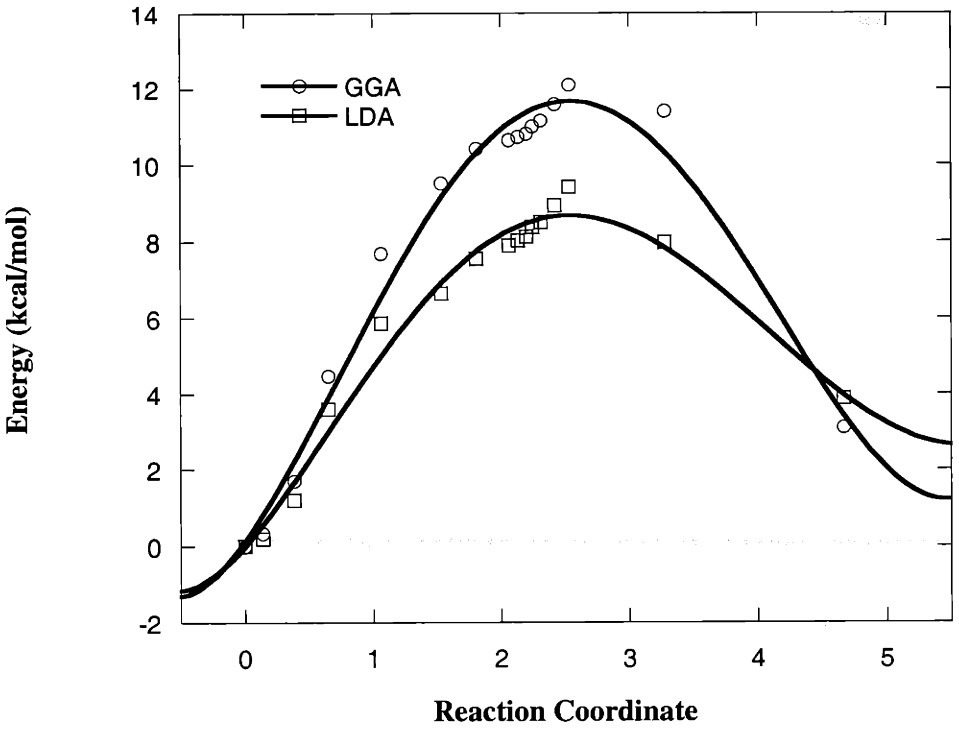

Figure 5.10 Potential Energy vs. Reaction Coordinate for the surface reaction $*AlC_2H_6 \Rightarrow *AlCH_3 + *CH_3$. The reaction coordinate is defined as $\sum_{\substack{carbon \\ atoms}} \sqrt{(\Delta X^2 + \Delta Y^2)}$.

Calculations were carried out with a 30 Ry plane wave cut-off and 4 **k** points in the surface Brillouin zone.

four-fold site and on to the opposite bridge site (V-VI). When aligned with hydrogen ligands parallel to rows of surface atoms, there must be at least a small barrier to hydrogen transfer through a 4-fold site, since a stable minimum was found in the row-parallel configuration. Other features of the **k**=0 calculation were consistent with the results in Figure 5.9, however. Both calculations predict a barrier for hydrogen motion over the surface atom into a bridge site, and both calculations find that adsorbate interactions cause the bridge VI site to be several kcal/mol more stable than site II.

In summary, at low coverage, and without strong adsorbate-adsorbate interactions, the AlH_2 transfer reaction should proceed without a significant barrier. The reaction pathway may involve motion either over the top of a surface atom with a small barrier, or in a path around the base of the adatom, through a 4-fold site, and into a bridge position.

The AlH_2 surface reaction illustrates the richness of aluminum-hydrogen chemistry, and the observed behavior is consistent with other studies that show hydrogen has many ways to interact with an aluminum surface.[81] These pathways of AlH_2 decomposition are also consistent with previous theoretical studies of hydrogen faceting on aluminum surfaces.[41]

Quantitative investigations of the unimolecular decomposition of $Al(CH_3)_2$ are shown in Figure 5.10. The reaction is also predicted to be exothermic, with a heat of reaction near –20 kcal/mol. Because of the size of the molecule fragment, only selected points along the expected reaction path were explored. Calculations were employed to explore methyl transfer across the surface atoms (I) and through the bridge site (II) to an adjacent "on top" site (III). Along the reaction coordinate, the second methyl ligand rotates atop the aluminum adatom to form the other reaction product, a MMAl fragment. The reaction path is predicted to have an activation barrier near 10-12 kcal/mol. The transition state is located near the bridge site (II) where the forces change sign from being attractive towards the adatom to the "on top" site. Due to the strong adsorbate-adsorbate interactions, the heat of reaction (~-20 kcal/mol) is not obtained from these calculations. The reaction barrier is thought to still be (at least semi-quantitatively) valid, however, since super-cells are fairly well separated at the transition-state, and a majority of the adsorbate repulsion is due to the MMAl fragment.

In analogy with the AlH_2 and $Al(CH_3)_2$ systems, and considering heats of reaction, $AlH(CH_3)$ would also be expected to have a low decomposition barrier. Hydrogen from $AlH(CH_3)$ should have the same pathways available to AlH_2, and the methyl groups may be expected to follow the reaction coordinate over the top of a surface atom and into a neighboring on-top site. Methyl chemistry on Al(100) is similar to hydrogen chemistry, but seems to be somewhat simpler due to steric constraints and a unfavorable interaction with 4-fold sites. Note that on Al(111), however, electronic structure calculations suggest an equivalence of bridge and 3-fold sites so that additional reaction pathways for MMAl and DMAl fragments may be present on that surface.

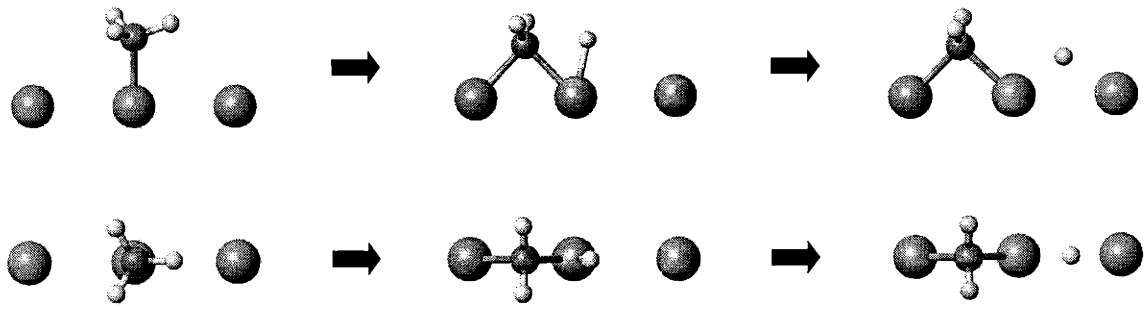

Figure 5.11 Illustration of the surface reaction pathway in methyl dehydrogenation, $*CH_3 \Rightarrow *CH_2 + *H$.

5.6 *Alternative Reaction Pathways*

Unimolecular decomposition and bimolecular recombination reactions involving mono and di substituted aluminum surface fragments characterize the disproportionation mechanism of growth. Other reactions of interest include the experimentally observed methyl dehydrogenation and methyl radial ejection. Methane formation, though not experimentally observed, is another reaction path of interest. Other reactions such as methyl or methylene coupling are also conceivable, but not considered here.

Methyl dehydrogenation on aluminum is important for predicting levels of carbon contamination as the process temperature is raised to promote faster growth. In addition, methyl dehydrogenation represents a simple first order reaction where the theoretical calculations can be compared directly with experimental data. An illustration of the reaction path, including reactant, transition state, and product, is illustrated in Figure 5.11. The geometry of the optimized transition-state is illustrated in Figure 5.12. The bond breaking reaction proceeds across the top of a surface atom as an on-top methyl group shifts into a bridge position and the carbon-hydrogen bond stretches over the surface atom. Reaction products are CH_2 and hydrogen bound in neighboring bridge sites. With products adequately separated, the heat of reaction is approximately +4 kcal/mol.

Figure 5.13 presents a plot of the potential energy surface (PES) along the reaction coordinate for the methyl dehydrogenation reaction. The activation barrier is predicted to

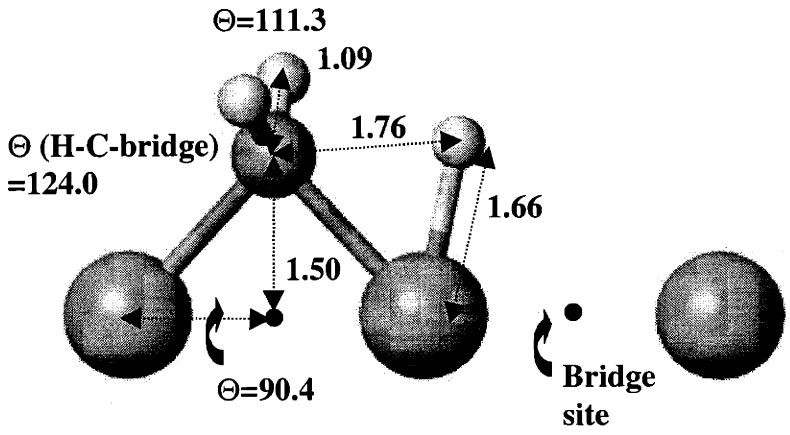

Figure 5.12 Structural parameters of the transition state for methyl dehydrogenation, $*CH_3 \Rightarrow *CH_2 + *H$.

be +36.8 kcal/mol, with a surface model of an Al(100) 2x2 cell on a 5 layer slab. The activation barrier is in good agreement with the experimental estimate of ~40 kcal/mol (Chapter 4). It should be noted that agreement between experiment and calculation could be better or worse depending on a lower or higher choice of the pre-exponential factor (the compensation effect). Nevertheless, the results are encouraging and suggest that surface theoretical calculations on systems such as this are accurate to within a approximately 5 kcal/mol.

As discussed in Chapter 4, high temperature growth with DMAH or TMA results in a surface stoichiometry near Al_4C_3. The observed Al/C ratio requires a second reaction involving surface methyl groups with an activation barrier similar to the dehydrogenation step. The most likely candidate is radical ejection, and temperature programmed desorption (TPD) experiments (Chapter 4) indicate a radical ejection barrier near +41 kcal/mol. The radical ejection pathway provides another useful measure of the accuracy for the present electronic structure calculations. The calculations predict a methyl radical ejection barrier (binding energy) of +39.4 kcal/mol, which is, again, in good agreement with experiments.

The formation of methane is an interesting issue since thermodynamics would favor it while experiments suggest its absence. Although extra hydrogen from the gas

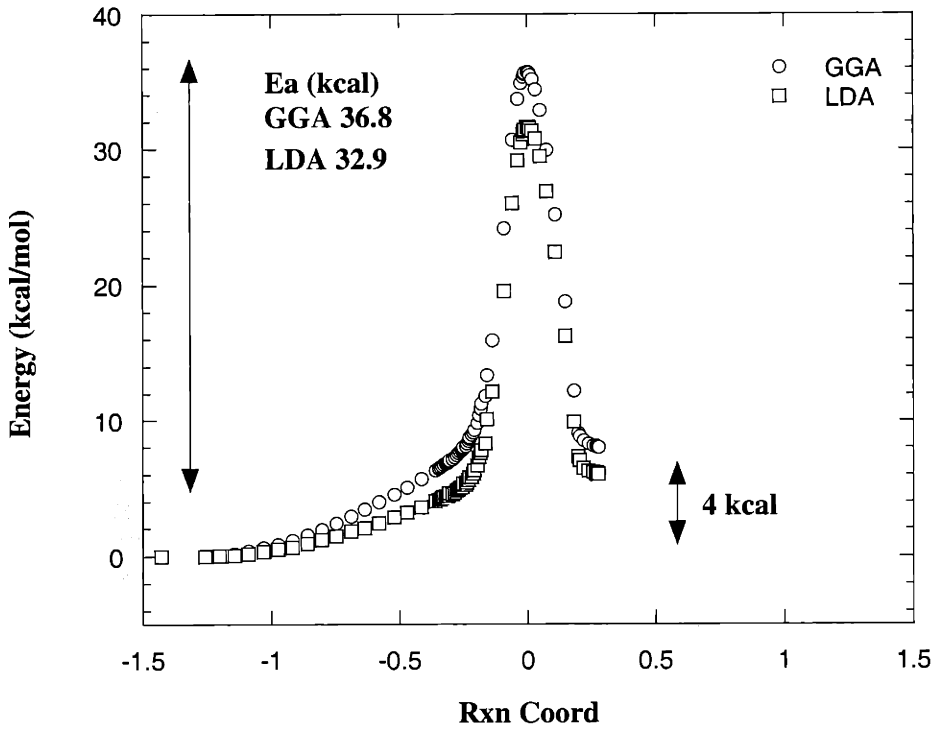

Figure 5.13 Potential Energy vs. Reaction Coordinate for methyl dehydrogenation on Al(100), $*CH_3 \Rightarrow *CH_2 + *H$.

phase would be necessary (and not likely on Al) for an all methane growth mechanism, thermodynamics would favor some methane elimination over an all-disproportionation chemistry. In addition, the reaction $CH_3* + H* \Rightarrow CH_4(g)$ is approximately thermo-neutral which indicates a symmetric barrier, which need not necessarily be very large in the forward direction (as would be the case in a largely endothermic reaction, for example). The absence of a methane pathway, if not an experimental oversight, could be attributed to several circumstances. One possibility is that under growth conditions there is a low steady state concentration of H or CH_3 groups and other recombination reactions dominate. Another possibility is that the complex nature of hydrogen on aluminum makes it difficult for hydrogen and methyl to interact (unfavorable entropy of activation). Lastly, the most obvious reason could be due to a large activation barrier. A large barrier would be consistent with observations that CH_4 exposure in the UHV chamber at pressures up to 10^6 Torr at temperatures of 650 K does not cause carbon contamination

on aluminum crystals. A high barrier for methane formation would be consistent with the low reactivity of free electron metals.[8]

The methane reaction pathway is an example of an issue that could be further investigated with theoretical surface chemistry tools to answer the above questions and expand upon DMAH and aluminum surface chemistry. Preliminary investigations find a repulsive interaction between H and CH_3 groups on the surface which hint at a high barrier, but a true transition state has not been located. Given that the corresponding reaction on the more reactive Ni(111) surface has a recombination-desorption barrier near +20, it is reasonable to imagine a large barrier on aluminum.[32] Molecular beam experiments to explore the reverse process, sticking of CH_4 on Al, would be a nice experiment-theory complementary study similar to the objectives of this thesis.[99] Additional investigation of the CH_4 reaction pathway is suggested in Chapter 7, Recommendations for Future Work.

5.7 Comments, Cluster vs. Slab

Before concluding this chapter on theoretical studies of the growth chemistry of DMAH, it is instructive to reflect on the choice of theoretical surface reaction models. The present investigations suggest that other than the strongest interaction (MMAl binding), a surface model of a three layer slab with 16 **k** points and a 40 Ry cutoff is sufficient for a semi-quantitative evaluation of surface reaction pathways. Thicker slabs, more **k** points, larger surface cells, and greater plane wave cutoffs can be used for more accurate calculations, but are not expected to change the semi-quantitative features of the reaction pathways. With sufficient convergence of the calculations, it is expected an accuracy akin to DFT calculations in the gas phase (~5 kcal/mol) may be realized. Improvements in pseudopotentials and optimization algorithms would serve to make the calculations more CPU efficient and bring additional aspects of surface reactions into range for study, (introducing defects and larger periodic cells, for example).

Table 5.14 Comparison between cluster and slab calculations for a few representative binding energy calculations (values in kcal/mol). In both the slab and cluster calculations, the surface is frozen in the bulk lattice arrangement, and the adsorbate is optimized.

	Cluster (9 Al atoms)	Slab (PWPP)
H top	69.1	46.1
CH_3 top	39.5	39.4
$AlCH_3$ 4-fold	67.3	67.4

To further reflect on the choice of PWPP calculations for surface chemistry, a small representative series of calculations were performed on aluminum clusters. Binding energies and adsorbate geometries were calculated for H, CH_3, and $AlCH_3$ on a nine atom cluster to compare with plane wave calculations (Table 5.14). Results are mixed. A binding energy for CH_3 in an on-top position comes out of the cluster calculation as +39.5 kcal/mol, which is nearly identical to the slab calculations at +39.4 kcal/mol. The binding energy of CH_3 is surprisingly good considering that 16 **k** points were needed to converge the PWPP calculation on a three-layer slab. The binding of $AlCH_3$ in a four-fold site, +67.3 kcal/mol, is also in excellent agreement with slab calculations, +67.4 kcal/mol. Unfortunately larger cluster calculations were not practical, and the calculations could not be confirmed to have converged with respect to cluster size. The good results may be an artefact of a cluster size dependence; previous studies have indicated that binding energies may vary dramatically with cluster sizes.[50] Results for hydrogen binding are closer to anticipated behavior, with errors > 20 kcal/mol. It should be noted that even if cluster calculations are sometimes good for binding energy calculations, they present a problem for bond breaking reactions (unless much larger clusters are used). However, the good agreement between slab and cluster calculations for CH_3 and $AlCH_3$ suggests that the cluster model may be useful for calculations of adsorbate zero point energies and thermal energy corrections, with slab calculations used as a reference for binding energies.

5.8 Summary and Conclusions

Theoretical surface calculations have been employed to investigate quantitative aspects of an experimentally proposed reaction mechanism for aluminum CVD with DMAH. Within a model of a perfect surface (no defects) and rigid lattice, most aspects of the reaction chemistry were considered. DMAH reaction thermodynamics were characterized by evaluating heats of reaction for each elementary step and generating a thermodynamic map of the disproportionation mechanism. The reaction kinetics of several important reaction steps in the disproportionation mechanism were characterized by evaluating activation barriers for elementary surface reactions. Alternative reaction pathways including methyl dehydrogenation and methyl radical ejection were also considered. Where experiment and theory overlap, agreement is good, within approximately 5 kcal/mol. Although calculations are currently limited to relatively small systems with simple adsorbates, they provide a powerful complement to surface chemistry experiments and allow complicated mechanisms to be characterized in a quantitative fashion.

Taking into account the quantitative description of the disproportionation reaction, the mechanism proposed in Chapter 4 does appear to be thermodynamically reasonable. The only area for concern is the ~+30 kcal/mol barrier for decomposition of MMAl fragments. Given the apparent activation energies of ~ 7-12 kcal/mol observed experimentally, a +30 kcal/mol barrier seems rather large. However, considering the calculation as an upper bound due to the rigid lattice and x-y constrained adatom approximations, and the possible role of surface defects, the barrier may be closer to 20-30 kcal/mol. As will be shown in the next chapter, such a value is consistent with the observed growth behavior.

5.9 References

(1) Payne, M. C.; Teter, M. P.; Allan, D. C.; Arias, T. A.; Joannopoulos, J. D. *Rev. Mod. Phys.* **1992**, *64*, 1045.

(2) Norskov, J. K. *Surf. Sci.* **1994**, *299/300*, 690.

(3) Ito, T. *J. Appl. Phys.* **1995**, *77*, 4845.

(4) Jing, Z.; Whitten, J. L. *Surf. Sci.* **1992**, *274*, 106.

(5) Ihara, S.; Ho, S. L.; Uda, T.; Hirao, M. *Phys. Rev. Lett.* **1990**, *65*, 1909.

(6) Yang, H. a. W., J.L. *J. Am. Chem. Soc.* **1991**, *113*, 6442.

(7) Lang, N. D. *Surf. Sci.* **1994**, *299/300*, 284.

(8) Norskov, J. K. *Rep. Prog. Phys.* **1990**, *53*, 1253.

(9) Hammer, B.; Norskov, J. K. *Surf. Sci.* **1995**, *343*, 211.

(10) Hammer, B.; Norskov, J. K. In *Chemisorption and Reactivity on Supported Clusters and Thin Films*; lambert, R. M., Pacchioni, G., Eds., 1997; pp 285.

(11) Ricart, J. M., Rubio,J., Illas,F., and Bagus, P.S. *Surf. Sci.* **1994**, *304*, 335.

(12) Ruban, A.; Hammer, B.; Stoltze, P.; Skriver, H. L.; Norskov, J. K. *pre-print* .

(13) Staufer, M.; Neyman, K. M.; Jakob, P.; Nasluzov, V. A.; Menzel, D.; Rosch, N. *Surf. Sci.* **1996**, *369*, 300.

(14) Jigato, M. P.; Somasundram, K.; Termath, V.; Handy, N. C.; King, D. A. *Surf. Sci.* **1997**, *380*, 83.

(15) van Santen, R. A.; Neurock, M. *Catal. Rev. Sci. Eng.* **1995**, *37*, 557.

(16) Whitten, J. L. *Chem. Phys.* **1993**, *177*, 387.

(17) van Santen, R. A. *Theoretical Heterogeneous Catalysis*; World Scientific: Singapore, 1991.

(18) Holmblad, P. M.; Larsen, J. H.; Chorkendorff, I.; Nielsen, L. P.; Besenbacher, F.; Stensgaard, I.; Laegsgaard, E.; Kratzer, P.; Hammer, B.; Norskov, J. K. *pre-print* .

(19) Li, Y. S.; van Daelen, M. A.; Wrinn, M.; King-Smith, D.; Newsam, J. M.; Delley, B.; Wimmer, W.; Klitsner, T.; Sears, M. P.; Carlson, G. A.; Nelson, J. S.; Allan, D. C.; Teter, M. P. *J. Comp. Aid. Mat. Des.* **1993**, *1*, 199-214.

(20) Hammer, B.; Norskov, J. K. *Nature* **1995**, *376*, 238.

(21) Kratzer, P.; Hammer, B.; Norskov, J. K. *Surf. Sci.* **1996**, *359*, 45.

(22) Gunderson, D.; Hammer, B.; Jacobsen, K. W.; Norskov, J. K.; Lin, J. S.; Milman, V. *Surf. Sci.* **1993**, *285*, 277.

(23) Chou, M. Y.; Chelikowsky, J. R. *Phys. Rev. Lett.* **1987**, *59*, 1737.

(24) Chou, M. Y.; Chelikowsky, J. R. *Phys. Rev. B* **1989**, *39*, 5623.

(25) Feibelman, P. J. *Phys. Rev. Lett.* **1991**, *67*, 461.

(26) Mlynarski, P. *J. Chem. Phys.* **1991**, *95*, 6050.

(27) Goursot, A. *J. Am. Chem. Soc.* **1992**, *114*, 7452-7458.

(28) Maruca, R.; Kusuma, T.; Hicks, V.; Companion, A. *Surf. Sci.* **1990**, *236*, 210.

(29) van Daelen, M. A.; Li, Y. S. *Chem. Phys. Lett.* **1994**.

(30) Cheng, H.; Reiser, D. B.; Mathias, P. M.; Dean, S. J. *Am. Inst. Chem. Eng.* **1998**, *44*, 188.

(31) Neurock, M. In *Dynamics of Surfaces and Reaction Kinectics in Heterogeneous Catalysis*; Froment, G. F., Waugh, K. C., Eds.; Elsevier: Belgium, 1997; Vol. 109; pp 3.

(32) Kratzer, P.; Hmmer, B.; Norskov, J. K. *J. Chem. Phys.* **1996**, *105*, 5595.

(33) Chelikowsky, J. R.; Schluter, M.; Louie, S. G.; Cohen, M. L. *Sol. State Comm.* **1975**, *17*, 1103.

(34) Feibelman, P. J. *Phys. Rev. Lett.* **1990**, *65*, 729.

(35) Stumpf, R.; Scheffler, M. *Phys. Rev. Lett.* **1994**, *72*, 254.

(36) Gillan, M. J. *J. Phys: Condens. Matter* **1989**, *1*, 689.

(37) Finnis, M. W. *J. Phys. Condensed Matter* **1990**, *2*, 331.

(38) Feibelman, P. J. *Phys. Rev. Lett.* **1992**, *69*, 1568.

(39) Gundersen, K.; Jacobsen, K. W.; Norskov, J. K.; Hammer, B. *Surf. Sci.* **1994**, *304*, 131.

(40) Hammer, B.; Jacobsen, K. W.; Norskov, J. K. *Phys. Rev. Lett.* **1992**, *69*, 1971.

(41) Stumpf, R. *Phys. Rev. Lett.* **1997**, *78*, 4454.

(42) Furthmuller, J.; Kresse, G.; Hafner, J.; Stumpf, R.; Scheffler, M. *Phys. Rev. Lett.* **1995**, *74*, 5084.

(43) Jacobsen, J.; Hammer, B.; Jacobsen, K. W.; Norskov, J. K. *Phys. Rev. B* **1995**, *52*, 14954.

(44) Pisani, C. *J. Mol. Catal.* **1993**, *82*, 229.

(45) Wahlgren, U. a. S., Per. In *Trends in Applied Theoretical Chemistry*; Montero, L. A., Smeyers, Y. G., Eds., 1992; pp 1-17.

(46) Das, T. In *Electronic Properties of Solids using cluster Methods*; Kaplan, T. A., Mahanti, S. D., Eds.; Plenum Press: New York, 1995; pp 1.

(47) Whitten, J. L. In *Electronic Properties of Solids using Cluster Methods*; Kaplan, T. A., Mahanti, S. D., Eds.; Plenum Press: New York, 1995; Vol. 53.

(48) Foresman, J. B.; Frisch, A. *Exploring Chemistry with Electronic Structure Methods*; Gaussian, Inc.: Pittsburgh, 1996.

(49) Goncalves, V.; Mijoule, C. In *Metal Ligand Interactions*; Russo, N., Salahub, D. R., Eds.; Kluwer Academic Publishers: Netherlands, 1996; pp 267.

(50) Masel, R. I. *Principles of Adsorption and reaction on Solid Surfaces*; John Wiley & Sons, Inc.: New York, 1996.

(51) Cohen, M. L. *Phys. Today* **1979**, 40.

(52) Troullier, N.; Martins, J. L. *Phys. Rev. B* **1991**, 1993.

(53) Car, R.; Parrinello, M. *Phys. Rev. Lett.* **1985**, *55*, 2471.

(54) Vanderbilt, D. *Phys. Rev.* **1990**, *41*, 7892.

(55) Laasonen, K.; Pasquarello, A.; Car, R.; Lee, C.; Vanderbilt, D. *Phys. Rev. B* **1993**, *47*, 10142.

(56) Phillips, J. C.; Kleinman, L. *Phys. Rev.* **1959**, *116*, 287.

(57) Ihm, J.; Zunger, A.; Cohen, M. L. *J. Phys. C: Solid State Phys.* **1979**, *12*, 4409.

(58) Wimmer, E. In *Density Functional Methods in Chemistry*; Labanowski, J. K., Andzelm, J. W., Eds.; Springer-Verlag: New York, 1991; pp 7.

(59) Denteneer, P. J. H.; Haeringen, W. v. *J Phys. C: Solid State Phys.* **1985**, *18*, 4127.

(60) Kresse, G.; Furthmuller, J. *Comp. Mater. Sci.* **1996**, *pre-print*.

(61) King-Smith, R. D.; Payne, M. C.; Lin, J. S. *Phys. Rev. B* **1991**, *44*, 13063.

(62) Hamman, D. R.; Schluter, M.; Chiang, C. *Phys. Rev. Lett.* **1979**, *43*, 1494.

(63) Bachelet, G. B.; Hamann, D. R.; Schluter, M. *Phys. Rev. B* **1982**, *26*, 4199.

(64) Vosko, S. H.; Wilk, L.; Nusair, M. *Can. J. Phys.* **1980**, *58*, 1200.

(65) Kleinman, L.; Bylander, D. M. *Phys. Rev. Lett.* **1982**, *48*, 1425.

(66) Kohn, W.; Becke, A. D.; Parr, R. G. *J. Phys. Chem.* **1996**, *100*, 12974.

(67) Perdew, J. P.; Chevary, J. A.; Vosko, S. H.; Jackson, K. A.; Pederson, M. R.; Singh, D. J.; Fiolhais, C. *Phys. Rev. B* **1992**, *46*, 6671.

(68) Perdew, J. P. In *Electronic Structure Theory of Solids '91*; Ziesche, P., Eschrig, H., Eds.; Akademie Verlag: Berlin, 1991; pp 11.

(69) Perdew, J. P. *Phys. Rev. B* **1986**, *33*, 8822.

(70) Hohenberg, P.; Kohn, W. *Phys. Rev.* **1964**, *136*, B864.

(71) Kohn, W.; Sham, L. J. *Phys. Rev.* **1965**, *140*, A1133.

(72) Parr, R. G.; Yang, W. In *Annu. Rev. Phys. Chem.*, 1995; Vol. 46; pp 701.

(73) Teter, M. P.; Payne, M. C.; Allan, D. C. *Phys. Rev. B* **1989**, *40*, 12255.

(74) Wood, D. M.; Zunger, A. *J. Phys. A* **1985**, *18*, 1343.

(75) Pulay, P. *Chem. Phys. Lett.* **1980**, *73*, 393.

(76) Monkhorst, H. J.; Pack, J. D. *Phys. Rev. B* **1976**, *13*, 5188.

(77) Evarestov, R. A.; Smirnov, V. P. *Phys. Stat. Sol. B* **1983**, *119*, 9.

(78) Neugebauer, J.; Scheffler, M. *Phys. Rev. B* **1992**, *46*, 16067.

(79) Mermin, N. D. *Phys. Rev.* **1965**, *137*, A1441.

(80) Methfessel, M.; Paxton, A. T. *Phys. Rev. B* **1989**, *40*, 3616.

(81) Hammer, B. A theoretical study of H_2 dissociation on aluminum, Danish Technical University, 1993.

(82) Garcia, A.; Elsasser, C.; Zhu, J.; Louie, S. G.; Cohen, M. L. *Phys. Rev. B* **1992**, *46*, 9829.

(83) Frisch, M. J.; Trucks, G. W.; Schlegel, H. B.; Gill, P. M. W.; Johnson, B. G.; Robb, M. A.; Cheeseman, J. R.; Keith, T. A.; Petersson, G. A.; Montgomery, J. A.; Raghavachari, K.; Al-Laham, M. A.; Zakrewski, V. G.; Ortiz, J. V.; Foresman, J. B.; Cioslowski, J.; Stefanov, B. B.; Nanayakkara, A.; Challachombe, M.; Peng, C. Y.; Ayala, P. Y.; Chen, W.; Wong, M. W.; Andres, J. L.; Replogle, E. S.; Gomperts, R.; Martin, R. L.; Fox, D. J.; Binkley, J. S.; Defrees, D. J.; Baker, J.; Stewart, J. P.; Head-Gordaon, M.; Gonzalez, C.; Pople, J. A. ; Gaussian, Inc.: Pittsburgh, 1995.

(84) Becke, A. D. *Phys. Rev. A* **1988**, *38*, 3098.

(85) Curtiss, L. A., Krishnan Ragavachari, Gary W. Trucks, and John Pople. *J. Chem. Phys.* **1991**, *94*, 7221.

(86) Hehre, W. J.; Radom, L.; Schleyer, P. v. R.; Pople, J. A. *Ab initio Molecular Orbital Theory*; John Wiley & Sons: New York, 1986.

(87) Hjelmberg, H. *Surf. Sci.* **1979**, *81*, 539.

(88) Kristyan, S.; Pulay, P. *Chem. Phys. Lett.* **1994**, *229*, 175.

(89) Mole, T. *Aust. J. Chem.* **1964**, *17*, 1050.

(90) Winkler, A.; Pozgainer, G.; Rendulic, K. D. *Surf. Sci.* **1991**, *251/252*, 886.

(91) Hammer, B., Jacobsen, K.W. and Norskov, J.K. *Phys. Rev. Lett.* **1993**, *70*, 3971.

(92) Kondoh, H.; Nishihara, C.; Nozoye, H.; Hara, M.; Domen, K. *Chem. Phys. Lett.* **1991**, *187*, 466.

(93) Paul, J. *Phys. Rev. B* **1988**, *37*.

(94) Simka, H.; Willis, B. G.; Lengyel, I.; Jensen, K. F. *Prog. Crystal Growth and Charact.* **1998**, *35*, 117.

(95) Steinfeld, J. I.; Francisco, J. S.; Hase, W. L. *Chemical Kinetics and Dynamics*; Prentice Hall: New Jersey, 1989.

(96) Truhlar, D. G.; Garrett, B. C.; Klippenstein, S. J. *J. Phys. Chem.* **1996**, *100*, 12771.

(97) Benson, S. W. *Thermochemical Kinetics*, 2nd ed.; John Wiley & Sons: New York, 1976.

(98) Dumesic, J. A.; Rudd, D. F.; Aparicio, L. M.; Rekoske, J. E.; Trevino, A. A. *The Mircokinetics of Heterogeneous Catalysis*; American Chemical Society: Washington, DC, 1993.

(99) Lee, M. B.; Yang, Q. Y.; Ceyer, S. T. *J. Chem. Phys.* **1987**, *87*, 2724.

Chapter 6

Putting it Together: Simulations of DMAH Growth

6.1 A "Complete" Mechanism

Compiling both experimental and theoretical investigations of the previous chapters, a fairly complete mechanism can be constructed for aluminum CVD with DMAH. The reaction mechanism embodies chemisorption of the DMAH precursor, disproportionation to produce TMA, a parallel disproportionation mechanism for alane, impurity incorporation, alternative reaction pathways, and surface diffusion. In addition to the surface reactions, it is also possible to include gas phase reactions, both for transport of stable species (investigated in Chapters 2 & 3) and gas phase pyrolysis products. Surface reaction pathways for gas phase pyrolysis fragments such as $Al(CH_3)_x$, AlH_x, and CH_x can be deduced from the surface chemistry investigations. Although not investigated in the present study, aluminum and carbon adatom dynamics, surface defect dynamics, carbon and hydrogen diffusion on the aluminum surface and into the bulk, and surface re-constructions might also be included. Including the above features into a growth model requires atomistic simulation techniques. In this chapter, a simplified, continuum approach is investigated.

A refined reaction mechanism, described below, is implemented and compared with experimental data. Kinetic parameters are estimated using a combination of information from previous chapters and micro-kinetic[1] style estimation of pre-exponential factors. Although the bulk of theoretical and experimental investigations were performed

Table 6.1 Refined Reaction Mechanism.

1.	$[AlH(CH_3)_2]_2(g) + *_d \overset{s}{\Rightarrow} 2^*Al(CH_3)_2 + 2^*H$
2.	$^*Al(CH_3)_2 + * \underset{krec}{\overset{kuni}{\Leftrightarrow}} {}^*Al(CH_3) + {}^*CH_3$
3.	$^*\#Al(CH_3)_2 + * \underset{krec}{\overset{kuni}{\Leftrightarrow}} {}^*\#Al(CH_3) + {}^*CH_3$
4.	$^*Al(CH_3) + * \underset{krec}{\overset{kuni}{\Leftrightarrow}} Al(bulk) + {}^*CH_3 + *_d$
5.	$^*\#Al(CH_3) + * \underset{krec}{\overset{kuni}{\Leftrightarrow}} Al(bulk/defect) + {}^*CH_3 + *$
6.	$^*Al(CH_3)_2 + {}^*CH_3 \overset{kdes}{\Rightarrow} Al(CH_3)_3(g) + * + *_d$
7.	$^*\#Al(CH_3)_2 + {}^*CH_3 \overset{kdes}{\Rightarrow} Al(CH_3)_3(g) + 2*$
8.	$^*H + {}^*H \overset{kdes}{\Rightarrow} H_2(g)$

with a model of the Al(100) surface, for the present simulations the Al(111) surface is modeled. Aluminum CVD films are often highly Al(111) textured[2], and this close-packed surface is most relevant to growth simulations. The results of the previous chapters are therefore viewed as a guide to developing a reaction mechanism. In any case, uncertainty in pre-exponential factors prohibits strict application of the calculations. The LSODE[3] integrator package was used for the simulations, and a downhill simplex code[4] was written to allow non-linear least squares parameter fitting.

6.2 A Refined Reaction Mechanism

A refined surface reaction mechanism is listed in Table 6.1. Reducing the large number of possible surface reactions to a core set for simulations was accomplished using experimental observations, theoretical calculations, and making some judicious assumptions. Justification for the mechanism trimming is detailed below for each class of surface reactions.

Note that each of the reactions listed in Table 6.1 occurs as an elementary reaction on the growing surface. However, in order to simulate the observed reaction behavior with a continuum approach, it is necessary to lump reaction and diffusion for some reaction steps. As discussed in Chapter 4, the complex sticking behavior of DMAH requires introduction of "defect" sites, where chemisorption may occur. These sites saturate quickly, and further adsorption can only occur once these sites are emptied. Clearing of the defect sites is assumed to occur when mono-methylaluminum fragments from the original, chemisorbed DMAH decompose to aluminum adatoms and surface methyl groups. Freeing of defect sites is therefore a combined reaction-diffusion step. It would also be reasonable to "release" the adsorption-active "defect" site after unimolecular decomposition of the $Al(CH_3)_2$ surface fragments. Using lattice gas/stochastic methods (Monte Carlo), diffusion could be included as a separate process, rather than coupled to reaction.

From TPD experiments, it is clear that many of the surface reactions are reversible. Unlike the chemisorption step, these reversible reactions are assumed to take place independently of the presence of adsorption-active "defect" sites. To incorporate reverse reactions apart from the defect sites, it is necessary to introduce two "types" of $AlCH_3$ and $Al(CH_3)_2$ adsorbates. One type resides on defect sites (from chemisorption), and the second type is created from a reverse/etching reaction. The reverse (etched) adsorbates are labeled with a # sign in Table 6.1. Both reactions are treated with identical kinetic parameters.

Chemisorption & Recombinative Desorption

For the present simulations of UHV scattering experiments, the only significant flux reaching the surface is the precursor, DMAH. Full reactor simulations would require allowing TMA as well as any pyrolysis fragments to reach on the surface. The theoretical calculations of Chapter 5, as well as steric arguments and classic aluminum organometallic chemistry[5], suggest the Al-H bond is the first to break in DMAH. Therefore, only chemisorption through breaking the Al-H bond is considered. From the studies of Chapters 2 and 3, it is clear that chemisorption of DMAH occurs through

higher oligomers such as the dimer and trimer. In the simulations, it assumed, for simplicity, that only dimers arrive at the surface. Based on the experiments and arguments listed below, it is assume the only products leaving the surface are hydrogen molecules and TMA.

Unimolecular Surface Decomposition of Chemisorbed Aluminum Fragments

Given the insignificant probability of hydrogen chemisorption (even as a carrier gas) on aluminum surfaces, and the low hydrogen surface coverage expected in DMAH growth, parallel reactions of hydrogen to form alane are not expected to be important for reactor simulations. Therefore, these etching reactions are omitted from the refined growth mechanism. However, hydrogen-etching reactions could be important for understanding aluminum surface morphology.

Hydrogen Desorption

Molecular hydrogen desorption is needed in the refined mechanism to balance the reaction. However, as discussed in Chapter 4, hydrogen is a complicated system on aluminum surfaces. Although there have been several investigations of hydrogen desorption from aluminum surfaces, these studies have focused on the high coverage limit. At high coverages, hydrogen desorption exhibits zero'th order desorption. The observed desorption behavior can be explained in terms of desorption from the aluminum bulk, desorption from densely packed islands, or desorption of alane. The rate parameters extracted from the above studies do not characterize the low coverage regime where hydrogen desorption may be second order. Based on the available experimental data, hydrogen desorption should be very fast at DMAH growth temperatures. In addition, considering the low surface coverage during DMAH growth, hydrogen desorption is not expected to be crucial to the growth simulations. Therefore, hydrogen desorption is not included in the simulations. It is assumed that hydrogen desorption is facile and that hydrogen does not interfere with the other reactions.

Impurity Mechanism

In the present simulations of scattering experiments, the temperature range is limited to regions where methyl groups are stable on the surface. Therefore, the impurity mechanism is not operative. An impurity mechanism could be included and compared with the high temperature scattering data of Chapter 4. However, according to the experimental observations, carbon diffusion into the bulk of aluminum becomes rapid at these high temperatures. Simulations of AlC_x growth would most likely have to include carbon bulk diffusion. In addition, the thermodynamic and kinetic description of the presently investigated reaction mechanism might change when the carbon coverage becomes significant.

Alternative Reaction Pathways

Alternative reaction pathways such as radical ejection, methane formation, and methyl coupling reactions are not included in the growth mechanism. Based on both experiments and theoretical calculations, radical ejection reactions are not expected be operative at temperatures characteristic of clean aluminum growth. The lowest barrier for such a reaction (methyl ejection) is predicted to be near +40 kcal/mol. Less is known concerning the methane formation pathway, but experimental investigations argue against such a pathway. Additionally, several studies on related systems support the absence of a methane pathway. In addition, the previous studies oppose a methyl coupling mechanism.[6-8]

6.3 Kinetic Parameters

Ideally, the quantum chemistry investigations of Chapter 5 could be combined with normal mode analyses and statistical mechanical relations to predict partition functions for the reactants, transition states, and products of the surface reactions. Combining the partition functions with calculated activation barriers would allow transition state theory estimates for surface reaction rate constants. Currently, such an approach is not practical. Therefore, estimates of rate constants are derived using both

quantum chemistry estimates of reaction barriers, and micro-kinetic concepts for pre-exponential factors.

Typical pre-exponential factors for first and second order surface reactions range from 10^{12}-10^{15} s^{-1} and 10^{-4}-10^{4} cm^2/s, respectively.[9] For second order bimolecular reactions, the lower limit of 10^{-3}-10^{-4}, corresponding to immobile activated complexes, seems appropriate for the present mechanism. To reduce the number of kinetic parameters and take advantage of the quantum chemistry calculations, forward and reverse rate constants are related through the equilibrium constant, K_c (units of molecules and cm^2). Given the above estimates for pre-exponential factors, K_c is expressed:

$$K_c = \frac{k_f}{k_r} = \frac{A_{unimolecular} * \exp\left(\frac{-Ea}{R*T}\right)}{A_{bimolecular} * \exp\left(\frac{-Ea}{R*T}\right)} \approx \frac{10^{13}\left(1/s\right)}{10^{-3}\left(cm^2/s\right)} * \exp\left(\frac{-\Delta H_0}{R*T}\right)$$

Heats of reaction are estimated from ΔE values of Chapter 5 (no zero-point energy or thermal corrections included). The prefactor ~10^{16} can be regarded as the entropy component (exp(ΔS/R)). The above expression provides a starting point for generating rate constants. From these initial values, a non-linear least squares procedure is used to adjust values to better fit experimental data.

Further refinement of the reaction mechanism is accomplished by relating adsorption-desorption steps. Assuming DMAH and TMA have similar sticking probabilities and using micro-kinetic arguments provides a relation between the sticking coefficient and the rate constant for recombinative desorption of TMA. The adsorption and desorption rate constants are expressed:

$$k_{ads} \approx 100 * s * \sqrt{\frac{k_b * T}{2 * \pi * M}} \quad cm/s$$

$$k_{bimolecular} \approx A_{bimolecular} * \exp\left(\frac{-Ea}{R*T}\right) \approx 10^{-3} * \exp\left(\frac{-Ea}{R*T}\right) \quad cm^2/s$$

Plugging in approximate values gives an estimate for K_c:

$$K_c = \frac{k_{des}}{k_{ads}} = \frac{A_{bimolecular} * \exp\left(\frac{-Ea}{R*T}\right)}{100 * \sqrt{\left(\frac{k_b * T}{2 * \pi * M}\right)} * s_o * \exp\left(\frac{-Ea}{R*T}\right)} \approx \frac{10^{-3}}{10^4} * \exp\left(\frac{-\Delta H_0}{R*T}\right)$$

Due to the complex nature of the adsorption step and reverse/etching reactions, two slightly arbitrary parameters were introduced into the reaction mechanism. These are the adsorption-active "defect" density (#/cm^2), and the aluminum adatom "defect" density (#/cm^2). Uncertainty regarding the sticking process requires the empirical parameter for the adsorption-active defect density. This parameter and the sticking coefficient are complementary parameters that determine the high temperature, low coverage, flux-limited growth rate. Therefore, given a flux, they are linearly dependent. The adatom density represents more of a problem since it is rather arbitrary. Recently, it has been suggested that hydrogen may extract aluminum ad-atoms from the bulk, and form mono-hydride units[xiv]. A similar feat might be expected for surface methyl groups. This type of mechanism is less intuitive than reaction with free adatoms or steps, and makes it difficult to quantify the etching reaction.

Due to the above complications with reverse/etching reactions, temperature programmed desorption simulations are not included in the present investigations. TPD simulations are not currently practical, because of uncertainties of the mechanism in the reverse direction. In addition to concerns about the reverse reactions, one of the problems with TPD simulations is the uncertainty of initial adsorbate coverages. Inaccurate estimations of both absolute coverage and relative adsorbate populations could bias estimation of kinetic parameters. With atomistic simulations and knowledge of adatom dynamics, however, TPD simulations could also be performed. Surface science data for carbon concentrations (after TPD experiments) gives an indication of surface methyl

[xiv] Presentation by J.E. Reutt-Robey at the 1998 American Vacuum Society (AVS) meeting, Baltimore, MY.

coverage, and this could also be employed to test the rate parameters. For the scattering simulations studied in the following section, reverse reactions are expected to be less crucial than for TPD simulations.

Based on the approach detailed above, kinetic parameters have been generated for each surface reaction. In cases where two different "types" of surface species exist, identical rate parameters are used. The rate parameters used in the present simulations are listed in Table 6.2. These values should be considered flexible since small deviations can be accommodated by a compensation effect among the other parameters.

Table 6.2 Rate parameters used in DMAH growth simulations. Units are cm^2 and seconds.

Forward Rate Constants		Equilibrium Constants
2&3.	$1x10^{13}$*exp(-8,000/RT)	$1.0x10^{15}$*exp(+18,000/RT)
4&5.	$5x10^{14}$*exp(-20,000/RT)	$1.0x10^{20}$*exp(-16,000/RT)
Desorption-Adsorption EQ		
6&7.		$4.0x10^{-8}$*exp(-6,500/RT)
Parameters		
s (sticking coefficient)		.31
*d (# of adsorption-active sites/cm^2)		$1x10^{13}$
*Al (# of etching active sites/cm^2)		$1x10^{7}$

6.4 Scattering Simulations

Kinetic simulations of the refined growth mechanism are illustrated along with experimental data in Figure 6.1. Simulations are performed for two different experiments, which differ by almost an order of magnitude in flux. For the kinetic regime of interest, the model provides a good fit to the experimental data. The small signal increase in the experimental data beyond ~420 K is due to an experimental artefact, and the simulations are shown up to this temperature. The background signal begins to rise at this temperature due to the hot button heater and the small size of the crystal. Experiments reported in Chapter 4 on larger Al(100) crystals show less drift. The most important aspect of the model behavior is the gradual slope that closely matches the

experimental data. The good agreement between the experimental and simulated scattering vs. temperature behavior indicates the simulations capture the low apparent activation energy. The mechanism faithfully reproduces the small apparent activation energies illustrated in the experimental data and reported in the literature, even though the "rate limiting" reaction has an activation barrier ~20 kcal/mol. The overall results are good, especially considering experimental uncertainties such as: ramp rate variations, geometric effects of the scattered flux, button heater characteristics, background signal, drift in the flux, and drift from the electronics.

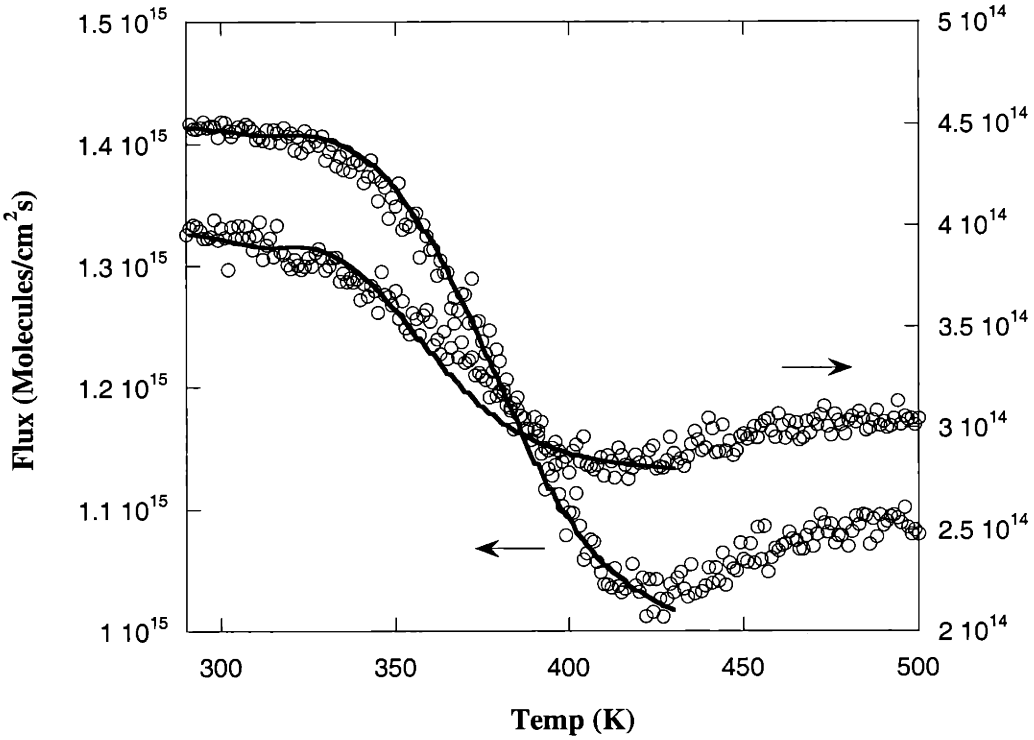

Figure 6.1 Comparison of scattering experiments and simulations, for two different fluxes. Dots represent experimental data, and the lines are simulation results.

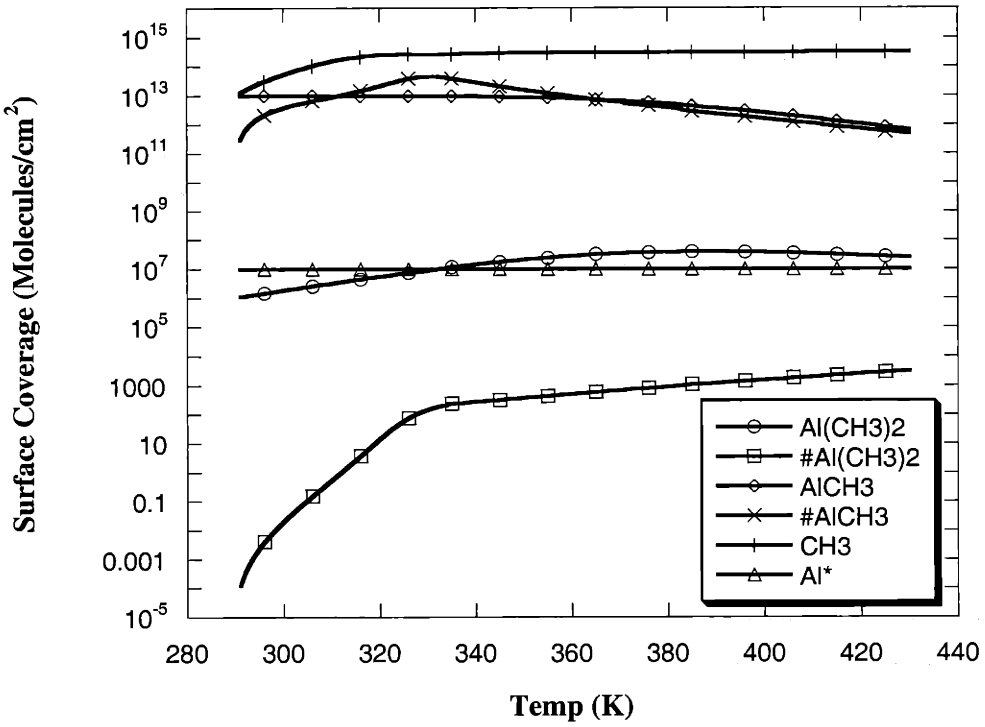

Figure 6.2 Log plot of adsorbate surface concentrations (molecules/cm^2) during DMAH scattering simulations.

Figures 6.2 and 6.3 illustrate surface coverage as a function of temperature during scattering simulations. As can be seen in the figure, at high temperatures methyl groups dominate the surface with high coverages, even though defect sites are needed for adsorption. These predictions are consistent with several experimental observations. The high methyl group coverage explains the large amounts of carbon detected on the surface, in spite of the small TMA desorption features observed. Large concentrations of methyl groups remain on the surface after experiments, and these methyl groups dehydrogenate at high temperatures to give surface carbon. Additionally, the large concentration of surface methyl groups, even at relatively low temperatures, lends support to one of the arguments presented in Chapter 4 regarding the complex sticking behavior of DMAH. Although adsorption-active "defect" sites are implemented in the current growth model, it is possible that high surface coverages of methyl groups inhibit DMAH chemisorption

and account for the low apparent surface coverage during TPD experiments. DMAH chemisorption may be very sensitive to methyl surface coverage, and the sticking coefficient may decrease accordingly.

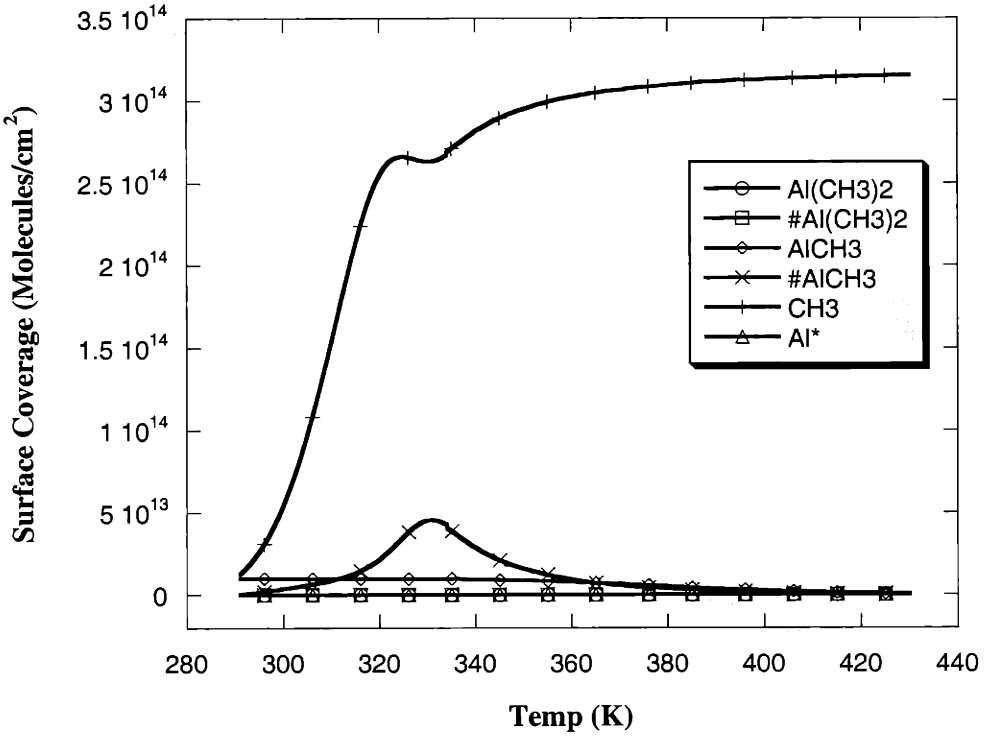

Figure 6.3 Linear plot of adsorbate surface concentrations (molecules/cm^2) during DMAH scattering simulations.

Due to the high methyl surface coverage, simulations predict a very small concentration of $Al(CH_3)_2$ adsorbates. These adsorbates encounter methyl groups and desorb, or decompose to $AlCH_3$ fragments rapidly. MMAl adsorbates have a significant coverage, which is approximately an order of magnitude smaller than the surface methyl coverage. Interestingly, etching reactions to form $\#AlCH_3$ are important, and simulations predict comparable $AlCH_3$ and $\#AlCH_3$ concentrations. Further etching to produce $\#Al(CH_3)_2$ is apparently less favorable, and their concentration is far below fresh DMAl fragments. Etching reactions to form MMAl species indicate the aluminum

adatom/defect concentration may be important. In the current model, the etching "active" adatom concentration is kept constant at $1x10^7$ atoms/cm^2. Given the importance of the etching reactions, surface coverages are expected to be sensitive to this parameter. High defect concentrations may shift the $AlCH_3/CH_3$ ratio towards the MMAl groups. Perhaps a sensitive HREELS (High Resolution Electron Energy Loss) spectrometer could be used to quantify surface methyl and MMAl groups and compare with simulations.

6.5 Extensions, Summary, and Conclusions

The principal accomplishment of the present growth simulations is that a complex growth mechanism has been broken down into its elementary reactions through a complimentary experimental and theoretical approach. A reaction mechanism consistent with both experimental data and thermodynamic calculations has been constructed, and elementary reaction rate parameters have been estimated from quantum chemistry calculations. The advantage of this procedure is that the detailed growth model has a physical basis upon which further improvements can be made. Many different choices of parameters could fit the observed experimental data, but the current simulations are consistent with all experimental observations and quantum chemistry calculations.

The above surface reaction mechanism can now be combined with a gas phase mechanism in reactor simulations to solve for both gas phase pyrolysis products and transport rates of species to the growing surface. Results could then be incorporated into growth models and feature profile evolution models and compared with further experimental data. Detailed surface reaction models can be used to perform growth simulations along with data from Al-diffusion (adatom dynamics) and physical vapor deposition (PVD) models to simulate surface morphology. It would be especially interesting to seek theoretical understanding of the differences between PVD and CVD deposition methods.

References

(1) Dumesic, J. A.; Rudd, D. F.; Aparicio, L. M.; Rekoske, J. E.; Trevino, A. A. *The Microkinetics of Heterogeneous Catalysis*; American Chemical Society: Washington, DC, 1993.

(2) Littau, K. A.; Mosely, R.; Zhou, S.; Zhang, H.; Guo, T. *Microelectron. Eng.* **1997**, *33*, 101.

(3) Hindmarsh, A. *ACM-SIGNUM Newsletter* **1980**, *15*, 11.

(4) Press, W. H.; Flannery, B. P.; Teukolsky, S. A.; Vetterling, W. T. *Numerical Recipes*; Cambridge University Press: Cambridge, 1989.

(5) Mole, T. *Aust. J. Chem.* **1964**, *17*, 1050.

(6) Squire, D. W. *J. Vac. Sci. Technol. B* **1985**, *3*, 1513.

(7) Francis, J. T.; Benson, S. W.; Tsotsis, T. T. *J. Phys. Chem.* **1991**, 4583.

(8) Squire, D. W.; Dulcey, C. S.; Lin, M. C. *Chem. Phys. Lett.* **1985**, *116*, 525.

(9) Zhdanov, V. P.; Pavlicek, J.; Knor, Z. *Catal. Rev. Sci. Eng.* **1988**, *30*, 501.

Chapter 7

Summary and Recommendations for Future Work

7.1 Introduction

The main objectives of this thesis have been to demonstrate how quantum chemistry calculations can compliment surface science experiments to develop detailed, quantified reaction models. To this end, both the gas phase and surface chemistry of DMAH have been investigated. Based on the studies, detailed reaction models with novel reaction pathways have been investigated. These models provide a basis for understanding aspects of the growth chemistry of DMAH, and they also provide an example of how quantum chemistry calculations can be used to solve practical problems, on real chemical systems. Results from the present studies illustrate how chemically accurate values for thermodynamic and kinetic parameters can be obtained from quantum chemistry calculations, although with considerable CPU resource requirements. Currently, accurate calculations are CPU limited, but further advances in computing technologies will invite greater accuracy and larger problems. Additionally, the present investigations have shown how computational chemistry methods are complementary to experiments, and how they can be used to develop detailed, physically based reaction models.

As a finale to the present body of work, several remaining issues are considered. Below are brief accounts of interesting aspects of DMAH growth chemistry that would complement the current studies. Although the present studies have sought to gain detailed knowledge of the DMAH growth system, there are several aspects of the growth

chemistry which remain unexplored. The purpose of this chapter is to acknowledge some of the more important issues that would be of interest, either from a basic surface science standpoint, or from applied perspectives. Many of these topics would be useful subjects for further study, either as a continued effort, or as introductory problems for new students with similar interests. The suggested topics are organized and discussed by chapter.

7.2 Comments, by Topic

7.2.1 Bridge Bonded Aluminum Compounds

Bridge bonded aluminum compounds have a place in quantum chemistry (QC) methods due to their sensitivity to electron exchange and correlation. It can be argued that an exchange-correlation functional which works well for these compounds, as well as the "standard" G2 set[1], may be a great improvement, with applications to diverse bonding arrangements. Therefore, it is worthwhile to pursue new exchange-correlation functionals introduced into the literature, and evaluate them for bridge bonded compounds. Such studies provide a benchmark for the universality of new functionals. Other, more detailed studies of the bonding in these compounds, akin to "reverse engineering" of exchange-correlation functionals, could also be useful.[2,3]

A second topic related to studies of Chapter 2 is prediction of the TMA monomer-dimer equilibrium. Unlike the case for DMAH, quantitative experimental data is available for the TMA equilibrium. TMA has long been established to exist as a dimer at room temperature. Quality *ab initio* simulations are, however, in substantial disagreement with the experimental data. Additionally, based on experimental and calculated thermodynamic values, the error does not appear to reside solely with the enthalpy of reaction. The other half of the equilibrium predictions, entropy calculations, are based on established statistical mechanical relations, and it seems unlikely these relations would produce the observed error. Additionally, calibration data from UHV experiments predict an effective mass for TMA near 90 amu, substantially less than TMA dimer (144 amu). Previous mass spectroscopy studies also did not observe significant

amounts of TMA dimer.[4] These observations may, in fact, be due to simple differences between experiments in solvents and observations at reduced pressures. However, it may be worthwhile to re-examine the TMA monomer-dimer equilibrium.

7.2.2 DMAH Gas Phase Reaction Pathways

The results of Chapter 3 hinge upon the analogy between DMAH and alane. While the analogy seems reasonable for a qualitative description of DMAH, quantitative aspects remain unexplored. These quantitative aspects include a more detailed study of DFT methods and their reliability for predicting transition state energetics. From Chapter 2, it is know DFT heats of reaction can be in substantial error for bridge-bonded complexes. The errors certainly appear in calculations of reverse rate constants (the unimolecular reactions). On the other hand, a detailed understanding of the applicability for predicting transition state barriers for forward reactions (before bridge-bonds completely form) is lacking. The best approach to this problem would be to explore high level QC methods with the alane reaction *2 dimer* $\Leftrightarrow$ *tetramer*. Also, this same reaction may be useful to explore differences between activation barriers for alane, DMAH, and aluminum nitride or alkoxide compounds. For DMAH, the CH_3 terminal groups are less electronegative than the H ligands of alane, so the activation barrier may be expected to increase or decrease depending on the relative influence of the electron density and steric interactions on the transition-state.

Lastly, full-scale reactor simulations of the DMAH mechanism could provide in-depth understanding as to the makeup of gas approaching the surface. Due to the relatively low temperatures involved in DMAH growth (< 300°C) it may be expected that gas phase pyrolysis of the precursors will not occur. However, other reactions such as the formation of pentamethyldialane and the gas phase disproportionation to form alane may be dependent on operating conditions (temperatures, residence times, boundary layer thickness, etc...). Given detailed surface chemistry models and some understanding of the sticking behavior, it may be possible to correlate the gas phase environment with characteristics of the resulting thin films.

7.2.3 DMAH Surface Chemistry - Experimental

The most significant aspect of the experimental surface chemistry that remains unknown is the sticking behavior of the aluminum organometallic precursors DMAH and TMA. While the present study has explored in great detail the surface reactions of DMAH growth, the most basic reaction, that of sticking, needs further study. Results indicate a complex sticking behavior, and in Chapter 4 it is hypothesized the sticking reaction proceeds through a bimolecular-like reaction between surface adatoms or "defects", and DMAH. If such a process were operative, it suggests there are different classes of low sticking behavior. Adsorption via defects implies a high sticking coefficient but with a low concentration of reactive surface species, and therefore an observed low sticking probability. On the other hand, a diminutive rate of adsorption could be due to an inherently low probability of reaction due to the dynamics of the process (inhibition by surface methyl coverage, for example). Different classes of sticking behavior could operate for different types of compounds (DMAH vs. TIBA vs. TTBA vs. TMA, etc.) Given that primary benefits of CVD processes for ULSI applications are the low reaction probabilities and extensive sampling of the growing surface, sticking behavior may be vital to a detailed understanding of growth morphology. Profile evolution would depend on the type of sticking mode operative.

Other complementary surface science experiments could seek to quantify surface intermediate populations. Plane wave pseudopotential calculations predict AlH, $AlCH_3$, and CH_3 fragments are the most stable on the surface. Experimental techniques such as vibrational spectroscopy and scanning tunneling microscopy could be used to identify surface intermediates and calculate surface concentrations. These experimental quantities could then be directly compared with atomistic simulations of growth based on *ab initio* calculations and detailed atomistic simulation techniques (Kinetic Monte Carlo methods). STM experiments could also be used to construct an accurate representation of a growing surface so that steps, adatoms, vacancies, and other surface topography could be included in atomistic simulations.

The present studies have focussed on the disproportionation mechanism for impurity-free growth of aluminum films. Surface science experiments also reveal an

interesting chemistry at high temperatures. While the surface does change at high temperatures due to carbon incorporation, the present studies suggest the same reaction pathways occur on the AlC_x surface, albeit with different rates. The two major pathways that lead to growth are methyl dehydrogenation and radical ejection of methyl groups into the gas phase. Given the higher activation of the radical ejection, it is expected the surface actually becomes more aluminum rich at higher temperatures. This observation is supported by experiments which show lower carbon/aluminum ratios at higher temperature versus the near Al_4C_3 ratio seen at ~650 K. The problem is complicated, though, by simultaneous surface reaction and diffusion of carbon atoms into the bulk. Auger Electron Spectroscopy scans of the surface after high temperature growth (AlC_x) show significant differences when taken several minutes apart. It is apparent that at high growth temperatures (700-800 K) diffusion of carbon into the bulk is rapid. It would be interesting to study depth profiles of growth under various conditions and compare them with a reaction-diffusion model. The problem is one-dimensional, and if not analytically solvable, still a straight forward computational problem.

7.2.4 DMAH Surface Chemistry - Theoretical

Surface quantum chemistry calculations require several levels of approximation, including finite super-cells and slab thicknesses, DFT exchange-correlation functionals, pseudopotentials, rigid lattice approximations, perfect periodicity, and plane wave cutoffs. The present work has covered some of these effects in a limited fashion, but the calculations were limited to pseudopotentials constructed with LDA all-electron calculations. As reasoned in Chapter 5, these pseudopotentials could be responsible for an Al-C bond length error. While it is not expected that major adjustments in the calculated energetics would occur, it would be worthwhile to explore GGA derived pseudopotentials and compare various calculations to establish a comparison.

In Chapter 5 it was argued that methane formation on aluminum may have a large barrier. A common understanding of the reactivity of transition metals is that partially occupied d-orbitals interact with adsorbate bonding and anti-bonding states during chemisorption, which aids in lowering the reaction barrier. SP bonded metals, on the

other hand, are thought to be less reactive due to the absence of such effects. Exploring methane formation/ chemisorption on aluminum would therefore contribute to both an applied and fundamental understanding of chemisorption. The problem is well stated and the only reason the methane pathway is not included in the present study is due to time constraints. Methane formation could be explored on Al(100) to be consistent with the present study, but a previously published transition state for methane chemisorption on a Ni(111) surface provides a guess for Al(111).[5]

In regards to future implementation of PWPP calculations using the slab approach, there is one additional feature that would greatly enhance its capabilities. The current geometry optimization scheme for surface adsorbates implements a molecular dynamics algorithm to minimize the forces. While this approach may be efficient for very few degrees of freedom, it became notably inefficient for studies of large molecules such as DMAH and TMA. A simple improvement would be to transform the coordinates of the adsorbate into internal coordinates, do the same for the forces, and update the geometry. In this way, unimportant degrees of freedom such as CH bonds and bond angles could be frozen.

7.2.5 DMAH Growth Simulations

In Chapter 6 a simplified growth mechanism was constructed from experiments and *ab initio* calculations to establish the disproportionation mechanism is consistent with experimental data. Further investigations of the growth chemistry of DMAH on aluminum would benefit from more detailed simulations which can introduce surface topography and surface diffusion. The calculations of Chapter 5 could be used to provide the necessary parameters. In addition, the literature could be consulted for existing models of aluminum homo-epitaxy and then incorporated these into advanced atomistic CVD models.

7.3 References

(1) Curtiss, L. A., Krishnan Ragavachari, Gary W. Trucks, and John Pople. *J. Chem. Phys.* **1991**, *94*, 7221.

(2) Tozer, D. J.; Handy, N. C.; Green, W. H. *Chem. Phys. Lett.* **1997**, *273*, 183.

(3) Green, W. H.; Tozer, D. J.; Handy, N. C. *Chem. Phys. Lett.* , *pre-print*.

(4) Tanaka, J.; Smith, S. R. *Inorg. Chem.* **1969**, *8*, 265.

(5) Kratzer, P.; Hmmer, B.; Norskov, J. K. *J. Chem. Phys.* **1996**, *105*, 5595.